Solid State Spectroscopy : Laser Selective Excitation Studies of Neodymium

A thesis
submitted for the Degree
of
Doctor of Philosophy in Physics
in the
University of Canterbury

by

T.P.J. Han

University of Canterbury
1988

To
my parents
and
my wife, Helen.

Acknowledgement

I wish to record my thanks to Professor B.G. Wybourne for making a Teaching Fellowship available which enabled me to undertake this research project.

I would like to express my gratitude to my supervisors Dr. G.D. Jones and Dr. R.W.G. Syme for their discussions and guidance.

I would also like to acknowledge and thank Dr. C.A. Freeth and Dr. M.F. Reid for their valuable discussions on crystal field calculations.

The patience and willing support from members of the Physics department technical staff; namely Wayne Smith, Ross Ritchie and Clive Rowe was greatly appreciated by myself. I would also like to express my gratitude to the late Terry Rowe whose skills and understanding helped many postgraduate students over the years.

I am indebted to my fellow research students for their friendship and support, particularly Andrew Riddell, Hughan Ross, Dr. B. Sherborne, Bill Brown, Steve Wood, Dr. R.J. Reeves and Dr. N.J. Cockroft.

Above all, I would like to thank my parents, Dr. and Mrs. D.W.F. Han, for their constant support and encouragement.

Finally, I am indebted to my wife, Helen, for editing much of this text, her support and faith in me during the final years of my studies.

Abstract

When trivalent rare earth (RE^{3+}) ions are introduced into the alkaline earth fluoride, they substitute for the divalent cation and some form of charge compensation is required for the crystal to maintain charge neutrality. A wide variety of symmetry configurations can be produced depending on the charge compensator(s) and the rare earth ion(s) in the lattice. The selective laser excitation technique was used to determine the symmetry of the various dopant centres in CaF_2 and SrF_2 doped with Nd^{3+} ions; both before and after hydrogenation treatment.

Previously unassigned energy levels of F^- charge compensating centres of tetragonal and orthorhombic symmetry in $CaF_2 : Nd^{3+}$ and $SrF_2 : Nd^{3+}$ have been identified by the energy upconversion processes. The upconversion mechanisms for the tetragonal centre are attributed to be dominated by the sequential two photon excitation process (STEP), whereas the two orthorhombic centres are attributed to be dominated by the phonon-assisted energy transfer upconversion process (ETU).

The hydrogenic analogues of the well established tetragonal centre in $CaF_2 : Nd^{3+}$ and $SrF_2 : Nd^{3+}$, and other hydrogenic charge compensating centres were studied. The fluorescence of some of the multiple charge compensating hydrogenic centres were found to exhibit 'bleaching' behaviours. These effects are attributed to the migration of the hydrogenic ions adjacent to the rare earth ion.

For the tetragonal centres, the C_{4V} irreducible representation designations of the crystal field levels were identified by their intensity variations in the polarisation studies.

Energy transfer between the rare earth ions within a cluster centre was established by studying the M' centres in the $CaF_2 : Nd^{3+}$ co-doped with Ce^{3+}, Gd^{3+} or Yb^{3+} rare earth ions. These multiple rare earth ion centres also exhibit energy upconversion processes similar to those observed for the orthorhombic centres in $CaF_2 : Nd^{3+}$.

Crystal field analyses have been carried out for the tetragonal centres observed in $CaF_2 : Nd^{3+}$ and $SrF_2 : Nd^{3+}$ and a simplified superposition model was used to analyse the distortions in these centres. The crystal field results are in satisfactory agreement with the experimental data and predicted the experimentally unobserved Z_4 energy level for the various C_{4V} centres.

Contents

List of Figures

List of Tables

Chapter 1

Introduction

The purpose of this thesis is to report on the experimental results obtained from a laser selective excitation study of trivalent neodymium ions doped in fluorite type crystals; both before and after hydrogenation treatment.

Neodymium is one of the lanthanide (or 'rare earth') series which is characterised by the progressive filling of the $4f$ electronic shell. As $4f^n$ configurations are partially shielded from fluctuations in the surrounding crystalline field by the outer closed $5s$ and $5p$ shells, the lanthanides all have very similar, though not identical, chemical behaviour. The trivalent ions have the xenon-like rare gas shell of 54 electrons in common and a partially filled $4f$ shell. Their trivalent salts have absorption spectra and, in most cases, fluorescence spectra with sharp lines in the visible, near-ultraviolet or near-infrared regions. It is generally agreed that these sharp line spectra arise from transitions between crystal field levels of the various LSJ multiplets of the $4f^n$ configuration. Neodymium has the $4f^3$ configuration, whose LSJ multiplet structure is given in Fig. 1.1. These multiplets are often labelled by single letters with the ground multiplet $^4I_{9/2}$ being labelled Z and the excited multiplets as shown in Fig. 1.1. The single letter notation is used extensively throughout this thesis and the LSJ labels are needed only to identify the different LSJ multiplets grouped under the single letter notation.

The triply ionized neodymium ion has been investigated in various host materials (Kaminskii et al. 1974, Partlow et al. 1967, Prokhorov et al. 1969, Asawa et al. 1966, Bonchkovskii et al. 1973, Barthem et al. 1985, Voron'ko et al. 1969, Reddy et al. 1983, Venkateswarlu et al. 1984, Vignaneswara et al. 1977) because it has desirable laser properties and, perhaps more importantly, because it is an excellent probe for investigating impurity ion interactions with host materials. The ^4I_J ground multiplets of Nd^{3+} are relatively pure and lend themselves to analysis in the Russell- Saunders basis; yet have sufficient number of levels, 26 in an electrostatic field of sufficiently low symmetry, to provide a stringent test of crystal field models. Moreover, each of its levels is a Kramers' doublet that may be split by a magnetic field giving Zeeman interaction information for detailed model calculations.

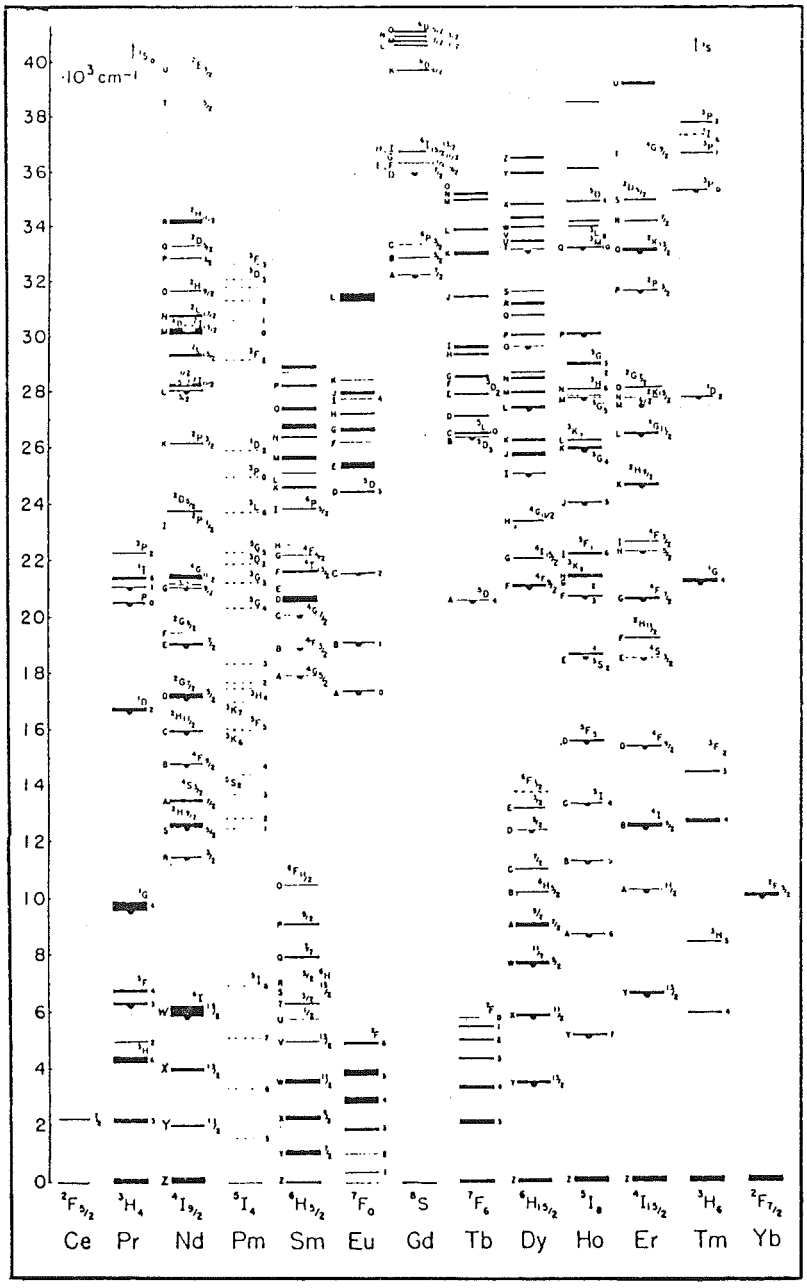

Figure 1.1: Observed energy levels of the rare earth ions. The thickness of each level represents the total crystal field splitting in $LaCl_3$. A pendant semicircle indicates that this level fluoresces in the $LaCl_3$ structures. Reproduced from Dieke 1968.

The alkaline-earth fluorides (CaF_2 , SrF_2 , BaF_2) consist of a simple cubic lattice of fluorine ions in which every other body centre position is occupied by a divalent alkaline-earth ion (Me^{2+}). They are good as hosts for the purpose of investigating trivalent rare-earth ions, because they are relatively easy to grow in large single crystal form and readily accept rare- earth dopants. In addition, the band gap for these materials is large (Hayes 1974) so that the optical spectra can be investigated to wavelengths as short as 120 nm.

When trivalent rare earth (RE^{3+}) ions are introduced into the alkaline-earth fluoride, they substitute for the divalent cation (Me^{2+}) and some form of charge compensation is required for the crystal to maintain charge neutrality. This can take place in several spatial configurations depending on the relative positions of the charge compensator(s) and the RE^{3+} ion(s) in the lattice. The charge compensating F^- ions can be substituted by oxygen ions, monovalent cations or, in this study, H^- , D^- and T^- ions. A wide spectrum of symmetry configurations have been observed ranging from single-RE^{3+} ion compensator pairs to multi-RE^{3+} ion clusters (Andreen et al. 1968, Voron'ko et al. 1965, Ashburner et al. 1965). The relative concentration of the various centres are found to be dependent upon the growth conditions, RE^{3+} concentrations and thermal treatment of the sample. When the charge compensation is remote from the rare earth ion the cubic (O_h) symmetry of the crystalline field at the Ca^{2+} site is preserved; but if it is sufficiently close, the symmetry of the electric field can be reduced from cubic to tetragonal, trigonal or even rhombic. A review of this topic is given by Baker (1974). The existence of many of these different configurations is established through a variety of techniques, with electron paramagnetic resonance (EPR) being a very powerful method for unravelling site symmetries (Kask et al. 1964, 1965, 1968, Edgar et al. 1977, Baker et al. 1980). A review of the results of different techniques applied to various rare earth ions can be found in Moore's thesis (1980).

The site symmetries of Nd^{3+} ions in CaF_2 and SrF_2 have been investigated mainly by electron paramagnetic resonance (EPR) (Kask et al. 1966, 1968a, b, c, Edgar et al. 1977, Baker et al. 1980,). These investigations showed the Nd^{3+} ions to be in fields of cubic, tetragonal or orthorhombic symmetry. The tetragonal symmetry centre in $CaF_2 : Nd^{3+}$ and, to a lesser extent, in $SrF_2 : Nd^{3+}$ has attracted particular attention in both experimental and theoretical investigations. The methods used include Ionic Thermocurrent (Popov et al. 1974), Zeeman Infrared (Edgar et al. 1977), Optical Zeeman (Stacy et al. 1973), EPR (Kask et al. 1964, 1966, 1968a, b, c, Edgar et al. 1977, Baker et al. 1980), ENDOR (Kiro et al. 1969, Secemski et al. 1970) and Fluorescence Lifetime (Kaminskii et al. 1965).

The principal aim of this research was to characterise the hydrogenic analogues of the well established tetragonal symmetry fluorine centres in $CaF_2 : Nd^{3+}$ and $SrF_2 : Nd^{3+}$; and also determine other hydrogenic com-

pensation centres and additional new fluorine centres present. Another research aspect was to investigate the energy transfer mechanisms involved in the different symmetry centres. This was motivated by the observation of energy upconversion in both single-ion and multi-ion centres and by the reported experimental results for $CaF_2 : Nd^{3+} : RE^{3+}$ (RE^{3+} : any trivalent rare earth ion from La^{3+} to Lu^{3+}) (Voron'ko et al. 1968, 1971, Batygov et al. 1973) which suggested the existence of multi-RE^{3+} ion centres. Fluorescence lifetimes were determined, where possible, for all identified centres.

Chapter 2

Theory

2.1 Crystal Field Theory

The complex energy level structures of the rare earth ions were successfully unravelled with the advent of powerful tensor operator techniques and crystal field theory. This work has been well documented by Condon and Shortley (1951), Judd (1963), Wybourne (1965), and Dieke (1968). The Hamiltonian for a rare earth ion in a crystalline potential field can be written as :

$$H_T = H_F + V \quad , \tag{2.1}$$

where H_F is the Hamiltonian of the free ion and V is the crystalline potential field experienced by the rare earth ion from the surrounding ions, called ligands. The Hamiltonian for a free ion of N electrons with a nuclear charge Ze is :

$$H = \left[-\frac{\hbar^2}{2m_e} \sum_{i=1}^{N} \nabla_i^2 - \sum_{i=1}^{N} \frac{Ze^2}{r_i} + \sum_{i<j}^{N} \frac{e^2}{r_{ij}} + \sum_i \xi(\underline{r}) \underline{l}_i \cdot \underline{s}_i \right] \quad , \tag{2.2}$$

where the terms are the kinetic energies of all the electrons, the electron-nuclear potential energy, the repulsive Coulomb potential energy of the interaction between pairs of electrons and the spin-orbit energy, respectively. The electrostatic interaction yields ^{2S+1}L (Russell-Saunders) terms with separations of the order of $10^4\ cm^{-1}$. The spin-orbit interaction splits these terms into J multiplets with typical separations of $10^3\ cm^{-1}$. The energies of these free ion LSJ states can be expressed in terms of the Racah parameters E^1, E^2 and E^3, and the spin-orbit parameter ξ. The J degeneracy of these free ion states is partially or fully removed by the crystalline potential field. For a configuration containing an odd number of electrons there is a remaining two-fold Kramers' degeneracy which can only be lifted by application of an external magnetic field. In the labelling of the rare earth ion states

the LSJ designation has the LS labels of the dominant Russell-Saunders component of the corresponding J multiplet eigenfunction.

For rare earth ions the above intermediate coupling scheme is found to be appropriate, where states of different L and S are mixed by a relatively small spin-orbit interaction. This mixing can be expressed in terms of intermediate coupling reduction factors which are obtained by diagonalising all the J matrices with each matrix of an order equal to the number of levels with that particular J. The resulting eigenfunctions give the intermediate coupling wavefunctions as linear combination of LS terms.

The crystalline potential field V can be treated as a perturbation on the free ion states. The crystal field potential is expanded in a series of spherical harmonic terms of the form :

$$V_{CF} = \sum_{i,k,q}^{N} B_q^k (C_q^{(k)})_i \quad , \tag{2.3}$$

where the B_q^k are crystal field parameters describing the strength of the crystalline field components, the $C_q^{(k)}$ are Racah tensor operator components with transformation properties corresponding to those of the spherical harmonics, and the sum is over the N electrons of the $4f^N$ configuration. The number and types of terms appearing in the expansion are derivable using group theory, given the point symmetry at the rare earth ion site. If only f-electrons are involved in the summation, the terms in the expansion are zero for k odd and for k greater than six. The matrix elements of these operators may be calculated using the formulae given by Wybourne (1965).

The tetragonal, C_{4V} , symmetry Hamiltonian is often written in terms of spherical tensors $C_q^{(k)}$ as :

$$H_{C_{4V}} = B_0^2 C_0^{(2)} + B_0^4 C_0^{(4)} + B_4^4 (C_4^{(4)} + C_{-4}^{(4)}) + B_0^6 C_0^{(6)} + B_4^6 (C_4^{(6)} + C_{-4}^{(6)}) \quad . \tag{2.4}$$

However, this formulation gives little indication of the magnitude of the cubic part of the crystal field. The tetragonal symmetry centres have approximately cubic, O_h , symmetry, with an interstitial charge compensating ion as the next nearest neighbour reducing the symmetry to C_{4V}. The parameterisation used by Freeth and Jones (1982) distinguishes an axial part :

$$H_{axial} = B_0^2 C_0^{(2)} + B_0^4 C_0^{(4)} + B_0^6 C_0^{(6)} \quad , \tag{2.5}$$

from a cubic part :

$$H_{cubic} = B^4 \left[C_0^{(4)} + \sqrt{\frac{5}{14}} \left(C_4^{(4)} + C_{-4}^{(4)} \right) \right]$$

$$+ B^6 \left[C_0^{(6)} - \sqrt{\frac{7}{2}} \left(C_4^{(6)} + C_{-4}^{(6)} \right) \right] \quad . \tag{2.6}$$

This is preferable to equation 2.4 but is not completely satisfactory because $C_0^{(4)}$ and $C_0^{(6)}$ do not have well defined transformation properties under O_h and are not orthogonal to the terms in equation 2.6.

Reid (1981) has shown that when an ion is placed in a crystal, it is more natural to use a chain of groups which reflect the exact symmetry of the centre. Using the chain of groups decomposition method Butler and Wybourne (1976) generated tables for all point groups. A crystal field Hamiltonian is more diagonal in such point group bases than in the JM basis. These basis states are therefore more 'physical' because they are a closer approximation to the eigenstates of the Hamiltonian, and the invariant tensors are more obvious. In the point group basis, following the notation of Butler (1981), the tetragonal crystal field Hamiltonian is written as :

$$\begin{aligned} H_{C_{4V}} \;=\; & X^{2+2+0+0} U^{2+2+0+0} + X^{4+0+0+0} U^{4+0+0+0} + X^{4+2+0+0} U^{4+2+0+0} \\ & + X^{6+0+0+0} U^{6+0+0+0} + X^{6+2+0+0} U^{6+2+0+0} \quad , \end{aligned} \tag{2.7}$$

where the labels refer to O_3 , O_h , D_4 and C_4 respectively. The crystal field parameters X^{ab00} and the point group unit tensors U^{ab00} are related to the B_q^k and the $C_q^{(k)}$ in the JM basis respectively. They can be transformed to the JM basis using the tables given by Butler (1981) :

$$\begin{aligned} U^{6+0+0+0} &= -\sqrt{\frac{1}{8}} C_0^{(6)} + \sqrt{\frac{7}{4}} \left[C_4^{(6)} + C_{-4}^{(6)} \right] \\ U^{4+0+0+0} &= \sqrt{\frac{7}{12}} C_0^{(4)} + \sqrt{\frac{5}{24}} \left[C_4^{(4)} + C_{-4}^{(4)} \right] \\ U^{6+2+0+0} &= \sqrt{\frac{7}{8}} C_0^{(6)} + \frac{1}{4} \left[C_4^{(6)} + C_{-4}^{(6)} \right] \\ U^{4+2+0+0} &= \sqrt{\frac{5}{12}} C_0^{(4)} - \sqrt{\frac{7}{24}} \left[C_4^{(4)} + C_{-4}^{(4)} \right] \\ U^{2+2+0+0} &= -C_0^{(2)} \quad . \end{aligned}$$

The two octahedral terms $U^{4+0+0+0}$ and $U^{6+0+0+0}$ are invariant under octahedral, O_h, symmetry and the other 3 terms only occur for the lower C_{4V} symmetry for which effects are expected to be smaller. The tetragonal symmetry crystal field Hamiltonian in the JM basis can be rewritten as :

$$H_{C_{4V}} \;=\; B_{tet}^2 \left[-C_0^{(2)} \right]$$

$$
\begin{aligned}
&+ B^4_{tet} \left[\sqrt{\frac{5}{12}}\, C^{(4)}_0 - \sqrt{\frac{7}{24}} \left(C^{(4)}_4 + C^{(4)}_{-4} \right) \right] \\
&+ B^6_{tet} \left[\sqrt{\frac{7}{8}}\, C^{(6)}_0 + \frac{1}{4} \left(C^{(6)}_4 + C^{(6)}_{-4} \right) \right] \\
&+ B^4_{oct} \left[\sqrt{\frac{7}{12}}\, C^{(4)}_0 + \sqrt{\frac{5}{24}} \left(C^{(4)}_4 + C^{(4)}_{-4} \right) \right] \\
&+ B^6_{oct} \left[-\sqrt{\frac{1}{8}}\, C^{(6)}_0 + \sqrt{\frac{7}{4}} \left(C^{(6)}_4 + C^{(6)}_{-4} \right) \right] \quad , \qquad (2.8)
\end{aligned}
$$

where

$$B^k_{tet} = X^{k+2+0+0}$$

$$B^k_{oct} = X^{k+0+0+0}$$

The $C^{(4)}$ and $C^{(6)}$ tetragonal terms are now orthogonal to the $C^{(4)}$ and $C^{(6)}$ octahedral terms. A crystal field Hamiltonian of this form is used for the crystal field analysis given in this thesis. The parameters of this Hamiltonian are related to those used by Freeth and Jones (1982) by the following relationships :

$$
\begin{aligned}
B^2_{tet} &= -B^2_0 \\
B^4_{tet} &= \sqrt{\frac{5}{12}}\, B^4_0 \\
B^6_{tet} &= \sqrt{\frac{7}{8}}\, B^6_0 \\
B^4_{oct} &= \sqrt{\frac{12}{7}} \left[B^4 + \frac{7}{12}\, B^4_0 \right] \\
B^6_{oct} &= -\sqrt{8} \left[B^6 + \frac{1}{8}\, B^6_0 \right] \quad .
\end{aligned}
$$

The resulting predicted energy levels are compared to the observed values and, by an iterative least squares fitting procedure, the crystal field parameters are adjusted to obtain an optimum fit to experimental data. The size of the standard deviation will indicate the validity of the theoretical description of the energy level structure of the symmetry centre being studied. It must be emphasized that a small standard deviation alone does not guarantee the correctness of the description. A correct theoretical description should also yield eigenfunctions that can be used to calculate other physical observables with a comparable precision.

2.2 Superposition Model

The crystal field parameters can be interpreted using a superposition model pioneered by Newman (1971). The superposition model makes no assumption about the interaction mechanism between the rare earth ion and its neighbours except that the effects of the individual ligand on the rare earth ion is taken to be independent and each has an axial (C_∞) symmetry.

Newman (1971) has shown that the crystal field parameters can be written as a function of the co-ordinates $(R\,,\theta\,,\phi)$ of each of the surrounding ions and of intrinsic parameters $\overline{A}_k$ for these ions. As the first shell of the surrounding ions is responsible for most of the crystal field, to a first approximation, in the context of the tetragonal symmetry centre, the summation includes the eight nearest neighbours and the interstitial charge compensating ions. The rare earth ion is at the origin with the nearest neighbours labelled 1 to 8 and the interstitial charge compensating ion, labelled 9, on the z axis, as shown in Fig. 2.1. The angular co-ordinates of the nearest neighbours are $(\theta_a\,,\pi/2(n-1/2))$ for $n = 1$ to 4 and $(\theta_b\,,\pi/2(n-1/2))$ for $n = 5$ to 8.

Newman (1978) has shown that for rare earth ions in cubic symmetry centres in CaF_2 , SrF_2 and BaF_2 the intrinsic parameters $\overline{A}_4$ and $\overline{A}_6$ follow a power law $(R_0/R)^{t_k}$ where R_0 is the mean distance between the rare earth ion and its surrounding neighbours, R is the distance between the rare earth ion and its surrounding neighbours, $t_4 = 6.3$ (± 1.4) and $t_6 = 10.1$ (± 1.1). The Racah tensor operators, $C_q^{(k)}$, already used in the crystal field expression equation 2.3, are defined by :

$$C_q^{(k)} = \sqrt{\frac{4\pi}{(2k+1)}}\; Y_{kq} \quad , \tag{2.9}$$

with the spherical harmonics Y_{kq} defined by :

$$Y_{kq}(\theta\,,\phi) = (-1)^q \sqrt{\frac{(2k+1)(k-|q|)!}{4\pi(k+|q|)!}}\; P_k^q(cos\,\theta)\; exp\;(iq\phi) \quad , \tag{2.10}$$

where the associated Legendre polynomials

$$P_k^q(w) = (1-w^2)^{\frac{q}{2}}\;(2^k k!)^{-1}\;\frac{d^{k+q}}{dw^{k+q}}\;(w^2-1)^q \tag{2.11}$$

and

$$w = cos\,\theta \quad .$$

Therefore for several ligands at different distances to the rare earth ion a given crystalline field parameter B_q^k can be expressed as :

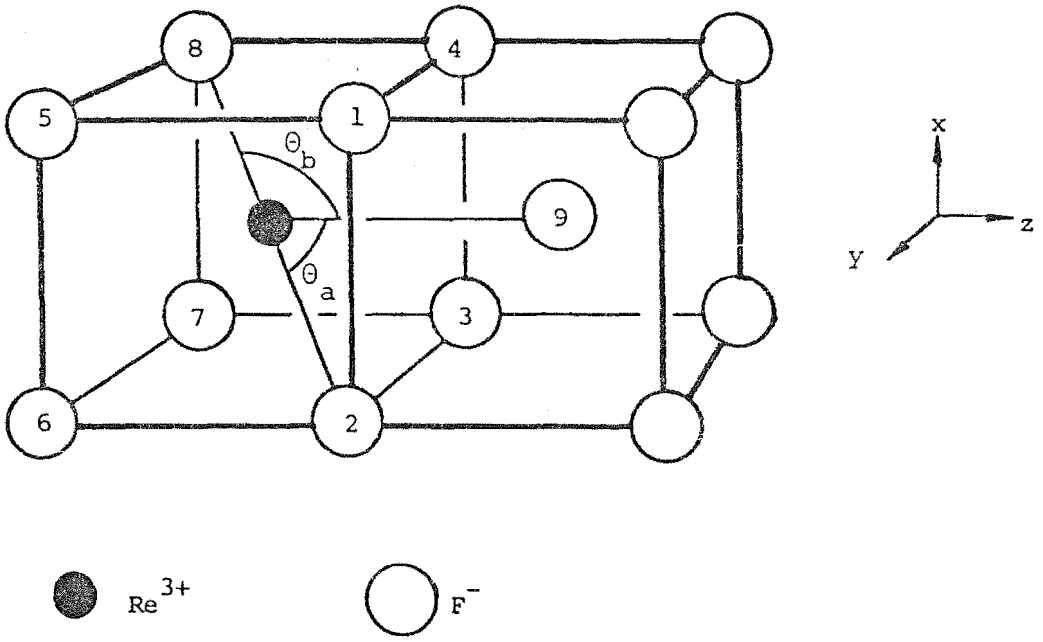

Figure 2.1 Model for the tetragonal symmetry centre. Numbers on the F^- ions identify them for the model calculation (Chapter 5).

$$B_q^k = \sum_L B_k'(L)\ C_q^{(k)}(\theta_L, \phi_L)\ (-1)^q \quad , \tag{2.12}$$

where $B_k'(L)$ is the same for 'chemically identical' ligands, i.e. the same distance and bonding, and θ_L, ϕ_L are the co-ordiantion angles.

The superposition model has been applied successfully to several systems by Newman (1971) and yields a significant reduction in number of parameters, especially for low symmetry centres. In addition, parameters deduced for one centre and a particular ligand may be used as a guide for the crystal field at a different centre with the same ligand through the previous mentioned power law dependency. The superposition model in the form described above is used to analyse the distortions of the tetragonal symmetry centres in $SrF_2 : Nd^{3+}$ and $CaF_2 : Nd^{3+}$ in Chapter 7.

2.3 Zeeman Splitting Factors

For an unambiguous assignment of the optical transition in terms of crystal field parameters it is helpful to study the Zeeman effect of the optical transitions. A measurement of the g-values for the various levels checks the assignment of centres to a particular symmetry and helps in assigning wavefunctions appropriate to the energy levels. Details of the Zeeman splitting factors are included as they are relevant to the inclusion of Zeeman data in the crystal field calculations in Chapter 7.

When an external magnetic field is applied to the crystal, the Kramers' degeneracy of the energy levels (of odd electron rare earth ions) is fully lifted. The applied magnetic field can be directed either parallel or perpendicular to the optical z axis of the crystal giving rise to the parallel or perpendicular Zeeman interaction spectra respectively. The Hamiltonian for the interaction between the N electrons and an external magnetic field B is given to first order of the magnetic field strength as :

$$H_z = \beta\ B \sum_{i=1}^{N} (\underline{l}_i + g_s \underline{s}_i) \quad , \tag{2.13}$$

where $\beta = e\hbar/2m$ is the Bohr magneton and the gyromagnetic ratio g_s of the electron is 2.0023.

In general, the perturbation produced by the magnetic field on the ion is smaller than that produced by the crystal field and thus it is advantageous to calculate the matrix elements of the operator $(\underline{l} + g_s \underline{s})$ using the basis functions which describe the crystal field levels.

The Zeeman operators of interest are $(\underline{l}_z + g_s \underline{s}_z)$ and $(\underline{l}_x + g_s \underline{s}_x)$ which give the parallel, $g_\parallel$, and perpendicular, $g_\perp$, Zeeman interactions respectively. In Zeeman spectroscopy it is more usual to define the parallel and perpendicular

splitting factors $s_{\|}$ and $s_{\perp}$ of the crystal field energy levels by the relationship :

$$s = \frac{\Delta E}{\beta B} \quad , \tag{2.14}$$

where ΔE is the energy separation between the components of a doublet in the magnetic field B. In EPR studies the corresponding splitting factors are usually written as $g_{\|}$ and $g_{\perp}$.

The matrix elements of the two Zeeman operators for LSJ levels can be calculated using the formulae given by Macfarlane (1970) where an orbital angular momentum reduction factor k is included, and the Zeeman operator becomes $(k\underline{L} + g_s\underline{S})$.

2.4 Localised Vibrational Modes

The presence of a point defect in an otherwise perfect crystal destroys the strict translational symmetry of the lattice and, at the same time, modifies its normal modes of vibration. Theoretical investigations of defects and lattice vibrations can be found in Born and Huang (1954) and Newman (1973), among others. Highly localised vibrational modes can occur when the defect consists of an impurity atom which is much lighter than the atoms of the host crystal, provided the force constants between this atom and its neighbours have a similar strength to or greater than, those between pairs of host crystal atoms. These local mode frequencies are determined by the exact environment of the impurity ions in the crystal lattice and the number of local mode frequencies in the fundamental and the harmonics yield some information about the symmetry of the defect centre. For ionic impurities, these localised modes of vibration are infrared active and can be observed in the low temperature infrared absorption as sharp absorption lines. Examples of such light impurity atoms are provided by hydride ions and the isotopes deuterium and tritium. Hydride ions have been observed to substitute for the anions in alkali halides (Schaefer 1960) and alkaline earth fluoride crystals (Elliott et al. 1965, Hayes et al. 1965). Early experimental results showed that the ratio of the local mode frequencies for D^- and H^- ions in $CaF_2 : Nd^{3+}$ is closely equal to the square root of the inverse mass ratio of D^- and H^-, supporting the idea that the lattice ions do not play a significant role in these highly localised modes. The mass of the H^- ion is so small in comparison to the masses of the lattice ions that the localised modes may be considered as oscillations of the hydrogen alone in the potential formed by an effectively static lattice. This anharmonic oscillator potential for C_{4V} symmetry sites is given by Maradudin and Peretti (1967) as :

$$V(r) = A_1(x^2+y^2) + A_2z^2 + B_1z^3 + B_2z(x^2+y^2) + C_1z^4 + C_2(x^4+y^4) + C_3z^2(x^2+y^2) + C_4x^2y^2 \ldots$$

The anharmonic terms lead to shifting and splitting of the energy levels of the harmonic oscillator potential $(A_1(x^2+y^2) + A_2z^2)$ and the results are given in the original paper by Maradudin and Peretti (1967). Reeves (1987) has listed some corrections to the expressions in the original Maradudin and Peretti paper (1967). The important result for the present analysis is that, the first excited level (N=1) decomposes into the two ${}^1\gamma_1 + {}^2\gamma_5$ irreducible representations (irreps) of C_{4V} and the second excited state (N=2) decomposes into five levels designated by $2\,{}^1\gamma_1 + {}^1\gamma_3 + {}^1\gamma_4 + {}^2\gamma_5$, as shown in Fig. 2.2.

2.5 Electron-Phonon Interaction

In the analysis of the hydrogenic C_{4V} symmetry centres the electron-phonon interaction can be treated as the coupling of the electronic energy levels of the rare earth ion with the energy levels of the localised anharmonic oscillator of the charge compensating hydride ion. The irreps of the wavefunctions in the combined electron-vibrational system is given by the direct product of the irreps of the coupled systems :

$$\Gamma = \Gamma_{(k)} \times \Gamma_{(l)} \ .$$

Multiplication tables for the irreps of the symmetry point group such as those found in Koster (1963) can be used to determine the symmetries of the combined levels. For the rare earth ion Nd^{3+}, its crystal field wavefunctions may be characterised by either the γ_6 or the γ_7 irreps of the C_{4V} point group. The irreps formed by coupling these wavefunctions with the two first N=1 wavefunctions ($\gamma_1(z)$ and $\gamma_5(x,y)$) of the anharmonic oscillator are :

$$\gamma_1(z) \times \gamma_6 \rightarrow \gamma_6 \qquad \gamma_1(z) \times \gamma_7 \rightarrow \gamma_7$$
$$\gamma_5(x,y) \times \gamma_6 \rightarrow \gamma_6 + \gamma_7 \qquad \gamma_5(x,y) \times \gamma_7 \rightarrow \gamma_6 + \gamma_7 \ .$$

Hence for the combined system, it is apparent that the (z) component of a fundamental vibronic level always has the symmetry of the parent electronic level while the (x,y) component gives two vibronic levels of $\gamma_6 + \gamma_7$ symmetry independent of the symmetry of the parent electronic level, as shown in Fig. 2.2. The energy separation of these vibronic levels from their parent electronic levels should closely match the local mode vibrational frequencies. The transition probabilities between the energy levels of this combined system are dependent on the strength of the electron-phonon interaction.

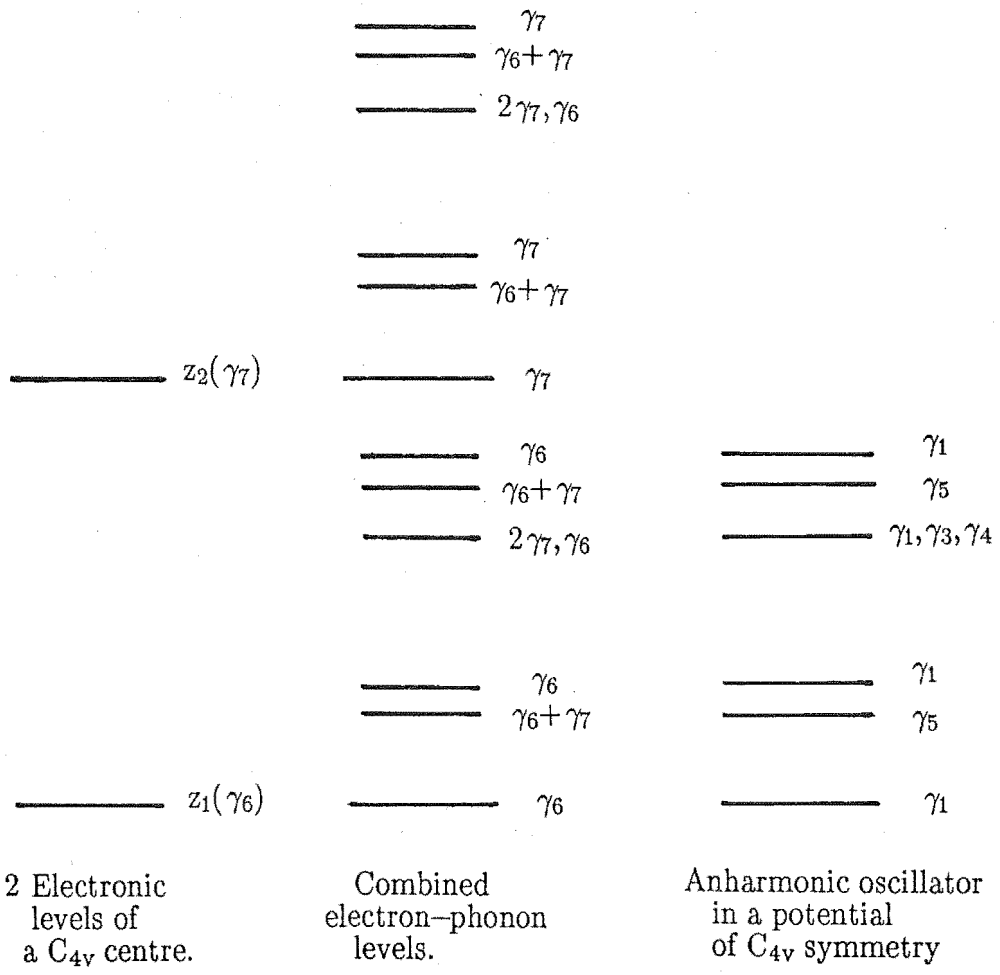

Figure 2.2: Schematic diagram of the low lying energy levels of the combined electron-vibrational system of a hydrogenated tetragonal centre in $CaF_2 : Nd^{3+}$.

2.6 Polarisation and Selection Rules for Electronic Transitions

The crystal field wavefunctions for the tetragonal symmetry centre can be labelled by both the octahedral (O_h) and tetragonal (C_{4V}) irreducible representations, irreps, Γ_i and γ_j respectively. For configurations with an odd number of electrons, the crystal field energy levels are labelled by the Γ_6, Γ_7 and Γ_8 irreps of the O_h double group and by the C_{4V} irreps into which these decompose viz γ_6, γ_7 and $\gamma_6 + \gamma_7$ respectively. Under the operations of the C_{4V} point group, the cartesian components of the electric dipole operator, $-\sum_i er_i$, transform as the γ_5 (x, y) and γ_1 (z) irreps of the C_{4V} group. The C_{4V} group multiplication table can now be used to determine the electric dipole selection rules for transitions between levels with various symmetries, the requirement being that an allowed transition must satisfy the product rule :

$$\gamma_a \times \gamma_{op} \subset \gamma_b \quad , \tag{2.15}$$

where γ_a and γ_b are the symmetries of the two energy levels involved in the transition and γ_{op} is the symmetry of the appropriate electric dipole operator involved. Thus the electric dipole selection rules for the transitions between energy levels of γ_6 and γ_7 symmetries are :

$$\begin{array}{llll} \gamma_6 \times \gamma_5 \rightarrow \gamma_6 + \gamma_7 & & \gamma_6 \times \gamma_1 \rightarrow \gamma_6 & \\ \gamma_7 \times \gamma_5 \rightarrow \gamma_6 + \gamma_7 & & \gamma_7 \times \gamma_1 \rightarrow \gamma_7 & . \end{array} \tag{2.16}$$

For polarised light with the E vector perpendicular to the principal symmetry axis (z), i.e. σ polarisation, transitions are allowed between levels of either symmetry; while for polarised light with the E vector parallel to the principal axis, i.e. π polarisation, the allowed transitions are only between levels of the same symmetry. These selection rules can be summarised as follows :

C_{4V}	γ_6	γ_7
γ_6	$\pi\sigma$	σ
γ_7	σ	$\pi\sigma$,

(2.17)

where π and σ polarisations are given relative to the principal symmetry (z) axis of the centre.

Following the convention used in Raman spectroscopy the polarisation notation adopted is specified as :

$$X(ab)Z \quad , \tag{2.18}$$

where X and Z designate the respective directions of propagation of the incident and emitted radiation, and a and b designate the polarisations of the incident laser beam and the fluorescence respectively. This polarisation

notation can be shortened to (ab) for convenience since the direction of the propagation of the incident laser beam and of the emitted fluorescence are fixed by the experimental geometry, used as shown in Fig. 2.3.

There are three possible orientations for C_{4V} centres in the crystal, which can be labelled x, y and z according to the orientations of the principal four-fold axis as in Fig. 2.3. Thus the total fluorescence intensities for the z and y polarisations of the laser are given by the electric dipole selection rules to be :

	(zy)	(zx)
x	$I_{\sigma\sigma}$	$I_{\sigma\pi}$
y	$I_{\sigma\pi}$	$I_{\sigma\sigma}$
z	$I_{\pi\sigma}$	$I_{\pi\sigma}$

(2.19)

or

	(yy)	(yx)
x	$I_{\sigma\sigma}$	$I_{\sigma\pi}$
y	$I_{\pi\pi}$	$I_{\pi\sigma}$
z	$I_{\sigma\sigma}$	$I_{\sigma\sigma}$

(2.20)

where I_{ab} is the combined intensity of the absorption and emission transitions involving operators with polarisations a and b respectively, $I_{ab} \propto I_a \cdot I_b$. Assuming equal population of x, y and z oriented centres the above tables show that there is no difference in the overall fluorescence intensity for the (zy) and (zx) polarisations, whereas there is a difference for the (yy) and (yx) polarisations. This difference can indicate possible symmetries of the levels involved in the given absorption and fluorescence transition. For example, if both the initial and the final transitions are between two levels of different symmetries, i.e. $\gamma_6 \rightarrow \gamma_7$, a 2:1 ratio is expected for the (yy):(yx) fluorescence intensities (equation 2.20).

The linear combination of $2(yx)+(yy)$ polarisation satisfies the isotropic condition where both the absorption and emission are represented by $2I_\sigma + I_\pi$ giving an overall intensity :

$$4I_\sigma I_\sigma + 2I_\sigma I_\pi + 2I_\pi I_\sigma + I_\pi I_\pi \quad . \tag{2.21}$$

Additional information can be deduced from the polarisation data and this can be clearly illustrated by the following example. If an energy level of γ_6 symmetry is excited to an energy level of γ_7 symmetry, only I_σ is involved for absorption and the effects are :

	(yy)	(yx)
x	$I_{\sigma\sigma}$	$I_{\sigma\pi}$
z	$I_{\sigma\sigma}$	$I_{\sigma\sigma}$

(2.22)

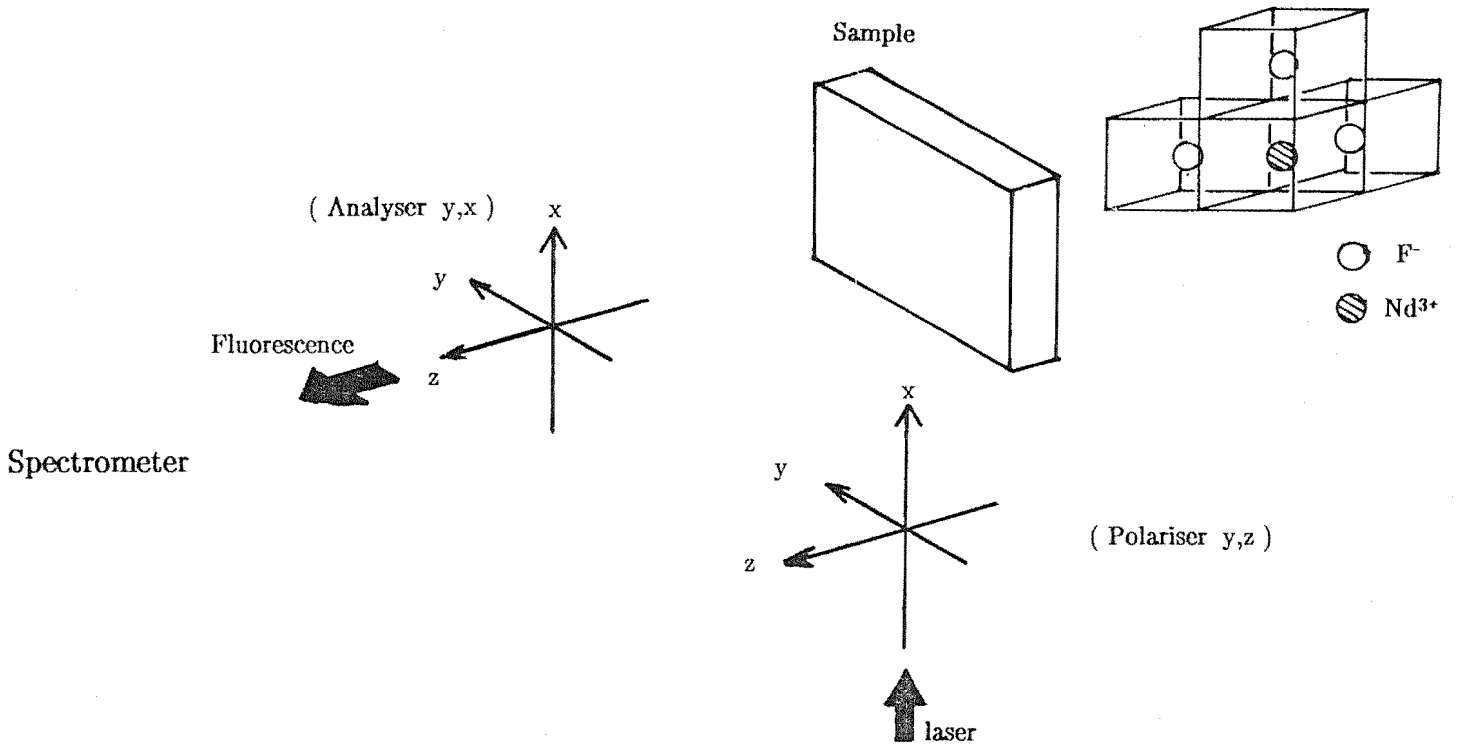

Figure 2.3: Schematic diagram of the experimental geometry used for the polarisation and 'bleaching' experiments.

where

$$I_{\sigma\sigma} = \frac{(yy)}{2} \quad , \tag{2.23}$$

and

$$I_{\sigma\pi} = (yx) - \frac{(yy)}{2} \quad . \tag{2.24}$$

The ratio of I_σ and I_π for emission is then given by :

$$I_\sigma : I_\pi = I_{\sigma\sigma} : I_{\sigma\pi} \quad . \tag{2.25}$$

The observed intensity ratio may then be compared with the results of a transition probability calculation for the two energy levels involved. Moreover, if the emission is also by I_σ, i.e. $\gamma_6 \rightarrow \gamma_7$, then a 2:1 ratio is expected for the (yy):(yx) polarisation as already mentioned above.

This approach will be discussed further in Chapter 5 with specific reference to the C_{4V} centre polarisation data.

2.7 Fluorescence Lifetimes

When an ion in a crystal lattice is raised to an excited state the system can decay by a number of relaxation processes. These can be classified into two types of processes, radiative or non-radiative. Thus the observed fluorescence lifetime, τ, of an excited level b is given by :

$$\tau^{-1} = \sum_a W^R_{a,b} + \sum_a W^{NR}_{a,b} \quad , \tag{2.26}$$

where the summations are for the transitions terminating on a final level a; W^R includes both purely electronic and phonon assisted vibronic radiative processes; the non-radiative processes W^{NR} include relaxation by multiphonon emission and effective energy transfer interactions. The relative probability of these two types of processes depends on several factors, including :

- the nature of the ion.
- the nature of the lattice.
- the energy gap between the fluorescing level and the next lowest energy levels.
- the coupling of the ion to the lattice.
- the coupling of two or more ions.

At low rare earth ion concentrations, or for simple isolated symmetry centres, the contribution from the coupling of two or more nearby ions can be neglected.

Multi-phonon relaxation may occur when the energy separation between the excited and the next lowest energy levels is larger than the highest energy phonon of the lattice. Several theoretical techniques have been developed to calculate the transition rates of the multi-phonon processes. Kiel (1964) treated the problem by applying conventional time dependent perturbation theory in high order. Subsequent theoretical treatments by Miyakawa and Dexter (1970) and Fong, Naberhuis and Miller (1972) yield more complex dependence of the rate of multi-phonon emission on the energy gap and temperature. Riseberg and Moos (1968) developed a phenomenological treatment which was found to be successful, within a factor of 2 to 3, when describing a wide body of experimental data on multi-phonon transition rates.

In a simple phenomenological approach of a single frequency phonon model (Partlow et al. 1967, Riseberg et al. 1967, 1968, Weber 1968), the spontaneous transition rate at low temperatures is taken to vary approximately as :

$$W^{(n)} \approx A\epsilon^{(n)} \quad , \tag{2.27}$$

where A is a constant and the order n is related to the energy gap dE by :

$$n = \frac{dE}{\hbar\omega} \quad , \tag{2.28}$$

ω being the dominant angular frequency of the phonons. The ratio of the n-th order transition rate to the $(n-1)$th order rate in a given host is given by a coupling constant ϵ where :

$$\epsilon = \frac{W^{(n)}}{W^{(n-1)}} \ll 1 \quad , \tag{2.29}$$

which reflects the strength of the RE^{3+} ion-phonon coupling and correlates with the magnitude of the crystalline fields.

The validity of this approach depends on the extent to which the precise features, associated with each individual phonon and set of participating levels, are statistically averaged out as a result of the number of phonons involved together with the number of equivalent processes for each phonon. This approach is discussed in Chapter 5, with specific reference to the hydrogenic C_{4V} and the F^- cluster centres.

Chapter 3

Experimental

3.1 Crystals

The single crystal samples used in this study were either obtained from Optovac Inc. (U.S.A.) or grown in this department by the Bridgman-Stockbarger method, using a 38 kilowatt radio frequency furnace manufactured by Arthur D. Little Company. All locally grown crystals were prepared from alkaline earth fluoride starting material supplied by Optovac Inc.. The rare earth dopant in the form of tri-fluoride, supplied by Ventron, Alfa Products U.S.A, was added to give the desired molar concentration of trivalent rare earth. A dopant concentration of 0.05% or less was used in this study, this being a compromise between having sufficient rare earth dopant to give observable spectral line intensities but not so much that complex clusters become dominant.

Hydrogen and its isotopes can be introduced into the crystals by the method of Hall and Schumacher (1962). The crystals were placed in a graphite boat in contact with a strip of aluminium wire inside the hydrogenation furnace. They were then heated to $100^{o}C$ under vacuum to remove absorbed gases and water vapour. Appropriate gas was then introduced to the desired pressure (0.3 atmospheric pressure) and the temperature raised to and maintained at $850^{o}C$ for the duration of the hydrogenation process. The variety of spectroscopically distinct hydrogenic centres was found to increase with the length of the hydrogenic treatment (Cockroft 1987). To avoid the formation of complex multi-ion clusters during the cooling down of the crystals, they were rapidly quenched by pulling them out of the furnace to room temperature. No significant difference was observed in the number of different cluster centres formed between quenching to room temperature or by immersing in liquid nitrogen.

Crystals oriented in the $\langle 100 \rangle$ direction were obtained using the (111) cleavage planes for reference, as illustrated in Fig. 3.1.

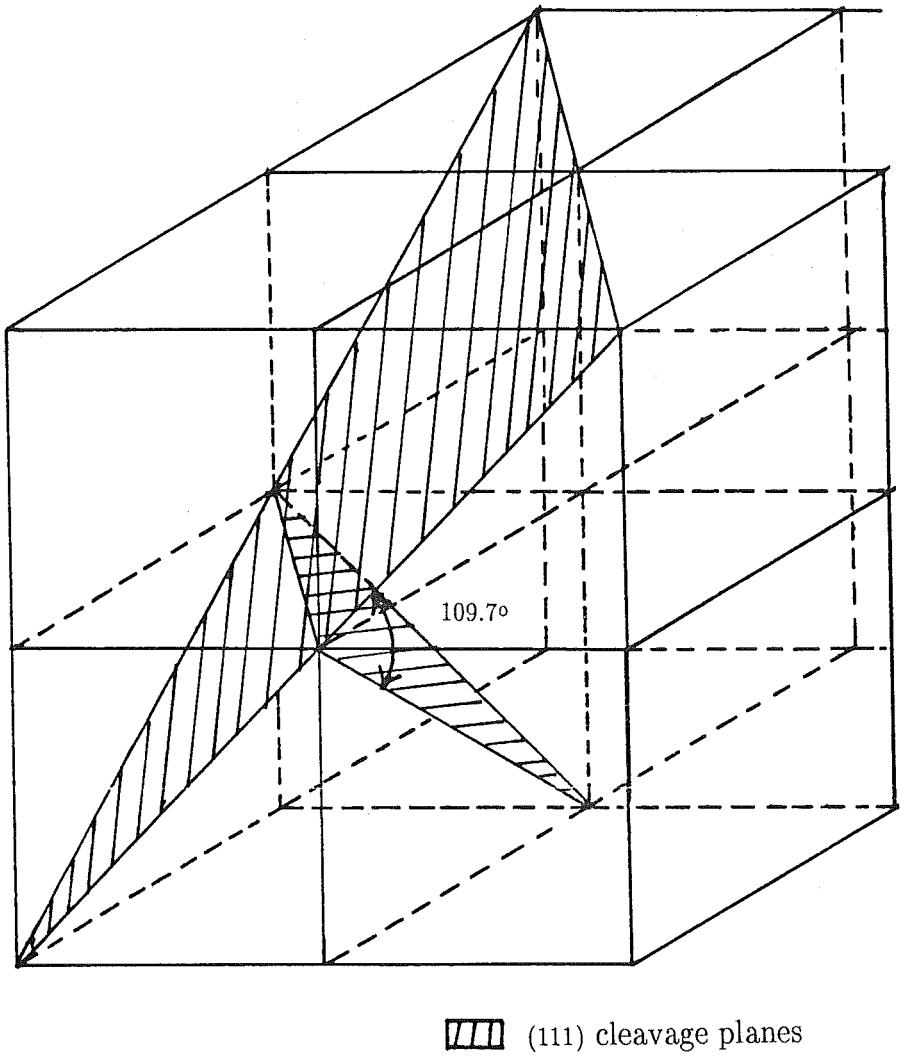

Figure 3.1: Diagram showing the (111) cleavage planes of the CaF_2 cubic structure.

3.2 Low Temperature Cryostat

A CTI-Cryogenic's Model 21C Cryodyne cryocooler was used to cool all the samples measured. The cryocooler consists of a Model 21 two stage cold head, a Model SCW (water cooled) compressor unit and accessories. It provides reliable refrigeration at temperatures down to 10 K for long continuous periods and the cold head could operate in any orientation without loss of performance. The manufacturer's specification of the refrigeration capacity is reproduced in Fig. 3.2 while Fig. 3.3 shows the cold head unit and the sample holders.

3.3 Optical Absorption

Optical absorption spectra were recorded photoelectrically on a Spex 1700 monochromator using a 100 watt Tungsten Halogen lamp, powered by a stabilised supply, as the light source. The monochromator had a 3/4 metre focal length Czerny-Turner optical configuration with an effective aperture of f/6.8. A plane grating with 1180 grooves/mm blazed at 750 nm gave a dispersion of 1.06 nm/mm in first order. The photomultiplier tubes used were an R.C.A. type C31034 (S20 spectral response) for wavelengths less than 880 nm and a R.C.A. type 7102 (S1 spectral response) for wavelengths greater than 880 nm. The 7102 tube was cooled to -100^oC using a liquid nitrogen cooler (TE-176- RF) supplied by Products for Research Inc.. The C31034 tube was cooled to -25^oC using a thermal electric cooler (TE-104-RF-002) supplied by Products for Research Inc.. The output of the photomultiplier was amplified by a Keithley Instruments 610B Electrometer and the output displayed on a Sekonic SS250F chart recorder. The weak absorption of the rare earth ions was usually measured with high gain setting and using a zero suppressor designed by the electronics workshop in this department.

3.4 Laser Selective Excitation Fluorescence and Excitation Measurements

A Spectra Physics Model 375 tunable dye laser with Rhodamine 6G dye was excited by a Spectra Physics Model 171 15 watt Argon-Ion laser. The dye laser was modified by Dr. R.J. Reeves to accommodate a Spectra Physics three-plate birefringent filter. This gave a capability to tune continuously across the desired frequency range with an added benefit of eliminating the troublesome sidebands associated with the original tuning wedge and etalon. Rotational motion of the birefringent filter was achieved by using a 0.5 mm/rev. micrometer shaft as shown in Fig. 3.4. An unidirection stepping

Refrigeration Capacity:

The values listed below represent the minimum refrigeration capacities of the second-stage cold station, assuming the following conditions:

- No heat load applied to the first-stage cold station
- An ambient temperature of 75°F
- No thermal radiation or gas conduction heat load

Applied Second-Stage Heat Load (watts)	Second-Stage Cold-Station Temperature for 60-Hz operation (K)
0	10.0
1.0	16.0
1.5	19.0

Temperature Stability under Constant Load: ± 1.0K
(At the Second-Stage Cold Station)

No-load Cooldown Time to 20K: 30 minutes; 50-Hz power

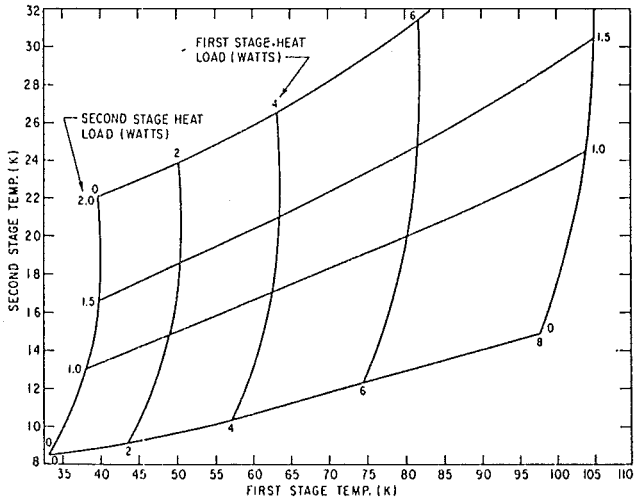

TYPICAL REFRIGERATION CAPACITY OF THE MODEL 21C CRYODYNE(R) CRYOCOOLER (50 HERTZ)

Figure 3.2: Specifications of the closed cycle refrigerator. Reproduced from the manufacturer's manual (CTI-Cryogenic Ltd.).

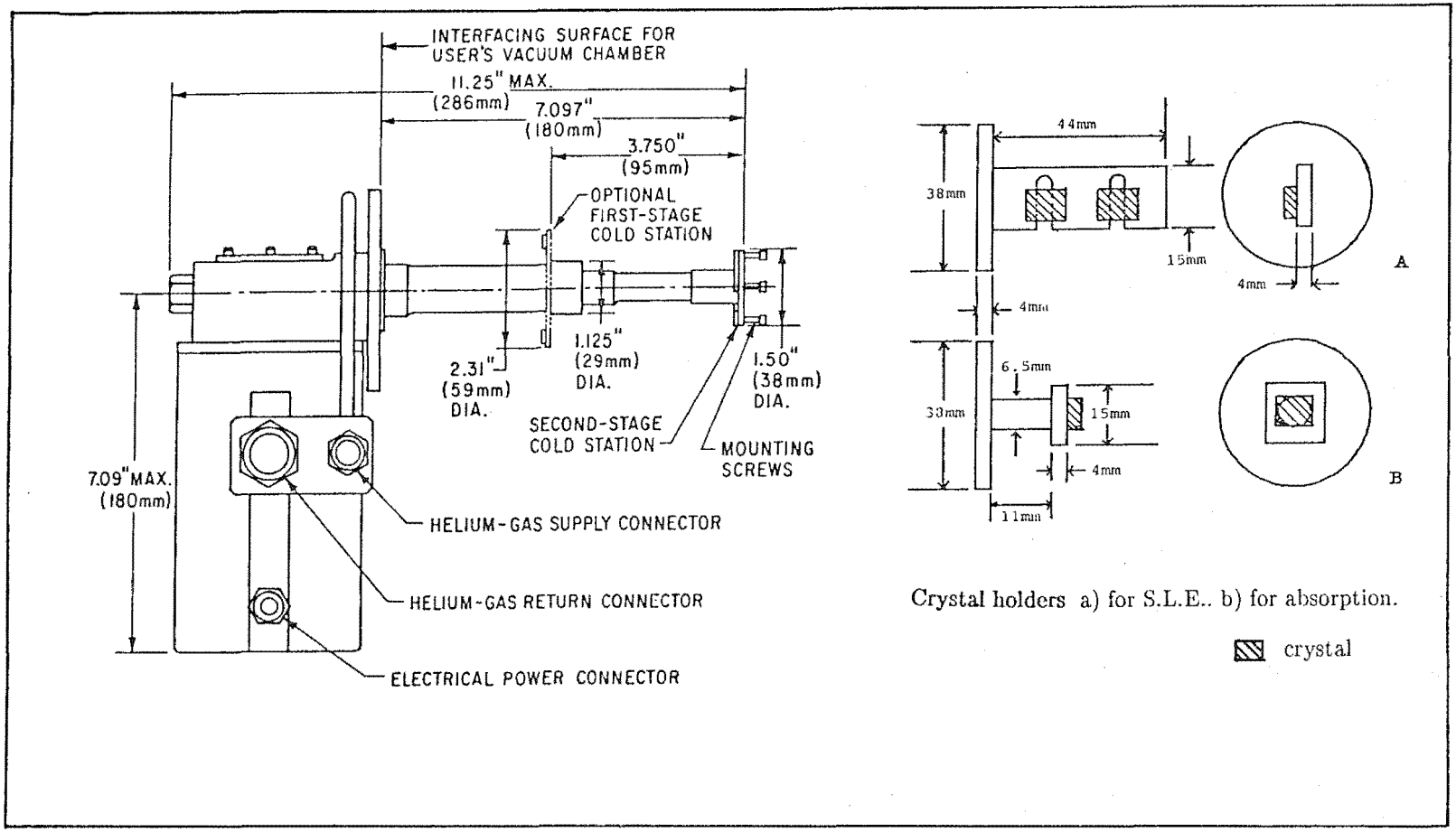

Figure 3.3: Schematic diagram showing the cold head and sample holder units.

motor was adapted to drive the micrometer for the excitation experiments. The line-width of the dye laser was approximately 1 cm^{-1} and the typical laser power used for the experiments was 100 mW. The strong near-infrared fluorescence from energy levels of the R multiplet to the levels of ^4I multiplets was measured photoelectrically with the equipment outlined above using the R.C.A. S1 spectral response photomultiplier tube.

3.5 Laser Selective Excitation Upconversion Fluorescence Measurements

The equipment used was the same as for the fluorescence experiments described above. The fluorescence spectrum was measured photoelectrically using a Spex 1403 double monochromator with a 0.85 metre focal length Czerny-Turner optical system. Plane gratings with 1800 grooves/mm blazed at 500 nm gave a dispersion of 10 cm^{-1}/mm at 514.5 nm. An R.C.A. C31034 photomultiplier was used and its output was sent to a discriminator Model 1121 and photon counter Model 1112 combination manufactured by Princeton Applied Research. The double monochromator was controlled by a Spex CD2A computer drive, which was in turn interfaced to an Apple IIe microcomputer. Data and relevant information for each spectrum were permanently stored on 5.25 inch floppy discs. Appendix A gives the specific details of the interfacing which was developed during the early stages of the present investigation.

3.6 Fluorescence Lifetime Measurements

A tunable pulsed dye laser system manufactured by Photochemical Research Associates Inc. was used as the exciting source. The system consisted of a Model LN1000 2 Megawatt TEA nitrogen laser, a Model LN107 high resolution dye laser and a Model DD1790 microprocessor scanning unit. The nitrogen laser produced sub- nanosecond pulses of 2 MW peak pulse power. The dye laser could produce peak pulse powers of 200 kW with a .04 nm band width when pumped by the nitrogen laser. It had a pulse width of approximately 500 picoseconds. The fluorescence was detected using the Spex 1700 monochromator and the R.C.A. C31034 photomultiplier tube as described for optical absorption experiments. The output of the photomultiplier was connected to a boxcar averager system manufactured by Stanford Research Systems Inc.. It consisted of a Model SR250 Gated Integrator Boxcar, a Model SR235 Analog Processor and a Model SR245 Computer Interface. This system was computer driven by an I.B.M. PC computer and the menu driven software package SR265 supplied by Standford Research Systems Inc..

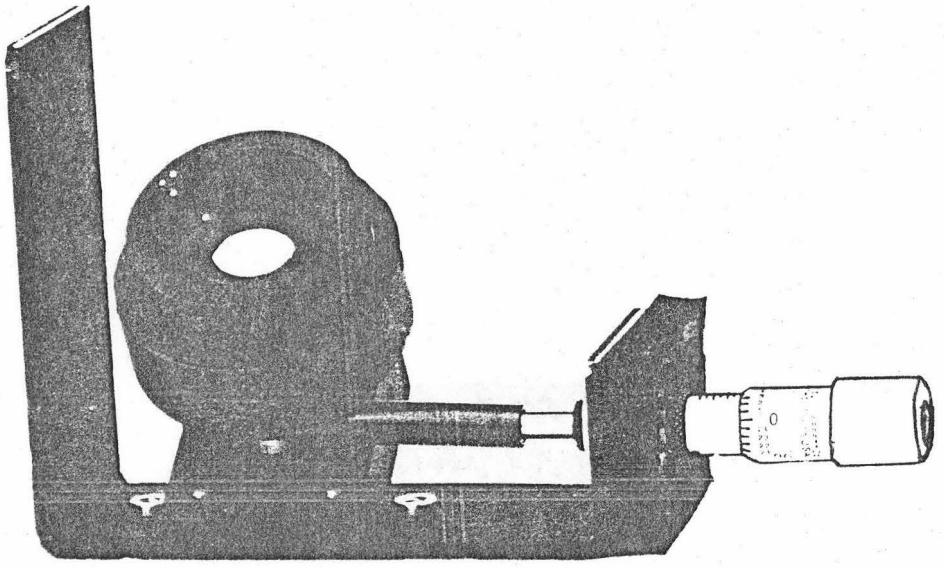

Figure 3.4: Diagram showing the birefringent filter unit.

The use of an EG&G Ortec Model 574 Timing Amplifier and/or a Model 9305 Fast Preamplifier did not significantly improve the signal to noise ratio.

Initial measurements were made using the conventional method of fast pulse amplifier with 50 ohm termination for impedance matching, but signals were found to be very weak and were comparable to noise. Several alternative approaches were considered (see Appendix B) and the integral method was chosen for its simplicity in design and implementation. It had the advantages of rejecting induced noise and a lack of requirement for impedance matching as reflected signals due to mismatch integrate to zero. The integral method was implemented in the form of a resetable integrator, as shown in Fig. 3.5, which was designed and tested by Mr. C.H. Rowe of the electronic work shop in this department. The fluorescence lifetime measurements obtained for several well documented centres in the $SrF_2 : Nd^{3+}$ and $CaF_2 : Nd^{3+}$ systems agree with other workers, within the uncertainties of the experimental data and the data reduction methods used, thus giving confidence in the integral method. A brief discussion of the analysis of the signal strength, the box-car averager, the integral method and the data reduction methods can be found in Appendix B.

Specifications :
–Response to a 10ns step input is 100ns (to 90%).
–Leakage is ≤ 20pA

RESETABLE INTEGRATOR

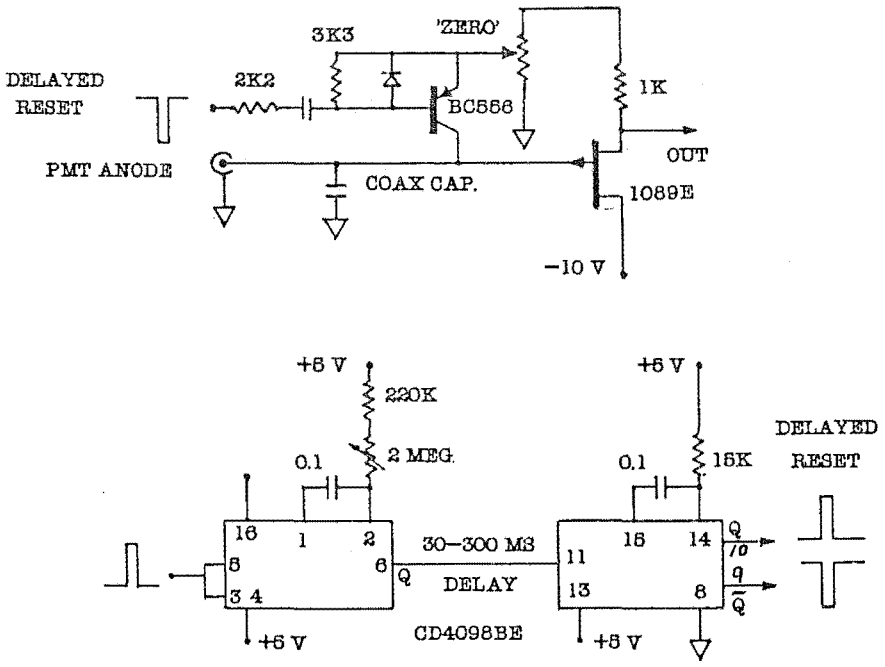

Figure 3.5: Circuit diagram of the resetable integrator.

Chapter 4

Optical absorption

4.1 Introduction

The optical absorption spectra of the trivalent rare earth ions at low temperatures usually consists of distinct groups of narrow lines of various intensities. These lines correspond to transitions from the lower crystal field levels of the ground LSJ multiplet to the crystal field levels of the upper LSJ multiplets of the $4f^n$ configuration.

The absorption spectra of $CaF_2 : Nd^{3+}$ and $SrF_2 : Nd^{3+}$ were measured at 10 K. At this temperature only transitions from the Z_1 ground state were present. Each symmetry centre has its own characteristic set of absorption lines. The measured absorption spectra comprised of a superposition of the lines of all centres present with relative intensities determined by the abundance of each centre in the crystal. Additional lines appeared in the higher temperature (77 K) absorption spectra corresponding to transitions from the thermally populated excited Z_2 crystal field level and such spectra are, therefore, more complex to analyse.

Extensive studies by many workers (Al'tshuler et al. 1970, Tallant et al. 1976, Andree et al. 1981, Jones et al. 1986, Reeves 1987) of fluoride crystals doped with RE^{3+}ions have established several possible charge compensation arrangements. Complex cluster charge compensation centres are dominant for RE^{3+} ion concentrations above 0.2% whereas for RE^{3+} ion concentrations less than or equal to 0.05% the single ion centre is dominant. Examples of some charge compensation centres are shown in Fig. 4.1.

As Nd^{3+} ion has an odd number of $4f$ electrons, all its crystal field levels are at least two fold degenerate (Kramers' degeneracy). For a given symmetry centre there can be, at most, $J+1/2$ crystal field levels for a given J multiplet. The absorption spectra of transitions to multiplets of low J value are therefore simplest to analyse. Consequently the absorption spectra of transitions to the $^2P_{1/2}$ (I), $^4F_{3/2}$ (R) and $^4D_{3/2}$ (L) multiplets were first studied.

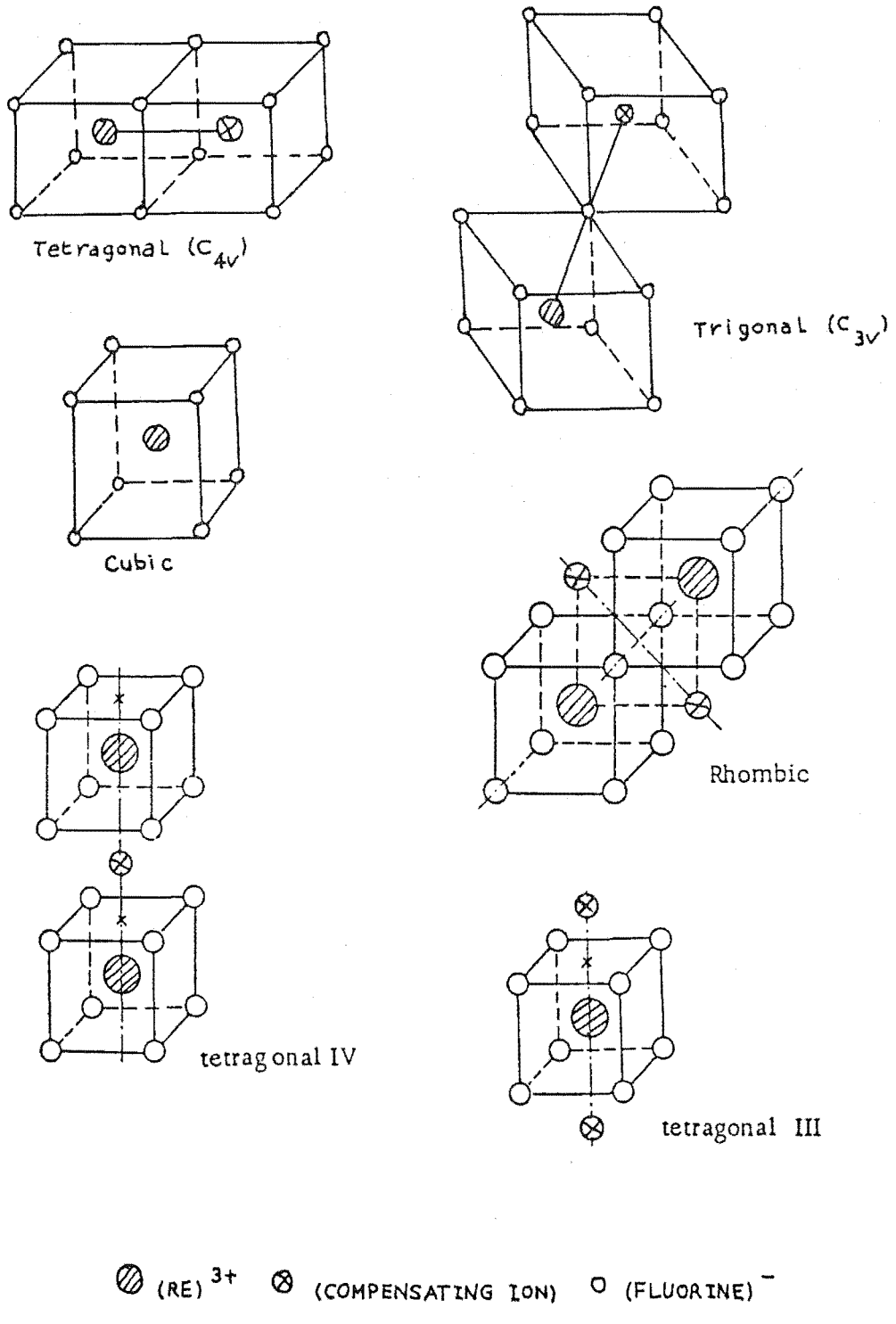

Figure 4.1: Examples of some charge compensation symmetry centres in CaF_2.

The absorption spectra of the R and L multiplets are of particular interest. While the former is the multiplet from which the Nd^{3+} ion's strongest fluorescence is observed, the latter was also found to fluoresce in an energy upconversion process. These fluorescence results are presented in Chapters 5 and 6.

The absorption spectra of the $^2H_{11/2}$ (C) and, $^4G_{5/2}$ and $^2G_{7/2}$ (D) multiplets were also studied because they lie within the frequency range of the Rhodamine 6G dye and are, therefore, candidates for laser selective excitation studies.

4.2 Absorption Spectra of Crystals Before Hydrogenation Treatment

The absorption spectra of the five multiplets studied are presented in Figs. 4.2 to 4.11.

At 0.05% Nd^{3+} ion concentration the low temperature absorption spectra of $CaF_2 : Nd^{3+}$ are similar to those of $SrF_2 : Nd^{3+}$ but are complicated by the fact that there are three dominant symmetry centres; one tetragonal (L or C_{4V}) and two orthorhombic (M, N) in $CaF_2 : Nd^{3+}$ whereas only one distinct tetragonal centre is present in $SrF_2 : Nd^{3+}$. Thermal treatment under vacuum with the same thermal cycling procedure as in the hydrogenation treatment, decreased the intensity of the absorption lines attributed to the two orthorhombic symmetry centres. This is consistent with their being multi-ion cluster centres which can be broken up by thermal treatment.

The tetragonal and the two orthorhombic symmetry centres found in $CaF_2 : Nd^{3+}$and the tetragonal centre in $SrF_2 : Nd^{3+}$ were identified by comparing the absorption spectra of the L and R multiplets both before and after thermal treatment. These results (see Chapter 5) are in complete agreement with earlier works (Voron'ko et al. 1965, 1966, 1969, Kask et al. 1968a, b, Osiko 1971).

The optical absorption spectrum of the C ($^2H_{11/2}$) multiplet was found to be very weak; only one line of the six expected for each symmetry centre was apparent in either $SrF_2 : Nd^{3+}$ or $CaF_2 : Nd^{3+}$. The weakness in the intensity was attributed to the predominant doublet character of the C multiplet.

The absorption spectrum of the D multiplet spans a wavelength range of approximately 10 nm and consists of the $^4G_{5/2}$ and $^2G_{7/2}$ multiplets. The $^2G_{7/2}$ multiplet has slightly higher energy than the $^4G_{5/2}$ multiplet and has relatively broad absorption lines. This broadness combined with an expected total of seven lines per symmetry centre makes the task of unravelling the energy levels of this multiplet difficult.

The absorption spectrum of the L ($^4D_{3/2}$) multiplet was surprisingly weak

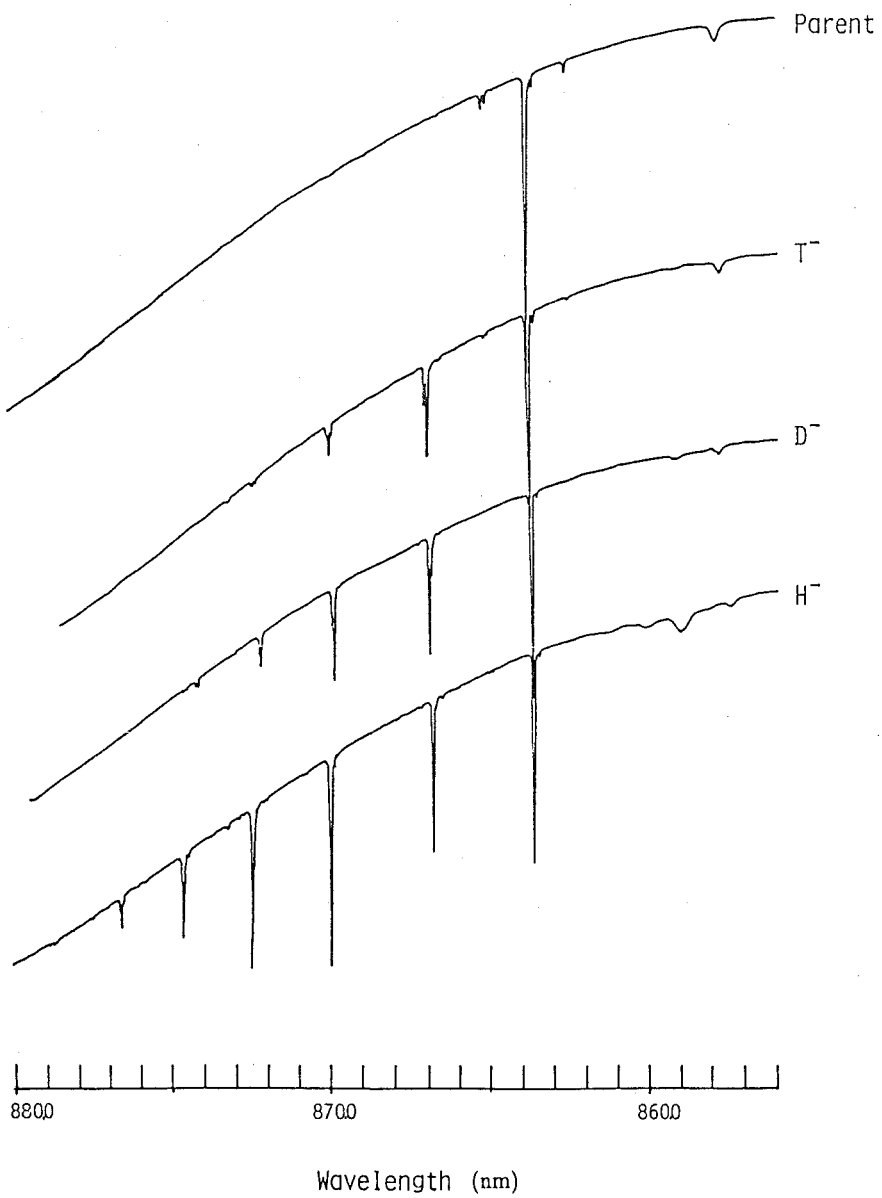

Figure 4.2: 10 K ${}^4F_{3/2}$ (R) multiplet absorption spectrum for $SrF_2 : (0.05\%)Nd^{3+}$ crystals before and after hydrogenation treatments.

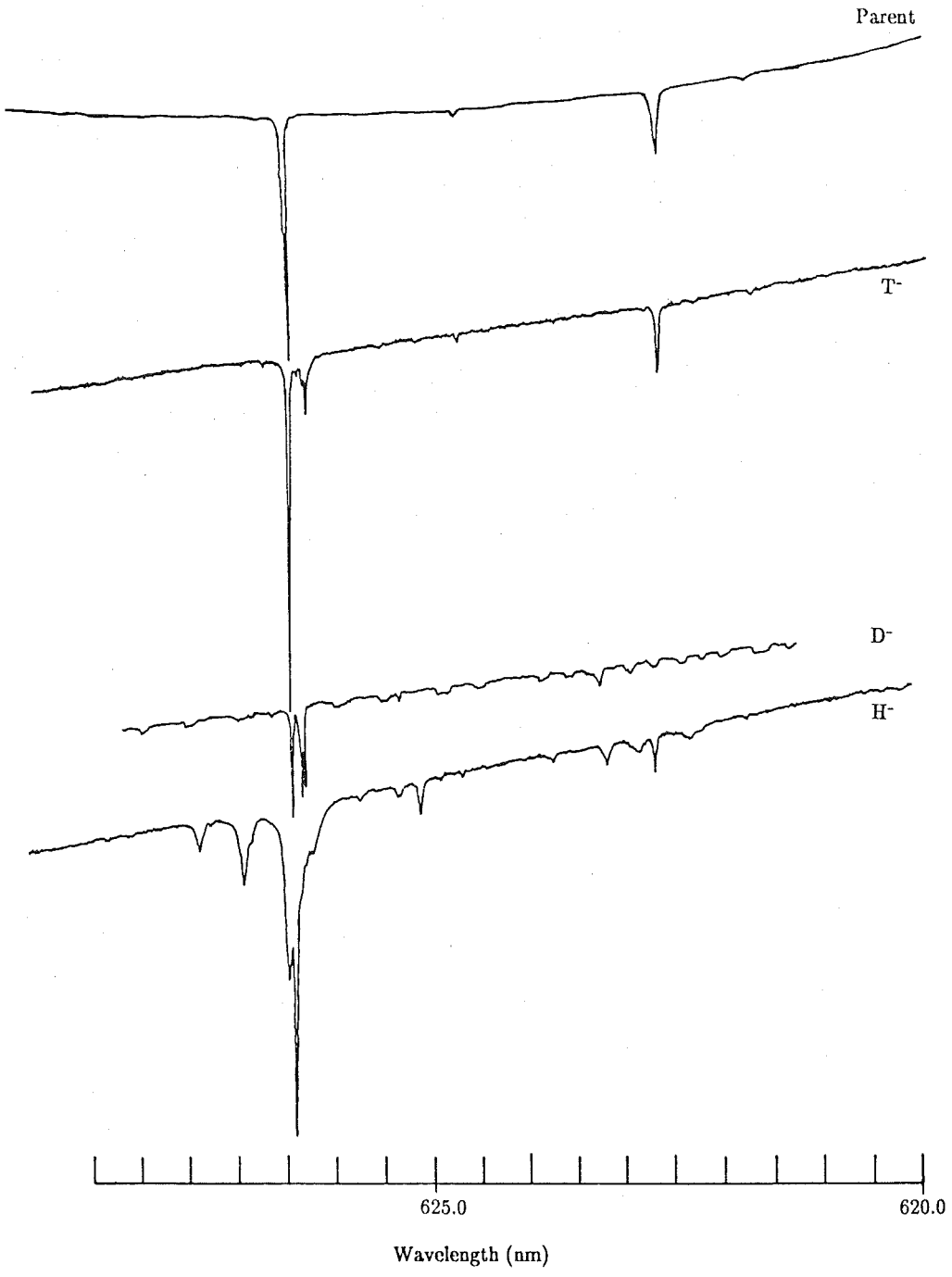

Figure 4.3: 10 K $^2H_{11/2}$ (C) multiplet absorption spectrum for $SrF_2 : (0.05\%)Nd^{3+}$ crystals before and after hydrogenation treatments.

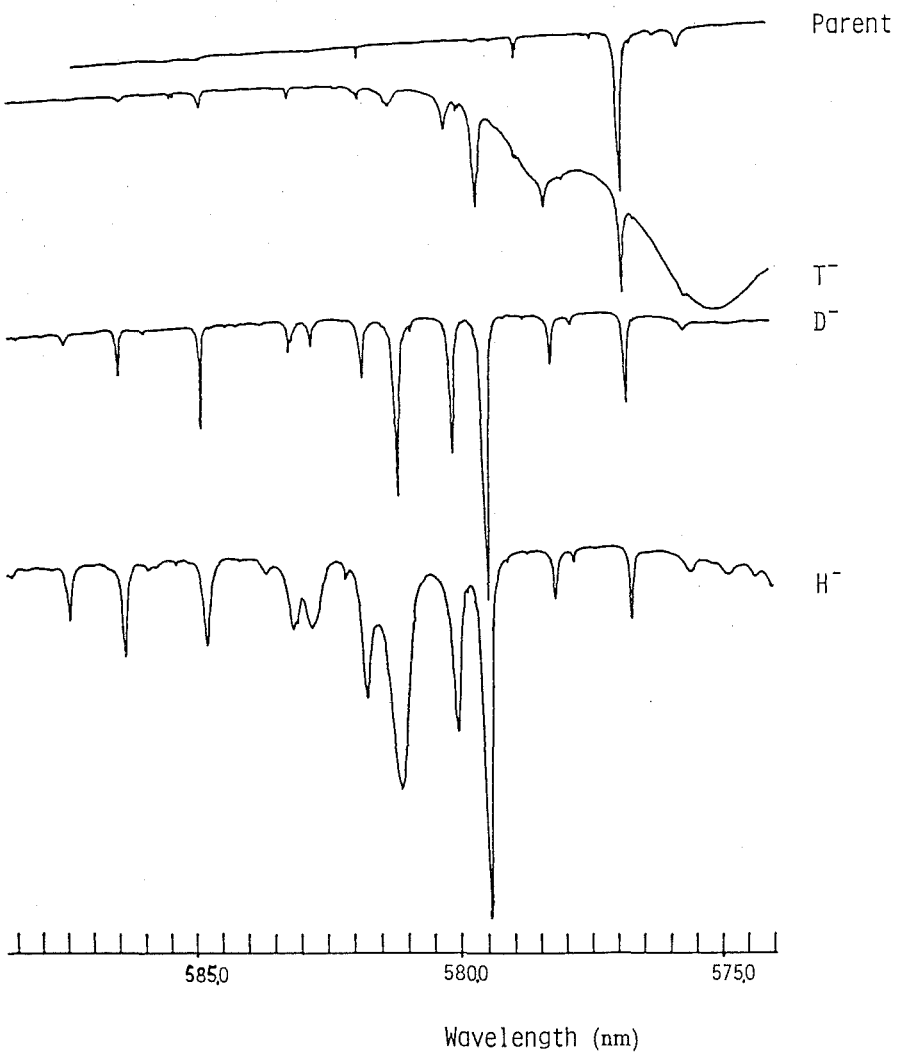

Figure 4.4: 10 K $^4G_{5/2}$ and $^2G_{7/2}$ (D) multiplets absorption spectrum for $SrF_2 : (0.05\%)Nd^{3+}$ crystals before and after hydrogenation treatments.

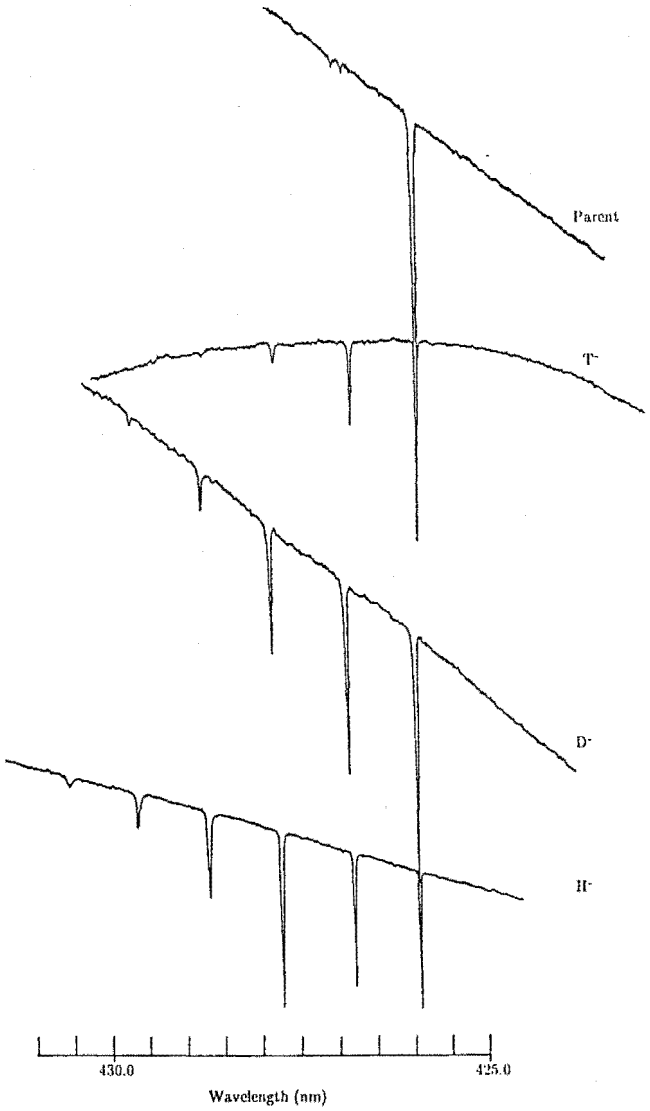

Figure 4.5: 10 K $^2P_{1/2}$ (I) multiplet absorption spectrum for $SrF_2 : (0.05\%)Nd^{3+}$ crystals before and after hydrogenation treatments.

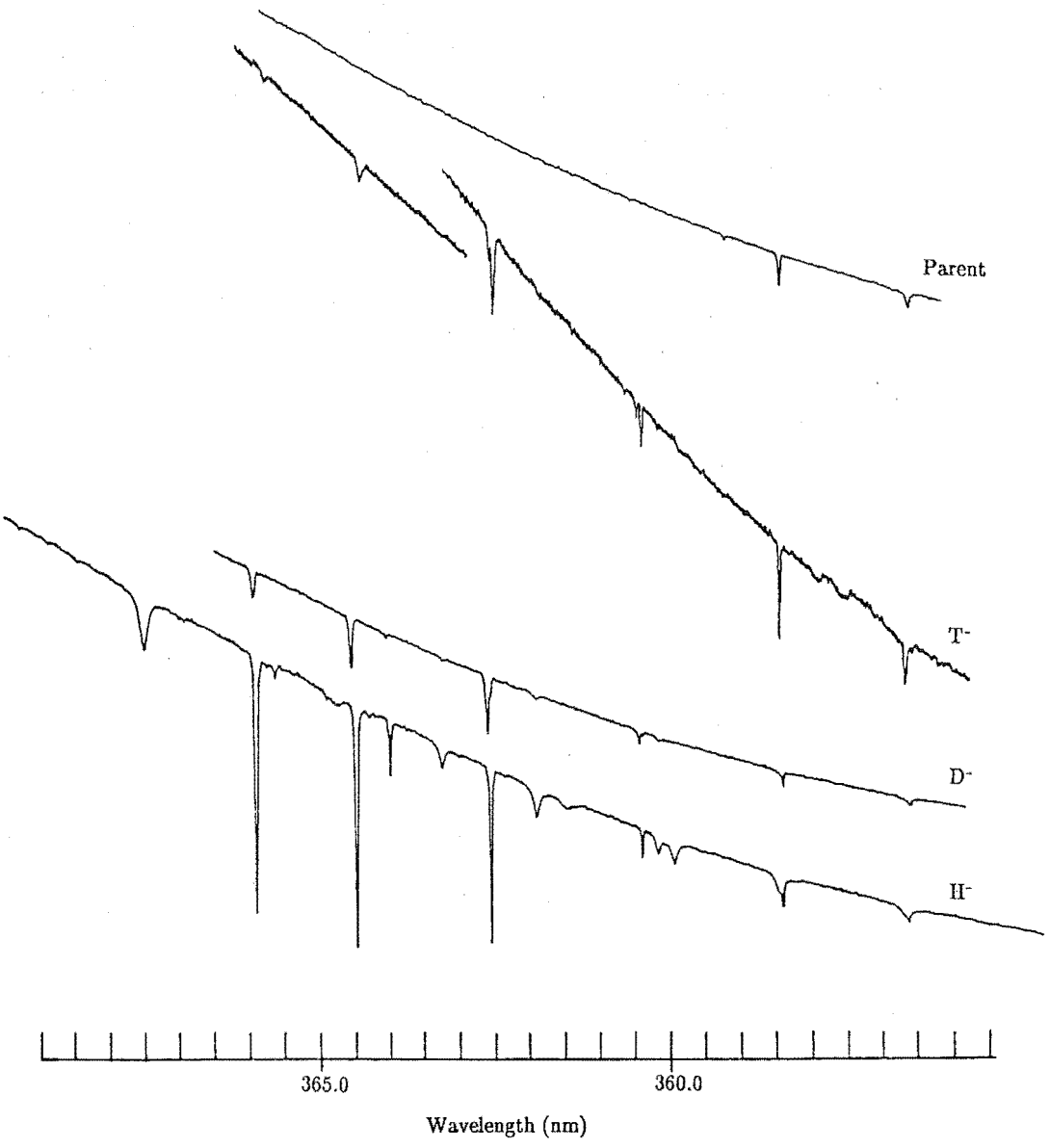

Figure 4.6: 10 K $^4D_{3/2}$ (L) multiplet absorption spectrum for $SrF_2 : (0.05\%)Nd^{3+}$ crystals before and after hydrogenation treatments.

when compared with other quartet multiplets. Its general appearance was found to be very similar to the R multiplet, namely two lines per symmetry centre for the two multiplets, as expected for $J = 3/2$ multiplets.

4.3 Absorption Spectra of Crystals After Hydrogenation Treatment

The absorption spectra of the hydrogenated crystals reveal additional lines for both $CaF_2 : Nd^{3+}$ and $SrF_2 : Nd^{3+}$ crystals and the spectra of the five multiplets studied are presented in Figs. 4.2 to 4.11 while the data are presented in Chapter 5. The number of additional lines was found to be a function of the length of the hydrogenation process as illustrated in Fig. 4.12. A detailed study of this aspect can be found in the work of Cockroft (1987) on $CaF_2 : Er^{3+}$. Isotope shifts were observed on comparison of H^-, D^- and T^- crystals confirming the hydrogenic nature of these additional lines.

A detailed analysis of the absorption spectra of the double light ion $H^- + T^-$ and $H^- + D^-$ crystals reveals additional structures near the hydrogenic lines. A comparison of the absorption spectra of the double hydrogenated crystals with those of crystals which were hydrogenated separately with different hydride ions indicates that some of these centres involve more than one hydride ion. A representative example is shown in Fig. 4.13 which demonstrates the multiple charge compensating nature of these centres.

4.4 Discussion

The results of the optical absorption measurements confirmed the findings of previous authors on the major fluorine charge compensation centres (Kariss et al. 1965, Voron'ko et al. 1965, 1969, Kask et al. 1968a, b, Presland 1974, Freeth 1980). The results for the hydrogenated $SrF_2 : Nd^{3+}$ crystals are all new, while the results for H^- and D^- centres in $CaF_2 : Nd^{3+}$ confirmed the R and L multiplets transitions observed by Presland (1974) whilst giving new results for the C and D multiplets.

The hydrogenic lines can be classified into distinct groups but no attempt was made to assign any of these lines to specific centres through the optical absorption data alone. The details of each absorption line observed in the R multiplet and the assignment to specific symmetry centres are discussed in Chapter 5 together with the corresponding laser selective excitation results.

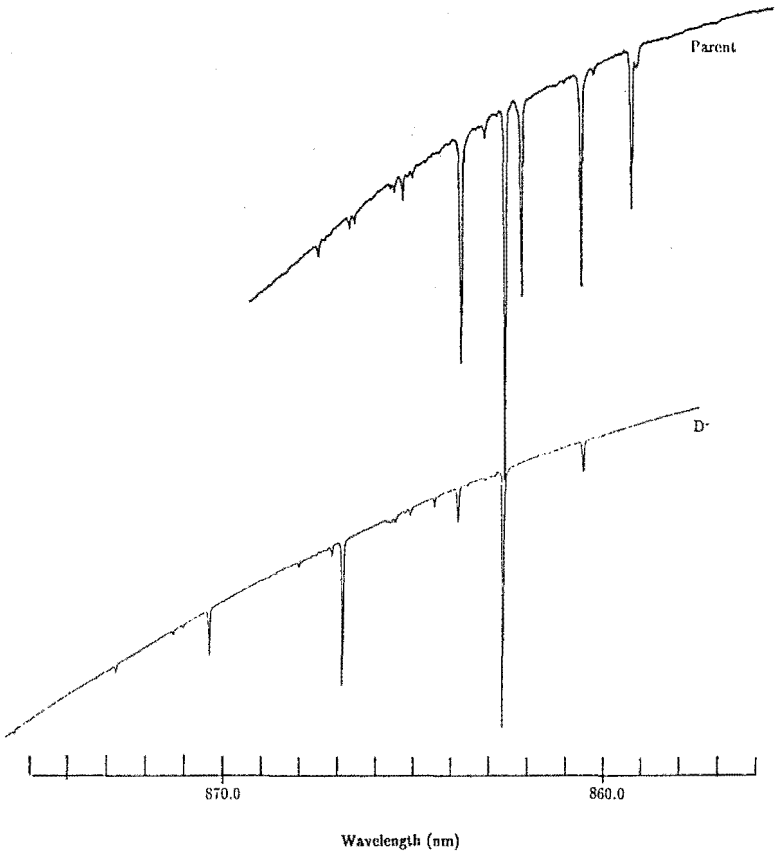

Figure 4.7: 10 K ${}^4F_{3/2}$ (R) multiplet absorption spectrum for $CaF_2 : (0.05\%)Nd^{3+}$ crystals before and after hydrogenation treatments.

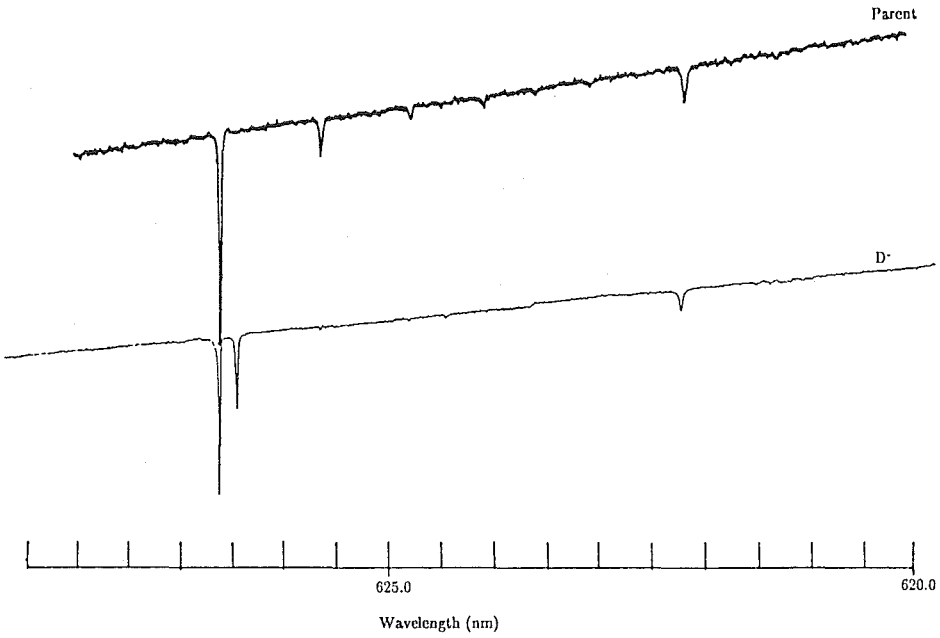

Figure 4.8: 10 K $^2H_{11/2}$ (C) multiplet absorption spectrum for $CaF_2 : (0.05\%)Nd^{3+}$ crystals before and after hydrogenation treatments.

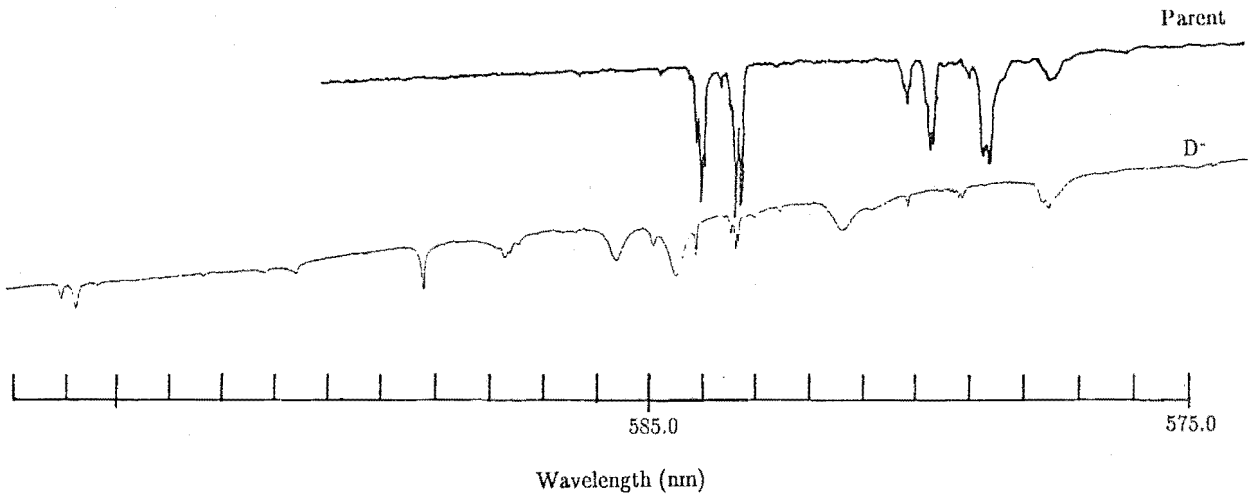

Figure 4.9: 10 K $^4G_{5/2}$ and $^2G_{7/2}$ (D) multiplets absorption spectrum for $CaF_2 : (0.05\%)Nd^{3+}$ crystals before and after hydrogenation treatments.

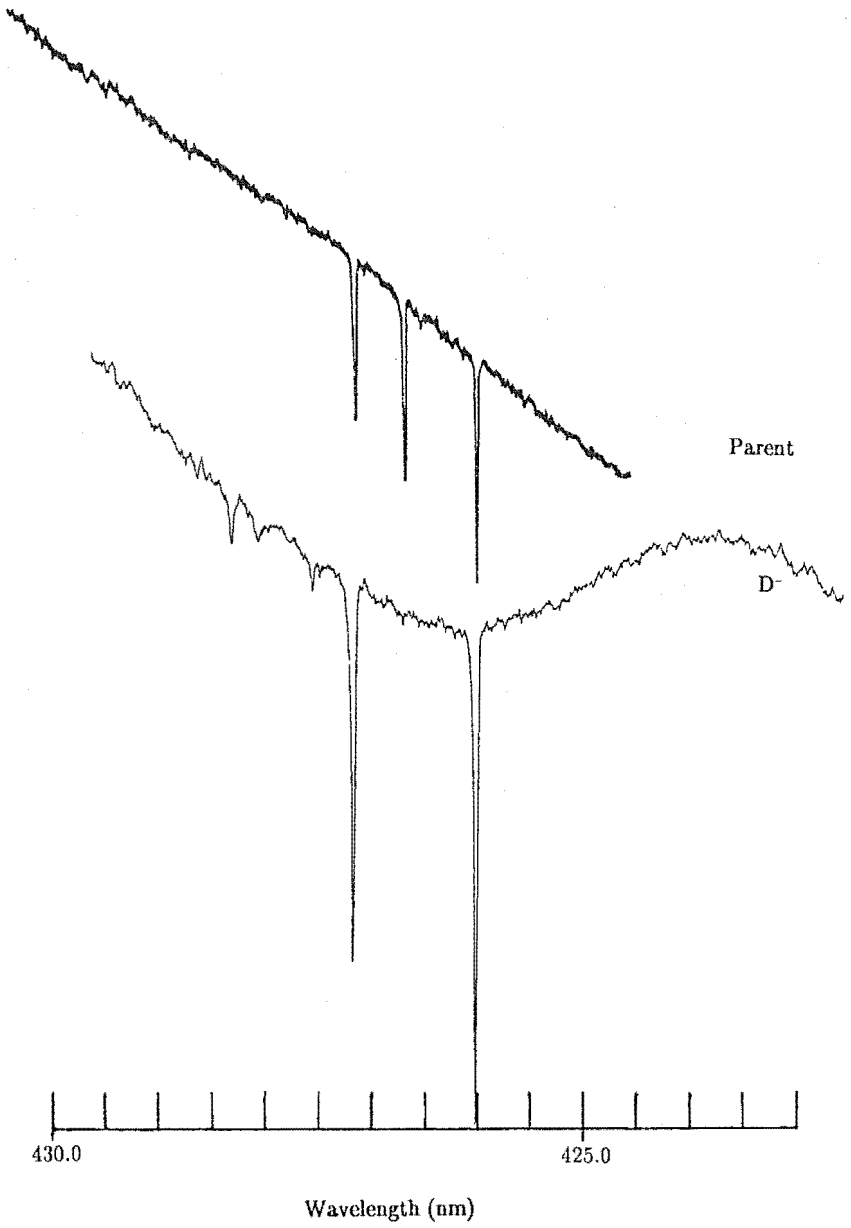

Figure 4.10: 10 K $^2P_{1/2}$ (I) multiplet absorption spectrum for $CaF_2 : (0.05\%)Nd^{3+}$ crystals before and after hydrogenation treatments.

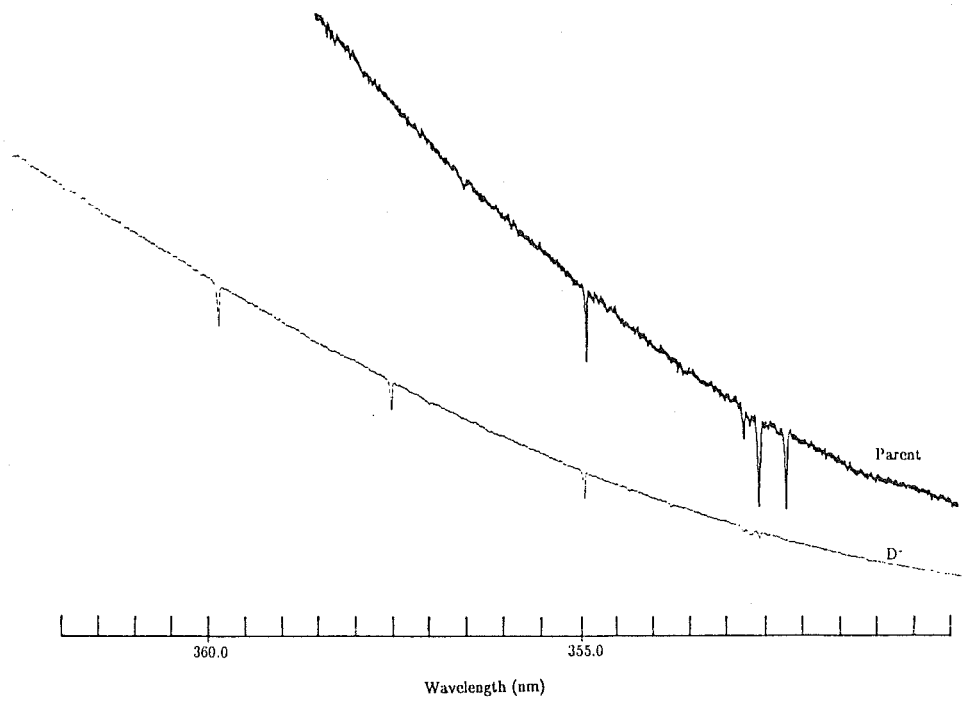

Figure 4.11: 10 K $^4D_{3/2}$ (L) multiplet absorption spectrum for $CaF_2 : (0.05\%)Nd^{3+}$ crystals before and after hydrogenation treatments.

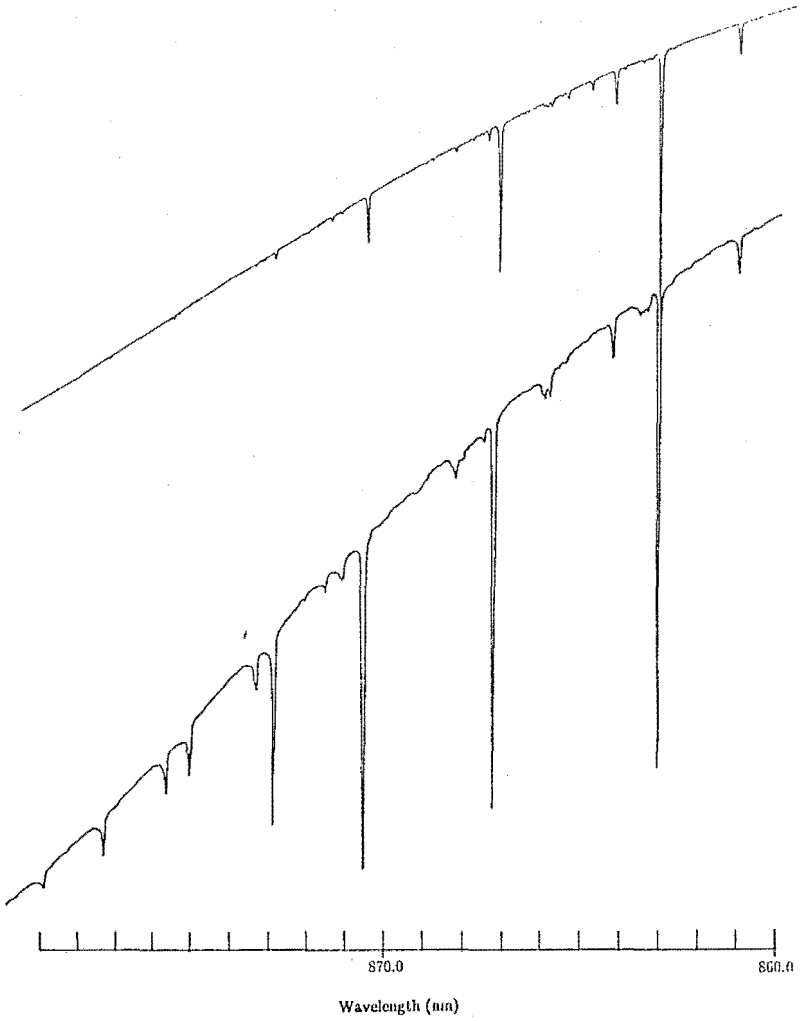

Figure 4.12: 10 K ${}^4F_{3/2}$ (R) multiplet absorption spectrum of deuterated SrF_2 : $(0.05\%)Nd^{3+}$ crystals for a) 68 hours (top); b) 102 hours (bottom).

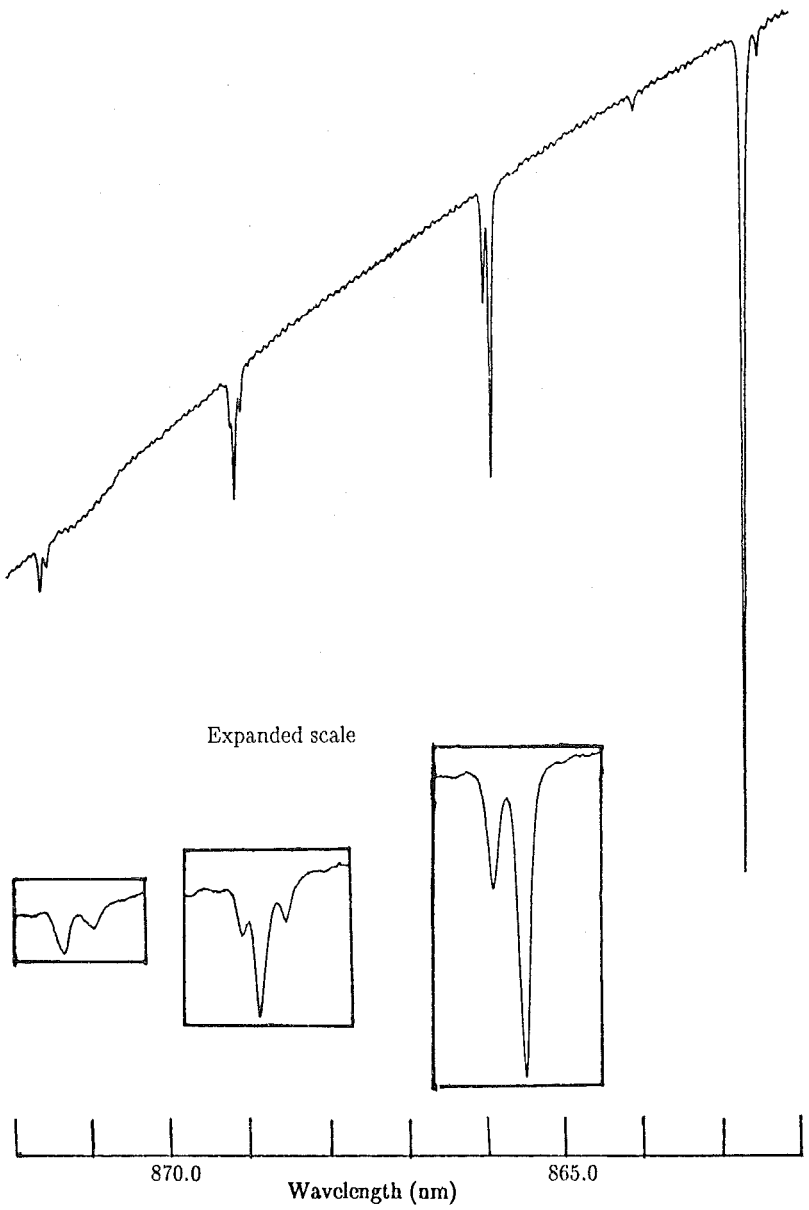

Figure 4.13: 10 K ${}^4F_{3/2}$ (R) multiplet absorption spectrum of a mixed $T^- + H^-$ $SrF_2 : (0.05\%)Nd^{3+}$ crystal.

Chapter 5

Laser Selective Excitation

5.1 Introduction

Traditionally assignment of RE^{3+} crystal field levels to specific symmetry centres is achieved by the method of concentration series (Voron'ko et al. 1966, 1969). Such assignments are confirmed by the observation of a common energy level separation, equal to the spacing between the two lowest crystal field levels of the ground multiplets, between pairs of absorption lines, together with temperature dependence of the intensities of these lines (Smalley 1971). An alternative method is to use the technique of laser selective excitation developed by Wright and co-workers (Tallant et al. 1976, Gustafson and Wright 1979).

The application of the technique of selective excitation to the alkaline earth fluorides can be traced back to Voron'ko et al. s' studies (1965) of CaF_2 : Er^{3+} where they used the combination of a strong white light source and a monochromator to selectively excite individual symmetry centres. They were able to separate, from the total absorption spectrum, the spectra belonging to three different types of centres, but were hampered by the low intensity and the band width of the light source. The development of the tunable dye laser provides an ideal intense light source for this technique, which was modified and improved by Wright and co-workers in their laser selective excitation studies (Tallant et al. 1976, Gustafson and Wright 1979).

The fluorescence spectrum of a specific RE^{3+} symmetry centre can be obtained by setting the dye laser wavelength into resonance with an absorption line associated with that centre and scanning the monochromator to record the fluorescence. Judicious choice of non- overlapping absorption lines makes it possible to determine the crystal field levels belonging to each individual symmetry centre from the total absorption spectrum. The converse experiment of monitoring non-overlapping fluorescence transitions while scanning the dye laser results in a single centre excitation spectrum which indicates the absorption lines belonging to the monitored centre. This technique gives much higher sensitivity and resolvability than optical absorption but, in prac-

tice, there are often near coincidences of transitions from different symmetry centres.

Laser selective excitation studies at 10K were carried out on all the centres identified in the absorption spectra of the $SrF_2 : Nd^{3+}$ and $CaF_2 : Nd^{3+}$ systems. The C and D multiplets were excited by a tunable dye laser using R6G dye, while monitoring the strong near-infrared fluorescence transitions from the R multiplet. The equipment used enabled the detection of the near-infrared fluorescence transitions from the R multiplet to the levels of Z and Y multiplets.

As a consequence of strong non-radiative processes involving hydrogenic ions both the H^- and D^- centres have weaker fluorescence than their corresponding F^- centres by factors of 10^4 and 10^2 respectively. Discrimination of H^- centres from other centres was hampered by the weak fluorescence of the H^- centre and by overlapping absorption lines of other F^- centres for the multiplets being excited; consequently the corresponding D^- centres were preferentially studied. In addition to the new hydrogenic symmetry centres identified in the absorption spectra, four new fluorine centres were identified for $SrF_2 : Nd^{3+}$ and six for $CaF_2 : Nd^{3+}$.

Excitation spectra were used to assign crystal field levels of the C and D multiplets; the assignment of other multiplets was obtained by correlation with additional results from energy upconversion measurements, which are to be presented in Chapter 6.

The results for each individual symmetry centre will be discussed in the remainder of this chapter together with their associated optical absorption results. As a general result for Nd^{3+}, no fluorescence was observed directly from the excited C and D multiplets, which indicates a very fast non-radiative de-excitation from these excited multiplets to the emitting R multiplet. This is consistent with earlier studies of Nd^{3+} ions in other host materials (Reddy and Venkatesvarlu 1983).

5.2 The Tetragonal Symmetry Centres (C_{4V}; L centre of Voron'ko et al. 1965)

5.2.1 Before Hydrogenation Treatment

At 0.05% Nd^{3+} ion concentration, the absorption spectra of the $SrF_2 : Nd^{3+}$ system is dominated by lines of the tetragonal symmetry charge compensating centre; the optical absorption spectra being that described in Chapter 4. The absorption lines pattern for the same tetragonal symmetry centre in $CaF_2 : Nd^{3+}$ closely resembles its counterpart in $SrF_2 : Nd^{3+}$.

The fluorescence spectra of this symmetry centre in both $SrF_2 : Nd^{3+}$ and $CaF_2 : Nd^{3+}$ were recorded and are shown in Figs. 5.1 and 5.2 respectively.

They exhibit the strongest fluorescence of all the centres observed for 0.05% Nd^{3+} ion concentration.

Analysis of the 60 K fluorescence spectra revealed transitions from the second crystal field level of the R multiplet, $R_2 \rightarrow Z_1$, at wavelengths of 857.05 ($\pm.05$) nm and 854.0 ($\pm.1$) nm for $SrF_2 : Nd^{3+}$ and $CaF_2 : Nd^{3+}$ respectively. The assigned energy levels of the C_{4V} F^- centre are listed in Tables. 5.1 and 5.2 for $SrF_2 : Nd^{3+}$ and $CaF_2 : Nd^{3+}$ respectively. A detailed analysis of the fluorescence spectra failed to locate the $R_1 \rightarrow Z_4$ transition in the region predicted by Freeth and Jones (1982) in their crystal field calculations. The presence of an additional energy level situated at 164 cm^{-1} in the $SrF_2 : Nd^{3+}$ system was observed confirming the observation of Freeth and Jones (1982). The two transitions at 869.6 nm and 875.9 nm associated with this energy level were found to have the same energy separation as the R_2 to R_1 separation. The observation of this energy level in energy upconversion, which is discussed in Chapter 6, reinforces Freeth's suggestion that this level belongs to the C_{4V} symmetry centre. However, an attempt to accommodate this level in the crystal field analysis failed to give a good overall fit and its absence in $CaF_2 : Nd^{3+}$ raises doubts as to its electronic origin. Results from the hydrogenated C_{4V} centres in $SrF_2 : Nd^{3+}$, presented below, also show similar additional structures on the $R_1 \rightarrow Z_3$ electronic transition. This suggests that the 164 cm^{-1} level is a vibronic feature associated with all the C_{4V} centres, which is apparent in SrF_2, but not in CaF_2.

5.2.2 After Hydrogenation Treatment

The fluorescence spectra of the C_{4V} H^- centres for both $SrF_2 : Nd^{3+}$ and $CaF_2 : Nd^{3+}$ were very weak and, as observations were also hampered by strong fluorescence from other centres, only a few of the $^4I_{9/2}$ multiplet energy levels were identified for this centre. Consequently the corresponding D^- and T^- centres were preferentially studied. Hydrogenic C_{4V} centre spectra for both $SrF_2 : Nd^{3+}$ and $CaF_2 : Nd^{3+}$ are presented in Figs. 5.1 to 5.3 and their corresponding energy levels are listed in Table 5.3.

All the hydrogenic C_{4V} centres observed have spectra with a similar fluorescence intensity pattern to that of the corresponding C_{4V} F^- spectrum. For the $R_1 \rightarrow Z_1$ transition only a small isotope shift was observed between H^-, D^- and T^- as indicated in the absorption spectrum of the $^4F_{3/2}$ multiplet, Fig. 5.4. A comparison of the optical absorption results confirmed the $R_1 \rightarrow Z_1$ transition to be at 8631.1 ($\pm.1$), 8664.6 ($\pm.2$), 8663.3 ($\pm.3$) and 8664.1 ($\pm.2$) nm for F^-, T^-, D^- and H^- analogues in $SrF_2 : Nd^{3+}$ respectively. The Z_2 energy levels of D^- and T^- centres in $SrF_2 : Nd^{3+}$ are similar and are situated approximately 82 cm^{-1} above the Z_1 energy level in each case, whereas for the D^- centre in $CaF_2 : Nd^{3+}$ the Z_2 to Z_1 separation

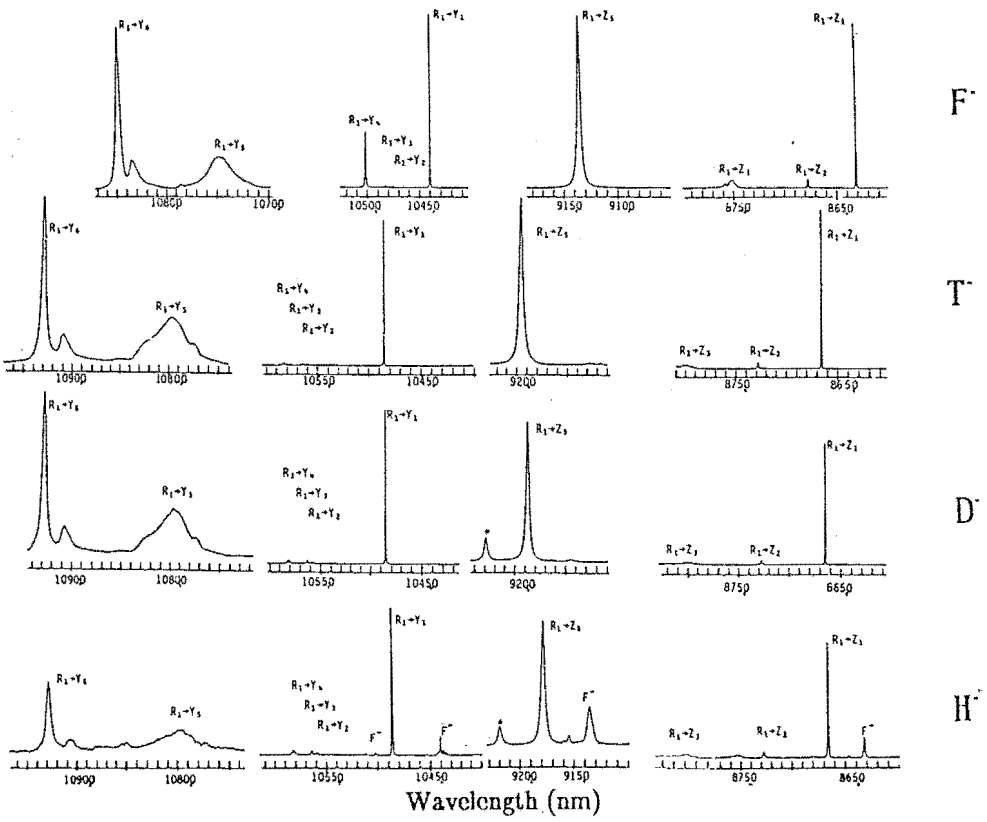

Figure 5.1: 10 K fluorescence spectra of the C_{4V} F^-, T^-, D^- and H^- centres of $SrF_2 : Nd^{3+}$ crystals. * **unidentified line.**

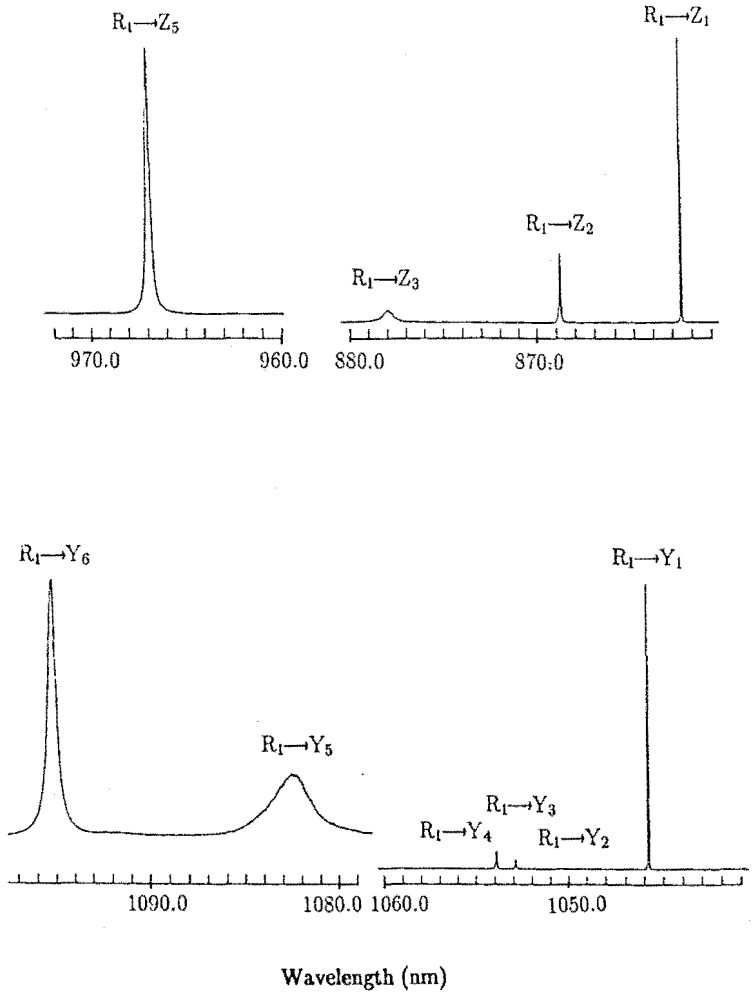

Figure 5.2: 10 K fluorescence spectra of $CaF_2 : Nd^{3+}$ C_{4V} F^- centre.

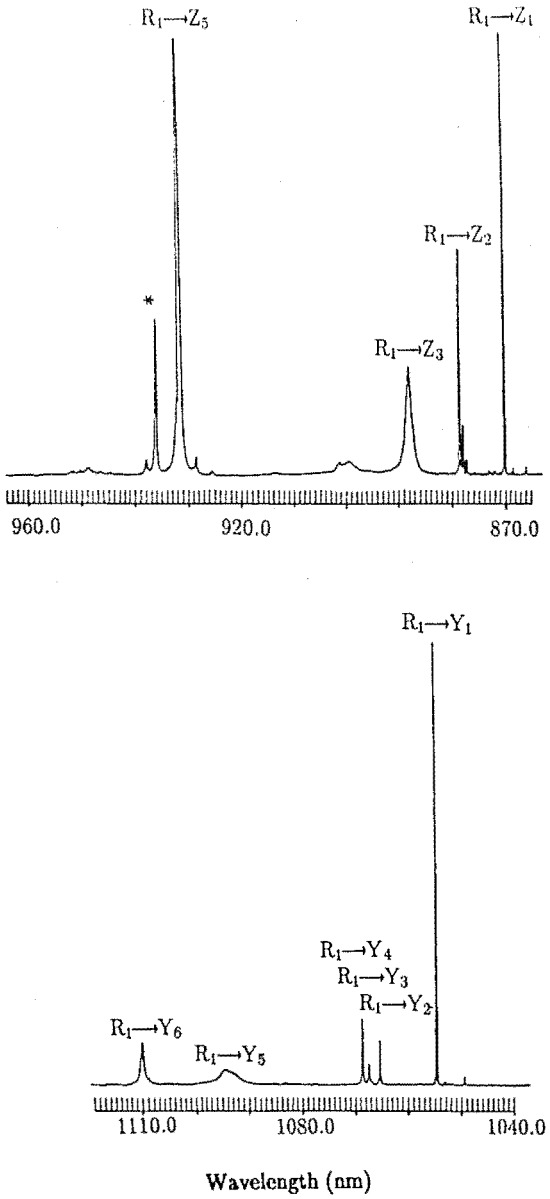

Figure 5.3: 10 K fluorescence spectra of CaF_2 : Nd^{3+} C_{4V} D^- centre. * unidentified line.

is 110 cm^{-1}. Additional structures were observed on the $R_1 \rightarrow Z_3$ electronic transition for H^-, D^- and T^- centres in $SrF_2 : Nd^{3+}$ but not for any centre in $CaF_2 : Nd^{3+}$. These correlate with the additional energy level (164 cm^{-1}) previously described for the $SrF_2 : Nd^{3+}$ C_{4V} F^- centre.

Another additional electronic transition was observed in the C_{4V} D^- and H^- analogues fluorescence spectra at 921.7 nm and 921.4 nm for $SrF_2 : Nd^{3+}$, and at 932.6 nm for the D^- analogue in $CaF_2 : Nd^{3+}$. It has the same tuning characteristics as the other electronic lines for the same centre, but its absence in the T^- and F^- spectra makes its origin uncertain. An attempt to treat it as terminating on either the Z_4 or Z_5 level in the crystal field analysis failed to give a good overall fit and it was therefore omitted in the final crystal field analysis to be presented in Chapter 7.

Local mode vibronic lines were observed for all the hydrogenic C_{4V} centres studied. The two vibronic lines associated with each electronic transition have energy separations from their parent electronic transition closely matching the local mode vibronic frequencies, which have been observed in infrared absorption studies (Edgar et al. 1977). The observed C_{4V} local mode vibronic frequencies of T^-, D^- and H^- for $SrF_2 : Nd^{3+}$ and $CaF_2 : Nd^{3+}$ are presented in Table 5.4. They match the predicted infrared D^- and T^- local mode frequencies, as deduced from the observed H^- local mode frequencies for reduced mass factors of 1.39 and 1.67 respectively. The $R_1 \rightarrow Z_5$ electronic transition showed the strongest and clearest vibronic lines which are presented in Figs. 5.5 and 5.6. Local mode vibronic lines corresponding to the additional transition observed in the 910 nm region in the D^- spectra were also evident as shown in Figs. 5.5 and 5.6. They have the same energy separation from their parent electronic transition as the vibronics corresponding to the other electronic lines of the C_{4V} D^- centre.

5.2.3 Polarisation

For $\langle 100 \rangle$ orientated crystals, the intensity pattern of the polarised fluorescence spectrum for the appropriate transitions is expected to closely follow the predicted ratios as discussed in Chapter 2. Polarised fluorescence spectra of the C_{4V} F^-, T^- and D^- centres, obtained by exciting different crystal field levels of the C and D multiplets, for both $SrF_2 : Nd^{3+}$ and $CaF_2 : Nd^{3+}$ are presented in Figs. 5.7 to 5.23. The complex intensity pattern of these polarised fluorescence spectra can be analysed following the phenomenological approach as discussed in Chapter 2.

Firstly, the absolute intensity measured is not significant due to different settings of slit width and gain for each set of polarisation spectra. Difficulties arise from not knowing the symmetry of the excited and the fluorescing levels. Fortunately, the symmetry of the various levels in the ^4I multiplets have been determined by Freeth and Jones (1982) in their Zeeman study of the C_{4V} F^-

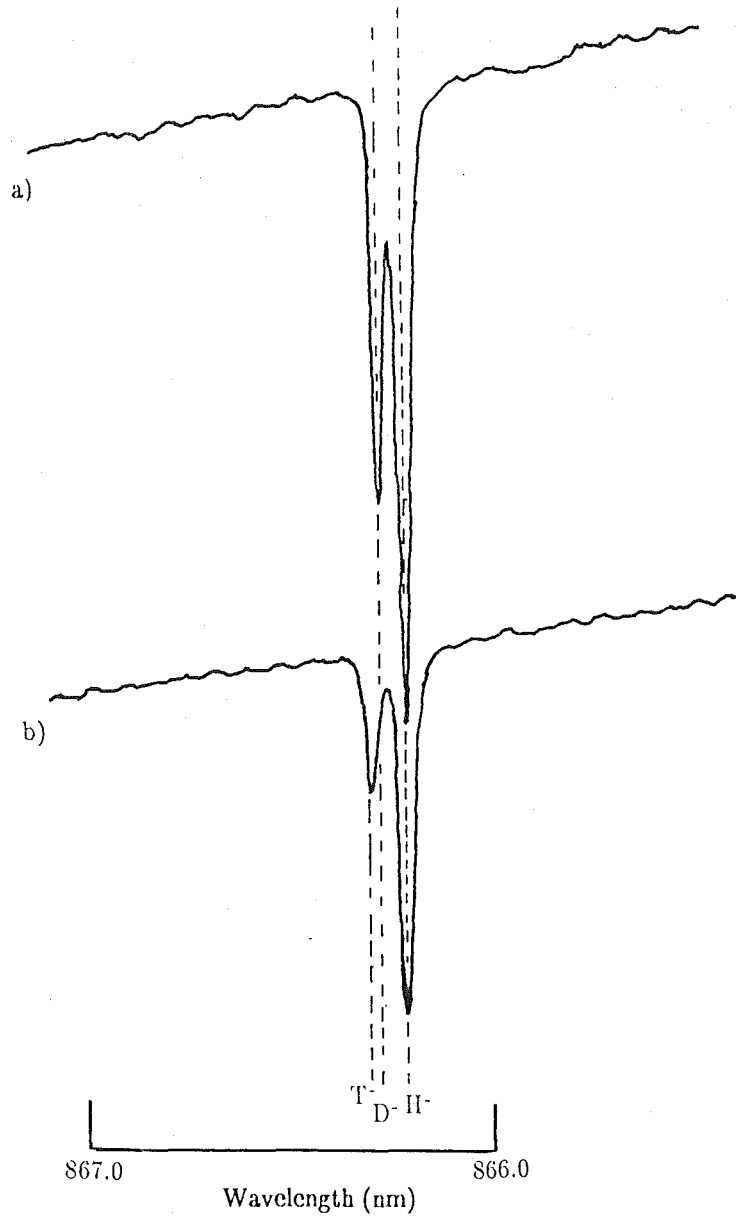

Figure 5.4: 10 K R multiplet absorption spectrum of $SrF_2 : Nd^{3+}$ showing the lines associated with the C_{4V} centre.
a) $D^- + H^-$; b) $T^- + H^-$.

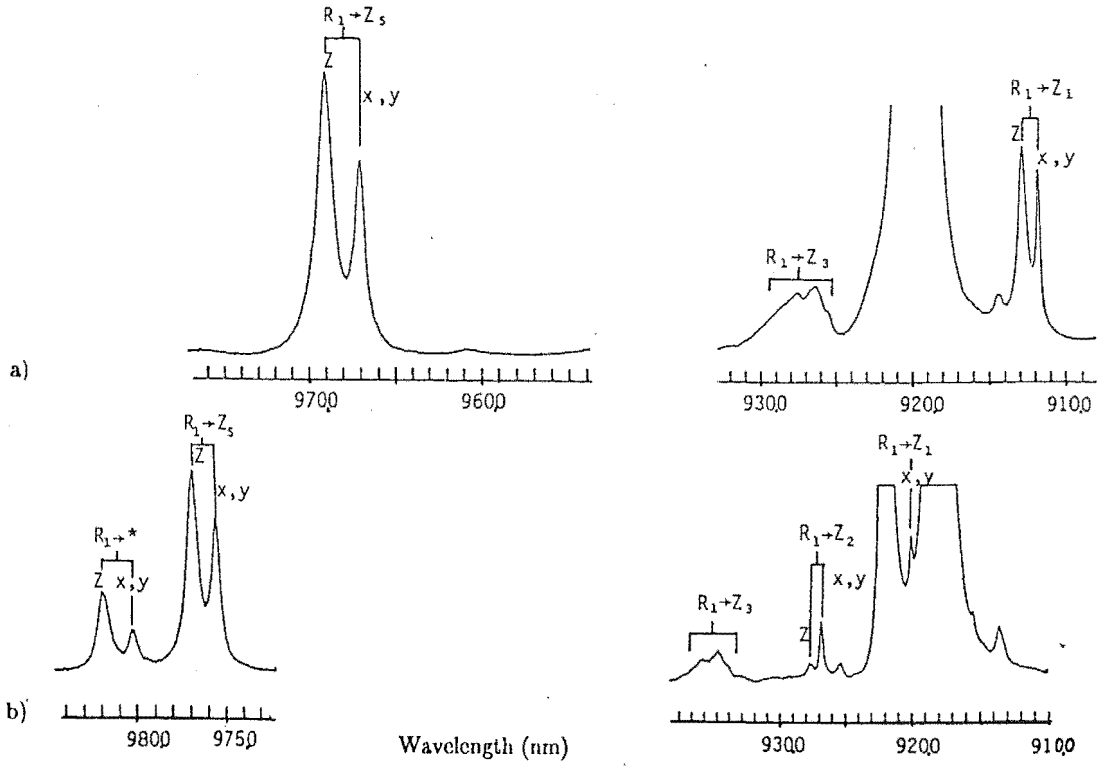

Figure 5.5: 10 K fluorescence spectrum showing the vibronic lines associated with the $R_1 \rightarrow Z_i$ transitions for the $SrF_2 : Nd^{3+}$ C_{4V} a) T^- and b) D^- centres. * unidentified line.

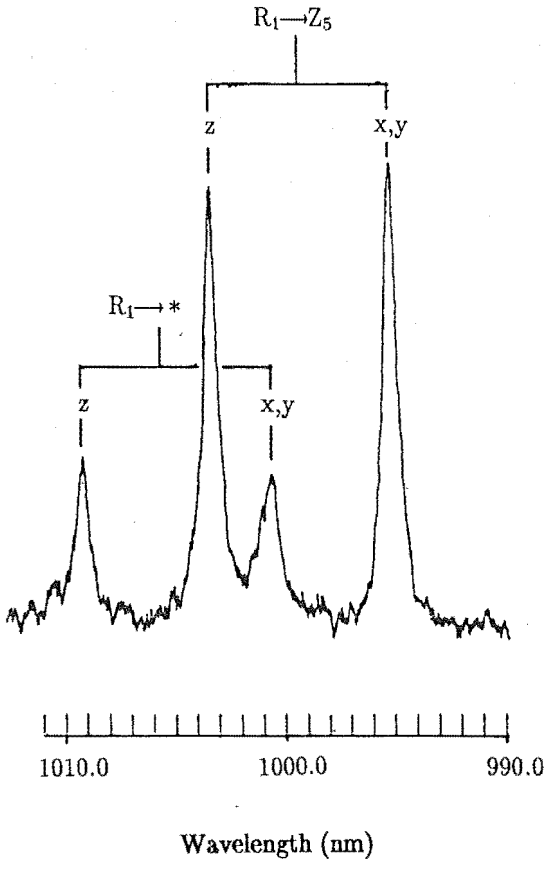

Figure 5.6: 10 K fluorescence spectrum showing the vibronic lines associated with the $R_1 \rightarrow Z_5$ transitions for the $CaF_2 : Nd^{3+}$ D^- C_{4V} centres. * unidentified line.

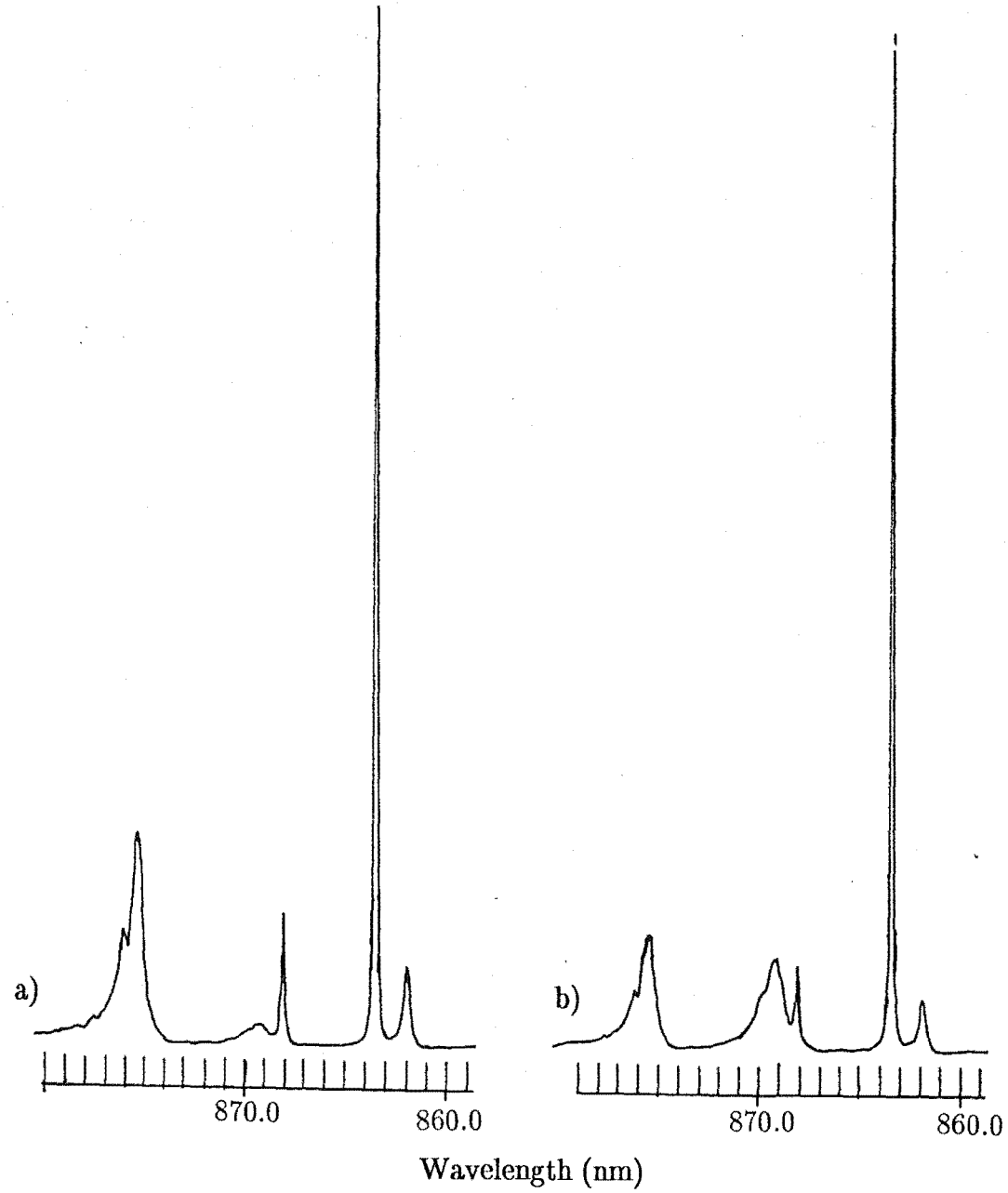

Figure 5.7: 60 K polarised fluorescence spectrum of $R_1 \rightarrow Z_{1,2,3}$ transitions for $SrF_2 : Nd^{3+}$ C_{4V} F^- centre with laser excitation at 17199 cm^{-1} (in air) for a) (yy) and b) (yx) polarisation.

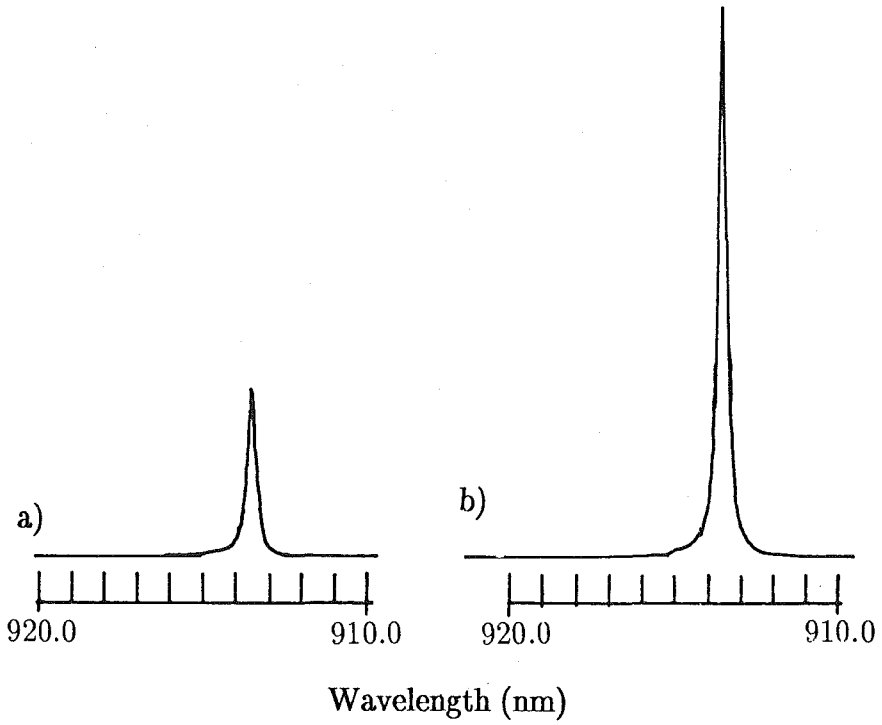

Figure 5.8: 10 K polarised fluorescence spectrum of $R_1 \rightarrow Z_5$ transition for $SrF_2 : Nd^{3+}\ C_{4V}\ F^-$ centre with laser excitation at 15968 cm^{-1} (in air) for a) (yx) and b) (yy) polarisation.

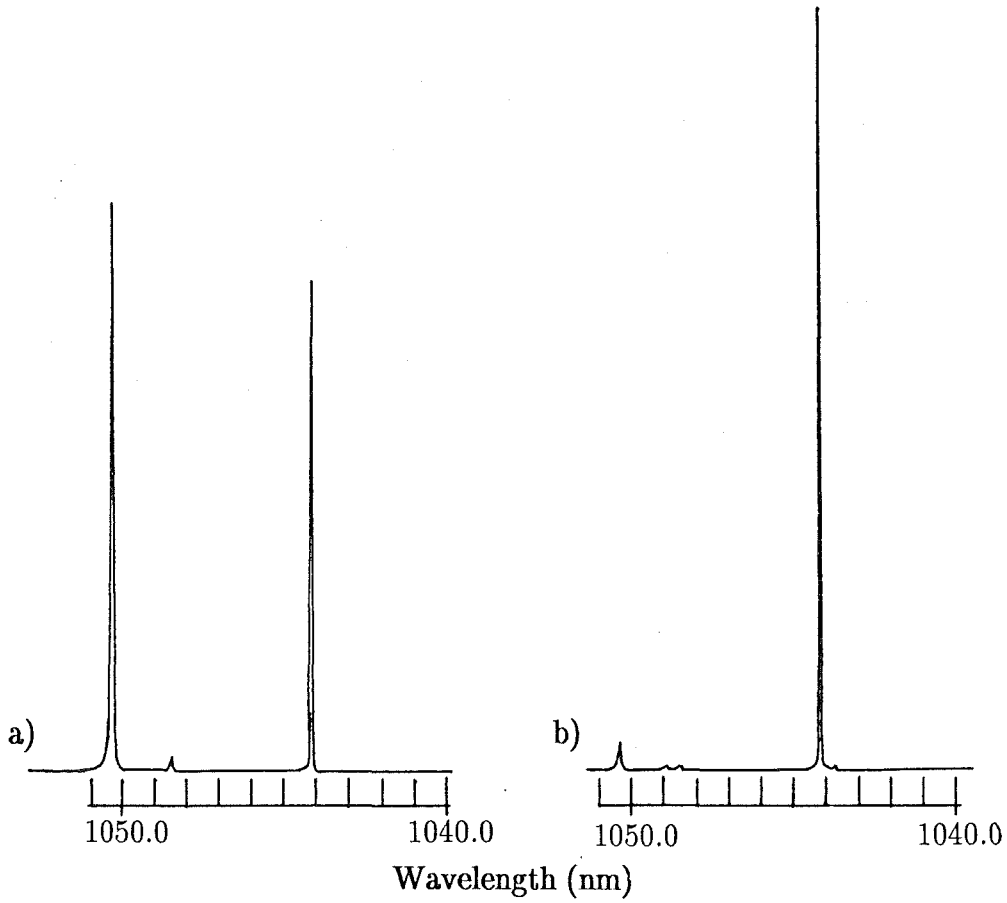

Figure 5.9: 10 K polarised fluorescence spectrum of $R_1 \rightarrow Y_{1,2,3,4}$ transitions for $SrF_2 : Nd^{3+}$ C_{4V} F^- centre with laser excitation at 15968 cm^{-1} (in air) for a) (yx) and b) (yy) polarisation.

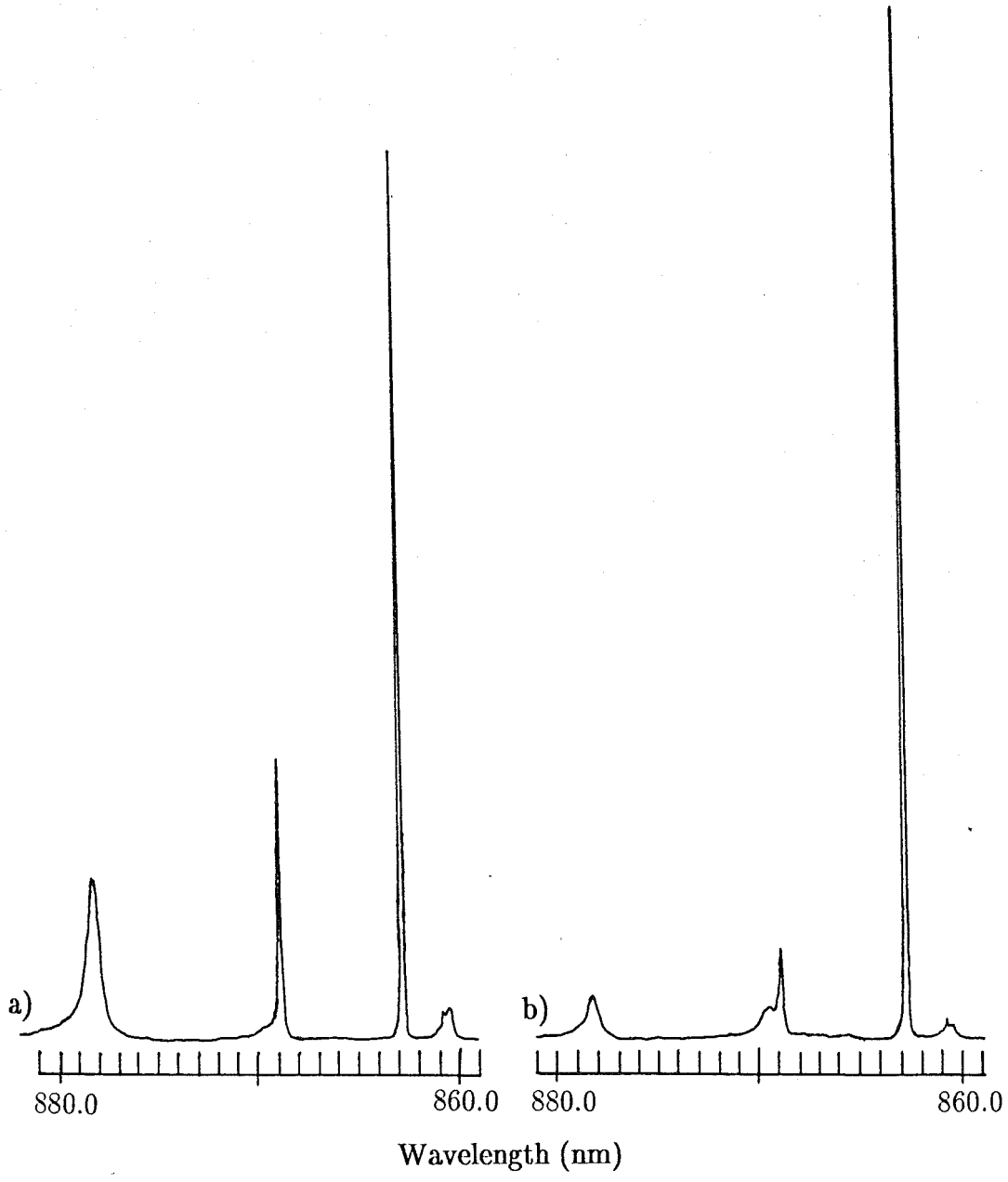

Figure 5.10: 60 K polarised fluorescence spectrum of $R_1 \rightarrow Z_{1,2,3}$ transitions for $CaF_2 : Nd^{3+}\ C_{4V}\ F^-$ centre with laser excitation at 17347 cm^{-1} (in air) for a) (yx) and b) (yy) polarisation.

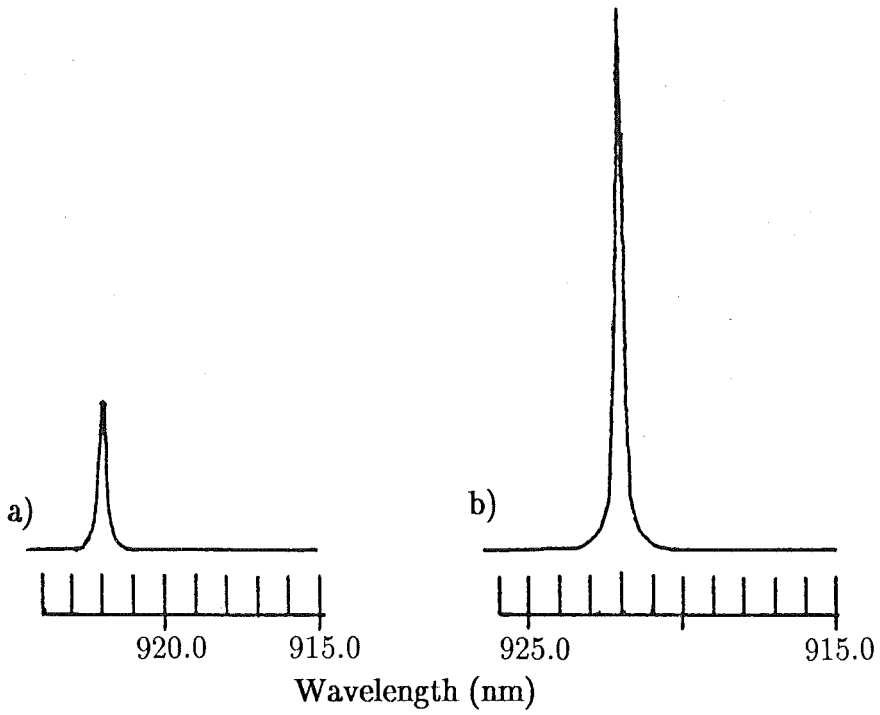

Figure 5.11: 60 K polarised fluorescence spectrum of $R_1 \rightarrow Z_5$ transition for $CaF_2 : Nd^{3+}$ C_{4V} F^- centre with laser excitation at 17347 cm^{-1} (in air) for a) (yx) and b) (yy) polarisation.

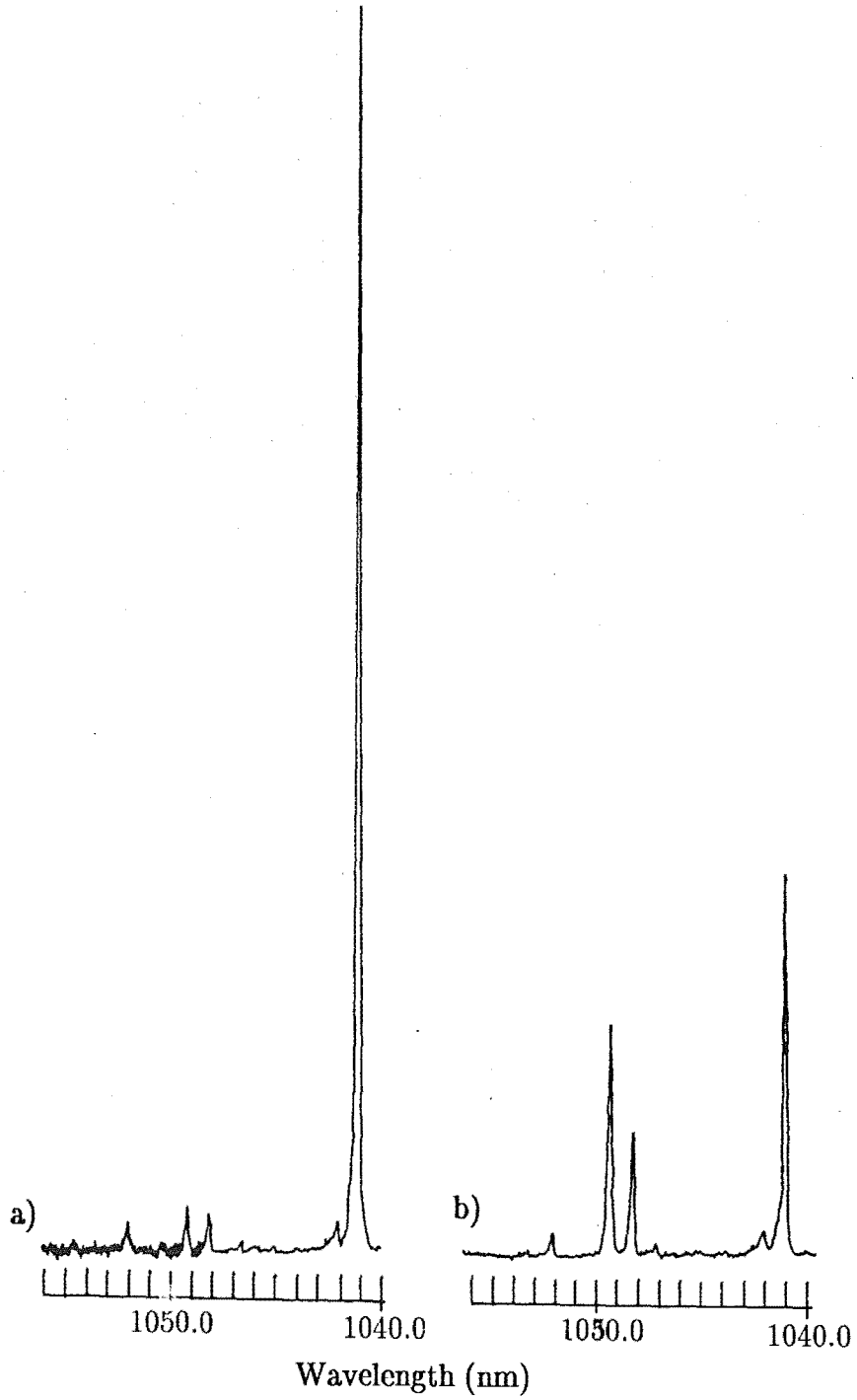

Figure 5.12: 60 K polarised fluorescence spectrum of $R_1 \rightarrow Y_{1,2,3,4}$ transitions for $CaF_2 : Nd^{3+}$ C_{4V} F^- centre with laser excitation at 17347 cm^{-1} (in air) for a) (yx) and b) (yy) polarisation.

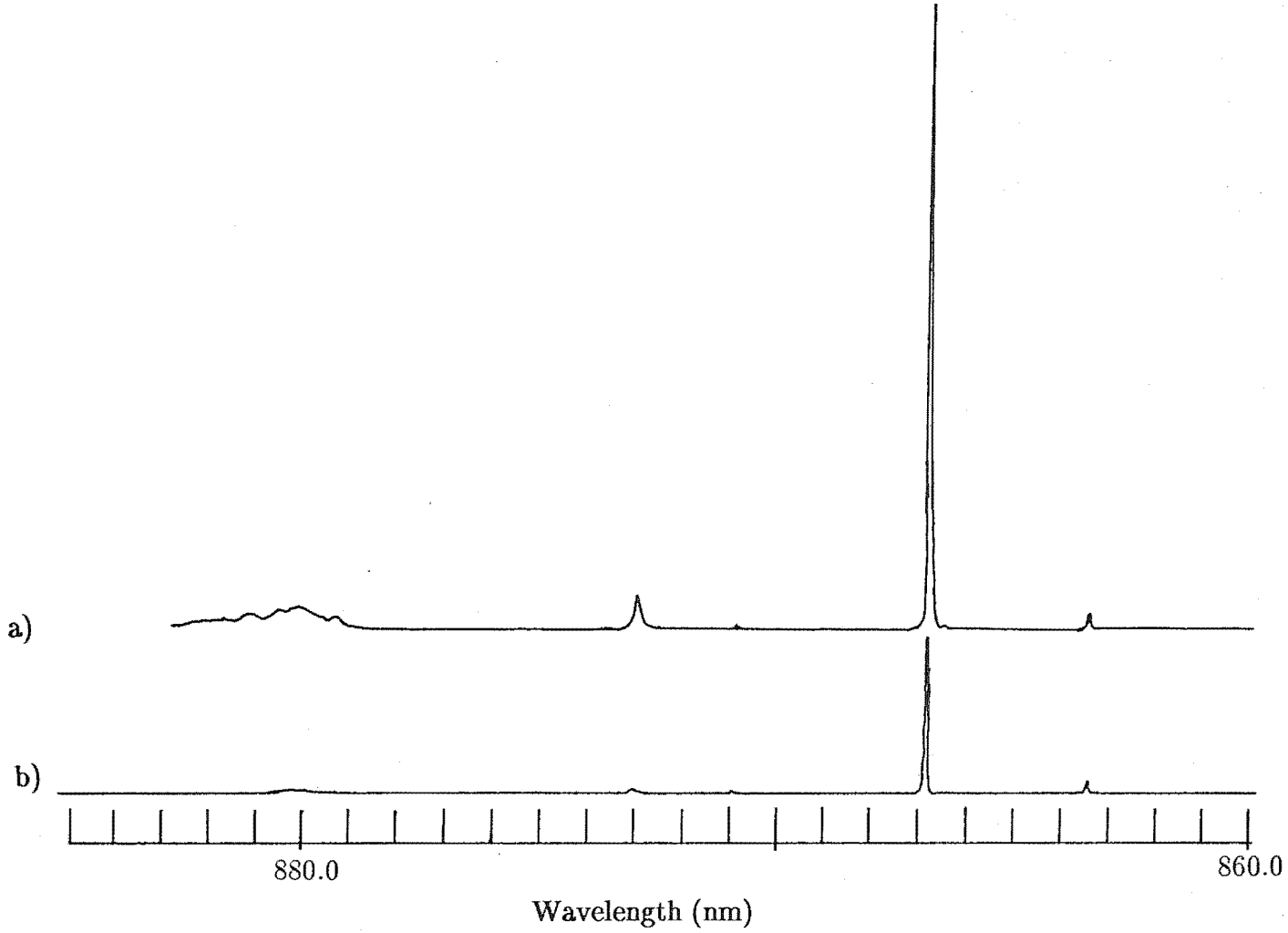

Figure 5.13: 10 K polarised fluorescence spectrum of $R_1 \rightarrow Z_{1,2,3}$ transitions for $SrF_2 : Nd^{3+}$ C_{4V} T^- centre with laser excitation at 17299 cm^{-1} (in air) for a) (yx) and b) (yy) polarisation.

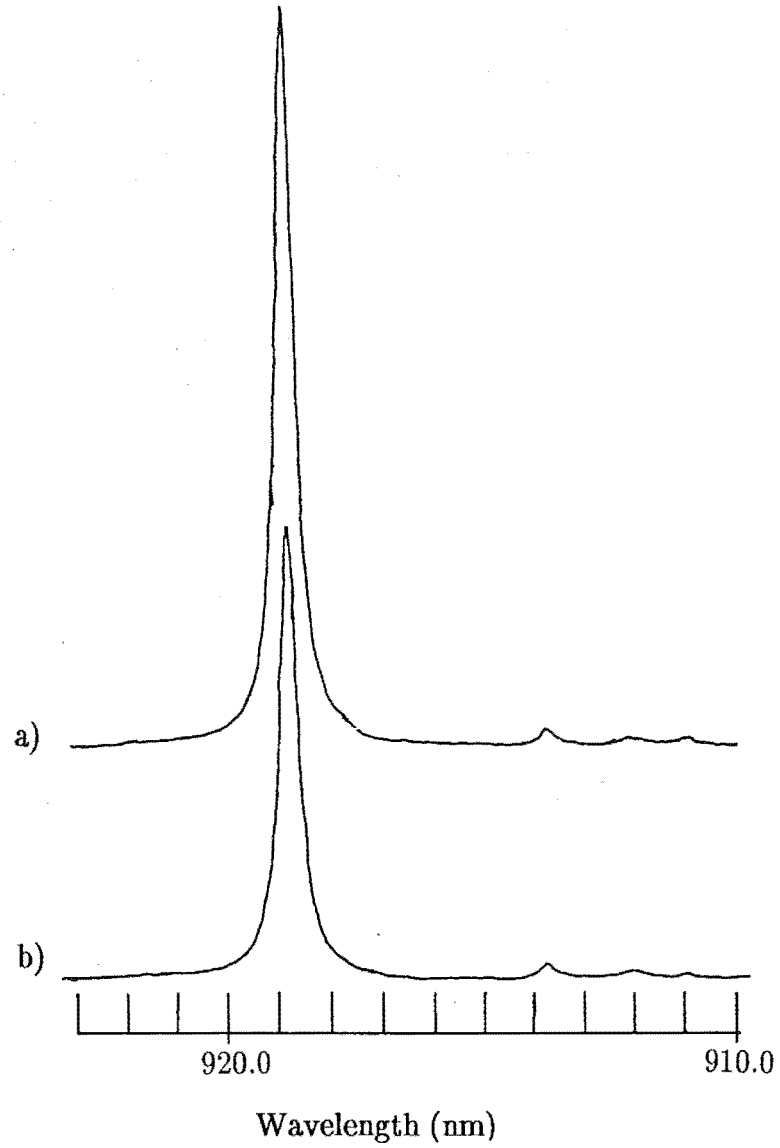

Figure 5.14: 10 K polarised fluorescence spectrum of $R_1 \rightarrow Z_5$ transition for $SrF_2 : Nd^{3+}$ C_{4V} T^- centre with laser excitation at 17299 cm^{-1} (in air) for a) (yx) and b) (yy) polarisation.

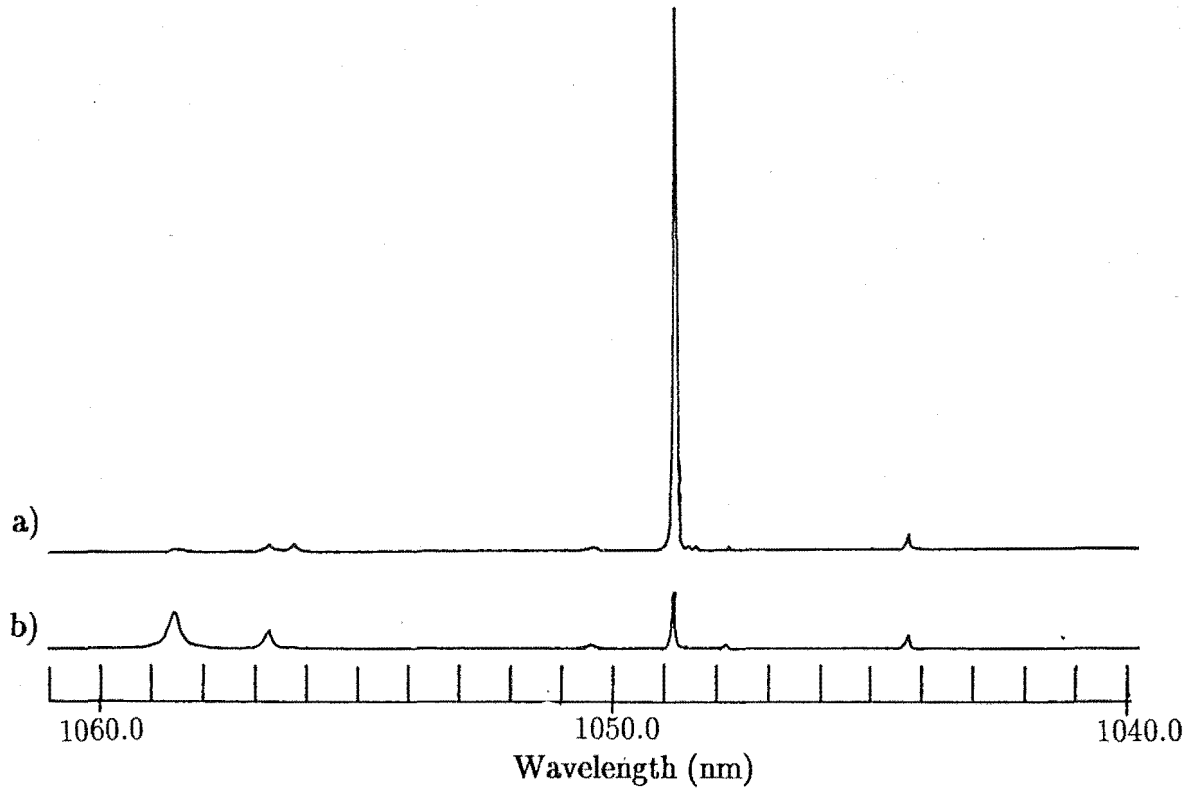

Figure 5.15: 10 K polarised fluorescence spectrum of $R_1 \rightarrow Y_{1,2,3,4}$ transitions for $SrF_2 : Nd^{3+}$ C_{4V} T^- centre with laser excitation at 17299 cm^{-1} (in air) for a) (yx) and b) (yy) polarisation.

centres in $CaF_2 : Nd^{3+}$ and $SrF_2 : Nd^{3+}$.

Using these results as a basis it was possible to deduce the possible symmetries of the excited and emitting levels. The present analysis based on the phenomenological approach is more clearly illustrated by way of examples. Consider the excitation of the energy level at 16061 cm^{-1} for the $SrF_2 : Nd^{3+}$ C_{4V} F^- centre. The intensity pattern of the electronic transitions terminating at levels having γ_7 symmetry showed an approximately 2:1 ratio for (yy):(yx) polarisation intensities. This suggests the emitting level, R_1, has a γ_6 symmetry and that the initial excitation involved σ polarisation only, i.e. $\gamma_6 \rightarrow \gamma_7$ transition, with the excited level having a γ_7 symmetry. From equation 2.22 the total effects can be summarised as follows :

(yy)	(yx)
$I_{\sigma\sigma}$	$I_{\sigma\pi}$
$I_{\sigma\sigma}$	$I_{\sigma\sigma}$.

(5.1)

The electric-dipole transition rules indicate a 2:1 ratio for (yy):(yx) polarisation intensities of transitions involving two energy levels of different symmetry, which is in close agreement with the present observation where :

$$\begin{array}{rcll} (yy):(yx) & = & 1.6 & (R_1\,\gamma_6 \rightarrow Z_2\,\gamma_7) \\ & & 1.8 & (R_1\,\gamma_6 \rightarrow Z_3\,\gamma_7) \\ & & 1.9 & (R_1\,\gamma_6 \rightarrow \text{'unidentified line'}) \\ & & 1.8 & (R_1\,\gamma_6 \rightarrow Y_1\,\gamma_7) \quad . \end{array} \tag{5.2}$$

All of the polarisation intensity ratios derived from the data have an uncertainty of up to $\pm 12\%$. For transitions between two levels of the same symmetry, the relationship is :

$$I_{\sigma\sigma} = \frac{(yy)}{2} \tag{5.3}$$

and

$$I_{\sigma\pi} = (yx) - \frac{(yy)}{2} \tag{5.4}$$

giving the fluorescence intensity ratios :

$$\begin{array}{rcl} I_\pi:I_\sigma & = & I_{\sigma\pi}:I_{\sigma\sigma} \\ & = & \begin{array}{ll} 0.92 & (R_1\,\gamma_6 \rightarrow Z_1\,\gamma_6) \\ 23.0 & (R_1\,\gamma_6 \rightarrow Y_4\,\gamma_6) \\ 0.22 & (R_2\,\gamma_7 \rightarrow Z_2\,\gamma_7) \\ 6.0 & (R_2\,\gamma_7 \rightarrow Z_3\,\gamma_7) \quad . \end{array} \end{array} \tag{5.5}$$

The assignment of γ_6 symmetry to the emitting level, R_1, is further supported by the observation of a 2:1 ratio for the (yy):(yx) polarisation intensities of the $R_2 \rightarrow Z_1$ transition. This means the symmetry of the R_2 energy level is γ_7.

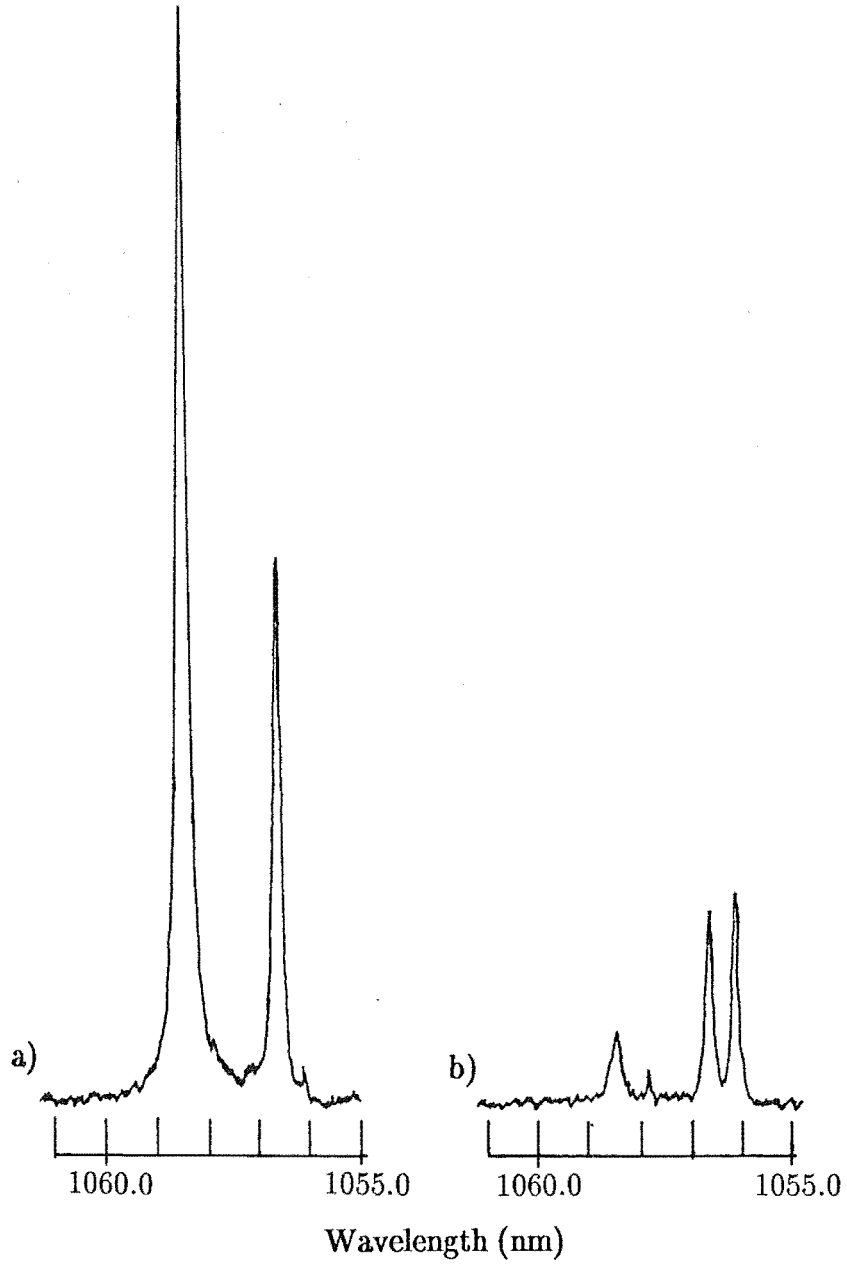

Figure 5.16: 10 K polarised fluorescence spectrum of $R_1 \rightarrow Y_{2,3,4}$ transitions for $SrF_2 : Nd^{3+}$ C_{4V} T^- centre with laser excitation at 17299 cm^{-1} (in air) for a) (yy) and b) (yx) polarisation.

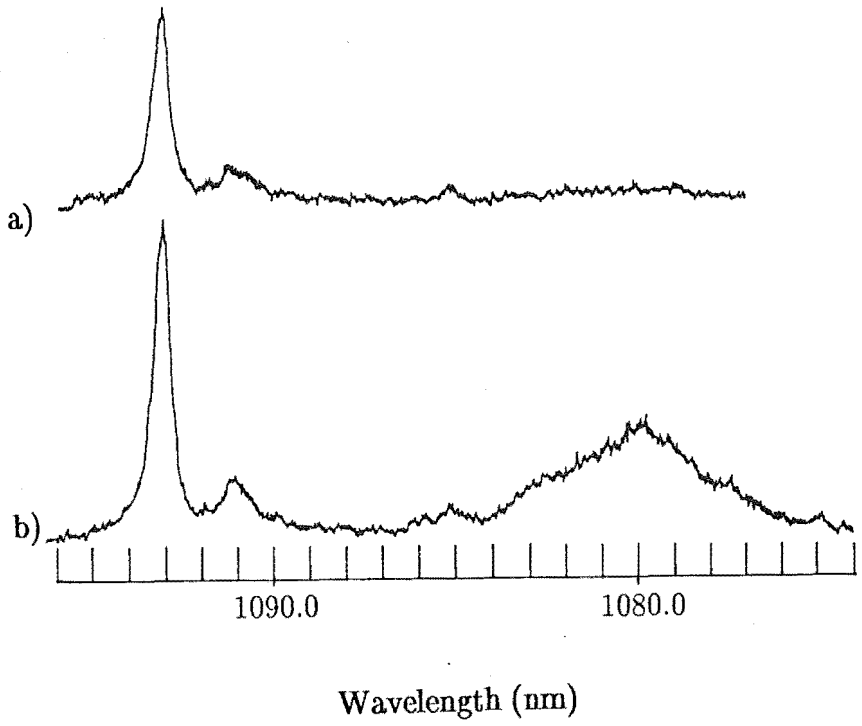

Figure 5.17: 10 K polarised fluorescence spectrum of $R_1 \rightarrow Y_{5,6}$ transitions for $SrF_2 : Nd^{3+}$ C_{4V} T^- centre with laser excitation at 17299 cm^{-1} (in air) for a) (yy) and b) (yx) polarisation.

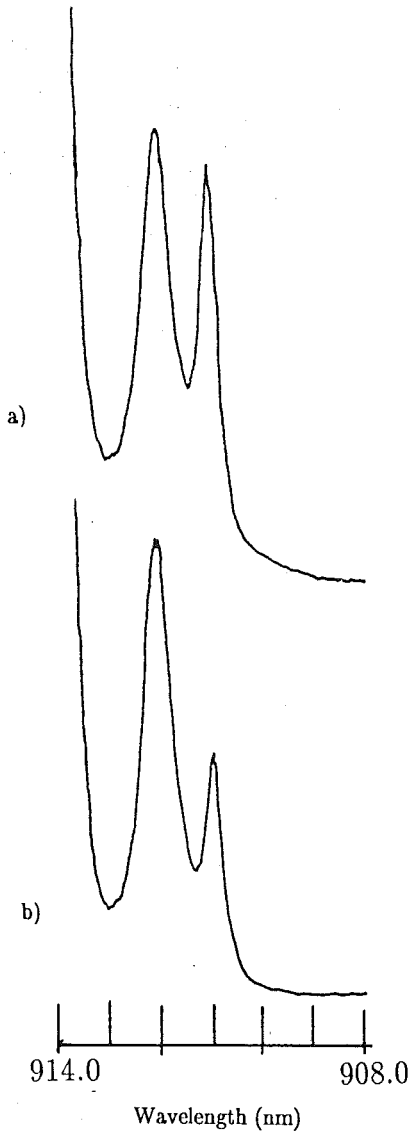

Figure 5.18: 10 K polarised fluorescence spectrum showing the vibronic lines associated with the $R_1 \rightarrow Z_1$ transitions for $SrF_2 : Nd^{3+}$ C_{4V} T^- centre with laser excitation at 17299 cm^{-1} (in air) for a) (yx) and b) (yy) polarisation.

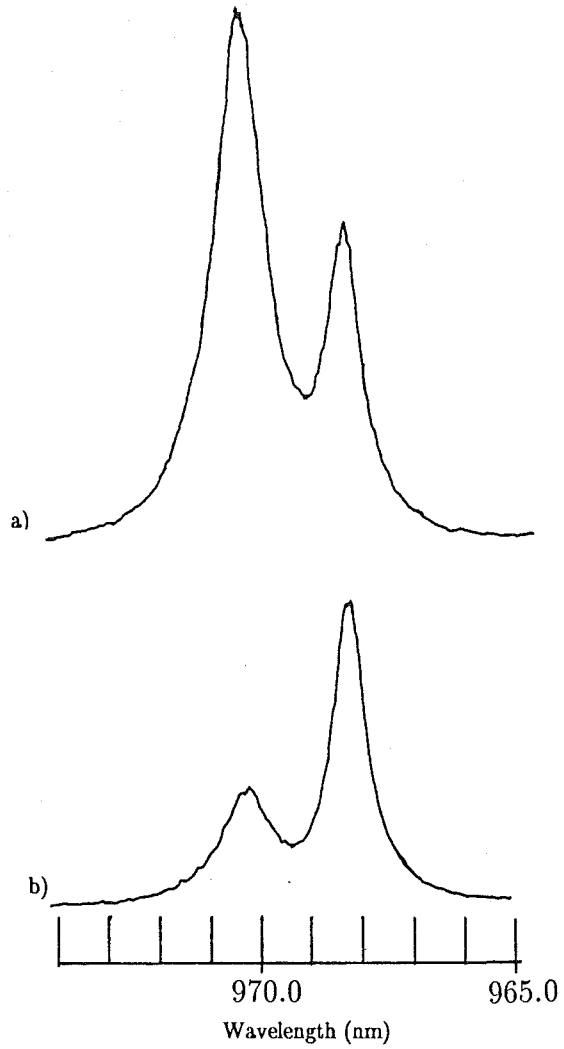

Figure 5.19: 10 K polarised fluorescence spectrum showing the vibronic lines associated with the $R_1 \rightarrow Z_5$ transition for $SrF_2 : Nd^{3+}$ C_{4V} T^- centre with laser excitation at 17299 cm^{-1} (in air) for a) (yx) and b) (yy) polarisation.

In contrast, for excitation of the energy level at 17346 cm^{-1}, there is not a 2:1 ratio for the fluorescent transitions involving levels of different symmetries. This indicates that both σ and π polarisations are involved in the initial excitation and that the excited level must have the same symmetry as the ground level, i.e. γ_6. The total effect is then given by equation 2.20 to be :

(yy)	(yx)
$I_{\sigma\sigma}$	$I_{\sigma\pi}$
$I_{\pi\pi}$	$I_{\pi\sigma}$
$I_{\sigma\sigma}$	$I_{\sigma\sigma}$.

(5.6)

Then for fluorescent transitions between levels of different symmetry :

$$I_{\sigma\sigma} = \frac{(yy)}{2} \tag{5.7}$$

and

$$I_{\pi\sigma} = (yx) - \frac{(yy)}{2} \tag{5.8}$$

and the absorption intensities ratios :

$$\begin{aligned} I_\pi{:}I_\sigma \;=\; I_{\pi\sigma}{:}I_{\sigma\sigma} \;=\; & 8.5 \quad (R_1\gamma_6 \rightarrow Z_2\gamma_7) \\ & 29.0 \quad (R_1\gamma_6 \rightarrow Z_3\gamma_7) \\ & 24.3 \quad (R_1\gamma_6 \rightarrow Y_1\gamma_7) \\ & 29.7 \quad (R_2\gamma_7 \rightarrow Z_1\gamma_6) \quad . \end{aligned} \tag{5.9}$$

These results are reasonably self consistent, with the exception of the $R_1 \rightarrow Z_2$ transition. This transition is situated very close to the more intense $R_2 \rightarrow Z_3$ transition, which might have had an effect on the intensity measurement. The calculated $\pi{:}\sigma$ ratio shows that the initial excitation is dominated by π, and for this case equation 5.6 can be reduced to :

(yy)	(yx)
$I_{\pi\pi}$	$I_{\pi\sigma}$,

(5.10)

giving rise to the following ratios $\pi{:}\sigma$ for transitions between levels of the same symmetry :

$$\begin{aligned} I_\pi{:}I_\sigma \;=\; (yy){:}(yx) \;=\; & 0.94 \quad (R_1\gamma_6 \rightarrow Z_1\gamma_6) \\ & 22.0 \quad (R_1\gamma_6 \rightarrow Y_4\gamma_6) \\ & 0.27 \quad (R_2\gamma_7 \rightarrow Z_2\gamma_7) \\ & 5.75 \quad (R_2\gamma_7 \rightarrow Z_3\gamma_7) \\ & 33.0 \quad (R_2\gamma_7 \rightarrow Y_1\gamma_7) \quad . \end{aligned} \tag{5.11}$$

These results compare favourably with those obtained in the first example mentioned above (see equation 5.5).

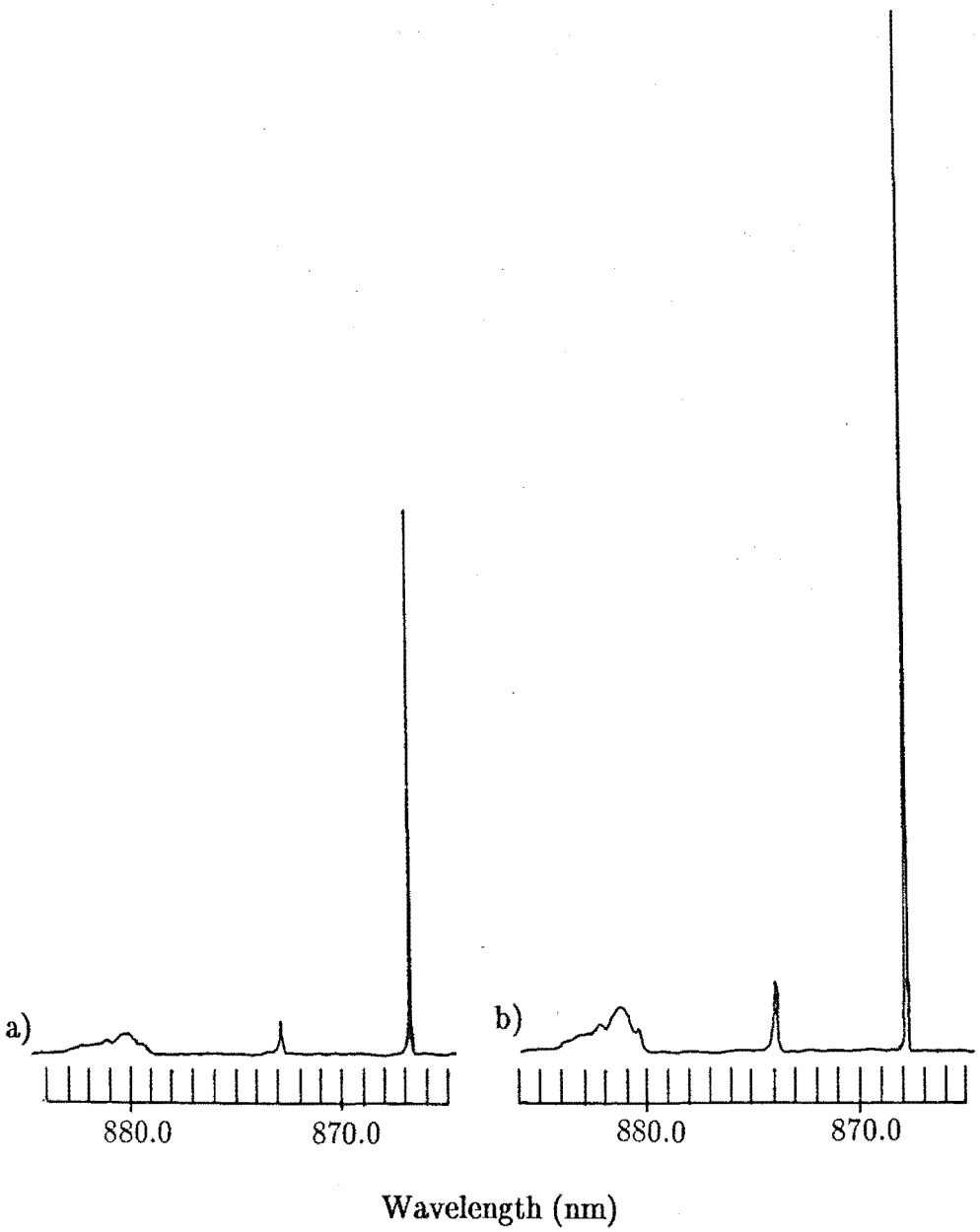

Figure 5.20: 10 K polarised fluorescence spectrum of $R_1 \rightarrow Z_{1,2,3}$ transitions for $SrF_2 : Nd^{3+}$ C_{4V} D^- centre with laser excitation at 15972 cm^{-1} (in air) for a) (yx) and b) (yy) polarisation.

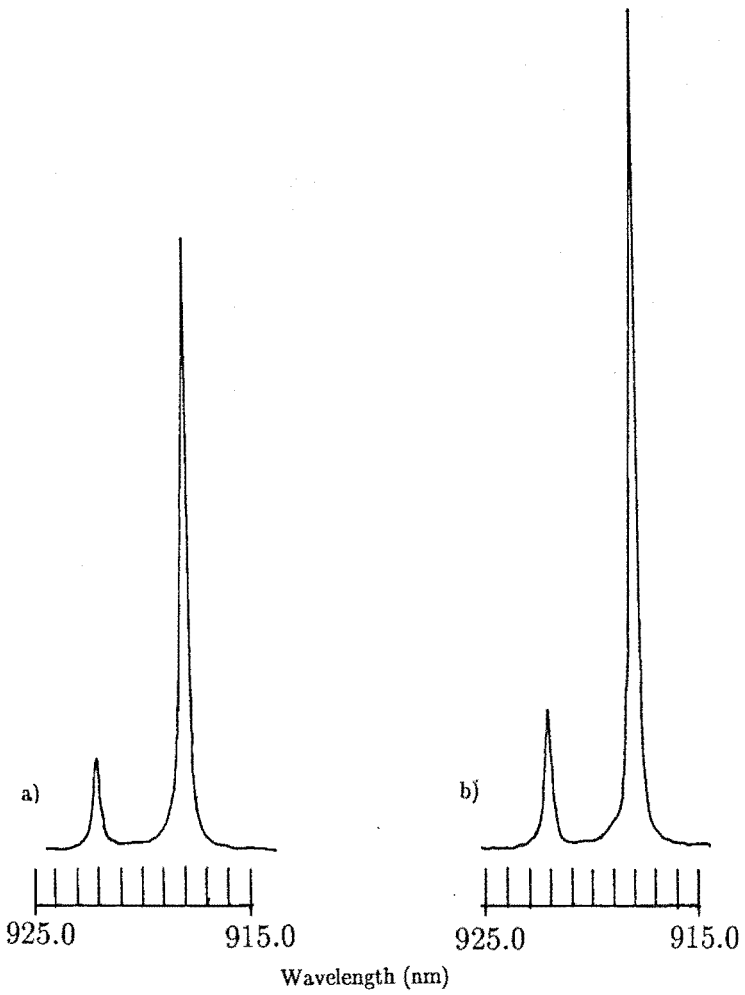

Figure 5.21: 10 K polarised fluorescence spectrum of $R_1 \rightarrow Z_5$ transition for $SrF_2 : Nd^{3+}$ C_{4V} D^- centre with laser excitation at 15972 cm^{-1} (in air) for a) (yx) and b) (yy) polarisation.

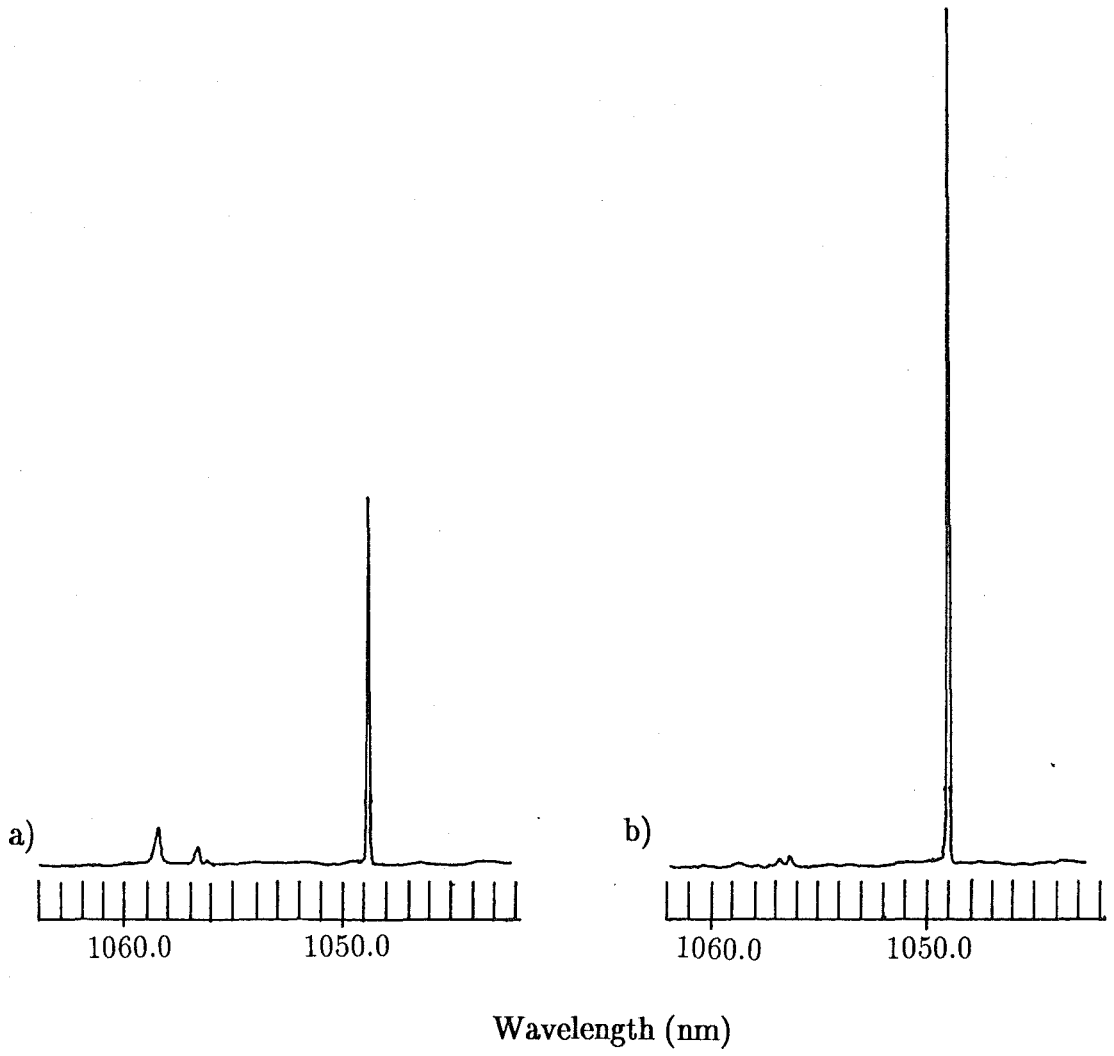

Figure 5.22: 10 K polarised fluorescence spectrum of $R_1 \rightarrow Y_{1,2,3,4}$ transitions for $SrF_2 : Nd^{3+}$ C_{4V} D^- centre with laser excitation at 15972 cm^{-1} (in air) for a) (yx) and b) (yy) polarisation.

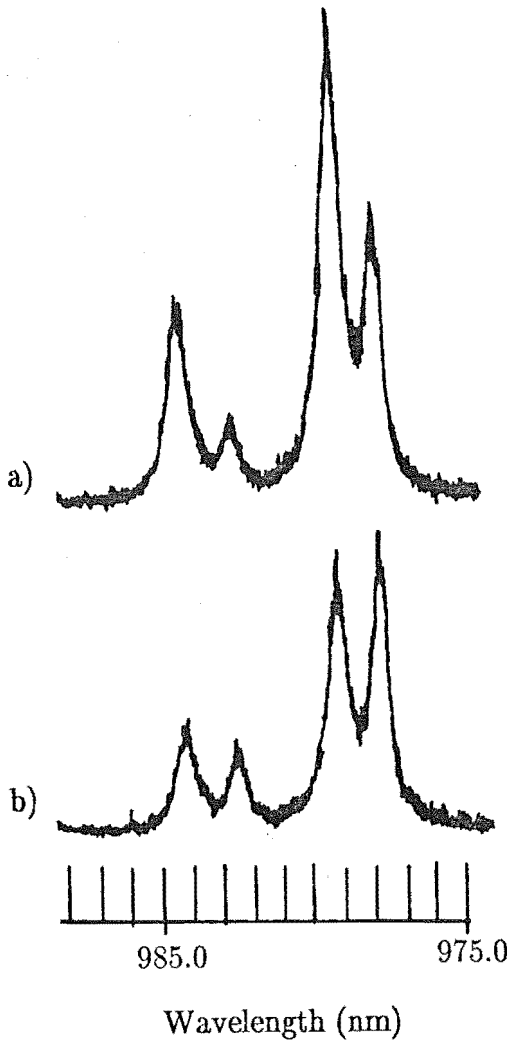

Figure 5.23: 10 K polarised fluorescence spectrum showing the vibronic lines associated with the $R_1 \rightarrow Z_5$ transitions for $SrF_2 : Nd^{3+}$ C_{4V} D^- centre with laser excitation at 15972 cm^{-1} (in air) for a) (yx) and b) (yy) polarisation.

The polarised fluorescence spectra of the C_{4V} D^- and T^- centres were similarly analysed. The derived symmetry for the various energy levels of the ^4I multiplets follows that of the C_{4V} F^- centre with the exception that the symmetries of the Y_2 and Y_3 energy levels are interchanged. This is consistent with the eigenfunctions obtained in the respective crystal field analyses to be discussed in Chapter 7. The intensity pattern of the vibronic lines can be derived from the electron-phonon interaction as discussed in Chapter 2. The observed intensity pattern of the (z) component of the vibronic lines showed close resemblance to that of the parent electronic level (see Chapter 2). This behaviour was also observed for the vibronic levels associated with the additional electronic transition observed for C_{4V} D^- centres in CaF_2 : Nd^{3+} and SrF_2 : Nd^{3+}.

5.2.4 Fluorescence Excitation Spectra

Excitation spectra of C_{4V} F^- and its hydrogenic analogues for both SrF_2 : Nd^{3+} and CaF_2 : Nd^{3+} are presented in Figs. 5.24 to 5.31. These spectra show the crystal field levels of the excited multiplets corresponding to this symmetry configuration. The results are consistent with the optical absorption observations and unambiguously reveal the weaker absorption lines that are difficult to obtain in optical absorption measurements. A comparison of the C multiplet obtained by the two techniques clearly demonstrates the sensitivity and resolvability of this technique over that of conventional optical absorption (see Figs. 5.20 and 4.8).

5.2.5 Fluorescence Lifetimes

Fluorescence decay lifetimes of the transitions between the emitting $^4F_{3/2}$ multiplet and the $^4I_{9/2}$ ground multiplet of the C_{4V} F^- centres and their D^- and T^- analogues were measured for both SrF_2 : Nd^{3+} and CaF_2 : Nd^{3+}. The C_{4V} H^- analogue proved to be very difficult to measure as a result of its very weak fluorescence and strong overlapping spurious fluorescence. The $R_1 \rightarrow Z_1$ fluorescence lifetimes for the C_{4V} F^- centre are found to be 1.7 ms ($\pm$10%) and 1.5 ms ($\pm$10%) for SrF_2 : Nd^{3+} and CaF_2 : Nd^{3+} respectively, which is in good agreement with other workers (Kaminskii et al. 1965, Voron'ko et al. 1969), giving confidence to the results for the D^- and T^- analogues. The large uncertainty quoted above is a reflection of the difficulty in extracting the lifetime of the transition from the actual experimental data; a discussion of this particular aspect can be found in Appendix B. The fluorescence lifetime results are presented in Table 5.5, while Fig. 5.32 shows a representative selection of the fluorescence decay spectra obtained. No fluorescence risetime was observed in the fluorescence of the $R_1 \rightarrow Z_1$ transition consistent with the general view that a very fast non-radiative de- excita-

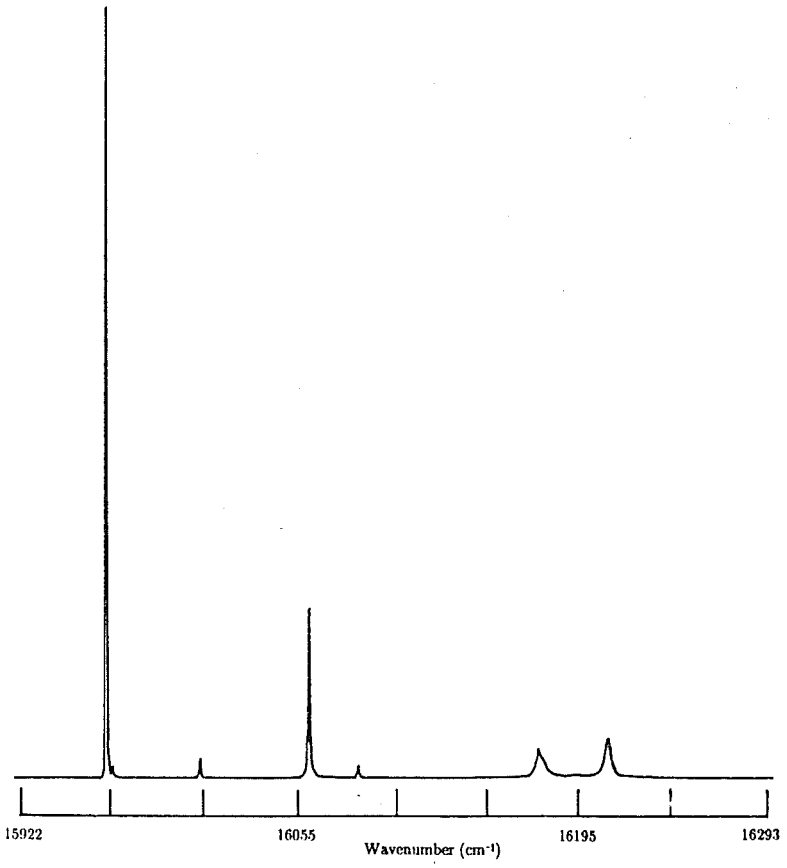

Figure 5.24: 10 K excitation spectrum of the C multiplet of the $SrF_2 : Nd^{3+}$ C_{4V} F^- centre.

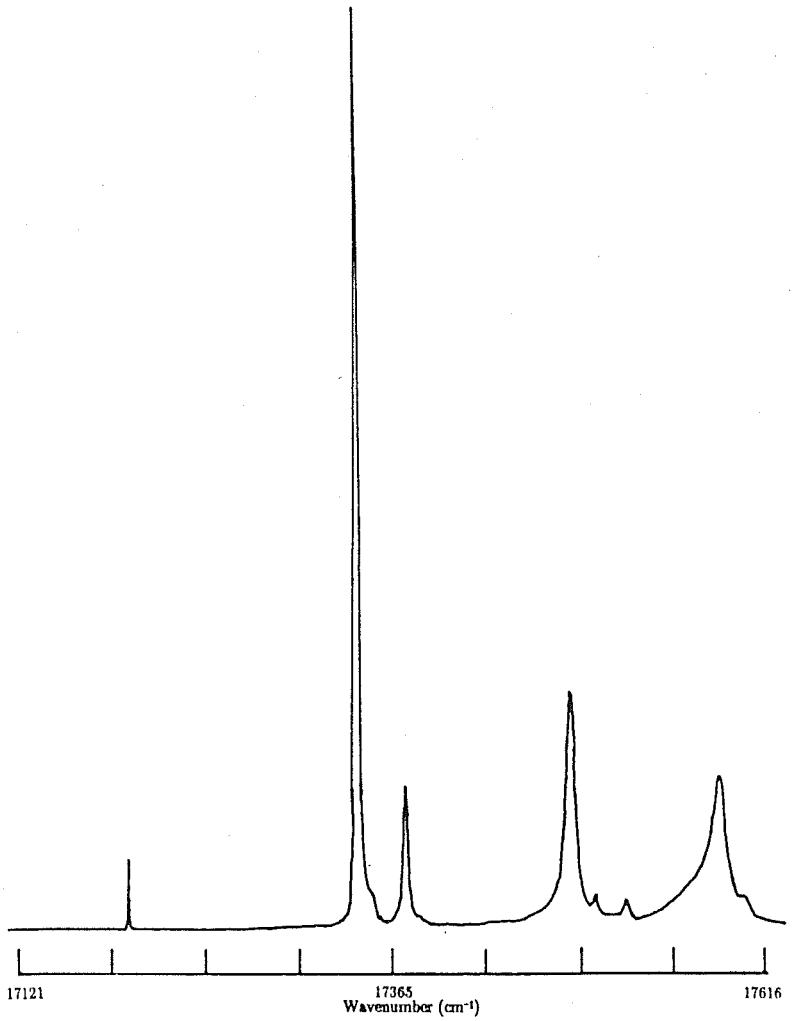

Figure 5.25: 10 K excitation spectrum of the D multiplet of the $SrF_2 : Nd^{3+}$ C_{4V} F^- centre.

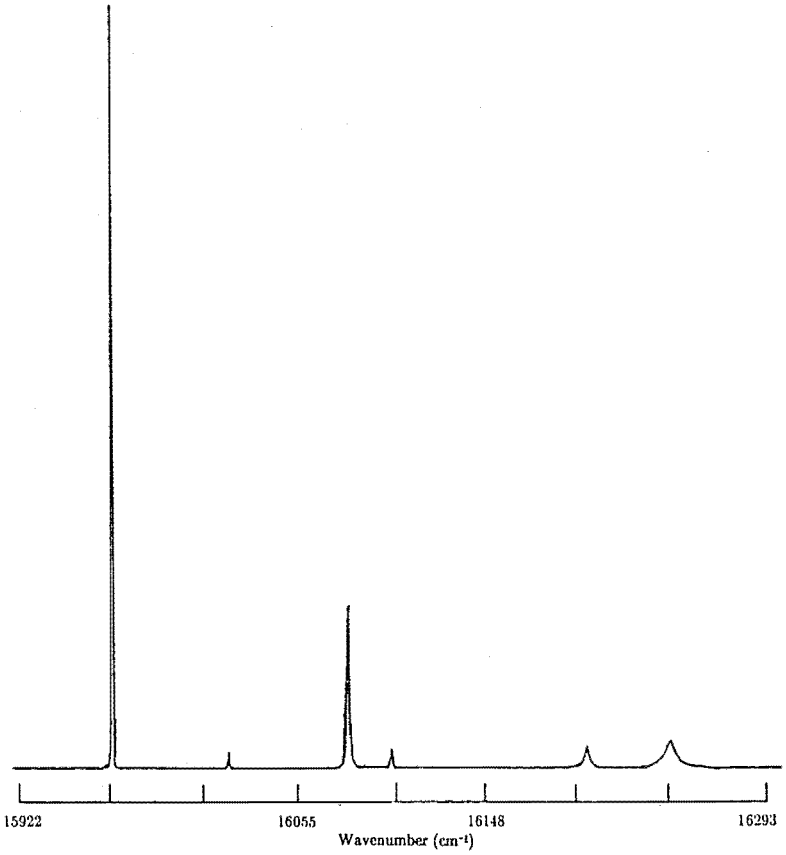

Figure 5.26: 10 K excitation spectrum of the C multiplet of the $CaF_2 : Nd^{3+}$ C_{4V} F^- centre.

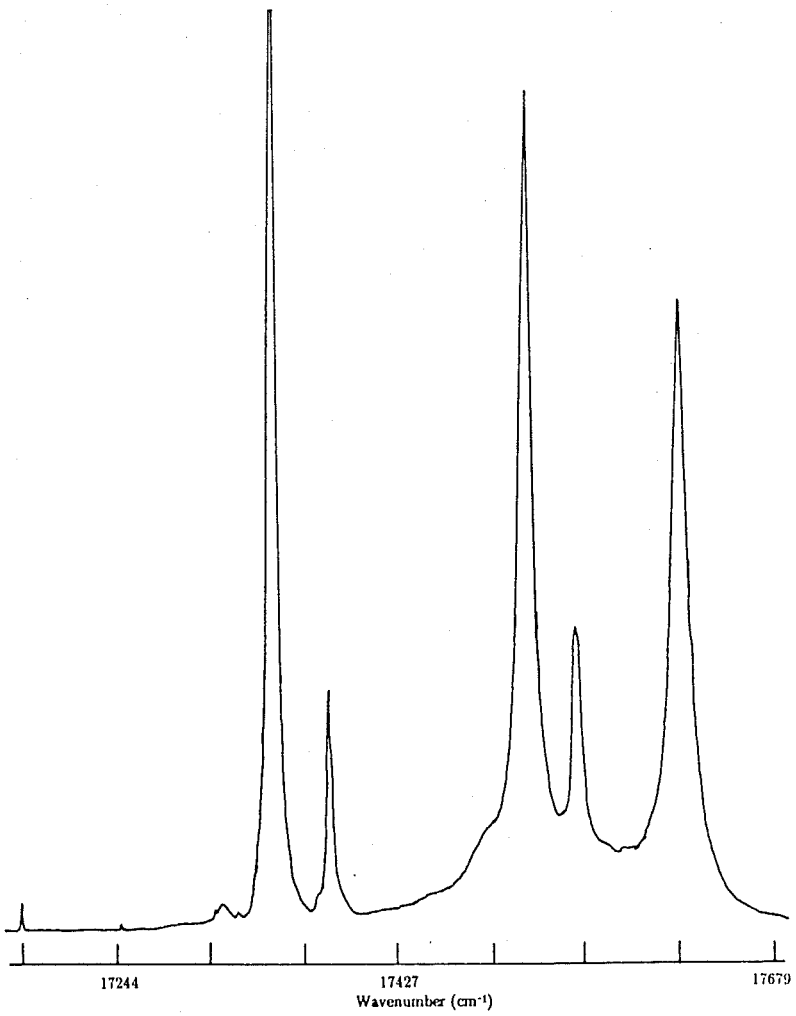

Figure 5.27: 10 K excitation spectrum of the D multiplet of the $CaF_2 : Nd^{3+}$ C_{4V} F^- centre.

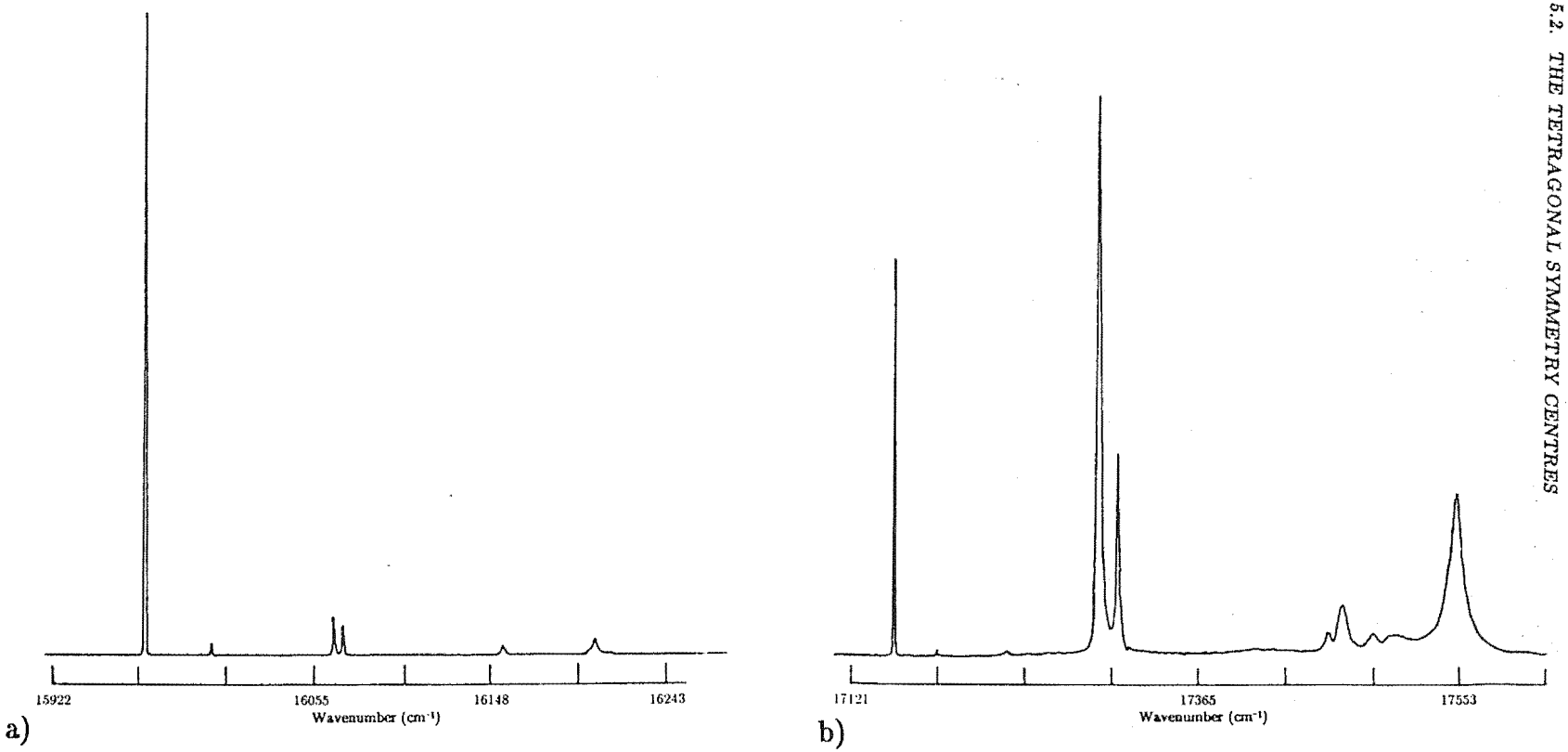

Figure 5.28: 10 K excitation spectrum of a) C and b) D multiplets of the $SrF_2 : Nd^{3+}$ C_{4V} T^- centre.

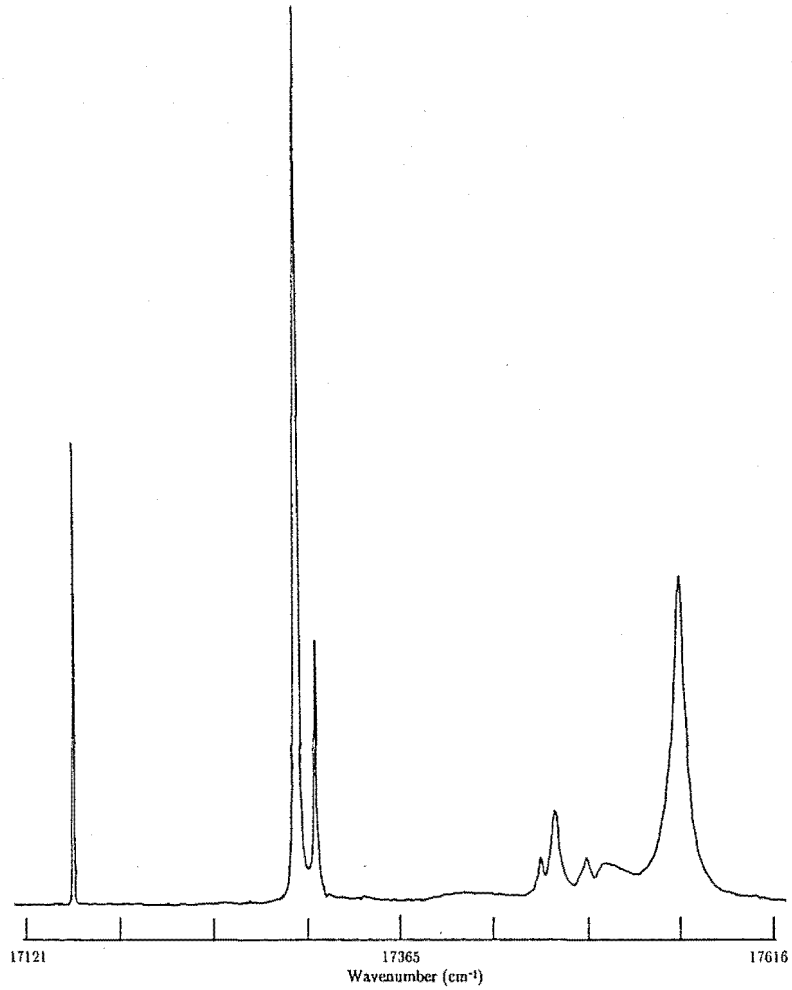

Figure 5.29: 10 K excitation spectrum of the D multiplet of the $SrF_2 : Nd^{3+}$ C_{4V} D^- centre.

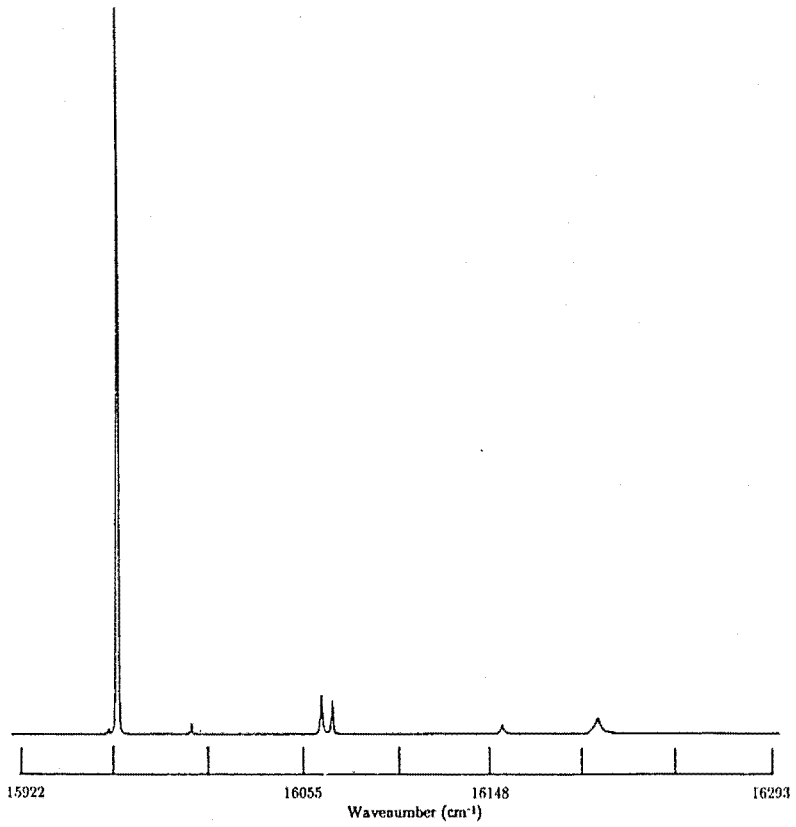

Figure 5.30: 10 K excitation spectrum of the C multiplet of the $SrF_2 : Nd^{3+}$ C_{4V} D^- centre.

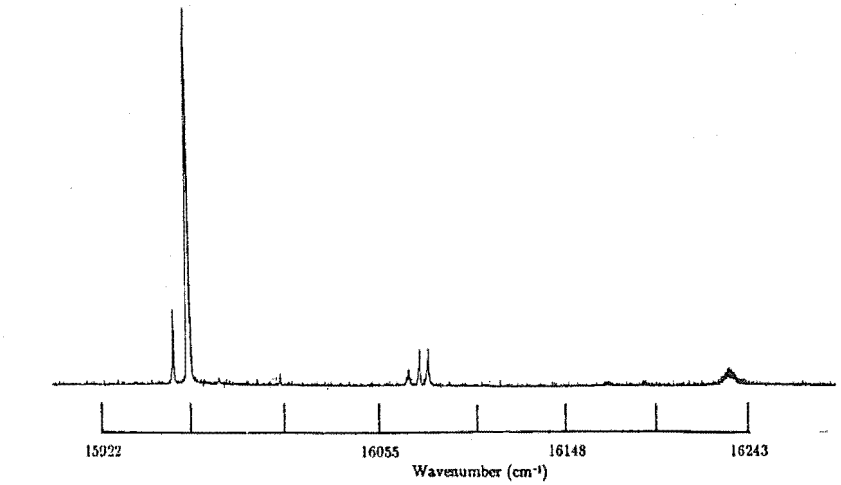

a)

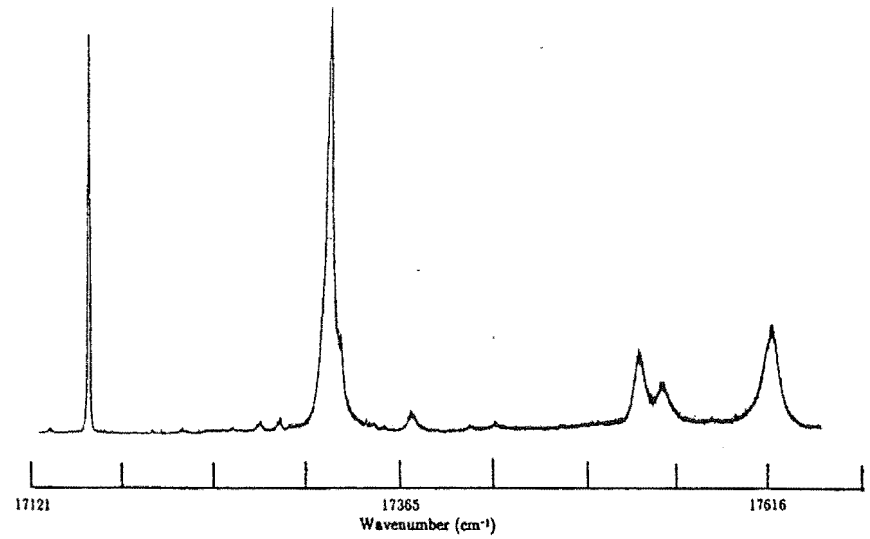

b)

Figure 5.31: 10 K excitation spectrum of a) C and b) D multiplets of the $CaF_2 : Nd^{3+}$ C_{4V} D^- centre.

tion takes place from the excited multiplet to the emitting R multiplet. The marked decrease of the decay rate coupled with the observed decrease of the fluorescence intensity in the order going from F^-, T^-, D^- to H^- indicates an increasing contribution from the non-radiative processes to the overall decay lifetime. As the hydrogenic ions are electronically identical, the variations are attributed to non-radiative processes involving the respective local mode phonons. The energy gap dependence of the multiphonon transition rate can be determined following the phenomenological approach discussed in Chapter 2.

In the phenomenological approach it is necessary to estimate the radiative transition rate of the fluorescing energy level and subtract it from the observed fluorescence decay rate to obtain the non-radiative transition rate. In a first approximation it is deemed reasonable to assume the fluorescence decay of the F^- ion is almost purely radiative, since the lattice frequencies of the F^- ions are low. Equation 2.26 is reduced to :

$$\begin{aligned} \tau_F^{-1} &= W_F^R \\ &= 595\ (\pm 10\%)\ s^{-1}\ . \end{aligned} \tag{5.12}$$

For pure radiative processes the spontaneous electric dipole transition probability is given by Reeves (1987) as proportional to :

$$\sum \left| B_q^k \left\langle \psi \left| C_q^k \right| \psi' \right\rangle \right|^2\ , \tag{5.13}$$

where B_q^k is a crystal field parameter, $C_q^{(k)}$ is a Racah tensor operator and, ψ and ψ' are the wavefunction of different states. This implies that the transition probabilities between the same two crystal field levels for equivalent hydrogenic centres are proportional to the squares of the appropriate crystal field parameters. The validity of this approach can be shown by considering the fluorescence measurements obtained by Jones et al. (1969) for $CaF_2 : Gd^{3+}$. The $^6P_{7/2} \rightarrow {}^8S_{7/2}$ transitions have an energy gap of 32000 cm^{-1} and its relaxation process is considered to be purely radiative. The fluorescence lifetimes for the C_{4V} F^-, D^- and H^- centres were measured to be 11 ($\pm$1) ms, 3 ms and 4.0 ($\pm$0.5) ms. The crystal field parameter B_0^2 was found to have the largest variation and was calculated (Edgar 1974) to be 653 cm^{-1} and 1055 cm^{-1} for F^- and H^- respectively. Following the above argument, the fluorescence lifetime for the H^- centre can be written as :

$$\begin{aligned} \tau_H &= \left| \frac{B_0^2(F)}{B_0^2(H)} \right|^2 \tau_F \\ &= 4.2\ \pm 0.4\ ms\ , \end{aligned} \tag{5.14}$$

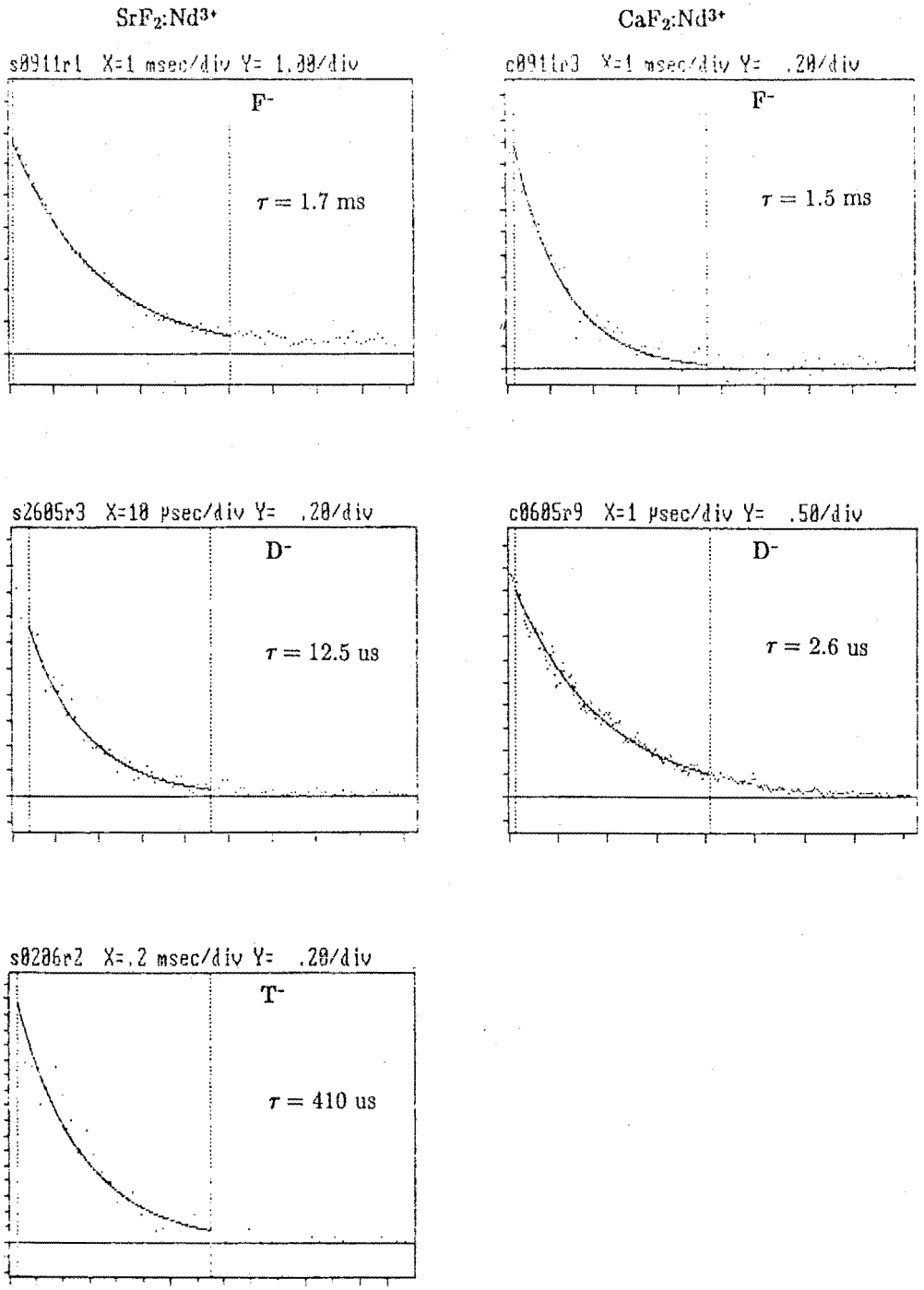

Figure 5.32: 10 K fluorescence decay spectrum for the $R_1 \rightarrow Z_1$ transition of the $SrF_2 : Nd^{3+}$ and $CaF_2 : Nd^{3+}$ C_{4V} centres.

which is similar to that measured.

In the present case, the crystal field parameter B_0^2 of the T^- and D^- centres was found to have the largest variation with an average increase of 46% over the corresponding F^- centre in $SrF_2 : Nd^{3+}$. Therefore the effective radiative transition rate for T^-, D^- and H^- centres can be deduced to be :

$$\begin{aligned} W_H^R &= \frac{1}{(0.69)^2 \tau_F} \\ &= 1249\ (\pm 10\%)\ s^{-1}\ . \end{aligned} \tag{5.15}$$

The order of the processes for the respective hydrogenic ions can be calculated using equation 2.29, while the non- radiative transition rate is given by :

$$W_H^{NR} = \frac{1}{\tau_H} - W_H^R\ , \tag{5.16}$$

and the coupling constant ϵ can be calculated from :

$$\begin{aligned} \epsilon^{(n)} &= \frac{W_T^{(n)}}{W_D} \\ \epsilon &= 0.12 \pm 0.05\ . \end{aligned} \tag{5.17}$$

This value compares well with the value of 0.2 ($\pm$0.02) obtained by Riseberg and Moos (1968), but is slightly more than double that obtained by Reeves (1987) in a similar calculation for $SrF_2 : Pr^{3+}$. Using the value of 0.12 for the coupling constant, the non-radiative transition rate W^{NR} for H^- is calculated to be :

$$\begin{aligned} (W_H^{NR})^{(5)} &= \frac{(W_D^{NR})^{(7)}}{\epsilon^{(7-5)}} \\ &= (5.5 \pm 2.8) \times 10^6\ s^{-1}\ , \end{aligned} \tag{5.18}$$

and subsequently the total fluorescence lifetime can be deduced as :

$$\begin{aligned} \tau_H &= \frac{1}{W_H^R + W_H^{NR}} \\ &= 180 \pm 90\ ns\ . \end{aligned} \tag{5.19}$$

Unfortunately the present data does not give this lifetime so cannot validate this calculation, but judging from the close agreement achieved by Riseberg and Moos (1968) and Reeves (1987) it is not unreasonable to expect an agreement to within a factor of 2 to 3.

A similar approach could be applied to $CaF_2 : Nd^{3+}$ but the present data are not sufficient to warrant such a calculation.

In the present approach where W^R is subtracted from τ^{-1}, the uncertainties in W^R can greatly affect the value and accuracy of W^{NR}. This is especially prominent in the case of T^-, where the multiphonon decay rates become smaller and approach the region where $W^R \approx W^{NR}$. Furthermore, the present approach, where W^R is deduced from the F^- centres for all the hydrogenic centres, is only a first approximation . This is certainly not strictly correct but the good agreement obtained by Reeves (1987) and the lack of additional data do not make it worthwhile at this stage to attempt a more complex calculation.

5.3 The L1 Centres

A new single RE^{3+} ion charge compensation centre has been identified for $SrF_2 : Nd^{3+}$ and $CaF_2 : Nd^{3+}$. Its fluorescence spectrum showed a marked resemblance to that of the C_{4V} F^- centres, but the intensity is down by a factor of 10. As for all other C_{4V} centres, there is a marked absence of the $R_1 \rightarrow Z_4$ transition in this centre. No additional transition was observed in the 910 nm region. The Z_2 to Z_1 energy level separation is 52.1 cm^{-1} for $SrF_2 : Nd^{3+}$ and 75.3 cm^{-1} for $CaF_2 : Nd^{3+}$, in each case being 8 cm^{-1} smaller than the corresponding separation for the F^- C_{4V} centres. The energy levels of this centre are listed in Table 5.6. Judging from the fluorescence line intensity pattern this centre is expected to have a closely related configuration to the C_{4V} symmetry centre.

5.4 The C_{Si} (i=1,3,..) Centres

5.4.1 Introduction

Optical absorption spectra of the hydrogenated $SrF_2 : Nd^{3+}$ and $CaF_2 : Nd^{3+}$ crystals show that there are three other hydrogenic centres in addition to the hydrogenic C_{4V} symmetry centre. Analysis of the mixed $H^- + D^-$ crystals and their comparison with the corresponding singly hydrogenated crystals revealed that these centres involved multiple hydrogenic charge compensating ions.

State			Experimental		State			Experimental	
$^4I_{9/2}$	Z_1	γ_6	0		$^4F_{7/2}$,	A_1	γ_7	13525	(± 2)
	Z_2	γ_7	60.0	(± 1.6)	$^4S_{3/2}$	A_2	γ_6	13581.0	(± 1.5)
	Z_3	γ_7	157.0	(± 1.8)		A_3		13723	(± 2)
			164.0	(± 1.8)		A_4		13731.0	(± 1.5)
	Z_4					A_5			
	Z_5	γ_6	637.0	(± 1.6)		A_6			
$^4I_{11/2}$	Y_1	γ_7	2006.0	(± 1.6)	$^4F_{9/2}$	B_1			
	Y_2	γ_6	2044.0	(± 1.8)		B_2	γ_7	14807	(± 3)
	Y_3	γ_7	2050.0	(± 1.8)		B_3	γ_6	14843	(± 3)
	Y_4	γ_6	2061.0	(± 1.6)		B_4			
	Y_5	γ_7	2280.0	(± 2.6)		B_5			
	Y_6	γ_6	2366.0	(± 1.6)					
					$^2H_{11/2}$	C_1		15968	(± 1)
$^4I_{13/2}$	X_1	γ_7	3942	(± 2)		C_2		16010	(± 3)
	X_2	γ_6	3984	(± 2)		C_3		16061	(± 3)
	X_3	γ_6	4009	(± 2)		C_4		16085	(± 3)
	X_4	γ_7				C_5		16175	(± 3)
	X_5	γ_7				C_6		16214	(± 3)
	X_6	γ_7	4348	(± 1)					
	X_7	γ_6	4365.0	(± 1.5)	$^4G_{5/2}$,	D_1		17199	(± 2)
					$^2G_{7/2}$	D_2		17346	(± 2)
$^4I_{15/2}$	W_1	γ_6	5784	(± 2)		D_3		17381	(± 2)
	W_1	γ_7	5923	(± 2)		D_4		17491	(± 3)
	W_3	γ_6	5946	(± 2)		D_5		17508	(± 3)
	W_4	γ_7				D_6		17529	(± 3)
	W_5	γ_6				D_7		17588	(± 3)
	W_6	γ_6	6516	(± 1)					
	W_7	γ_7	6527	(± 2)	$^2P_{1/2}$,	I_1		23485	(± 2)
	W_8	γ_7	6593	(± 2)	$^2P_{5/2}$	I_2			
						I_3			
$^4F_{3/2}$	R_1	γ_6	11586.0	(± 1.5)					
	R_2	γ_7	11668.0	(± 1.5)	$^2P_{3/2}$	K_1	γ_6	26336	(± 3)
						K_2			
$^4F_{5/2}$,	S_1	γ_6	12557.0	(± 1.5)					
$^2H_{9/2}$	S_2	γ_6	12631.0	(± 1.5)	$^4D_{3/2}$	L_1	γ_7	28182	(± 1)
	S_3	γ_7	12635.0	(± 1.5)		L_2			
	S_4	γ_6	12709.0	(± 1.5)					
	S_5	γ_7	12722.0	(± 1.5)					
	S_6		12725.0	(± 1.5)					
	S_7		12942.0	(± 1.5)					
	S_8								

Table 5.1: 10 K energy levels (in air cm^{-1}) of the C_{4V} F^- centre in $SrF_2 : Nd^{3+}$.

State			Experimental		State		Experimental	
$^4I_{9/2}$	Z_1	γ_6	0		$^4F_{7/2}$,	A_1	13538	(± 1)
	Z_2	γ_7	82	(± 1)	$^4S_{3/2}$	A_2	13590	(± 1)
	Z_3	γ_7	198	(± 2)		A_3	13756	(± 1)
	Z_4					A_4	13766	(± 1)
	Z_5	γ_6	746	(± 3)		A_5	13801	(± 1)
						A_3	13806	(± 1)
$^4I_{11/2}$	Y_1	γ_7	2032	(± 1)				
	Y_2	γ_7	2086	(± 1)	$^4F_{9/2}$	B_1		
	Y_3	γ_6	2096	(± 1)		B_2	14769 ?	(± 1)
	Y_4	γ_6	2105	(± 1)		B_3	14780 ?	(± 1)
	Y_5	γ_7	2354	(± 3)		B_4	14817 ?	(± 3)
	Y_6	γ_6	2462	(± 2)		B_5	14864 ?	(± 3)
$^4I_{13/2}$	X_1	γ_7	3960	(± 1)	$^2H_{11/2}$	C_1	15967	(± 2)
	X_2	γ_6	4022	(± 1)		C_2	16022	(± 2)
	X_3	γ_6	4045	(± 3)		C_3	16077.0	(± 1.5)
	X_4	γ_7				C_4	16100	(± 2)
	X_5	γ_7				C_5	16195	(± 5)
	X_6	γ_7	4442 ?	(± 3)		C_6	16241	(± 3)
	X_7	γ_6	4465	(± 1)				
					$^4G_{5/2}$,	D_1	17183	(± 2)
$^4I_{15/2}$	W_1	γ_6	5764	(± 1)	$^2G_{7/2}$	D_2	17312	(± 2)
	W_1	γ_7	5952	(± 1)		D_3	17347	(± 2)
	W_3	γ_6	5974 ?	(± 3)		D_4	17385	(± 3)
	W_4	γ_7	6036 ?	(± 3)		D_5	17518	(± 5)
	W_5	γ_6				D_6	17549	(± 5)
	W_6	γ_6	6632	(± 1)		D_7	17620	(± 3)
	W_7	γ_7	6639	(± 1)				
	W_8	γ_7			$^2P_{1/2}$,	I_1	23486.9	(± 2.5)
					$^2D_{5/2}$	I_2		
$^4F_{3/2}$	R_1		11594.0	(± 1.5)		I_3		
	R_2		11707.0	(± 1.5)				
					$^2P_{3/2}$	K_1	28109	(± 3)
$^4F_{5/2}$,	S_1		12558	(± 1)		K_2		
$^2H_{9/2}$	S_2		12628	(± 1)				
	S_3		12658	(± 1)	$^4D_{3/2}$	L_1	26310	(± 3)
	S_4		12728	(± 1)		L_2		
	S_5		12750	(± 1)				
	S_6		12764	(± 1)				
	S_7							
	S_8							

Table 5.2: 10 K energy levels (in air cm^{-1}) of the C_{4V} F^- centre in $CaF_2 : Nd^{3+}$. ? Tentative assignment.

State			$SrF_2 : Nd^{3+}$ T^-		$SrF_2 : Nd^{3+}$ D^-		$SrF_2 : Nd^{3+}$ H^-		$CaF_2 : Nd^{3+}$ D^-	
$^4I_{9/2}$	Z_1	γ_6	0		0		0		0	
	Z_2	γ_7	81.2	(± 1.8)	80.3	(± 1.5)	79.4	(± 1.5)	110.0	(± 1.5)
			161.4	(± 1.2)	165.2	(± 1.2)	162.5	(± 1.2)		
	Z_3	γ_7	172.4	(± 1.6)	174.9	(± 1.5)	173.2	(± 1.5)	234.0	(± 1.5)
			185.8	(± 1.3)	188.2	(± 1.3)	185.7	(± 1.3)		
			193.5	(± 1.5)	195.1	(± 1.5)	193.7	(± 1.5)		
	Z_4									
	Z_5	γ_6	651.5	(± 1.5)	643.8	(± 1.2)	642.8	(± 1.2)	762.7	(± 1.2)
					693.0	(± 1.8)	691.3	(± 1.8)	891.3	(± 1.8)
$^4I_{11/2}$	Y_1	γ_7	2002.8	(± 1.2)	2004.6	(± 1.4)	2005.7	(± 1.4)	2023.5	(± 2.5)
	Y_2	γ_7	2069.7	(± 1.3)	2068.8	(± 1.4)	2071.2	(± 1.4)	2119.8	(± 1.2)
	Y_3	γ_6	2074.2	(± 1.6)	2074.2	(± 1.2)	2076.0	(± 1.2)	2129.1	(± 1.1)
	Y_4	γ_6	2090.3	(± 1.7)	2089.4	(± 1.4)	2092.3	(± 1.4)	2148.9	(± 2.3)
	Y_5	γ_7	2276.8	(± 2.2)	2276	(± 3)	2279.9	(± 3.0)	2371.9	(± 2.3)
	Y_6	γ_6	2388.7	(± 1.3)	2389.6	(± 1.4)	2391.6	(± 1.4)	2500.1	(± 1.2)
$^4F_{3/2}$	R_1		11541.2	(± 2.2)	11543	(± 2)	11542	(± 2)	11542	(± 2)
	R_2									
$^2H_{11/2}$	C_1		15970	(± 2)	15972	(± 2)	15971	(± 2)	15966	(± 2)
	C_2		16002	(± 2)	16007	(± 2)	16007	(± 2)	15974	(± 2)
	C_3		16063	(± 2)	16068	(± 2)	16068	(± 2)	16083	(± 2)
	C_4		16068	(± 2)	16073	(± 2)	16062	(± 2)	16088	(± 2)
	C_5		16155	(± 2)	16159	(± 2)	16158	(± 2)	16179	(± 2)
	C_6		16125	(± 2)	16209	(± 2)	16209	(± 2)	16243	(± 2)
$^4G_{5/2}$	D_1		17155	(± 2)	17162	(± 2)	17175	(± 2)	17134	(± 2)
$^2G_{7/2}$	D_2		17299	(± 2)	17301	(± 2)	17265 ?	(± 2)	17289	(± 2)
	D_3		17313	(± 2)	17314	(± 2)	17272	(± 2)	17346	(± 2)
	D_4		17463	(± 3)	17336	(± 3)	17301	(± 3)	17498	(± 3)
	D_5		17473	(± 5)	17463	(± 5)	17431	(± 5)	17517	(± 5)
	D_6		17496	(± 5)	17494	(± 5)			17588	(± 5)
	D_7		17555	(± 3)	17556	(± 3)				

Table 5.3: 10 K energy levels (in air cm^{-1}) of the C_{4V} hydrogenic centres in $SrF_2 : Nd^{3+}$ and $CaF_2 : Nd^{3+}$. ? Tentative assignment.

Centres			$SrF_2 : Nd^{3+}$		$CaF_2 : Nd^{3+}$
C_{4V}	T^-	(x,y)	556		
		(z)	578		
	D^-	(x,y)	668		732
		(z)	684		812
	H^-	(x,y)	929	927.0 ($\pm$0.7) !	
		(z)	944	941.5 ($\pm$0.8) !	
C_{S1}	T^-	(A)	554, 479, 441		
		(B)			
	D^-	(A)	696, 572, 530		
		(B)	611, 560		
	H^-	(A)	960, 789, 731 *	957.8, 775.2, 724.2 !	
C_{S3}	D^-	(A)	541, 481		
		(B)	612, 559, 520		
C_{S4}	D^-	(A)	586, 534, 461		
		(B)	598, 515, 497		

Table 5.4: Local mode vibronic frequencies (in air cm^{-1}) of various symmetry centres in hydrogenated $SrF_2 : Nd^{3+}$ and $CaF_2 : Nd^{3+}$ crystals. *) inferred from D^- C_{S1} centre using a reduced mass ratio of 1.38 (Jacobs 1971); !) data of Edgar et al. 1977.

Centres		$SrF_2 : Nd^{3+}$	$CaF_2 : Nd^{3+}$
C_{4V}	F^-	1.7 *ms*	1.5 *ms*
	T^-	410 *us*	
	D^-	12.5*us*	2.6 *us*
M	F^-		92 *us*
N	F^-		35 *us*
$M1$	F^-		520 *us*
$M2$	F^-	237 *us*	450 *us*
$M3$	F^-	262 *us*	580 *us*
$M4$	F^-		490 *us*
A'	O_2	2.4 *ms*	3 *ms*
C_{S1}	T^-	136.4 *us*	
	D^-	3.6 *us*	
C_{S3}	D^-	2.3 *us*	
C_{S4}	D^-	1.7 *us*	
			$Nd^{3+} - RE^{3+}$
M'	$Nd^{3+} - Ce^{3+}$		610 *us*
	$Nd^{3+} - Gd^{3+}$		590 *us*
	$Nd^{3+} - Yb^{3+}$		83.1 *us*

Table 5.5: 10 K fluorescence lifetime measurements of the various symmetry centres in $SrF_2 : Nd^{3+}$, $CaF_2 : Nd^{3+}$ and $CaF_2 : Nd^{3+} : RE^{3+}$ crystals. Uncertainty is $\pm 10\%$ for all measurements.

State		$SrF_2 : Nd^{3+}$		$CaF_2 : Nd^{3+}$	
$^4I_{9/2}$	Z_1	0		0	
	Z_2	52.1	(± 1.3)	75.3	(± 1.5)
	Z_3	151.1	(± 1.2)	150.0	(± 1.2)
	Z_4				
	Z_5	637.1	(± 1.3)	645.5	(± 1.5)
$^4I_{11/2}$	Y_1	2014.0	(± 1.2)	2002.9	(± 1.2)
	Y_2	2039.0	(± 1.4)	2038.2	(± 1.2)
	Y_3	2045.0	(± 1.2)	2077.7	(± 1.3)
	Y_4	2055.9	(± 1.2)	2116.9	(± 1.2)
	Y_5	2279.6	(± 1.4)	2270.5	(± 1.3)
	Y_6	2362.9	(± 1.2)	2393.2	(± 1.3)
$^4F_{3/2}$	R_1	11589.0	(± 1.2)	11534	(± 2)
	R_2				
$^2H_{11/2}$	C_1	15967	(± 2)		
	C_2	16015	(± 2)		
	C_3	16061	(± 2)		
	C_4	16088	(± 2)		
	C_5	16182	(± 2)		
	C_6	16214	(± 2)		
$^4G_{5/2}$,	D_1	17200	(± 2)		
$^2G_{7/2}$	D_2	17349	(± 2)		
	D_3	17375	(± 2)		
	D_4	17489	(± 3)		
	D_5	17496	(± 5)		
	D_6	17525	(± 5)		
	D_7	17598	(± 3)		

Table 5.6: 10 K energy levels (in air cm^{-1}) of the $L1$ F^- centres in $SrF_2 : Nd^{3+}$ and $CaF_2 : Nd^{3+}$.

The similarity of their fluorescence spectra in deuterated $SrF_2 : Nd^{3+}$ crystals indicates that the underlying symmetry configurations of these three centres are very similar, hence they are labelled C_{S1}, C_{S3} and C_{S4}. However, each centre has its own distinct characteristics and is discussed separately, together its optical absorption results. Figs. 5.33 to 5.38 show a representative example of the excitation spectra for each of the C_{Si} centres.

The optical absorption spectrum of the R multiplet proves to be the most convenient for analysing the absorption. The H^- analogues of the three centres have an extremely weak fluorescence and observation was hampered by strong overlapping fluorescence from other centres, so consequently only limited data were obtained. The T^- analogues of the C_S centres were only observed in $SrF_2 : Nd^{3+}$ as there was no tritiated $CaF_2 : Nd^{3+}$ crystal available.

5.4.2 The C_{S1} Centre

Detailed analysis of the optical absorption spectrum (Fig. 5.39) shows the C_{S1} centre involves two charge compensating ions. It reveals that the centre line observed in the mixed $H^- + D^-$ crystal can be attributed to two identical hydrogenic ions whereas the lines at each side are a result of combinations of the two different hydrogenic ions. This indicates that the position of the two compensating hydrogenic ions involved is not equivalent relative to the rare earth ion. Therefore, the effects of the $H^- D^-$ and the $D^- H^-$ ion pairs on the Nd^{3+} electronic levels are different, whereas the effects the $H^- H^-$ and the $D^- D^-$ ion pairs are very similar.

The fluorescence spectra of H^-, D^- and T^- analogues of the C_{S1} centre in $SrF_2 : Nd^{3+}$ are presented in Figs. 5.40 to 5.45. In $CaF_2 : Nd^{3+}$ the fluorescence of the C_{S1} centre was obscured by the easily excited A' centre which involved an oxygen charge compensating ion. The $R_1 \rightarrow Z_1$ transitions of the C_{S1} and A' centres (to be described later) in $CaF_2 : Nd^{3+}$ coincide at 869.7 nm, consequently the fluorescence of the C_{S1} centre was not resolved. The intensity pattern of the C_{S1} centre in $SrF_2 : Nd^{3+}$ is similar to the C_{4V} symmetry centre which suggests that the configuration of the C_{S1} centre could be derived from the single H^- C_{4V} centre. As the $R_1 \rightarrow Z_4$ transition cannot be unambiguously identified in the C_{S1} centres, the values of the Z_4 energy level presented in Table 5.7 are only a tentative assignment.

Local mode vibronic frequencies were observed for the C_{S1} T^- and the C_{S1} D^- centres in $SrF_2 : Nd^{3+}$. The ratio of the local mode vibronic frequencies of the D^- and T^- analogues is similar to the corresponding ratio for the C_{4V} centre, i.e. close to the reduced mass ratio of the isotopes. The expected C_{S1} H^- local mode frequencies were predicted on this basis and are presented in Table 5.4 together with the observed C_{S1} D^- and C_{S1} T^- local mode frequencies. The predicted C_{S1} H^- local mode frequencies are similar

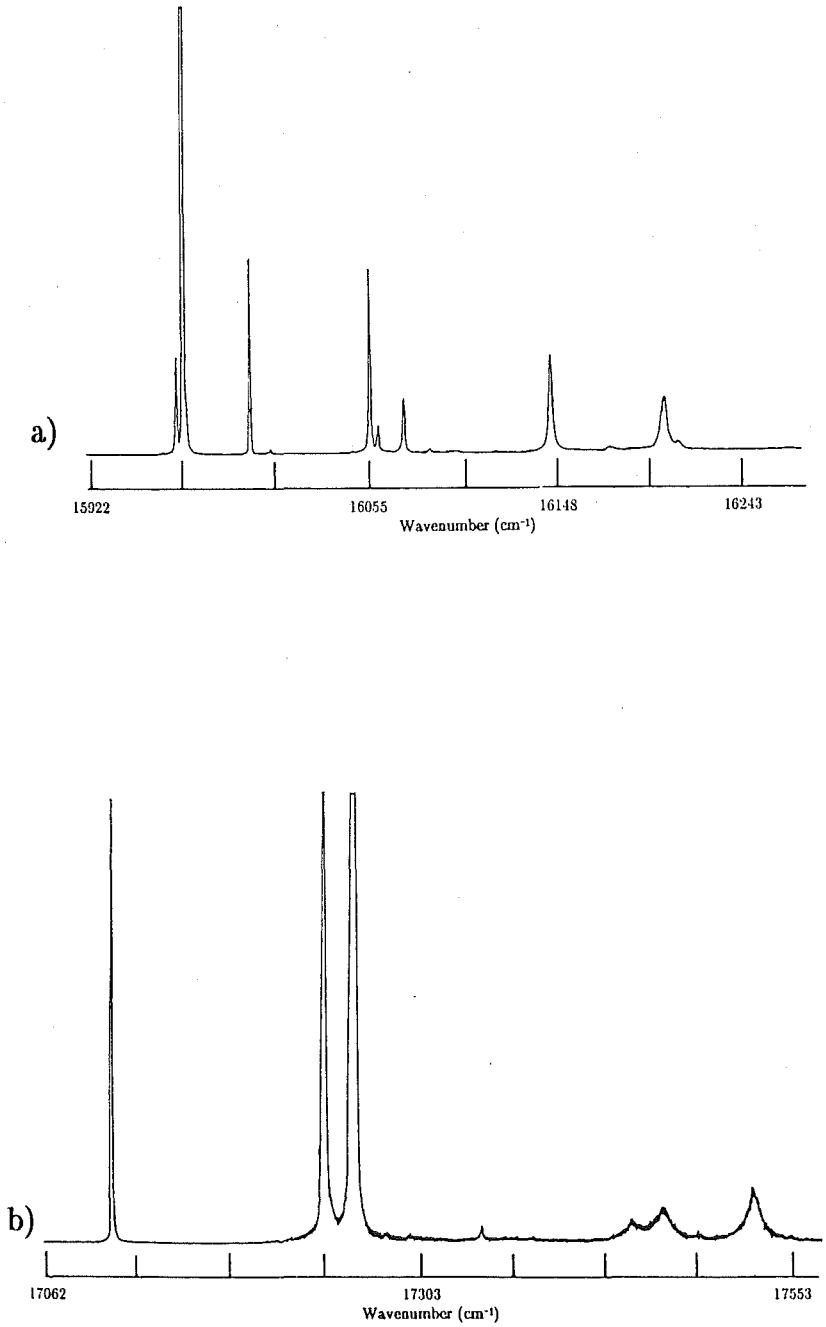

Figure 5.33: 10 K excitation spectrum of a) C and b) D multiplets for $SrF_2 : Nd^{3+}$ D^- C_{S1} centre.

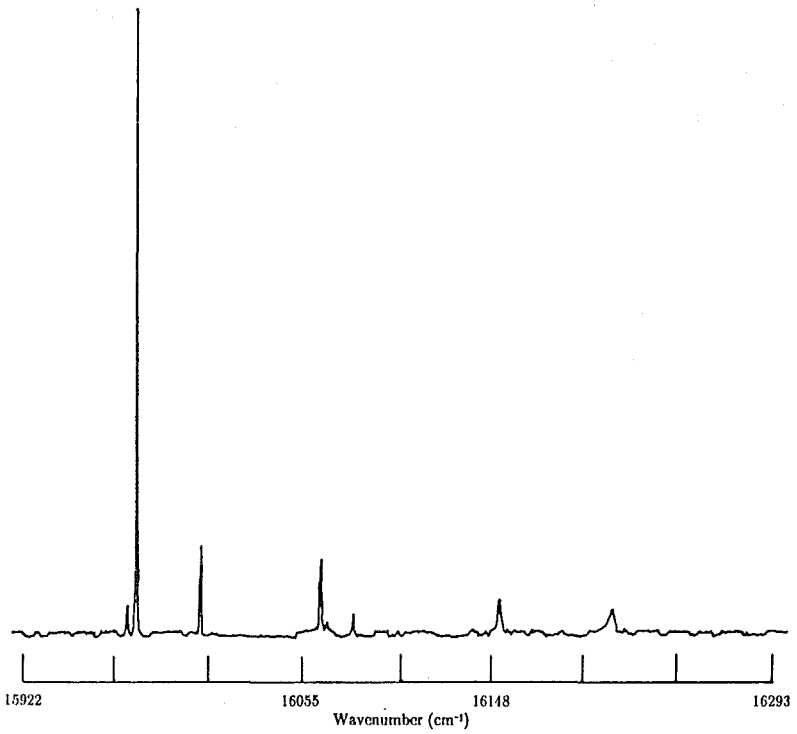

Figure 5.34: 10 K excitation spectrum of the C multiplet for $SrF_2 : Nd^{3+}$ T^- C_{S1} centre.

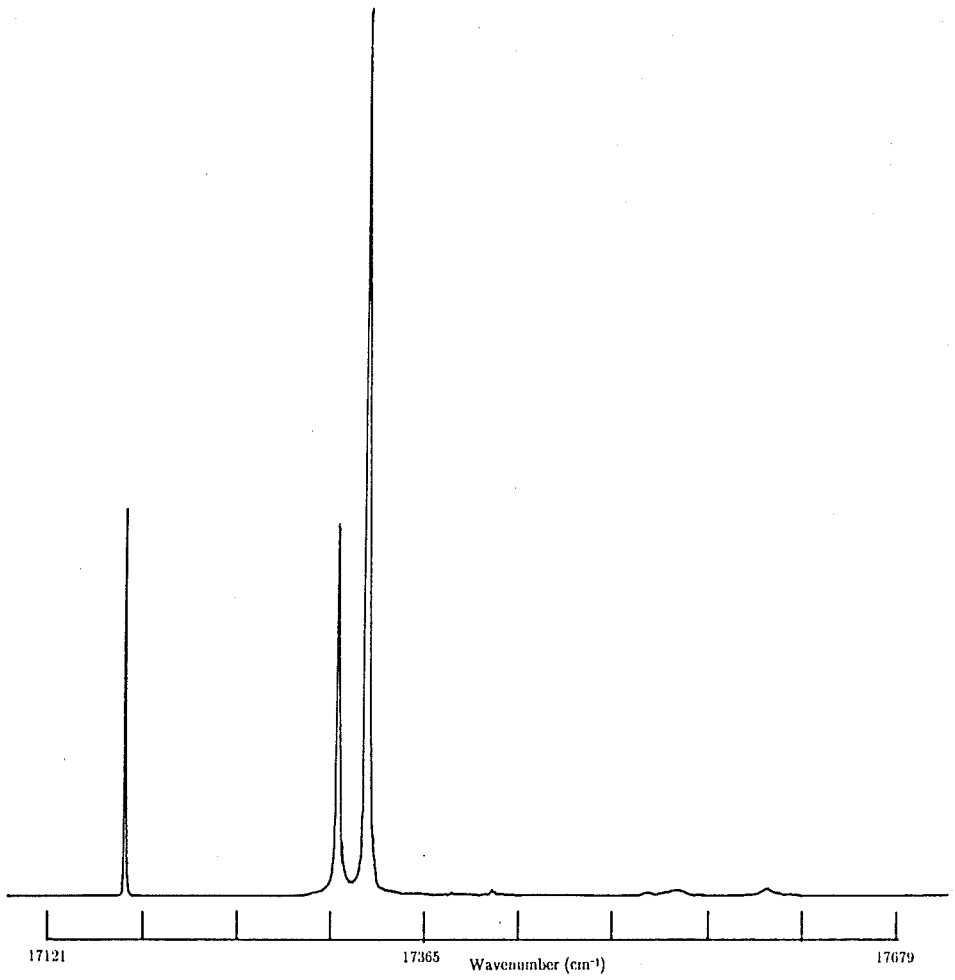

Figure 5.35: 10 K excitation spectrum of the D multiplet for $SrF_2 : Nd^{3+}$ T^- C_{S1} centre.

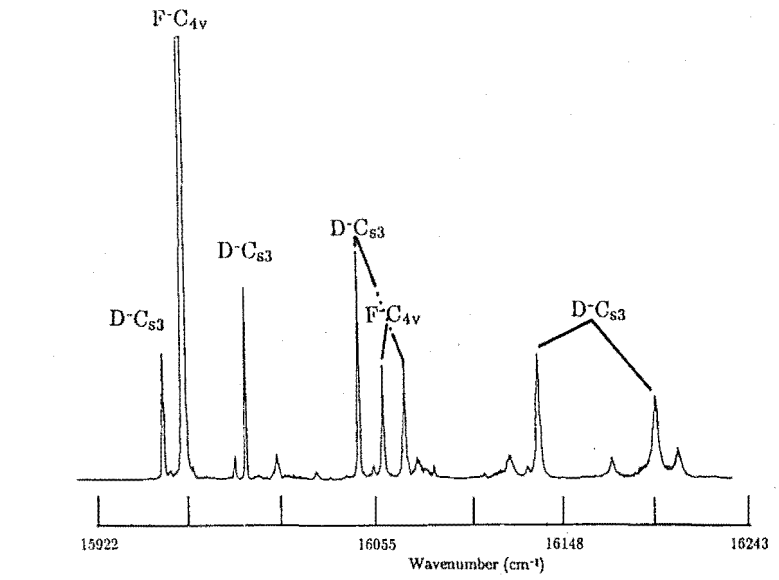

a)

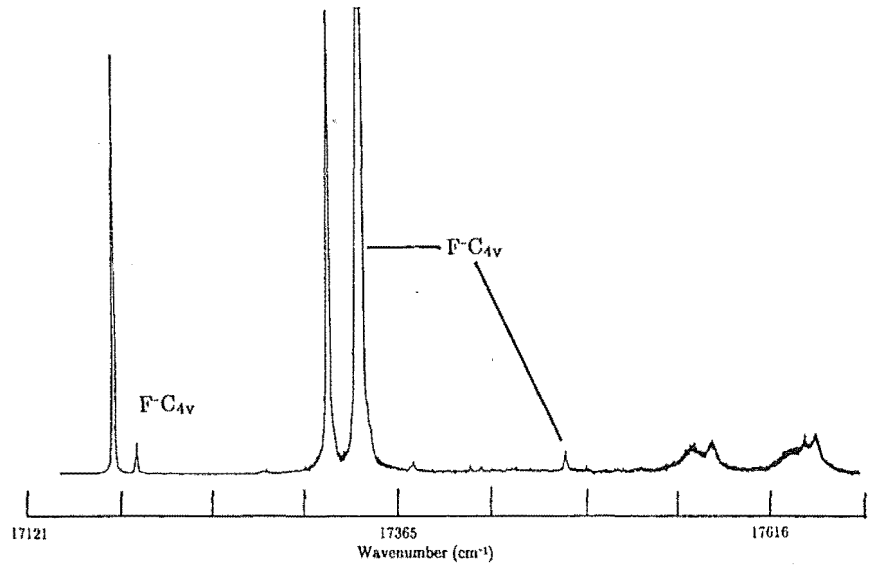

b)

Figure 5.36: 10 K excitation spectrum of a) C and b) D multiplets for $SrF_2 : Nd^{3+}$ D^- C_{S3} centre.

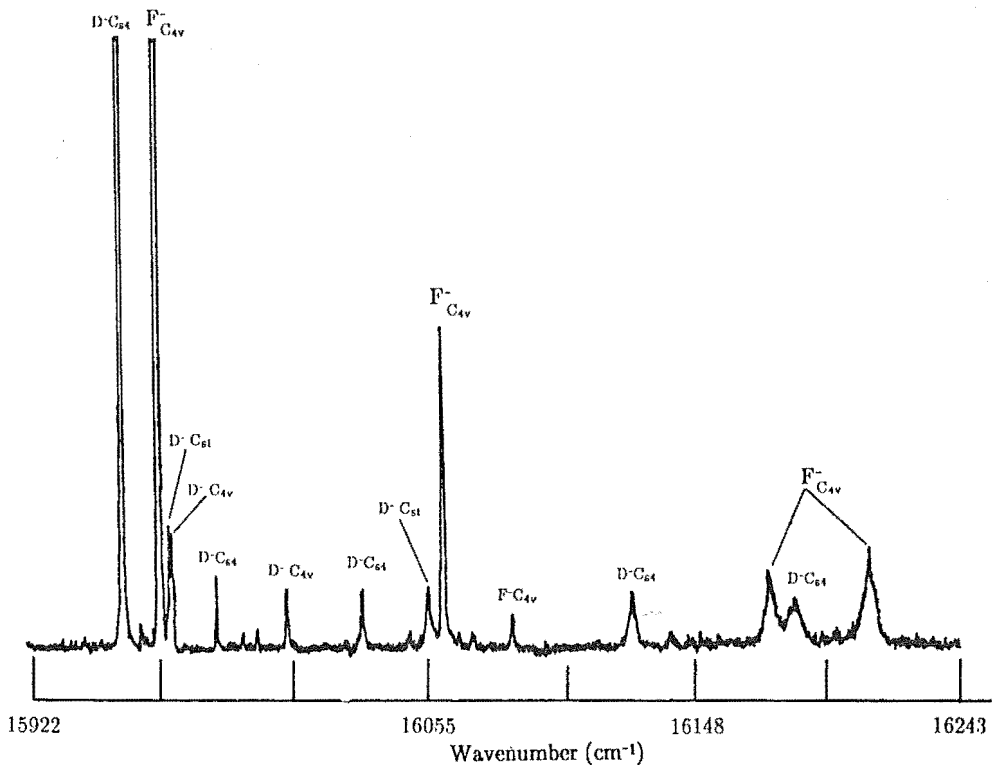

Figure 5.37: 10 K excitation spectrum of the C multiplet for $SrF_2 : Nd^{3+}$ D^- C_{S4} centre.

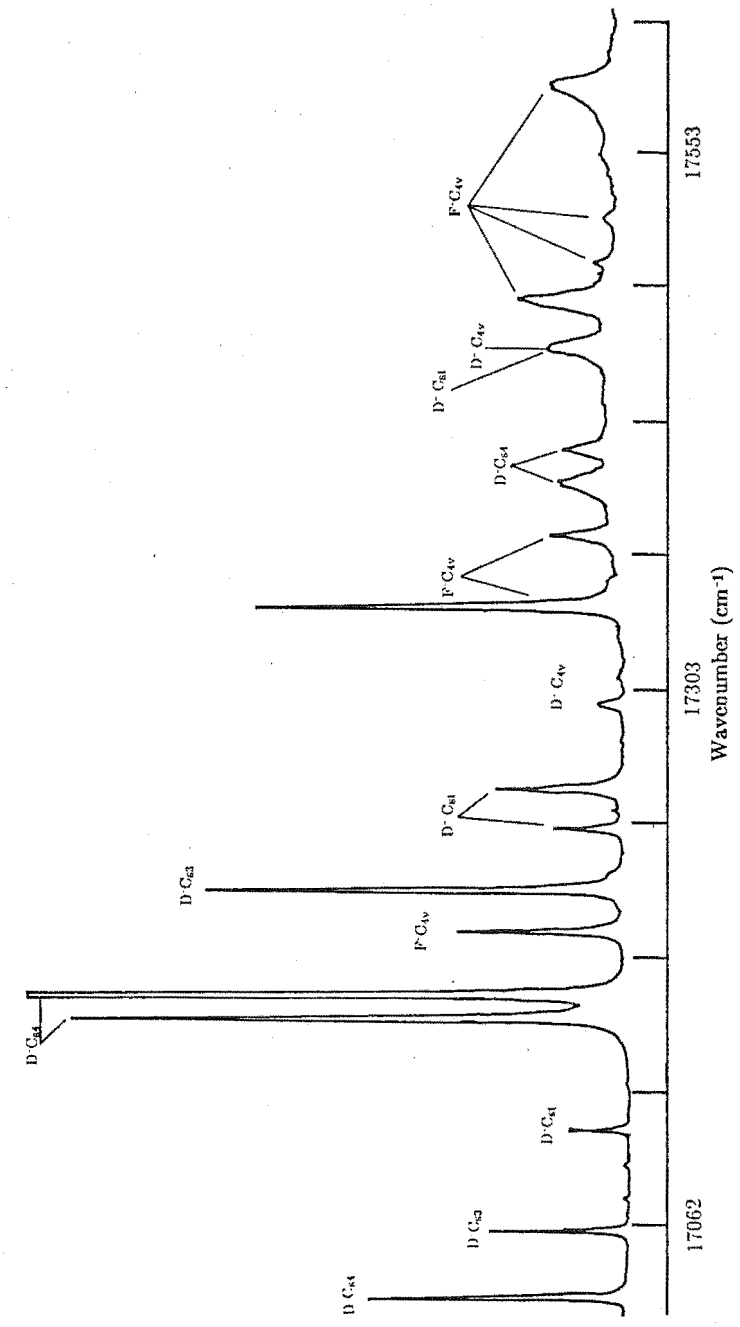

Figure 5.38: 10 K excitation spectrum of the D multiplet for $SrF_2 : Nd^{3+}$ D^- C_{S4} centre.

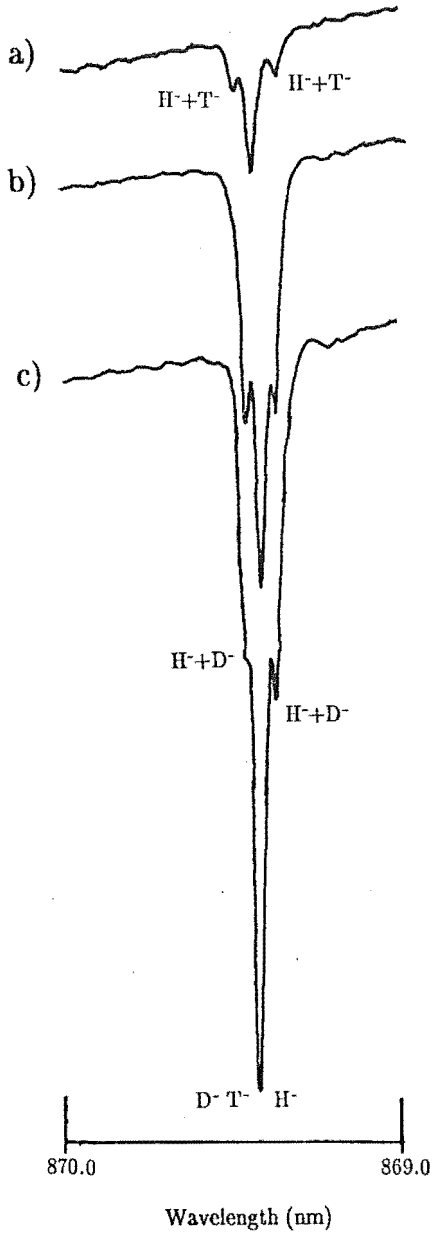

Figure 5.39: 10 K R multiplet absorption spectrum of the C_{S1} centre for the following $SrF_2 : Nd^{3+}$ crystals :
a) $T^- + H^-$; b) $D^- + H^-$; c) $D^- + H^-$ and H^- in series.

to those of the C_S centre observed in the infrared by Edgar et al. (1977), with an average deviation of 13 cm^{-1}. They proposed a model for the C_S centre which involved two charge compensating ions, as shown in Fig. 5.46. Their explanation for the observed local mode frequencies was that the rare earth ion perturbed the substitutional hydrogenic ion and partly lifted the degeneracy of the three fold degenerate tetrahedral centre line into two lines; one of which is doubly degenerate. The more distant interstitial hydrogenic ion further splits the doubly degenerate line and shifts the frequencies of all three lines. Consequently the local mode frequencies of the C_{4V} centre must also be present and are expected to be similarly perturbed by the substitutional ion. The results do not unambiguously confirm the presence of the C_{4V} local mode vibronic frequencies as their intensities were extremely weak and they were also overlapped by a strong electronic transition. Two extremely weak transitions were observed to terminate at 611 and 560 cm^{-1}, which could be the perturbed C_{4V} local mode frequencies but there is insufficient evidence to verify this.

5.4.3 The C_{S3} Centre

The fluorescence spectra of the H^-, D^- and T^- analogues of the C_{S3} centre were observed in $SrF_2 : Nd^{3+}$ but only the D^- analogue was observed in $CaF_2 : Nd^{3+}$. The recorded fluorescence spectra are presented in Figs. 5.47 to 5.53 and the energy levels are listed in Table 5.8.

Analysis of the optical absorption spectra reveals the C_{S3} centre also involved two charge compensating hydrogenic ions. Fig. 5.54 shows the absorption lines of the C_{S3} centre with various combinations of singly hydrogenated crystals. The absorption line in the centre of the absorption spectrum of the mixed $D^- + H^-$ crystal is associated with combinations of two different hydrogenic ions whereas the lines at each side are due to the $D^- D^-$ and the $H^- H^-$ ion pairs. The isotope shift for the $Z_1 \rightarrow R_1$ transition in $SrF_2 : Nd^{3+}$ is 1.70 $\pm$0.06 cm^{-1} for H^- to D^- and is 1.99 $\pm$0.06 cm^{-1} for H^- to T^-.

The fluorescence intensity pattern of the C_{S3} centre is very similar to that of the C_{S1} centre. The fluorescence of the C_{S3} centre is weaker than that of the C_{S1} centre. This was particularly so for the T^- analogue, which is attributed to the low concentration of the T^- ions in the tritiated crystal. This is the reason for being unable to observe the local mode vibronic frequencies in the T^- analogue. Five local mode frequencies were observed for the C_{S3} D^- centre in $SrF_2 : Nd^{3+}$ which can then be separated into two groups on the basis of their relative intensities. The first group consists of 612, 559 and 520 cm^{-1} while the remaining frequencies 541 and 481 cm^{-1} form the second group, as shown in Fig. 5.49.

The fluorescence pattern of the C_{S3} D^- centre in $CaF_2 : Nd^{3+}$ is similar

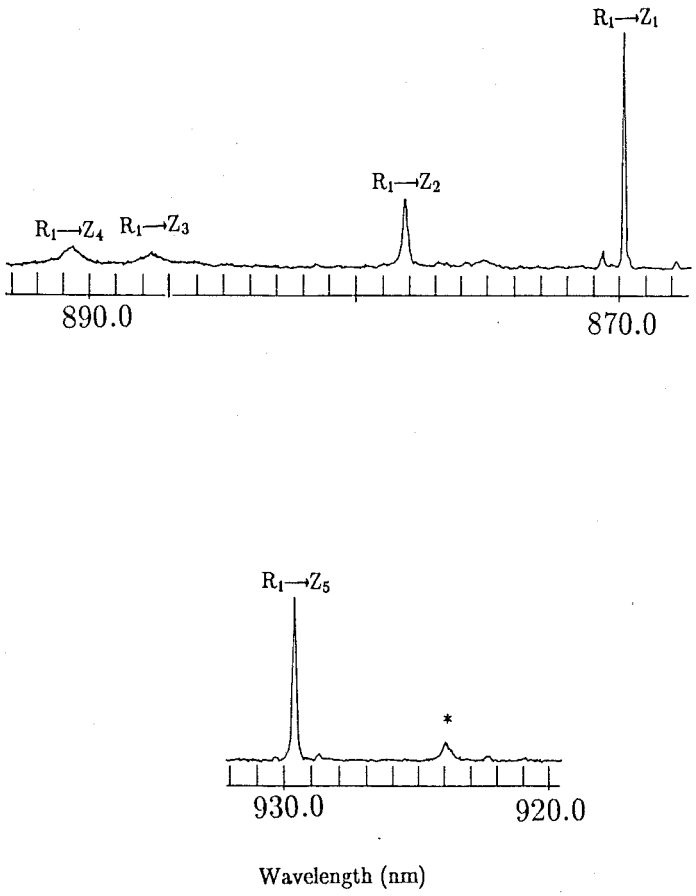

Figure 5.40: 10 K fluorescence spectrum of the $SrF_2 : Nd^{3+}$ C_{S1} H^- centre. * unidentified line.

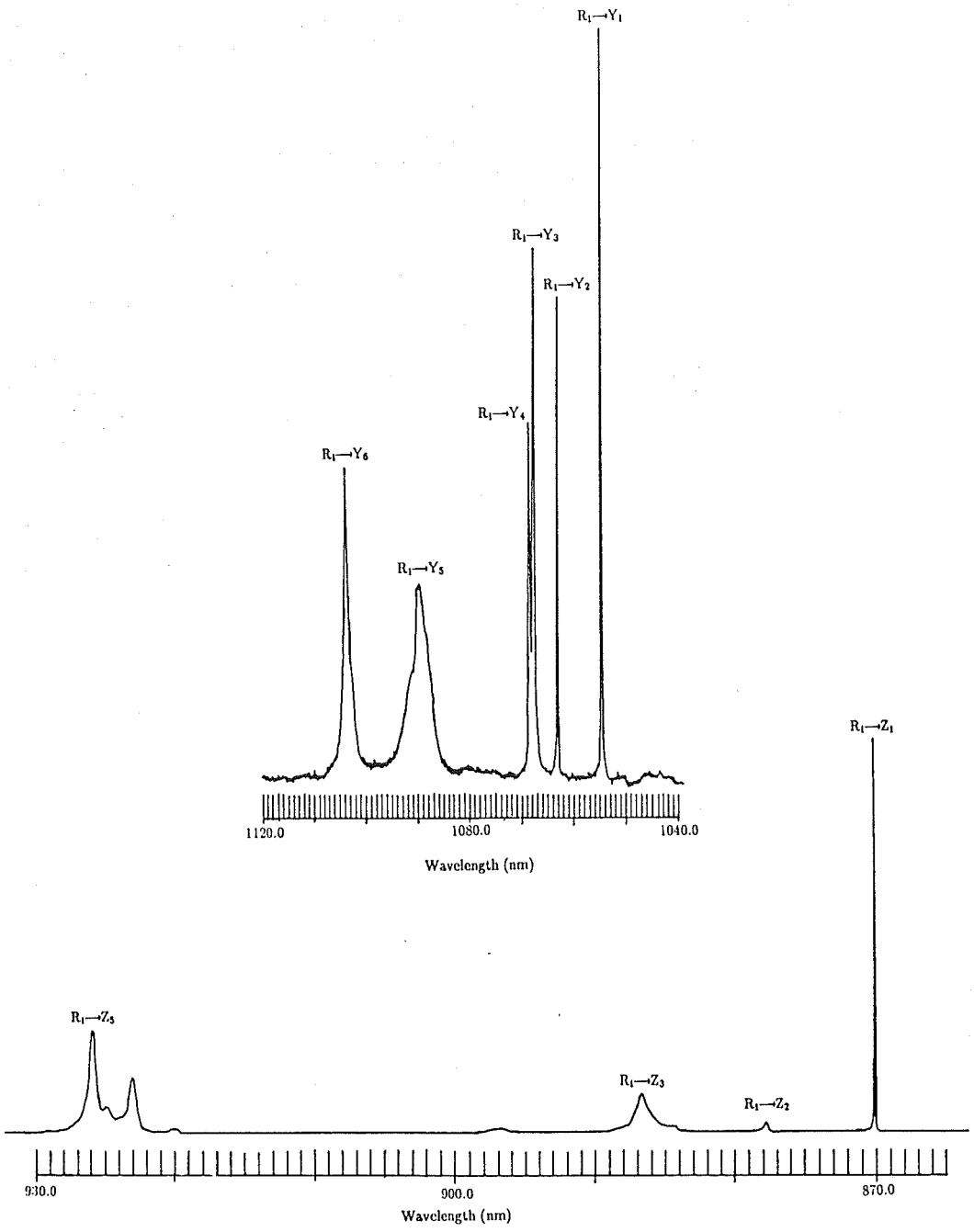

Figure 5.41: 10 K fluorescence spectrum of the $SrF_2 : Nd^{3+}$ C_{S1} D^- centre.

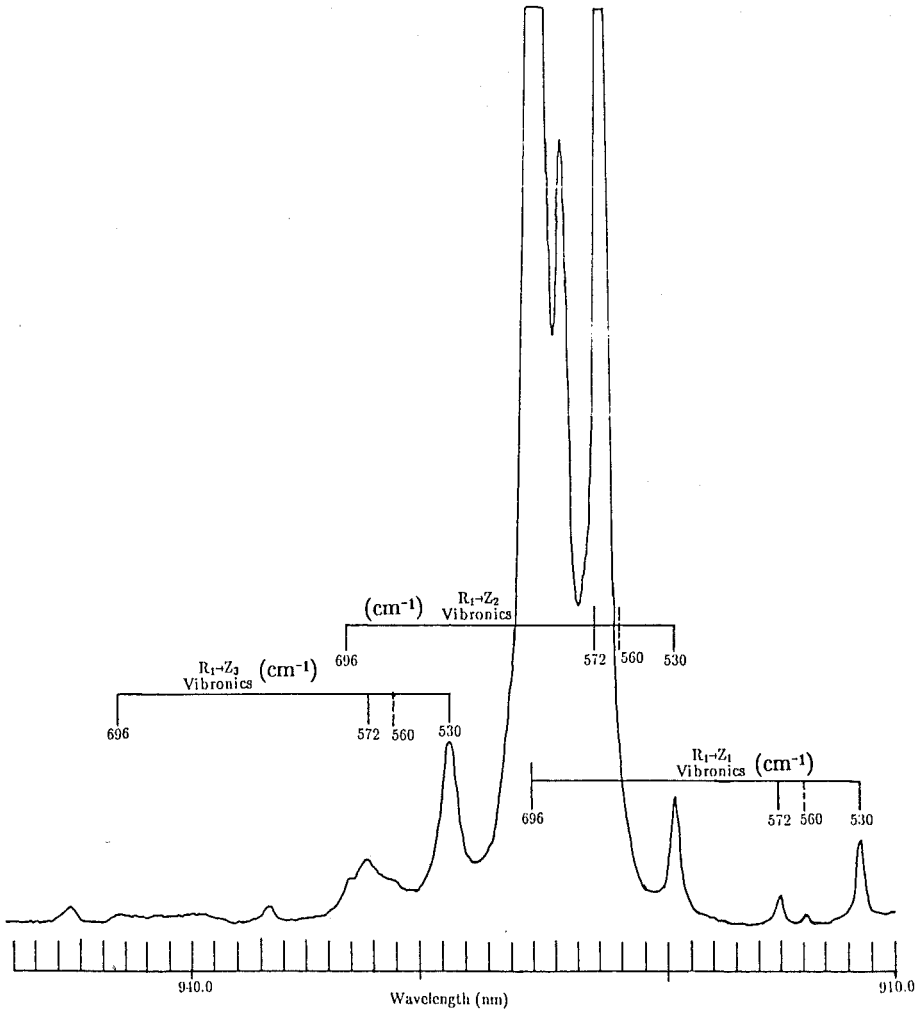

Figure 5.42: 10 K fluorescence spectrum showing the vibronic lines associated with the $R_1 \rightarrow Z_{1,2,3}$ transitions for the $SrF_2 : Nd^{3+}$ C_{S1} D^- centre.

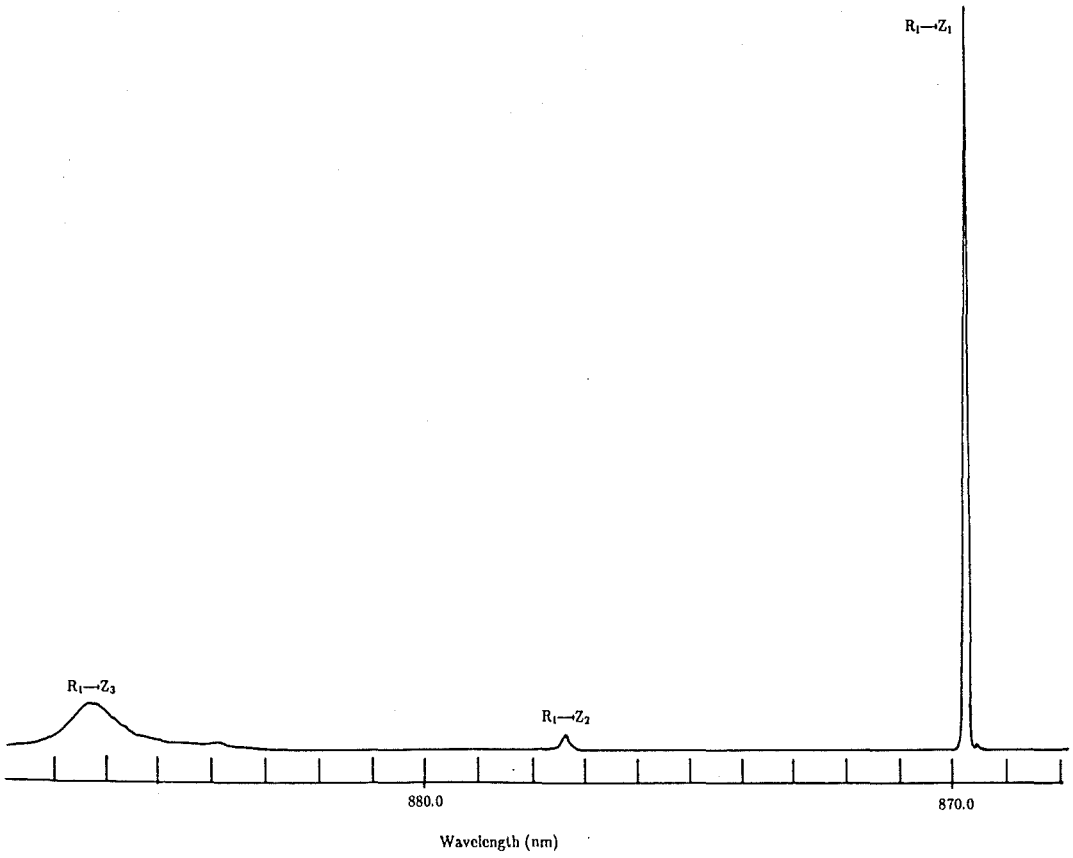

Figure 5.43: 10 K fluorescence spectrum for the $R_1 \rightarrow Z_{1,2,3}$ transitions of the $SrF_2 : Nd^{3+}$ C_{S1} T^- centre.

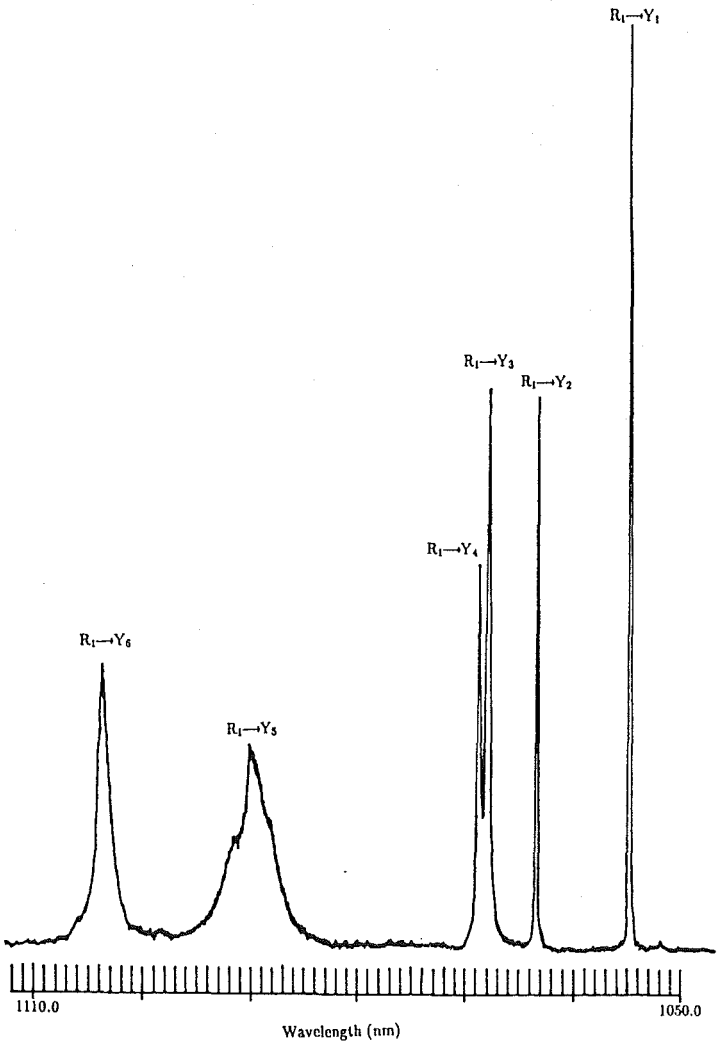

Figure 5.44: 10 K fluorescence spectrum for the $R_1 \rightarrow Y_{1,2,3,4,5,6}$ transitions of the $SrF_2 : Nd^{3+}$ C_{S1} T^- centre.

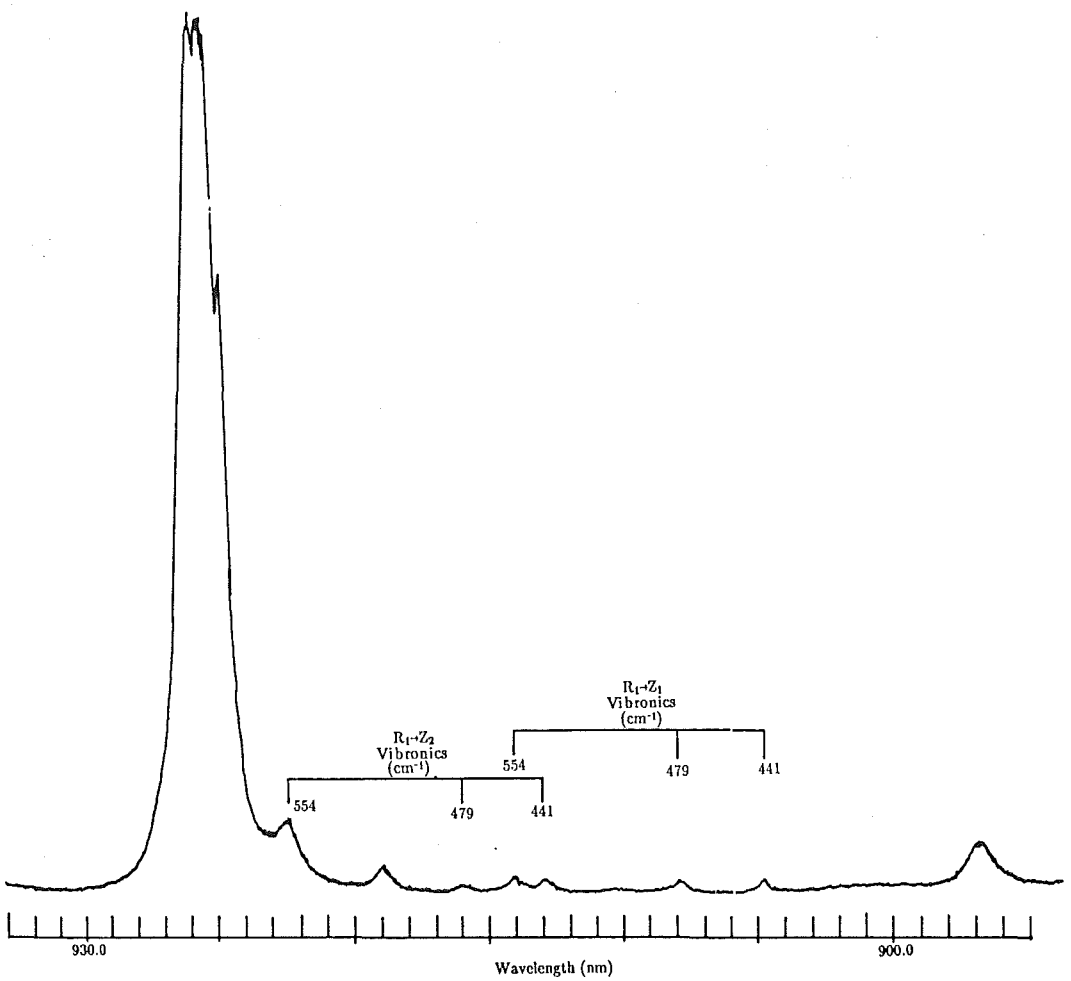

Figure 5.45: 10 K fluorescence spectrum showing the vibronic lines associated with the $R_1 \rightarrow Z_{1,2}$ transitions for the $SrF_2 : Nd^{3+}$ C_{S1} T^- centre.

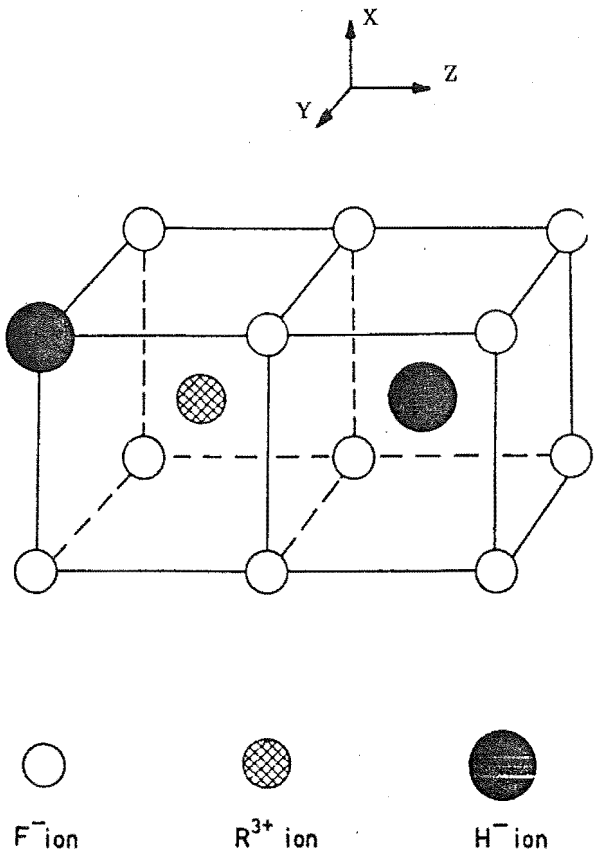

Figure 5.46: Schematic diagram of C_S symmetry centre involving two charge compensating ions, proposed by Edgar et al. 1977.

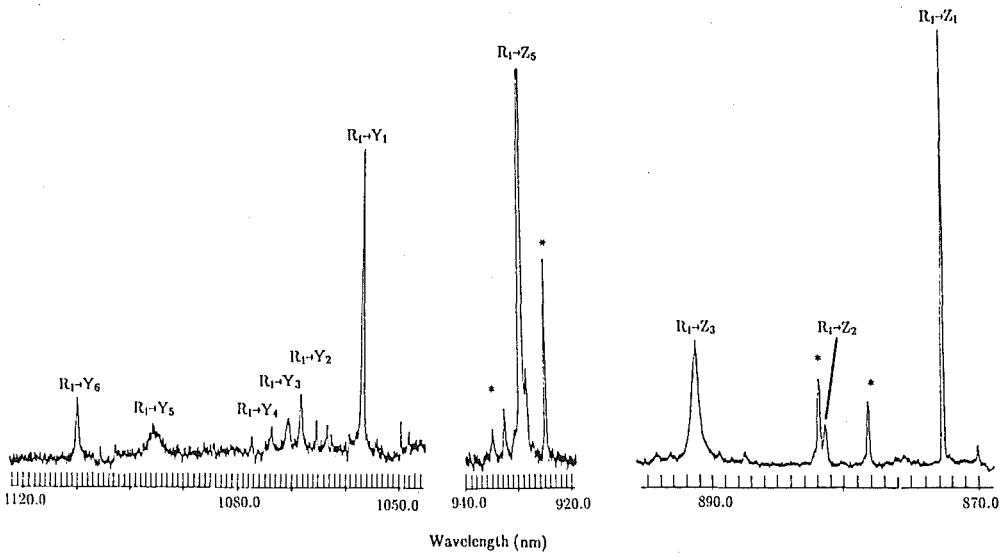

Figure 5.47: 10 K fluorescence spectrum of the $SrF_2 : Nd^{3+}$ C_{S3} H^- centre. * unidentified line.

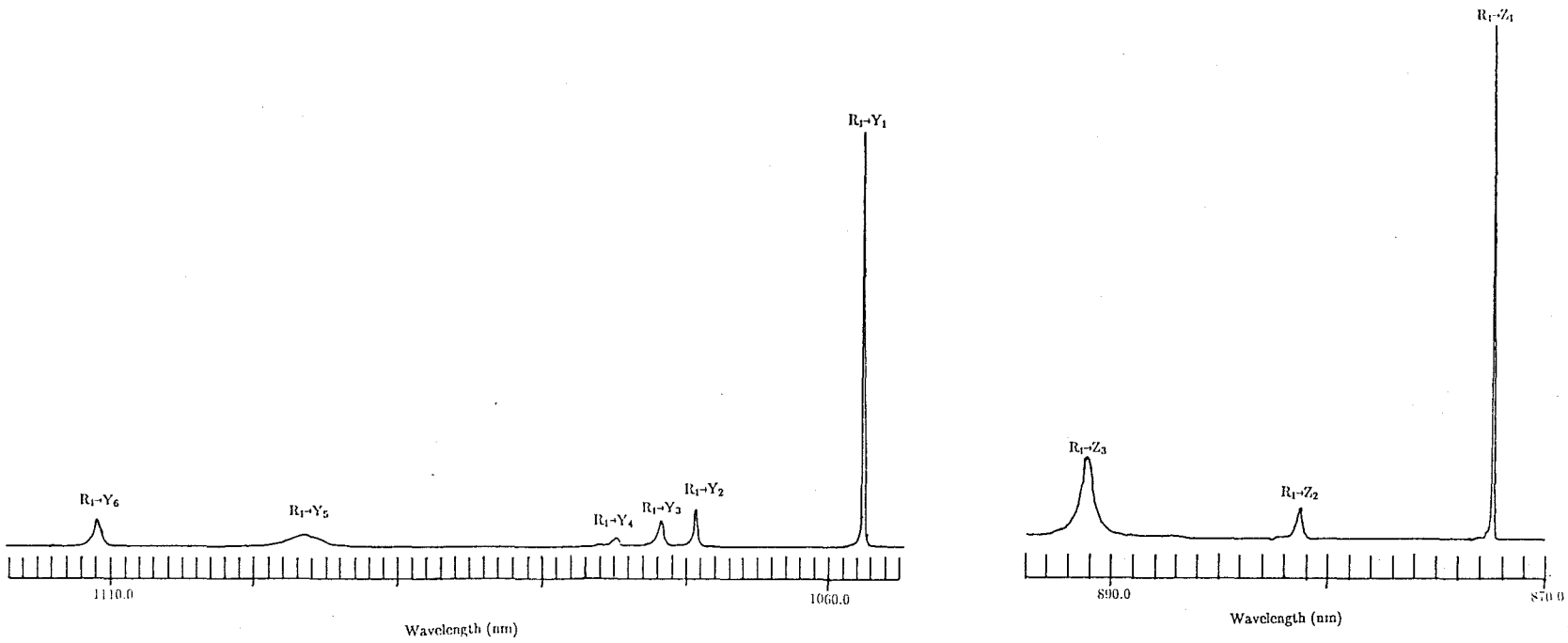

Figure 5.48: 10 K fluorescence spectrum of the $SrF_2 : Nd^{3+}$ C_{S3} D^- centre.

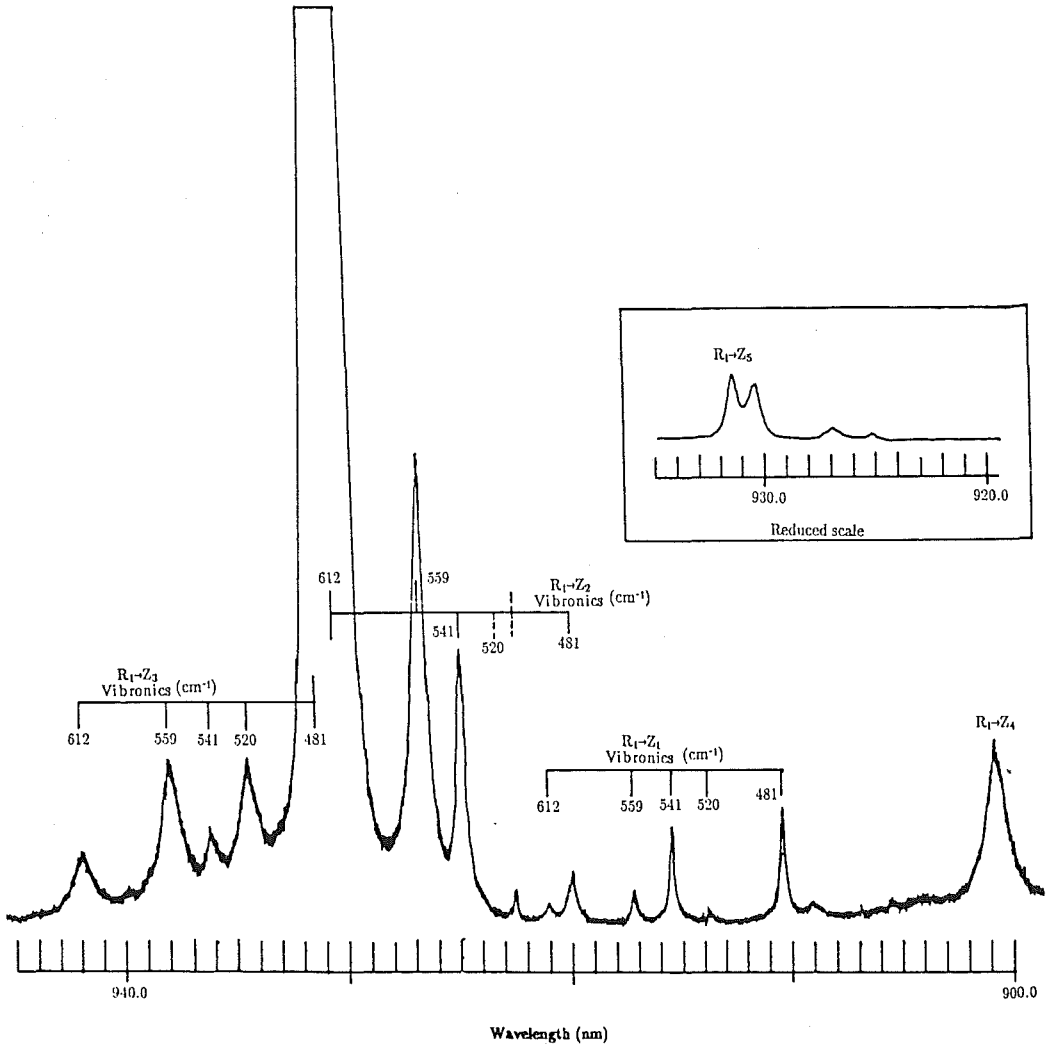

Figure 5.49: 10 K fluorescence spectrum showing the vibronic lines associated with the $R_1 \rightarrow Z_{1,2,3}$ transitions for the $SrF_2 : Nd^{3+}$ C_{S3} D^- centre.

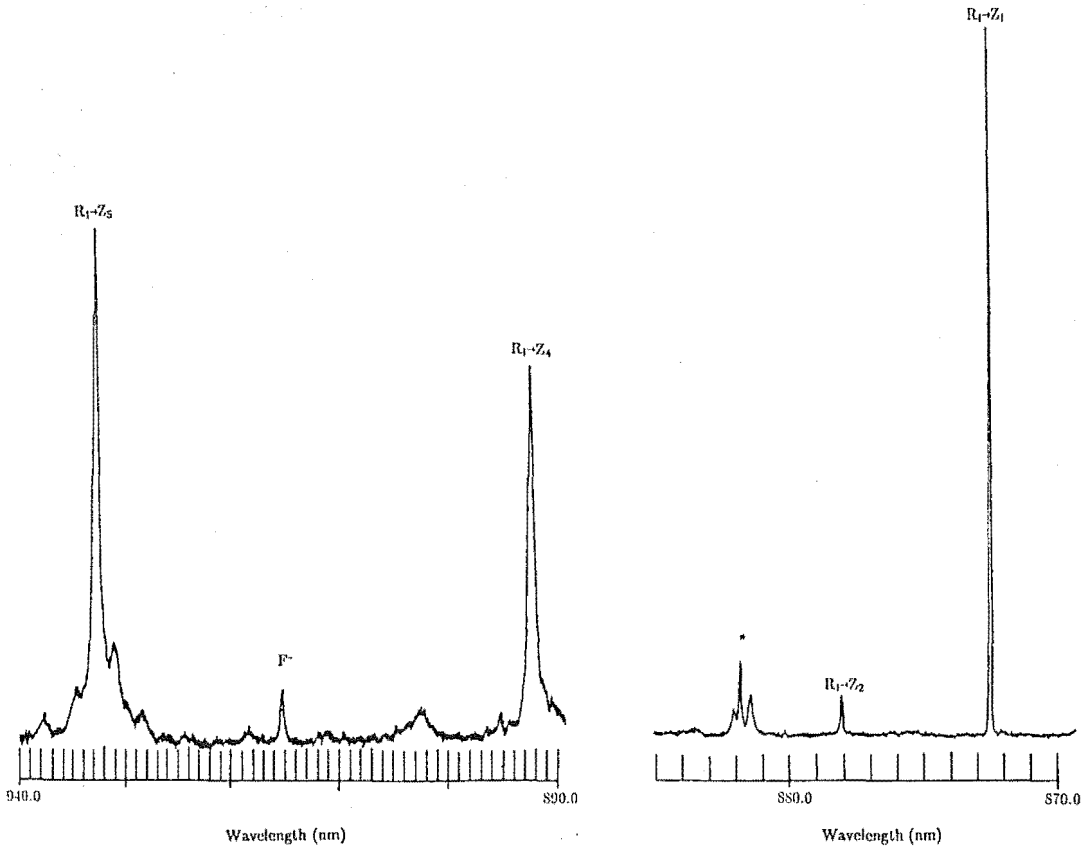

Figure 5.50: 10 K fluorescence spectrum for the $R_1 \rightarrow Z_{1,2,3,4,5}$ transitions of the $SrF_2 : Nd^{3+}$ C_{S3} T^- centre. * unidentified line.

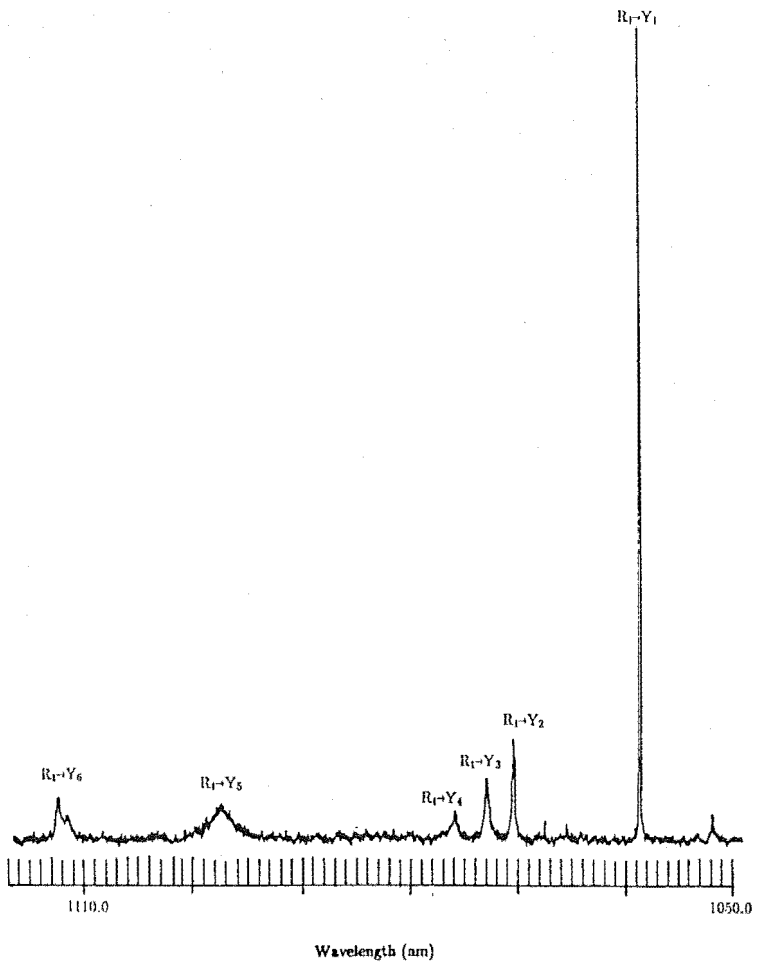

Figure 5.51: 10 K fluorescence spectrum for the $R_1 \rightarrow Y_{1,2,3,4,5,6}$ transitions of the $SrF_2 : Nd^{3+}$ C_{S3} T^- centre.

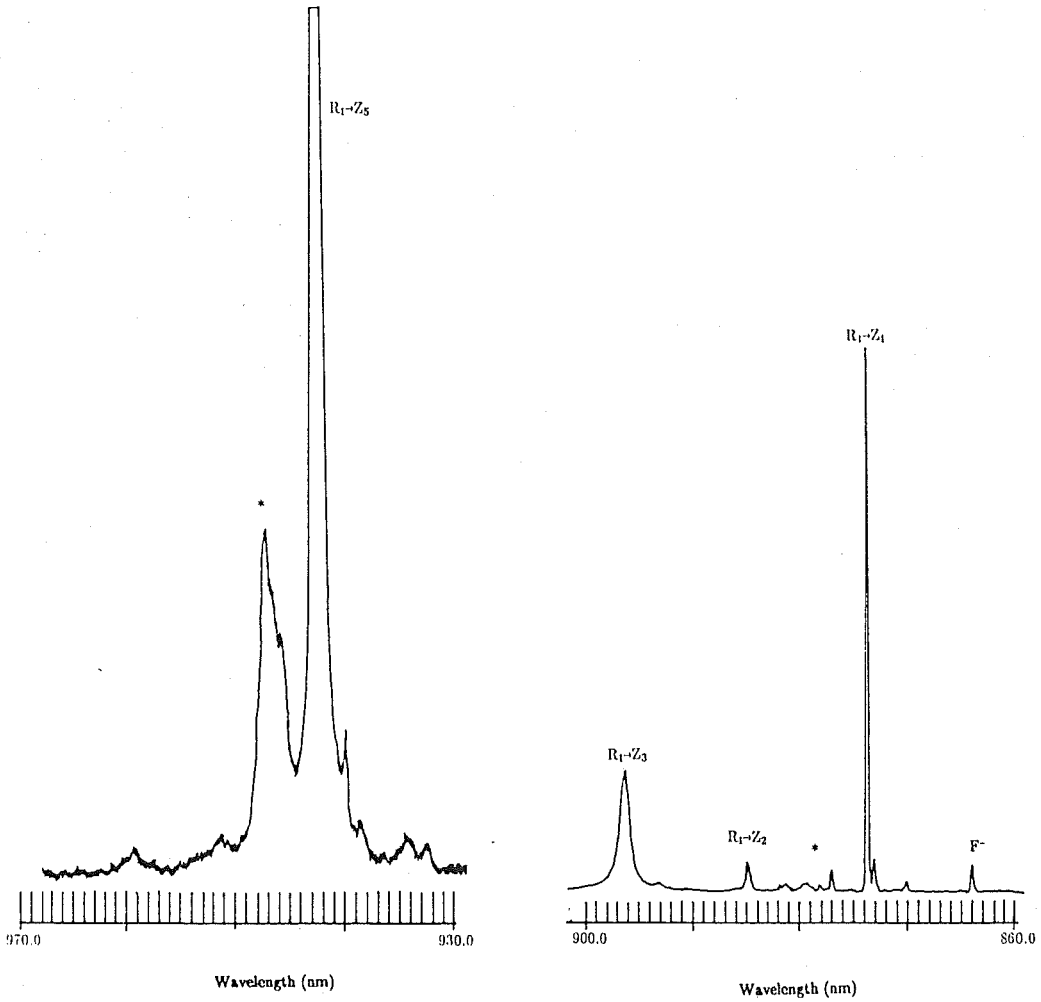

Figure 5.52: 10 K fluorescence spectrum for the $R_1 \rightarrow Z_{1,2,3,5}$ transitions of the $CaF_2 : Nd^{3+}$ C_{S3} D^- centre. * unidentified line.

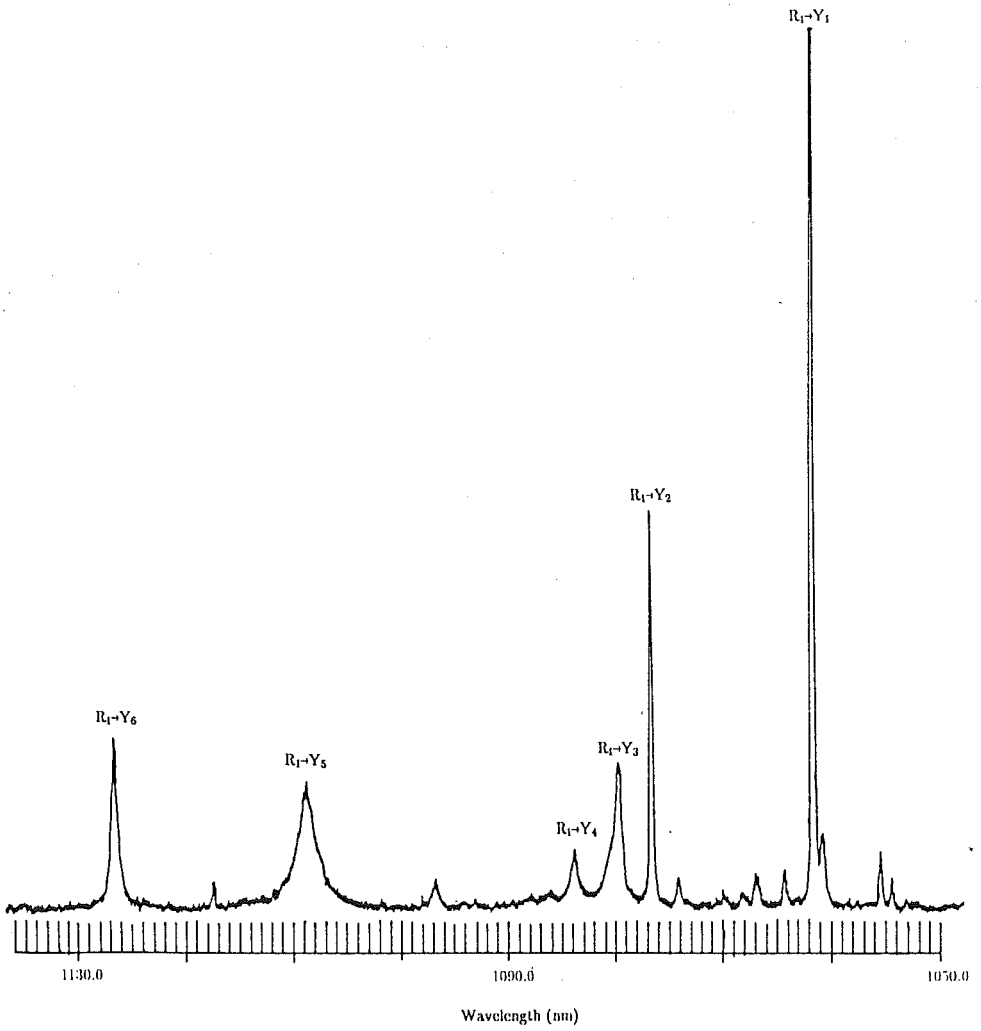

Figure 5.53: 10 K fluorescence spectrum for the $R_1 \rightarrow Y_{1,2,3,4,5,6}$ transitions of the $CaF_2 : Nd^{3+}$ C_{S3} D^- centre.

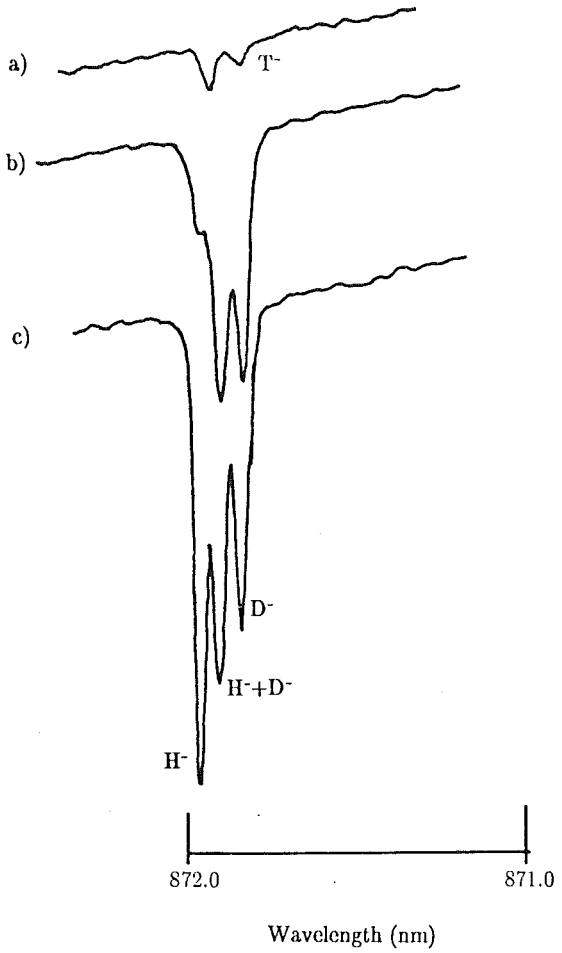

Figure 5.54: 10 K R multiplet absorption spectrum of the $SrF_2 : Nd^{3+}$ C_{S3} centre for a) $T^- + H^-$; b) $D^- + H^-$; c) $D^- + H^-$ and H^-.

to, but weaker in intensity than its corresponding counterpart in $SrF_2 : Nd^{3+}$. It was observed that the C_{S3} D^- centre in $CaF_2 : Nd^{3+}$ possessed non-recoverable bleaching properties. The term 'bleach' as used within this thesis describes a decrease of the observed fluorescence intensity with an increase in time of exposure to the pump laser. No extensive study of these properties was carried out, but the following results are a preliminary investigation of this bleaching behaviour. It must be noted that similar bleaching effects, both recoverable and non-recoverable, have been observed in other rare earth doped fluoride crystals studied (Cockroft et al. 1987, Reeves et al. 1987).

It was observed that for a $\langle 100 \rangle$ orientated hydrogenated $CaF_2 : Nd^{3+}$ crystal, using the same geometry as in the polarisation studies for the C_{4V} centre, the fluorescence intensity of the C_{S3} centre decreases with respect to time to a final intensity of approximately 1/8 of its initial value in a time interval of 200 seconds, for a laser power of 60 mW. When the polarisation of the laser was rotated 90^o the fluorescence intensity recovered, but to a lower level than previously. Successive alternation of the polarisation of the laser results in a complete bleaching of the fluorescence of the C_{S3} centre to a similar final intensity level for each polarisation (see Fig. 5.55). The fluorescence intensity for the C_{S3} D^- centre in $CaF_2 : Nd^{3+}$ shows a complicated time dependence for the (y) and (z) polarisations of the laser. Fig. 5.56 shows that there is more than one time constant in each decay for the two polarisations of the laser and that a time constant of the order of 100 seconds is obtained for the bleaching curve beyond 20 seconds. The time constant for the initial part of each decay was difficult to determine reliably because of the complexity of ensuring the same starting condition for each decay. Similar behaviour of the fluorescence intensity was observed for temperatures up to 55 K, as shown in Fig. 5.56. No attempt was made to find the precise lowest temperature at which the fluorescence intensity would fully recover. No noticeable recovery of the fluorescence was observed for temperatures up to 55 K, but recycling the crystal by warming it up to room temperature and then recooling it caused the recovery of the fluorescence to its initial level. This bleaching behaviour and its relatively fast decay rate made it difficult to obtain a good fluorescence spectrum and consequently even harder to obtain the much weaker local mode vibronic lines.

5.4.4 The C_{S4} Centre

The optical absorption spectrum of a mixed $D^- + H^-$ hydrogenated $SrF_2 : Nd^{3+}$ crystal showed four absorption lines for the C_{S4} centre (see Fig. 5.57). Detailed analysis of combinations of different hydrogenated crystals reveals that the lines at each side of the main absorption line are associated with the $H^- H^-$ and the $D^- D^-$ ion pairs. This result is consistent with a centre involving three charge compensating ions. The isotope shift of the $Z_1 \rightarrow R_1$

transition in $SrF_2 : Nd^{3+}$ is 2.22 $\pm$0.06 cm^{-1} for H^- to D^- and is 2.35 $\pm$0.06 cm^{-1} for H^- to T^-.

The fluorescence spectrum was recorded in deuterated $SrF_2 : Nd^{3+}$ crystals only (Fig. 5.58 and Table 5.9), because the fluorescence of the H^- analogue was very weak and was masked by strong overlapping spurious fluorescence from other centres. The fluorescence intensity pattern of the C_{S4} D^- centre in $SrF_2 : Nd^{3+}$ is similar to that of the C_{S1} and C_{S3} centres, with the exception of an additional transition in the region near the $R_1 \rightarrow Z_4$ and $R_1 \rightarrow Z_5$ transitions (see Fig. 5.58). This additional transition has the same tuning characteristics as the $R_1 \rightarrow Z_1$ transition, which makes the assignment of the Z_4 and Z_5 energy levels ambiguous. Six local mode vibronic frequencies were observed for the C_{S4} D^- centre (Fig. 5.59), with higher relative intensity to the electronic lines than their counterparts in C_{S1} and C_{S3} centres. They were separated into two groups on the basis of their intensities and by comparison with the results for C_{S1} and C_{S3} centres. The first group consists of the frequencies 598, 515 and 497 cm^{-1} while the second group is formed by the remaining frequencies of 586, 534 and 461 cm^{-1}.

The fluorescence of the C_{S4} centre in $SrF_2 : Nd^{3+}$ was also observed to possess bleaching characteristics. The bleached fluorescence of an $\langle 100 \rangle$ oriented crystal is recoverable by rotating the plane of polarisation of the laser by 90° (see Fig. 5.60). The geometry of the experiment is the same as that described for the C_{S3} centre. In this preliminary investigation it was observed that the bleaching characteristics vary with excitation of different energy levels in the $^4G_{5/2}$ multiplet of the C_{S4} centre. Excitation of the energy levels at 17026 and 17154 cm^{-1} gave bleaching decay rates of 39.4 and 166.7 seconds respectively (Figs. 5.61 and 5.62), whereas excitation of the energy level at 17164 cm^{-1} gave no sign of bleaching, but removed any asymmetry induced by previous excitation of either of the other levels. For a $\langle 111 \rangle$ oriented crystal, excitation of the energy levels at 17154 and 17164 cm^{-1} gave no sign of bleaching while excitation of the energy level at 17026 cm^{-1} gave bleaching with a complicated time dependence for both orientations of the plane of polarisation of the laser, as illustrated in Fig. 5.63.

A preliminary search for a photoproduct associated with the bleaching was carried out for the C_{S4} D^- centre in $SrF_2 : Nd^{3+}$. The term 'photoproduct' in this context is defined as the creation of a new symmetry centre from the original centre by the bleaching process. The spectrometer was set at 'zero order' to pass all frequencies of the fluorescence, but with a pair of red filters (Corning glass filters C.S.2-64 and C.S.2-62) at its entrance slit to limit the response of the photo-multiplier to wavelengths longer than 850 nm. The tunable dye laser was scanned across the $^4G_{5/2}$ multiplet at 20 mW laser power producing a 'zero order' excitation spectrum. A photoproduct was observed in the 'zero' order excitation spectra after excitation of the energy level at 17026 cm^{-1} for 300 seconds at 180 mW laser power,

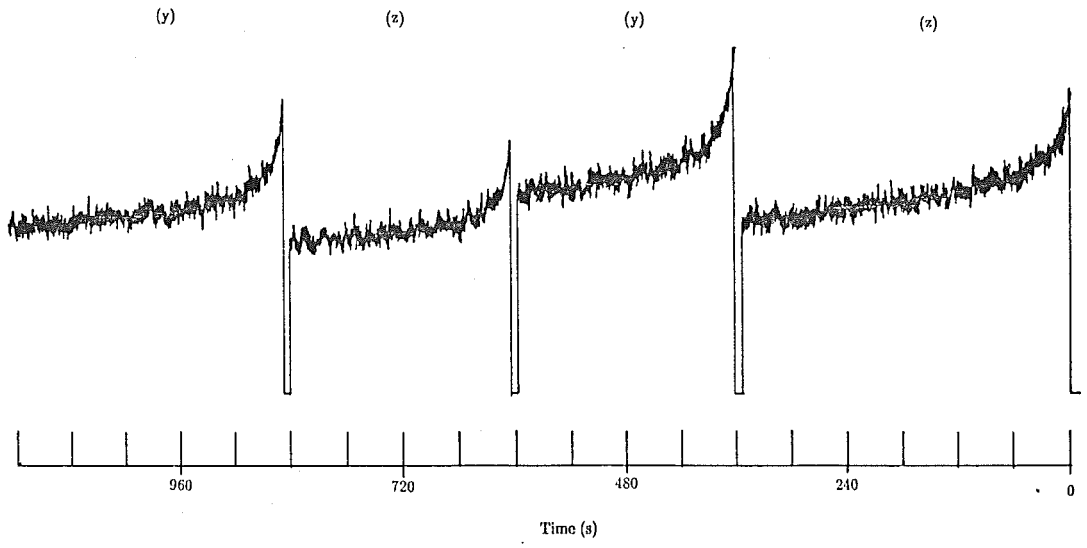

Figure 5.55: 10 K bleaching curves of the fluorescence for CaF_2 : Nd^{3+} C_{S3} D^- centre with 60 mW laser power for (y) and (z) polarisations of the incident laser and using $\langle 100 \rangle$ oriented crystals.

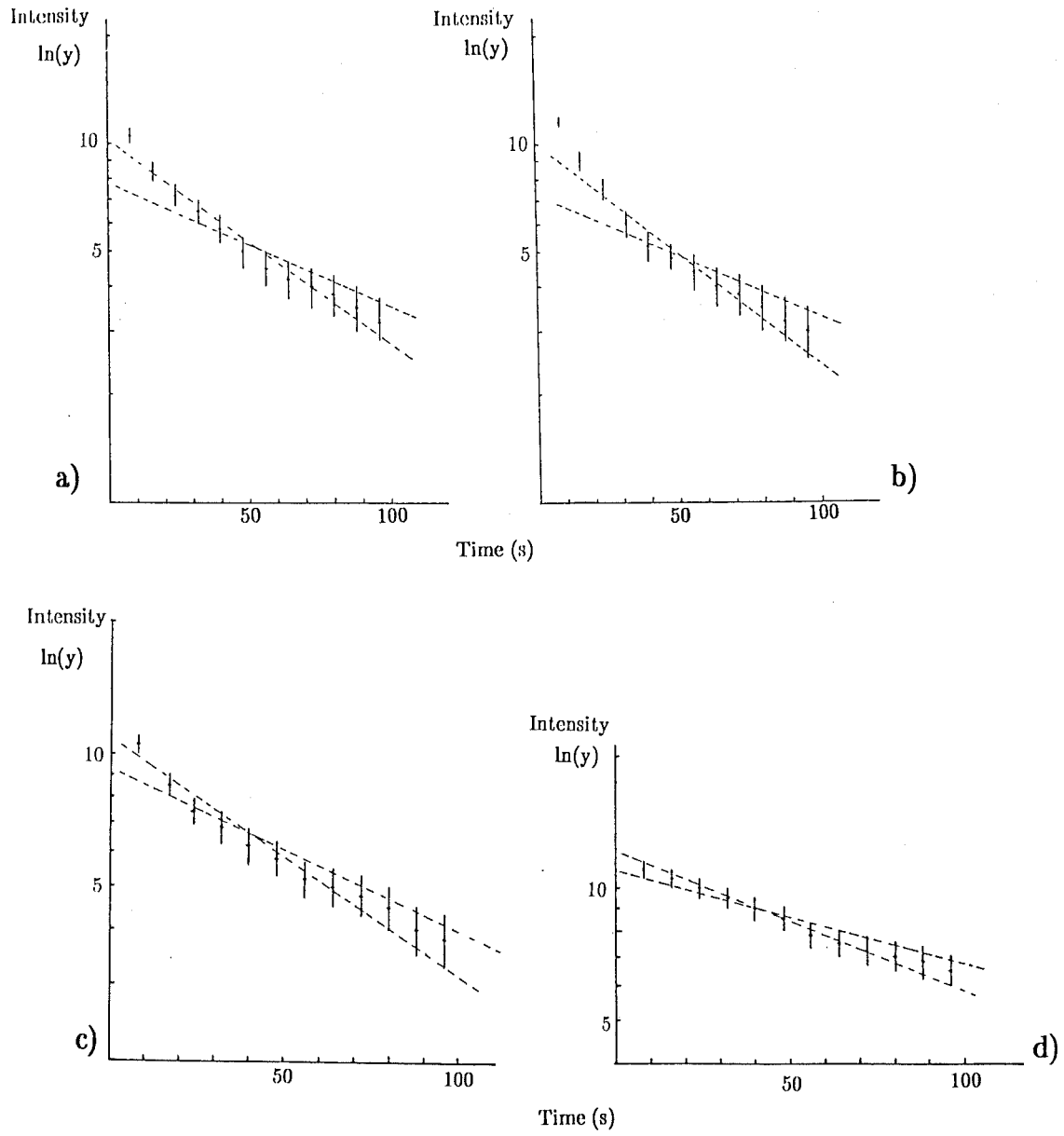

Figure 5.56: Bleaching plots of the fluorescence of the $CaF_2 : Nd^{3+}$ C_{S3} D^- centre in $\langle 100 \rangle$ oriented crystals. Fluorescence decay constants after about 20 seconds are :
for (y) polarisation a) 101.3 $\pm$ 24.9 s (55 K); b) 99.3 $\pm$ 28.4 s (28 K);
for (z) polarisation c) 99.1 $\pm$ 18.5 s (55 K); d) 167.9 $\pm$ 41.3 s (28 K).

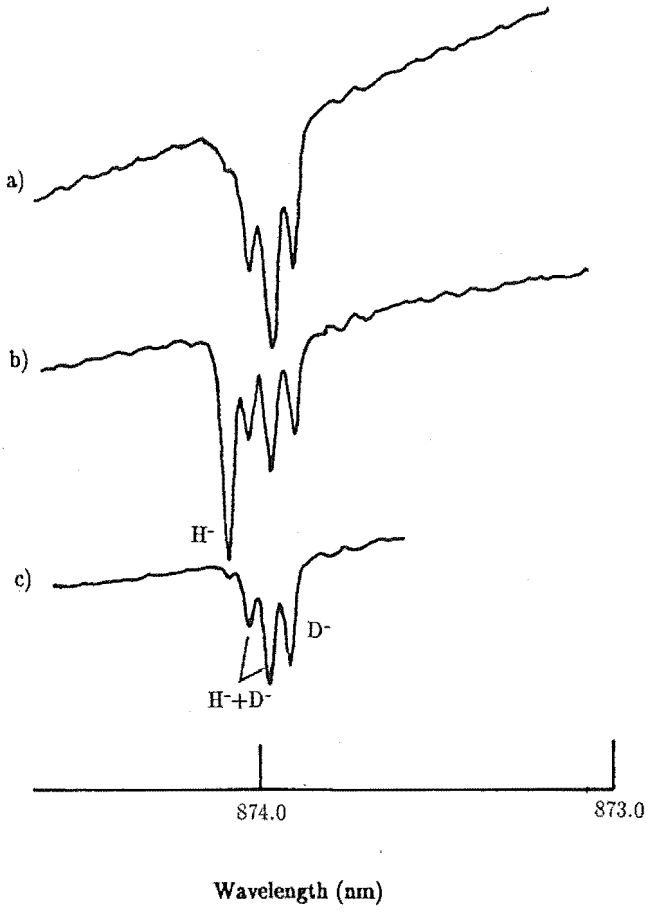

Figure 5.57: 10 K R multiplet absorption spectrum of the $SrF_2 : Nd^{3+}$ C_{S4} centre a) $D^- + H^-$; b) $D^- + H^-$ and H^-; c) $D^- + H^-$ and D^-.

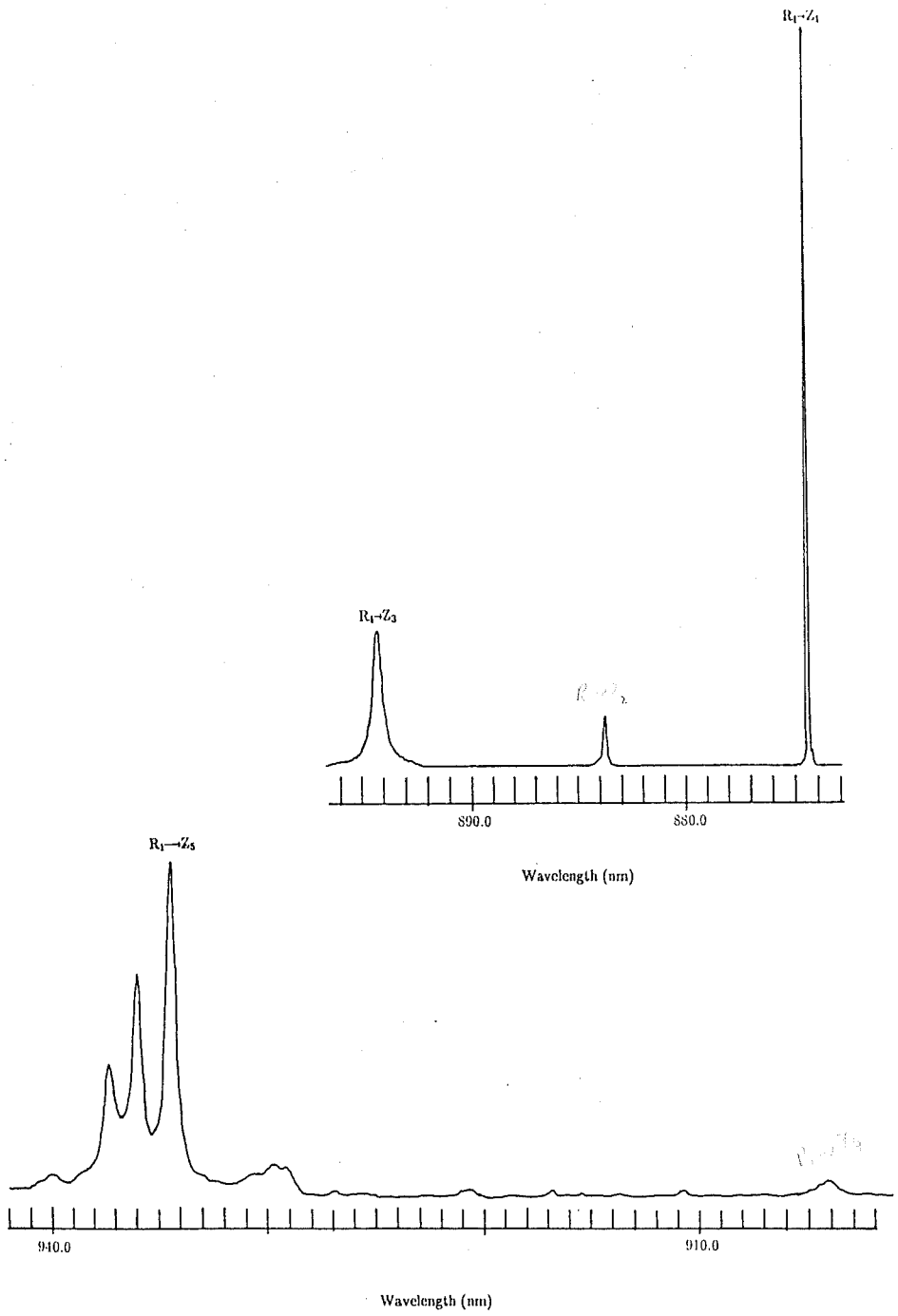

Figure 5.58: 10 K fluorescence spectrum for the $R_1 \rightarrow Z_{1,2,3,5}$ transitions of the $SrF_2 : Nd^{3+}$ C_{S4} D^- centre.

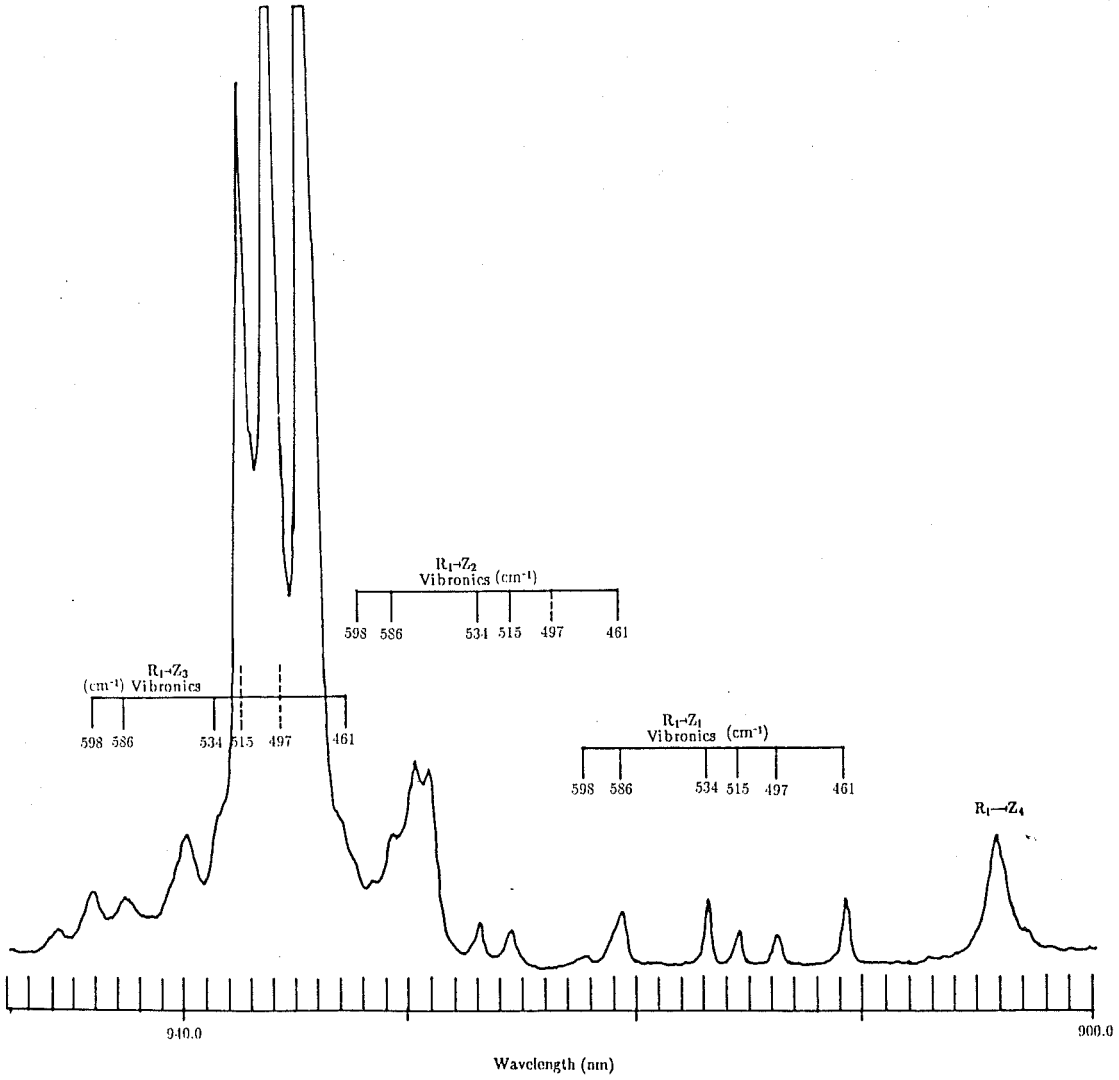

Figure 5.59: 10 K fluorescence spectrum showing the vibronic lines associated with the $R_1 \rightarrow Z_{1,2,3}$ transitions for the $SrF_2 : Nd^{3+}$ C_{S4} D^- centre.

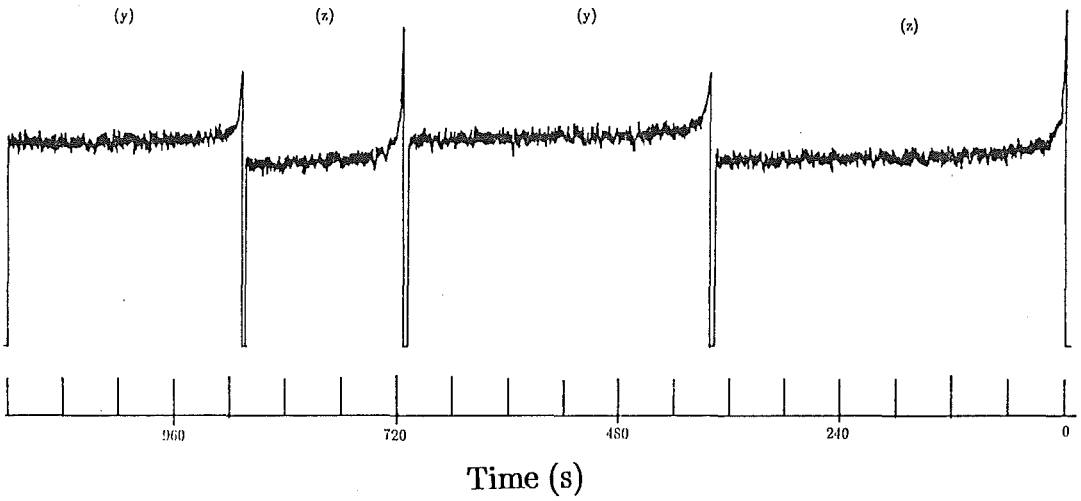

Figure 5.60: 10 K bleaching curves of the fluorescence for the $SrF_2 : Nd^{3+}$ C_{S4} D^- centre with 180 mW laser power for (y) and (z) polarisations of the incident laser and using $\langle 100 \rangle$ oriented crystals.

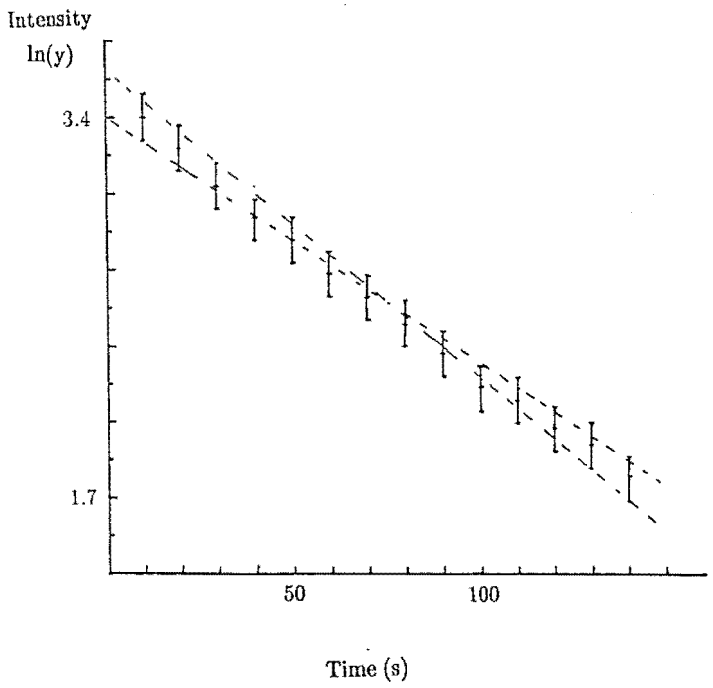

Figure 5.61: Bleaching plots of the fluorescence for the $SrF_2 : Nd^{3+}$ C_{S4} D^- centre in $\langle 100 \rangle$ oriented crystals with laser excitation of 180 mW at 17154 cm^{-1} (in air). The fluorescence decay constant is 166.7 $\pm$ 28.6 s at 10 K.

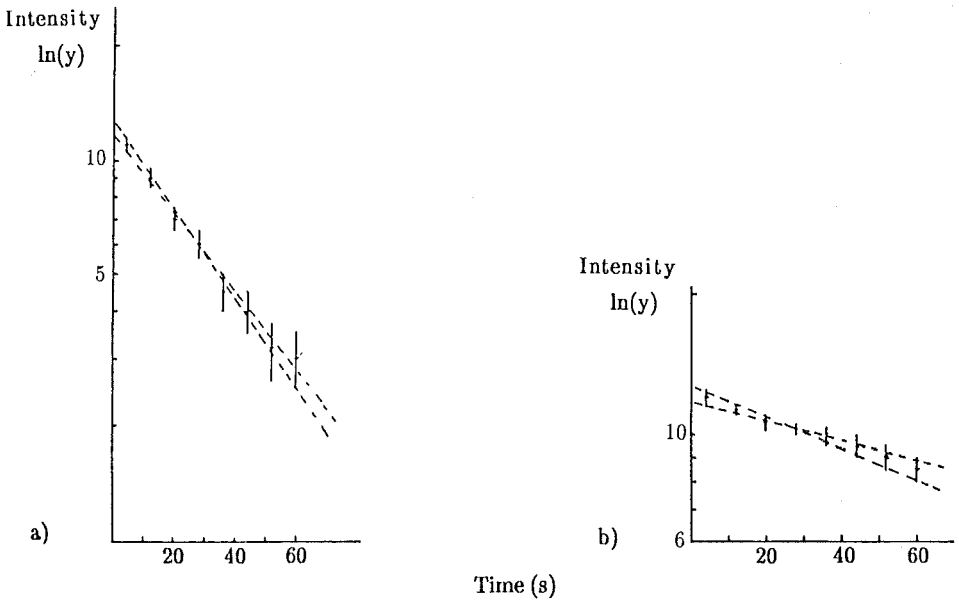

Figure 5.62: 10 K bleaching curves of the fluorescence for a) $SrF_2 : Nd^{3+}$ C_{S4} D^- centre and b) its photoproduct with laser excitation of 180 mW at 17026 cm^{-1} (in air) and using $\langle 100 \rangle$ oriented crystals. The fluorescence decay constant is 30.4 $\pm$ 1.1 s for a) and 123.8 $\pm$ 27.2 s for b).

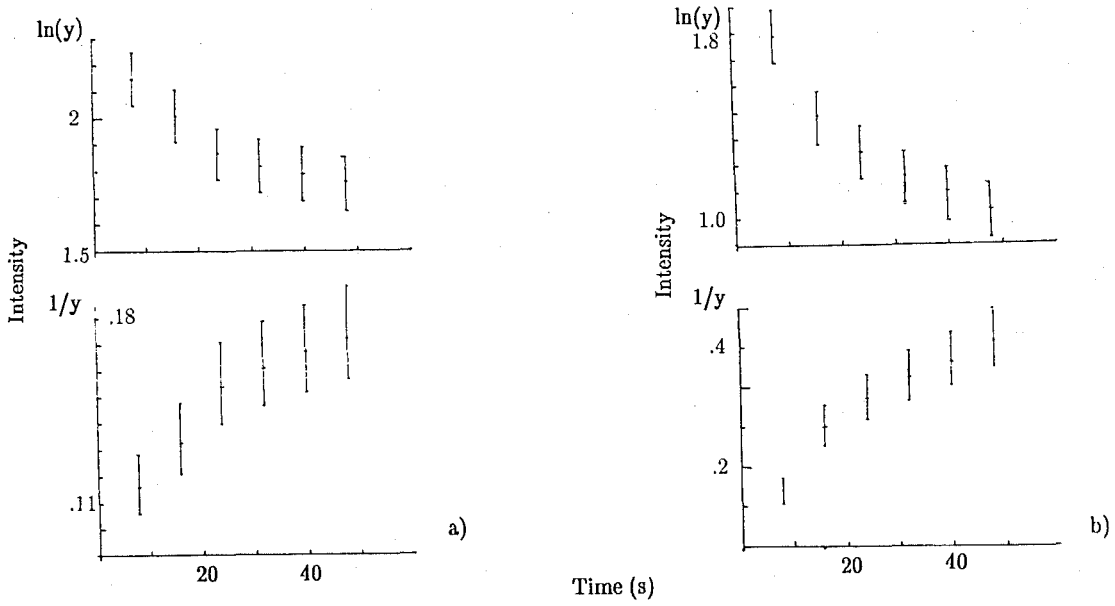

Figure 5.63: 10 K bleaching plots of the fluorescence for the $SrF_2 : Nd^{3+}$ C_{S4} D^- centre with laser excitation of 180 mW at 17026 cm^{-1} (in air) for the a) (z) and b) (y) polarisation of the incident laser and using $\langle 111 \rangle$ oriented crystals.

as shown in Fig. 5.64. The fluorescence intensity obtained by pumping the 17026 cm^{-1} and its photoproduct varies exponentially with time (Fig. 5.62). It was observed that in the 'zero order' excitation spectra obtained with 20 mW laser power there were no noticeable changes in the intensity or the line width of the 17026 cm^{-1} line, after pumping the line or its photoproduct with 180 mW laser power. This peculiar observation indicates a possibility that the bleaching and the production of the photoproduct are the result of a particular frequency, much narrower than the 1 cm^{-1} line width of the laser, within the contour of the energy level at 17026 cm^{-1}. However, a high resolution laser would be needed to verify this hypothesis. Another possibility is that the appropriate absorption and emission coefficients are such that the experiment is particularly sensitive to a small concentration of the photoproduct. There is insufficient evidence at this stage to verify the above hypotheses. It would be valuable to have additional experimental data for the laser power and temperature dependence to give an improved understanding of the bleaching characteristics of the C_{S4} centre.

5.4.5 Discussion

The results reveal that the C_{Si} centres are cluster centres which involve two or three charge compensating ions. This is substantiated by the fluorescence lifetime measurements of these centres, which are presented in Table. 5.5. All the C_{Si} hydrogenic centres have a shorter fluorescence lifetime than the corresponding hydrogenic C_{4V} centre, which is attributed to the increase in the number of possible multi-phonon relaxation channels caused by the presence of the extra hydrogenic ion(s) involved in the charge compensation.

The local mode vibronic frequencies of the H^- analogue derived from group A of the C_{S1} centre are in close agreement with those of the C_S H^- centre observed by Edgar et al. (1977). A simple model involving two charge compensating ions can be treated as a modification of the simple tetragonal symmetry with the second charge compensating ion located in position 1, 5 or 9, as shown in Fig. 5.65. The configuration having the second hydrogenic ion in position 1 is the same as the model proposed by Edgar et al. (1977) for their C_S centre and the similarity of the results for the H^- local mode frequencies supports this configuration being proposed for the C_{S1} centres.

A similar model involving two charge compensating ions is proposed for the C_{S3} centre. For the C_{S3} D^- centre in $SrF_2 : Nd^{3+}$ the ratio of the average frequency of group A and the average frequency for the tetrahedral centre is 0.94 for the C_{S1} centre and is 0.8 for the C_{S3} centre. The splitting of the (x, y) component for group A of the C_{S1} centre is 42 cm^{-1} and for the C_{S3} centre is 60 cm^{-1}. This greater perturbation of the tetrahedral centre frequencies for the C_{S3} centre suggests a closer proximity of the two charge compensating hydrogenic ions. If the frequencies in group B of the C_{S3} centre are taken to

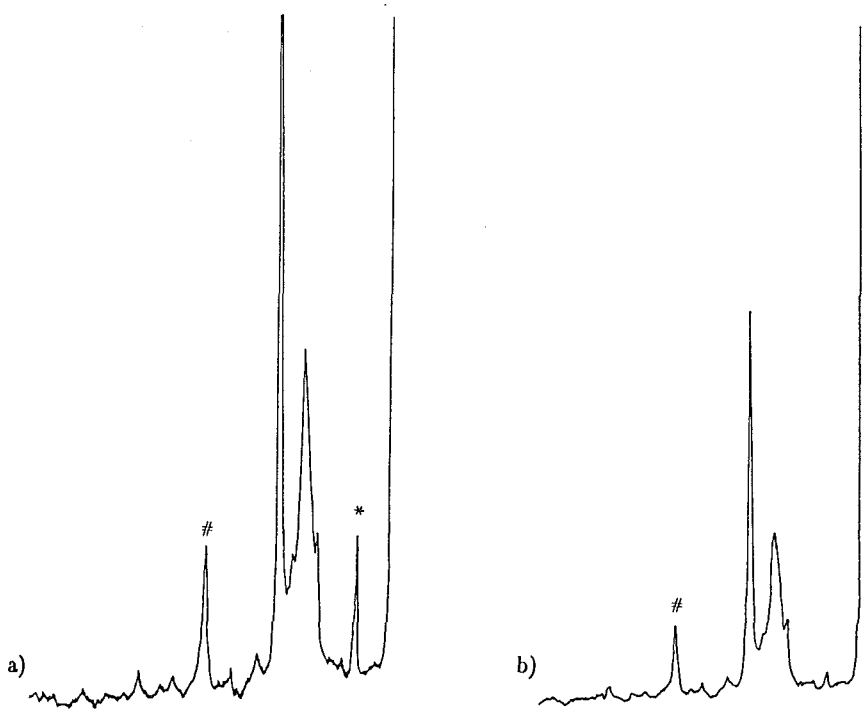

Figure 5.64: 10 K 'zero' order excitation spectrum recorded at 20 mW laser power after laser bleaching at 180 mW for 300 s of a) # the $SrF_2 : Nd^{3+}$ C_{S4} D^- centre line at 17026 cm^{-1} (in air) and b) $*$ its photoproduct line.

be the perturbed C_{4V} local mode frequencies, then the ratio of the average frequency of group B of the C_{S3} centre and the average frequency for the C_{4V} centre is 0.84, which agrees with the ratio of 0.8 obtained for the tetrahedral centre. On this basis the configuration with the second hydrogenic ion at position 5 is proposed for the C_{S3} D^- centre in $SrF_2 : Nd^{3+}$. This model could explain bleaching behaviour when one considers the migration of the hydrogenic ions as shown in Fig. 5.66. As these migrations are reversible, there is expected to be recoverable bleaching between the two orientations of the laser polarisation. As no bleaching is observed for the C_{S3} D^- centre in $SrF_2 : Nd^{3+}$ and only a non recoverable bleaching is found for the C_{S3} D^- centre in $CaF_2 : Nd^{3+}$, this model needs further development. Consideration of the relative magnitudes of the σ and π absorption cross-sections for the two incident laser polarisations is needed to account for the absence of the predicted bleaching behaviour.

A simple model involving three charge compensating ions is proposed for the C_{S4} centres observed in $SrF_2 : Nd^{3+}$. The ratio of the average frequency for group A of the C_{S4} centres and for the tetrahedral centre lines is 0.79 and the ratio of the average frequency for group B of the C_{S4} centres and for the C_{4V} centres is 0.84. These results suggest a close coupling between the interstitial and the substitutional charge compensating hydrogenic ions in the C_{S4} centre. The splitting of the (x, y) component for group A of the C_{S4} centre is 73 cm^{-1} which is similar to the corresponding splitting for group A of the C_{S3} centre. No additional local mode vibronic frequencies were observed suggesting that the two substitutional hydrogenic ions are in either position 5 and 6 or 5 and 8. The splitting of the (x, y) component for group B of the C_{S4} centre is approximately half of the corresponding splitting for group B of the C_{S3} centre. This suggests the position of the third hydrogenic ion could have averaged out the overall effects of the two hydrogenic ions, hence reducing the perturbation on the C_{4V} centre. There is insufficient evidence to distinguish between the two possible positions of the third hydrogenic ion in the C_{S4} centre. The observed bleaching behaviour and the production of its photoproduct could be the result of the migration of the hydrogenic ions in the two models as shown in Figs. 5.67 and 5.68.

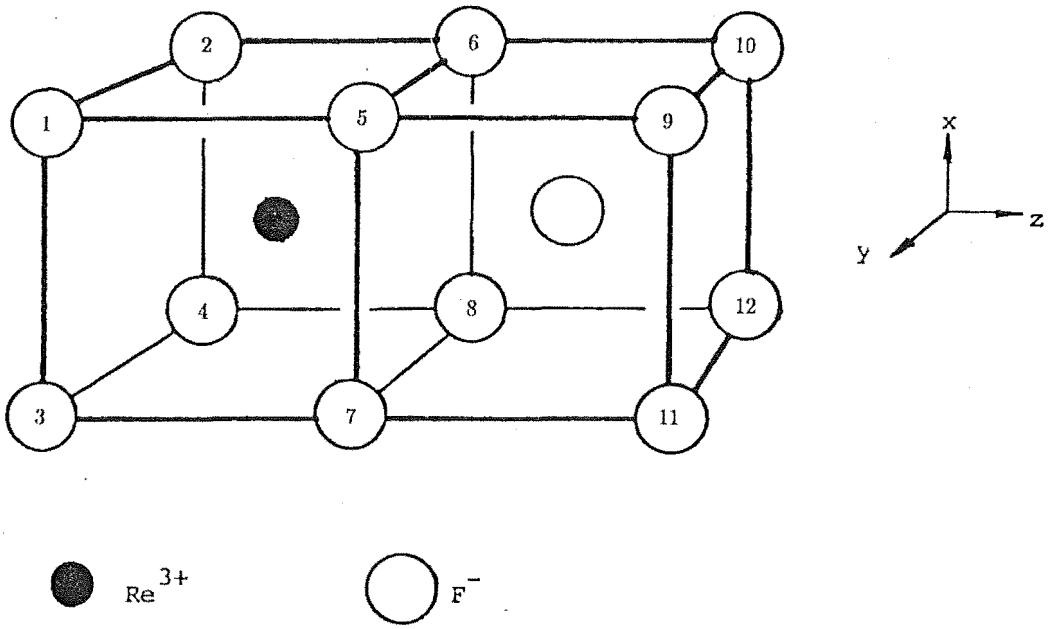

Figure 5.65: Schematic diagram of the C_{4V} symmetry centre with its surrounding F^- ions numbered.

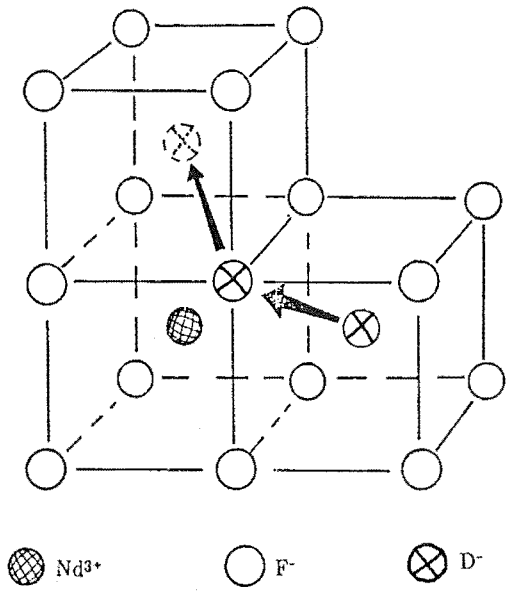

Figure 5.66: Schematic diagram of a possible symmetry centre for the C_{S3} centre involving two charge compensating ions. Arrows indicate the possible migration path for the D^- ions resulting in two identical configurations orthogonal to each other.

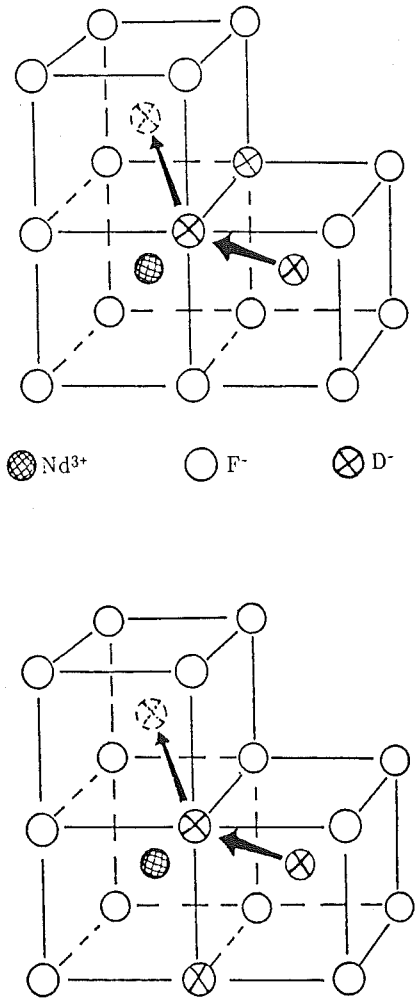

Figure 5.67: Schematic diagram of a possible symmetry centre for the C_{S4} centre involving three charge compensating ions. Arrows indicate the possible migration path for the D^- ions resulting in two identical configurations orthogonal to each other.

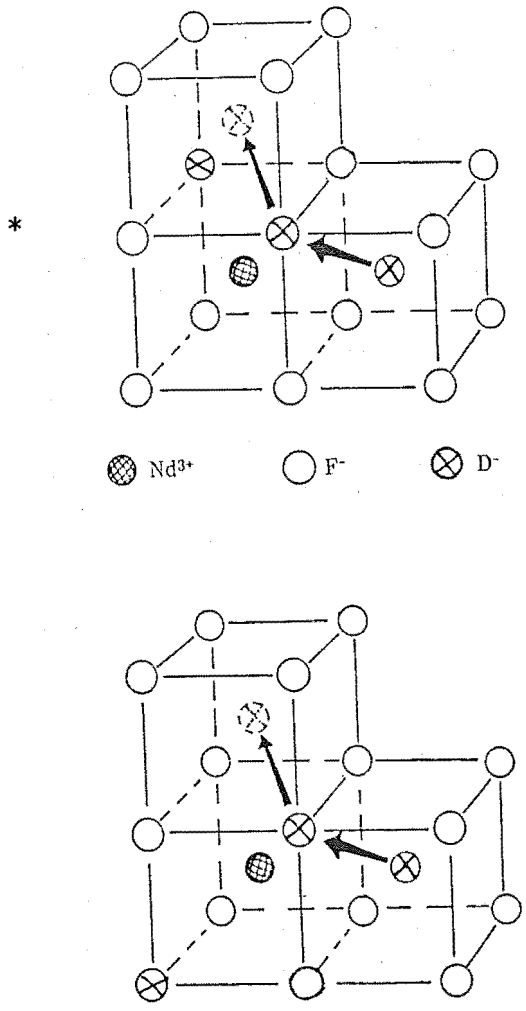

Figure 5.68: Schematic diagram of a possible symmetry centre for the C_{S4} centre involving three charge compensating ions. Arrows indicate the possible migration path for the D^- ions resulting in two slightly different configurations; $*$ is considered to be the photoproduct of the original configuration.

State		T^-		D^-		H^-	
$^4I_{9/2}$	Z_1	0		0		0	
	Z_2	101.4	(± 1.6)	98.1	(± 1.6)	109.8	(± 1.6)
	Z_3	213.3	(± 1.8)	212.6	(± 1.8)	231.7	(± 1.8)
	Z_4	344.3	(± 1.8)			268.4 ?	(± 1.8)
				659.3	(± 1.6)		
	Z_5	688.1	(± 1.6)	691.0	(± 1.6)	739.8	(± 1.6)
$^4I_{11/2}$	Y_1	2004.6	(± 1.3)	2004.8	(± 1.3)		
	Y_2	2080.6	(± 1.8)	2080.0	(± 1.8)		
	Y_3	2121.3	(± 1.8)	2120.6	(± 1.8)		
	Y_4	2129.2	(± 1.6)	2128.5	(± 1.6)		
	Y_5	2310.9	(± 2.3)	2312.0	(± 2.3)		
	Y_6	2426.0	(± 1.6)	2426.2	(± 1.6)		
$^4F_{3/2}$	R_1	11501.3	(± 1.6)	11500.6	(± 1.6)	11500.6	(± 1.6)
	R_2						
$^2H_{11/2}$	C_1	15972	(± 2)	15970	(± 2)		
	C_2	16002	(± 2)	16002	(± 2)		
	C_3	16061	(± 2)	16060	(± 2)		
	C_4	16076	(± 2)	16076	(± 2)		
	C_5	16150	(± 2)	16149	(± 2)		
	C_6	16208	(± 2)	16207	(± 2)		
$^4G_{5/2}$,	D_1	17109	(± 2)	17109	(± 2)	17107	(± 2)
$^2G_{7/2}$	D_2	17246	(± 2)	17246	(± 2)		
	D_3	17266	(± 2)	17265	(± 2)		
	D_4	17448	(± 3)	17461	(± 3)		
	D_5	17467	(± 5)	17470	(± 5)		
	D_6	17459	(± 5)	17483	(± 5)		
	D_7			17529	(± 3)		

Table 5.7: 10 K energy levels (in air cm^{-1}) of the C_{SI} hydrogenic centres in $SrF_2 : Nd^{3+}$. ? Tentative assignment.

State		$SrF_2 : Nd^{3+}$ T^-		$SrF_2 : Nd^{3+}$ D^-		$SrF_2 : Nd^{3+}$ H^-		$CaF_2 : Nd^{3+}$ D^-	
$^4I_{9/2}$	Z_1	0		0		0		0	
	Z_2	115.0	(± 1.6)	114.2	(± 1.6)	113.8	(± 1.6)	143.4	(± 1.6)
	Z_3	238.6	(± 1.8)	240.4	(± 1.8)	238.7	(± 1.8)	286.4	(± 1.8)
	Z_4								
				716.1	(± 1.8)	657.5	(± 1.8)	834.5	(± 1.8)
	Z_5	726.0	(± 1.6)	727.7	(± 1.6)	709.8	(± 1.6)	888.5	(± 1.6)
$^4I_{11/2}$	Y_1	2005.8	(± 1.6)	2007.2	(± 1.6)	2008.2	(± 1.6)	2029.6	(± 1.6)
	Y_2	2110.3	(± 1.8)	2110.8	(± 1.8)	2108.2	(± 1.8)	2162.2	(± 1.8)
	Y_3	2131.2	(± 1.8)	2131.7	(± 1.8)	2128.3	(± 1.8)	2188.1	(± 1.8)
	Y_4	2159.0	(± 1.6)	2157.8	(± 1.6)	2156.1	(± 1.6)	2224.1	(± 1.6)
	Y_5	2340.9	(± 2.3)	2339.7	(± 2.3)	2298.7	(± 2.3)	2432.9	(± 2.3)
	Y_6	2464.1	(± 1.6)	2461.4	(± 1.6)	2458.1	(± 1.6)	2575.8	(± 1.6)
$^4F_{3/2}$	R_1	11468.3	(± 1.6)	11468.8	(± 1.6)	11467.5	(± 1.6)	11467.8	(± 1.6)
	R_2								
$^2H_{11/2}$	C_1			15959	(± 2)			15961	(± 2)
	C_2			15997	(± 2)				
	C_3			16053	(± 2)				
	C_4			16074	(± 2)				
	C_5			16142	(± 2)				
	C_6			16202	(± 2)				
$^4G_{5/2}$,	D_1	17061	(± 2)	17063	(± 2)	17059	(± 2)	17030	(± 2)
$^2G_{7/2}$	D_2			17078	(± 2)				
	D_3			17198	(± 2)				
	D_4			17218	(± 3)				
	D_5								
	D_6			17427	(± 5)				
	D_7			17509	(± 3)				

Table 5.8: 10 K energy levels (in air cm^{-1}) of the C_{S3} hydrogenic centres in $SrF_2 : Nd^{3+}$ and $CaF_2 : Nd^{3+}$.

State		$SrF_2 : Nd^{3+}$ D^- C_{S4}		$H1$		$H2$	
$^4I_{9/2}$	Z_1	0		0		0	
	Z_2	118.9	(± 1.6)	72.2	(± 1.6)		
	Z_3	250.6	(± 1.8)	165.3	(± 1.8)		
	Z_4	732.1 ?	(± 1.8)				
	Z_5	750.4 ?	(± 1.8)	631.6	(± 1.8)		
		765.3 ?	(± 1.6)				
$^4I_{11/2}$	Y_1			1979.1	(± 1.6)		
	Y_2			1994.5	(± 1.8)		
	Y_3			2045.6	(± 1.8)		
	Y_4						
	Y_5			2074.1	(± 1.6)		
	Y_6						
$^4F_{3/2}$	R_1	11438.8	(± 1.6)	11492.9	(± 1.6)	11489.6	(± 1.6)
	R_2						
$^2H_{11/2}$	C_1			15928	(± 2)		
	C_2						
	C_3						
	C_4						
	C_5						
	C_6						
$^4G_{5/2}$,	D_1	17026	(± 2)	17093	(± 2)	17105	(± 2)
$^2G_{7/2}$	D_2	17154	(± 2)				
	D_3	17164	(± 2)				
	D_4						
	D_5						
	D_6						
	D_7						

Table 5.9: 10 K energy levels (in air cm^{-1}) of the D^- C_{S4} , H^- $H1$ and H^- $H2$ centres in $SrF_2 : Nd^{3+}$. ? Tentative assignment.

5.5 Other Hydrogenic Centres

The fluorescence spectra of two new H^- centres were observed in hydrogenated $SrF_2 : Nd^{3+}$ crystals. The $R_1 \rightarrow Z_1$ transitions of these two centres are very close to each other at 8701.1 and 8703.5 nm, hence the centres are labelled *H1* and *H2*. Their extremely weak fluorescence and the absence of any absorption lines suggest a very low abundance of these centres in the crystals studied. Fig. 5.69 shows the fluorescence spectrum of the combined *H1* and *H2* centres and the energy levels are presented in Fig. 5.9. It was impossible to resolve the *H1* centre from the *H2* by selective excitation because of an overlapping of their energy levels in the excited multiplets, or possibly as a result of coupling between these two centres. It was observed that both the *H1* and *H2* centres possess bleaching behaviour, and the bleaching of one centre subsequently caused the recovery of the other centre. Fig. 5.70 shows the bleaching and recovery behaviour of the *H1* and *H2* centres for a $\langle 100 \rangle$ orientated crystal. The geometry of the equipment used for this bleaching study was the same as that used in the polarisation studies for the C_{4V} symmetry centre. The bleaching of the *H1* centre by the excitation of the energy level at 17093 cm^{-1} could be restored by exciting the energy level of the *H2* centre at 17105 cm^{-1}. No recovery of the bleached fluorescence was observed when the polarisation of the laser was varied between the two possible orthogonal orientations. Fig. 5.71 shows the bleaching and recovery characteristics of these two centres. The differences in recovery and decay rates of the two centres suggest that there is more than one mechanism involved in the interconversion between these centres.

No local mode vibronic lines were observed because of the extremely weak fluorescence of the *H1* and *H2* centres. A method of enhancing the abundance of these centres is required before more useful data can be obtained.

5.6 The A' Centre

The fluorescence spectrum of the A' centre was only observed in $CaF_2 : Nd^{3+}$ and $SrF_2 : Nd^{3+}$ crystals that had been hydrogenated or oxygenated and is presented in Figs. 5.72 to 5.75. The wavelength of the $R_1 \rightarrow Z_1$ transition is found to be the same for all for hydrogenation treatment with different isotopes suggesting a strong possibility of an oxygen charge compensation centre.

The energy levels of the two lowest multiplets in $CaF_2 : Nd^{3+}$ verify the results of Kariss et al. (1965) but contradict the results for the A centre reported by Toledano (1972). The energy separation of the Z_2 and Z_1 levels is 324 cm^{-1} for $CaF_2 : Nd^{3+}$ and 355 cm^{-1} for $SrF_2 : Nd^{3+}$. The energy levels are presented in Table 5.10 together with the results of Kariss and

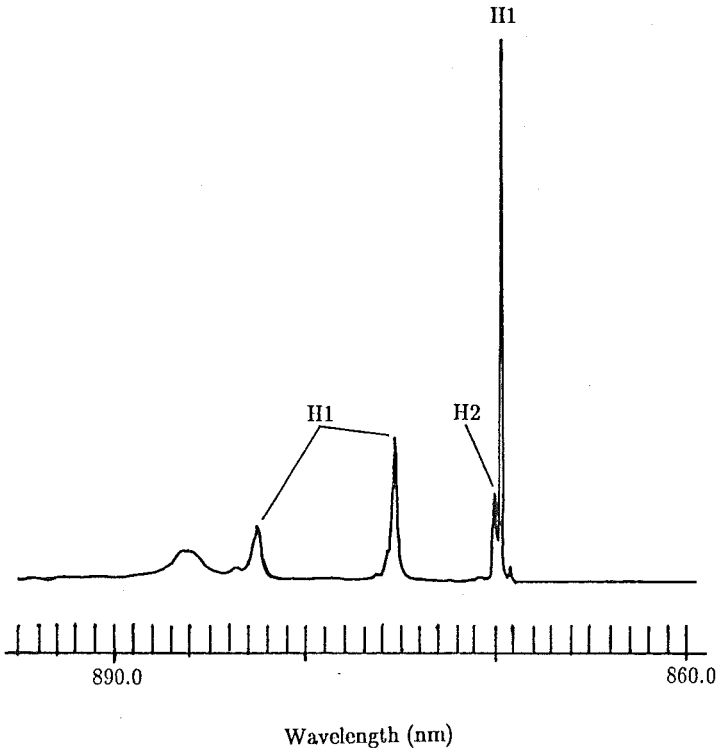

Figure 5.69: 10 K fluorescence spectrum of the $SrF_2 : Nd^{3+}$ H^- $H1$ and H^- $H2$ centres.

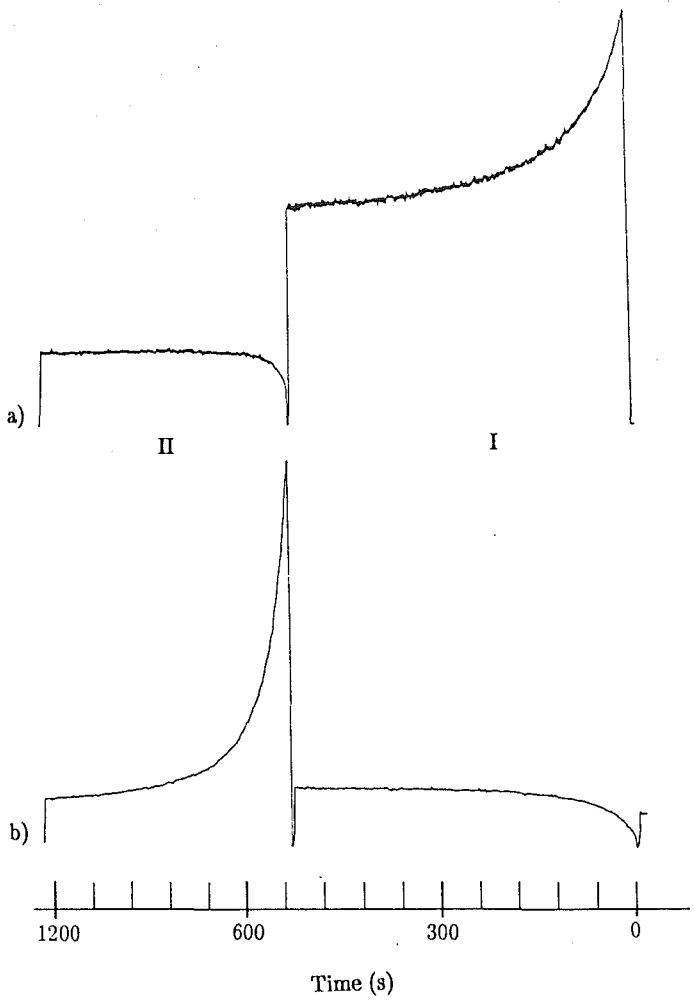

Figure 5.70: Bleaching and recovering curves of a) the 8669.2 nm H^- $H1$ line and b) the 8702 nm H^- $H2$ line for the laser excitation at (I) 17105 cm^{-1} and (II) 17093 cm^{-1}.

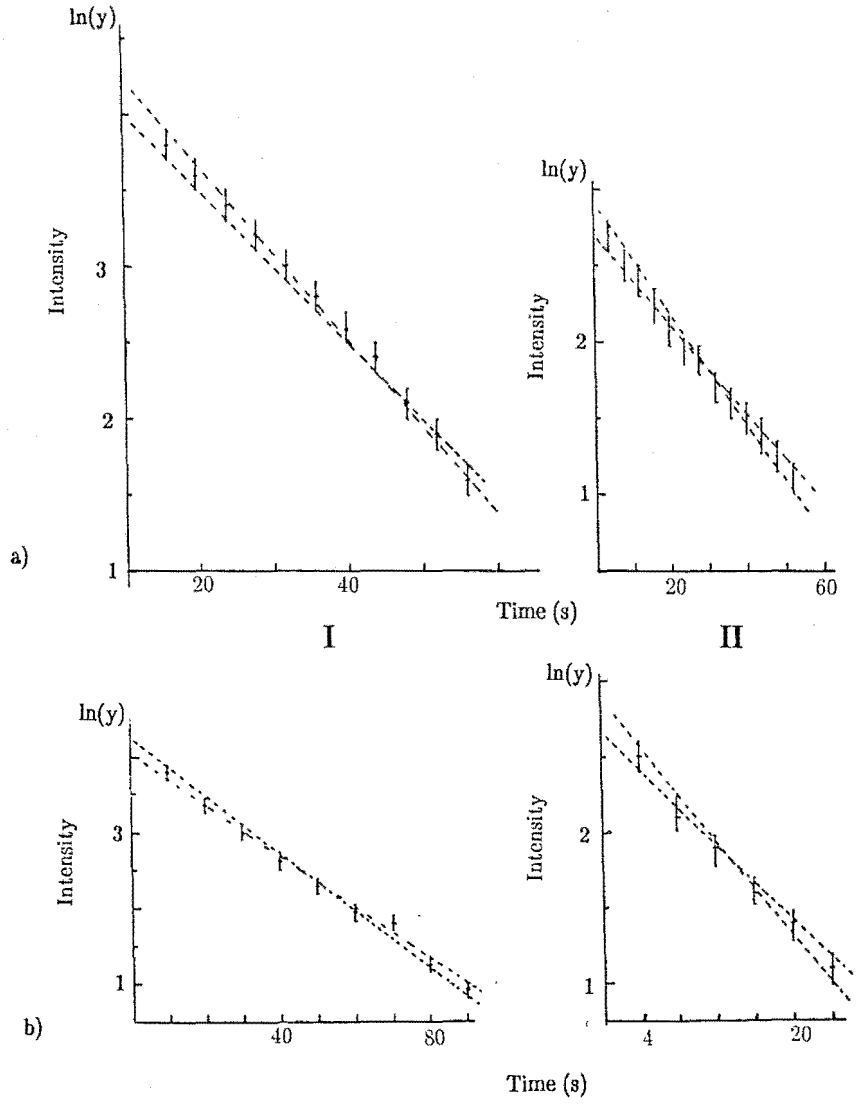

Figure 5.71: Bleaching (I) and recovery (II) plots of the fluorescence for the $SrF_2 : Nd^{3+}$ H^- $H1$ (8699.2 nm) and H^- $H2$ (8702 nm) centres. Time constants for a) (I) 18.9 $\pm$2.5 s, (II) 30.3 $\pm$10.1 s; b) (I) 55.6 $\pm$6.3 s, (II) 14.3 $\pm$4.4 s.

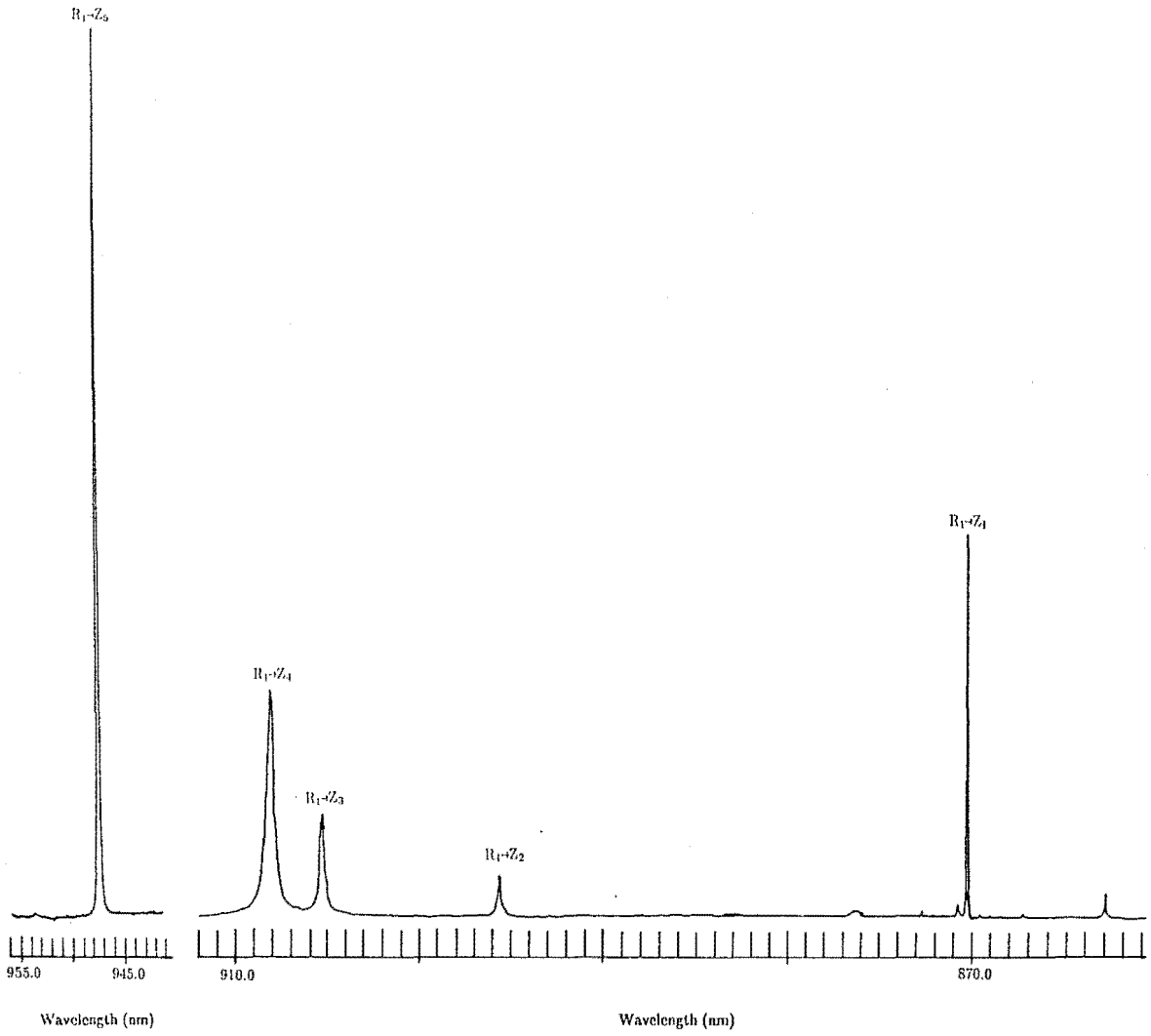

Figure 5.72: 10 K fluorescence spectrum for the $R_1 \rightarrow Z_{1,2,3,4,5}$ transitions of the $CaF_2 : Nd^{3+}$ A' centre.

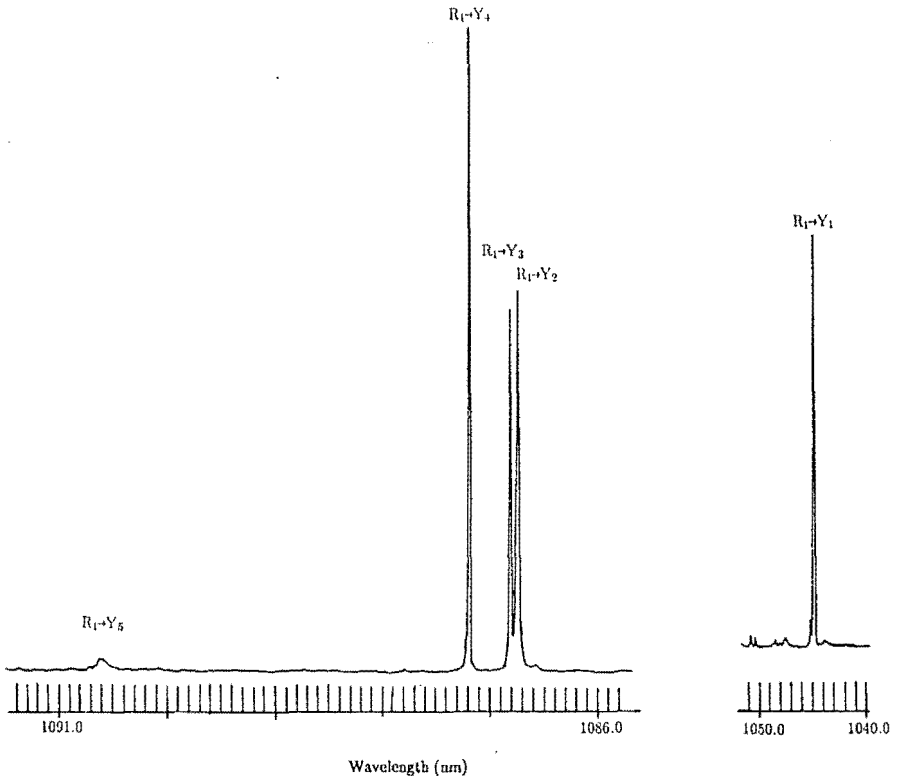

Figure 5.73: 10 K fluorescence spectrum for the $R_1 \rightarrow Y_{1,2,3,4,5,6}$ transitions of the $CaF_2 : Nd^{3+}$ A' centre.

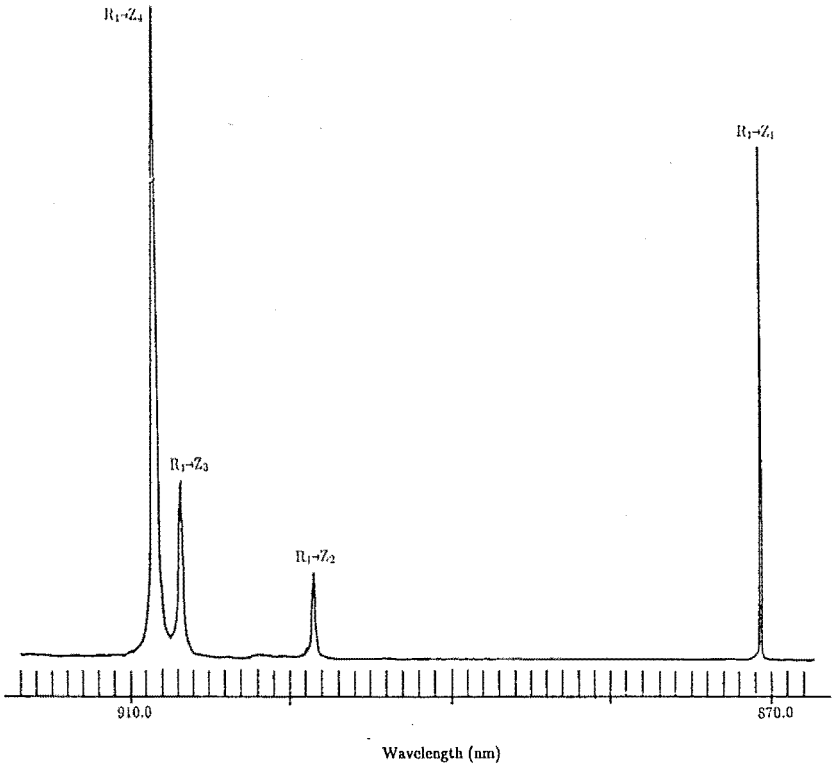

Figure 5.74: 10 K fluorescence spectrum for the $R_1 \rightarrow Z_{1,2,3,4,5}$ transitions of the $SrF_2 : Nd^{3+}$ $A^{'}$ centre.

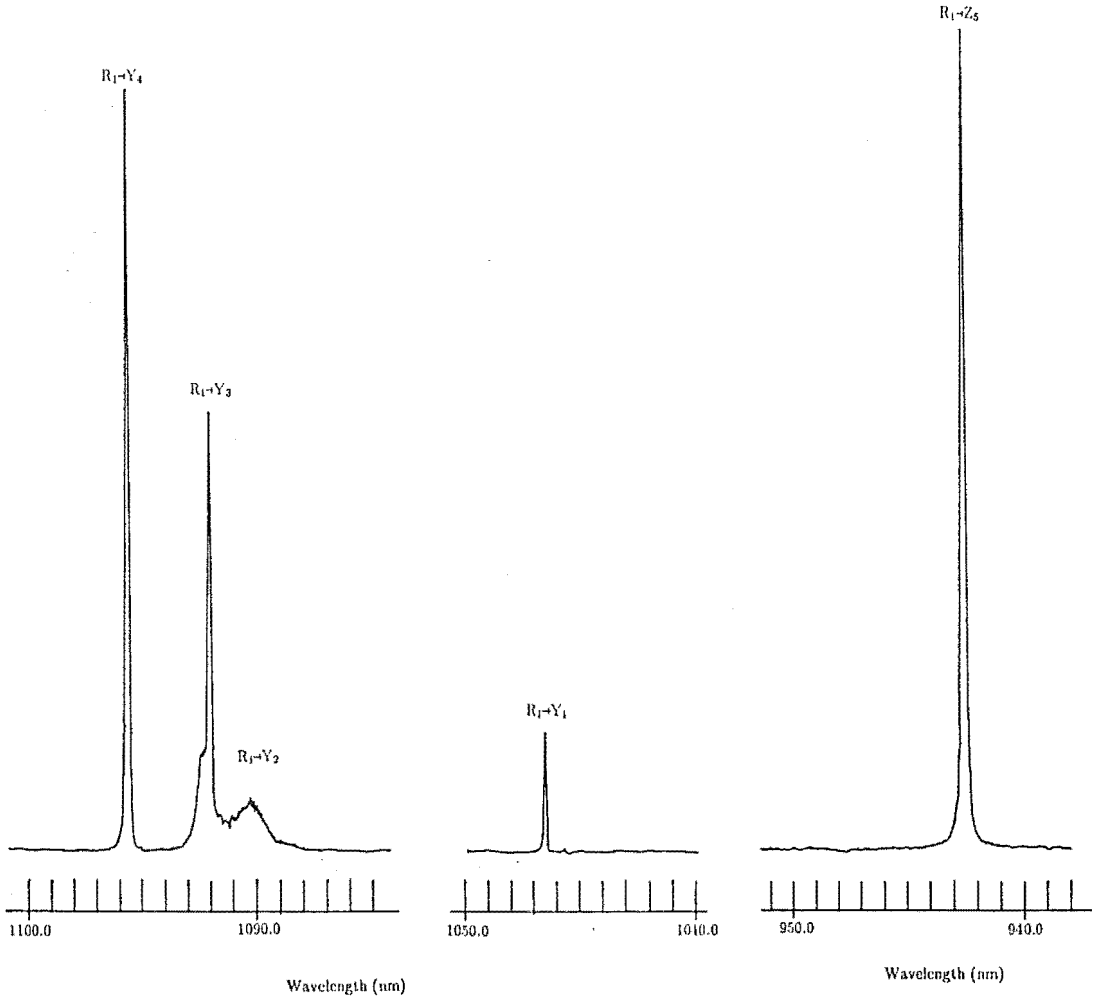

Figure 5.75: 10 K fluorescence spectrum for the $R_1 \rightarrow Y_{1,2,3,4,5,6}$ transitions of the $SrF_2 : Nd^{3+}$ $A^{'}$ centre.

Toledano for comparison.

In contradiction to Toledano (1972), the $Z_1 \rightarrow R_1$ transition was not observed in the optical absorption spectrum of the $^4F_{3/2}$ multiplet in $CaF_2 : Nd^{3+}$. The relatively strong absorption line observed in the 870 nm region belonged to the hydrogenic C_{S1} centre. This was confirmed by the observation of isotope shifts for different hydrogenic ions, as shown in Fig. 5.39.

In the D multiplet, the A' centre was characterised by two very strong absorption lines at 17173 and 17224.5 cm^{-1} for $CaF_2 : Nd^{3+}$ and at 17217 and 17226 cm^{-1} for $SrF_2 : Nd^{3+}$. Figs. 5.76 and 5.77 show the excitation spectra of the A' centre in $SrF_2 : Nd^{3+}$. It was observed that the transmitted laser intensity was greatly reduced when the laser was in resonance with either one of the two absorption lines, as expected for strong absorption lines.

The presence of the A' centre in crystals that had short periods of hydrogenation treatment suggests that it could be a single ion charge compensating centre. These results confirm the observations of Kariss and indicate that the centre observed by Toledano is not identical to the observed A' centre. It was therefore not surprising to observe no intensity variation in the polarisation studies of $\langle 111 \rangle$ and $\langle 100 \rangle$ oriented crystals. A detailed discussion of the expected intensity variation in the polarisation study of a trigonal symmetry centre can be found in Cockroft (1987). Kask et al. (1966) have proposed several models for oxygen charge compensating centres but additional data, possibly from an optical Zeeman experiment, are needed before the configuration of this centre can be confirmed.

The fluorescence lifetime of the $R_1 \rightarrow Z_1$ transition for the A' centre is 3 ($\pm 10\%$) ms for $CaF_2 : Nd^{3+}$ and 2.4 ($\pm 10\%$) ms for $SrF_2 : Nd^{3+}$. The $CaF_2 : Nd^{3+}$ result agrees with the fluorescence lifetime of 2.3 ms observed by Kariss et al. (1965) at 77 K. The absence of energy upconversion in the A' centre could be attributed to the small absorption cross section of this centre in the R multiplet.

5.7 The M and N F^- centres

5.7.1 Introduction

The M and N F^- centres in $CaF_2 : Nd^{3+}$ observed by Voron'ko et al. (1966) and Smalley (1971) in their optical absorption studies are normally attributed to cluster centres and are determined by EPR (Kask et al. 1967) to be orthorhombic in symmetry. The M and N centres were both found to be present at a Nd^{3+} ion concentration of 0.05% and the M centre was still apparent at 0.02% concentration. Thermal treatment, by heating the crystal to 850 ^oC in a vacuum, caused the disintegration of the N centre and a reduction in the abundance of the M centre. This supports the hypothesis that the N centre is a more complex cluster centre than the M centre. The

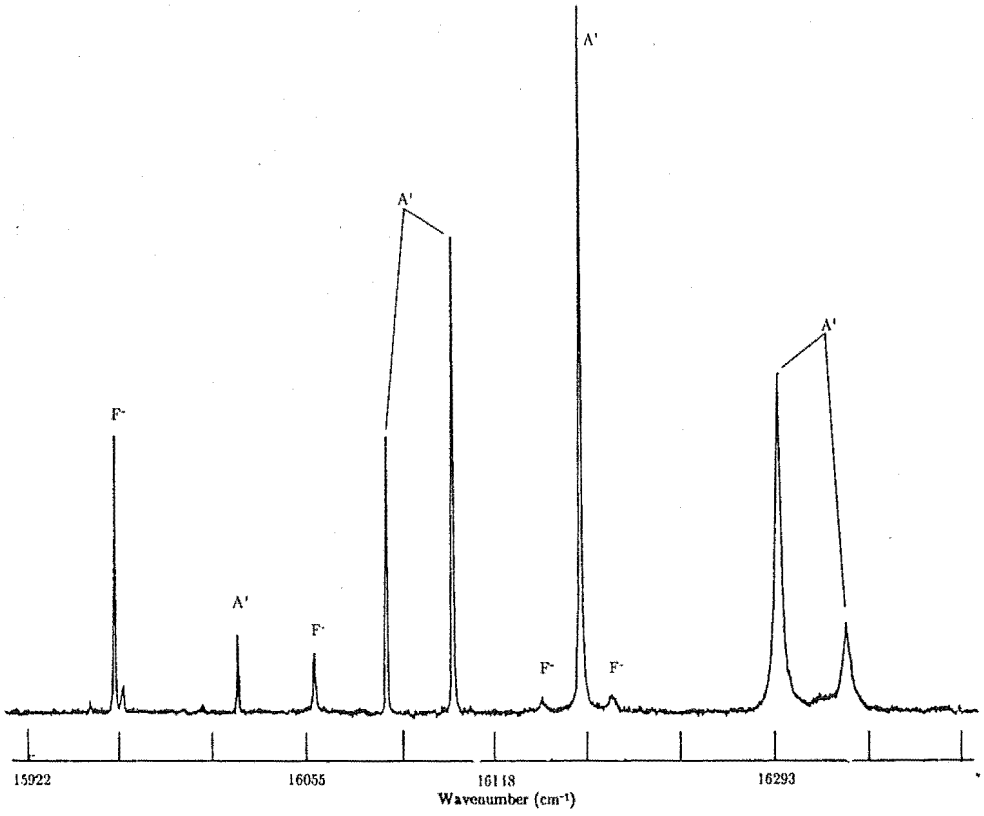

Figure 5.76: 10 K C multiplet excitation spectrum of the $SrF_2 : Nd^{3+}$ A' centre.

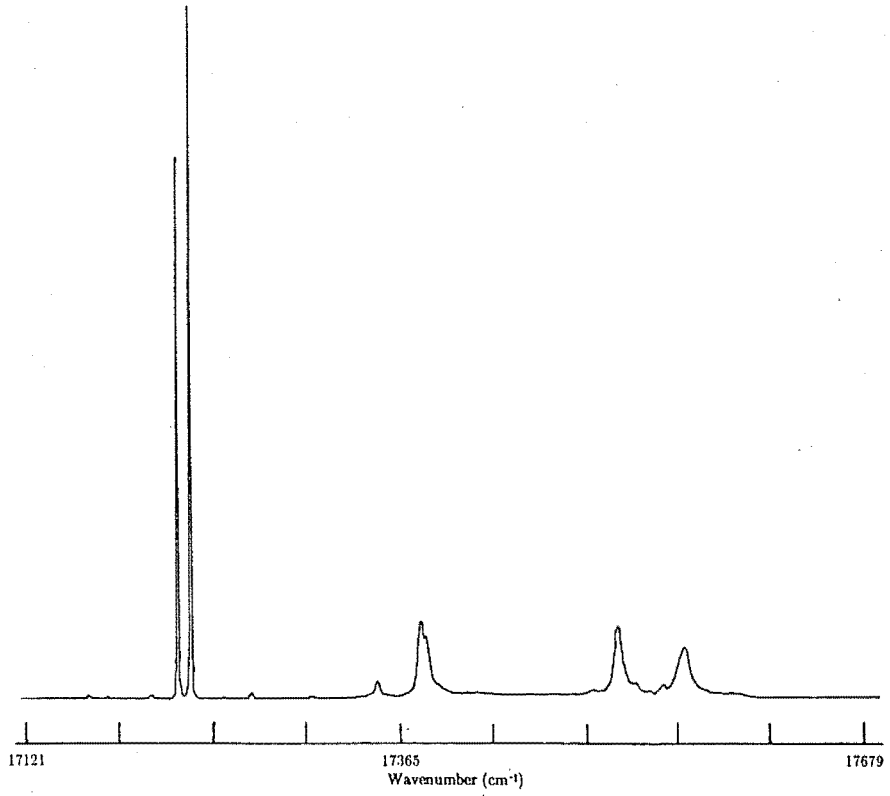

Figure 5.77: 10 K D multiplet excitation spectrum of the $SrF_2 : Nd^{3+}$ A' centre.

absorption spectra of transitions to multiplets of low J value are the simplest to analyse, hence the R multiplet was chosen. The results show that the energy difference between the R_1 and R_2 levels is 42.2 ($\pm$ 3.2) and 39.7 ($\pm$ 3.2) cm^{-1} for the M and N centres respectively. A model involving two Nd^{3+} ions has been proposed for the M centre and an even more complex model for the N centre involving four to six Nd^{3+} ions (Osiko 1965, Osiko and Shcherbakov 1971), as shown in Fig. 5.78, but so far neither model has been confirmed.

The optical absorption spectrum of $SrF_2 : Nd^{3+}$ shows only one dominant single ion centre at low concentrations, namely the C_{4V} symmetry centre. An EPR study (Kask and Kornienko 1968) revealed the presence of orthorhombic and cubic symmetry centres in $SrF_2 : Nd^{3+}$ but as yet no direct optical observation of these centres has been reported.

5.7.2 The M centre in $CaF_2 : Nd^{3+}$

The fluorescence spectrum of the M centre is presented in Fig. 5.79. The assignment of the energy levels of the ^4I multiplets was completed with the help of the energy upconversion data (Chapter 8) and is listed in Table 5.11.

The fluorescence intensity pattern was characterised by the two intense electronic transitions, $R_1 \rightarrow Z_1$ and $R_1 \rightarrow Z_2$, separated by 35.3 ($\pm$ 1.6) cm^{-1}, and all the expected energy levels of the Z and Y multiplets were observed. Figs. 6.15 and 6.16 show that in the M centre the strong infrared fluorescence from the R_1 energy level was accompanied by an extremely weak fluorescence from the C and D levels when the D multiplet was excited. No noticeable variation of the fluorescence intensity pattern was found in the polarisation studies of the $\langle 100 \rangle$ and $\langle 111 \rangle$ oriented crystals.

Excitation spectra as shown in Figs. 5.80 and 5.81 reveal an unusual double line pattern on the three $^4G_{5/2}$ energy levels within D multiplet. The energy difference between the two peaks of the double line pattern is 1 cm^{-1} and it is identical for all three energy levels. This splitting was also observed in the corresponding optical absorption spectrum. The excitation spectrum of the upconverted fluorescence also shows this pattern but with a slightly different intensity distribution. This pattern cannot be explained by the lifting of the Kramers' degeneracy of the energy levels since such a splitting is not observed in the R or the L multiplets. The results obtained for the double rare earth doped crystals, as discussed in Chapter 8, suggest that this pattern is due to coupling of the excited energy levels of the two rare earth ions within the M centre (i.e. a pair splitting).

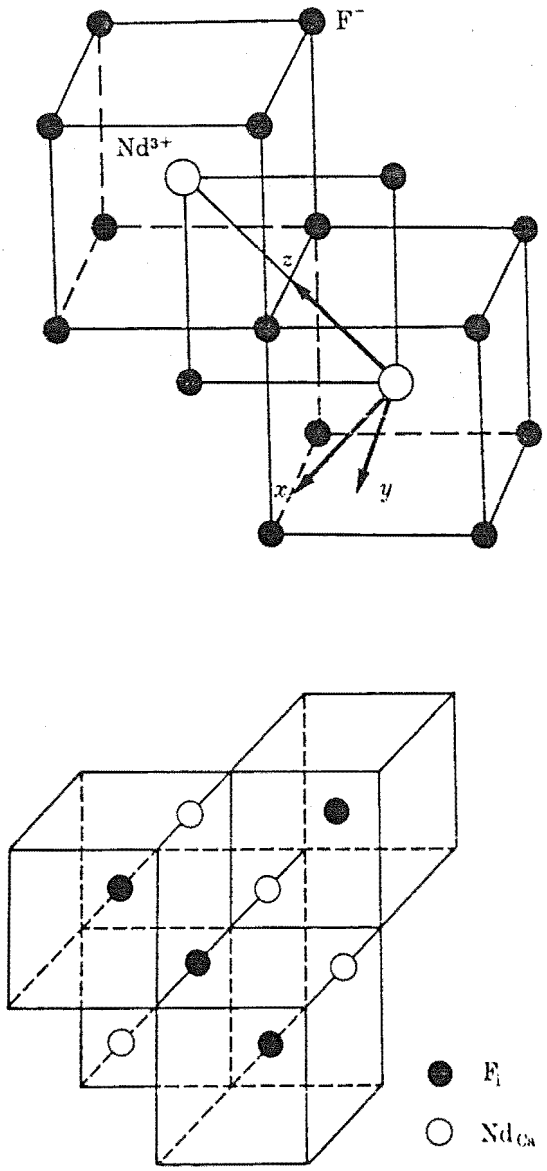

Figure 5.78: Schematic diagram of a possible configuration for the M and N symmetry centres. The configuration having two Nd^{3+} ions (top) has been proposed for the M centre by Osiko (1965).

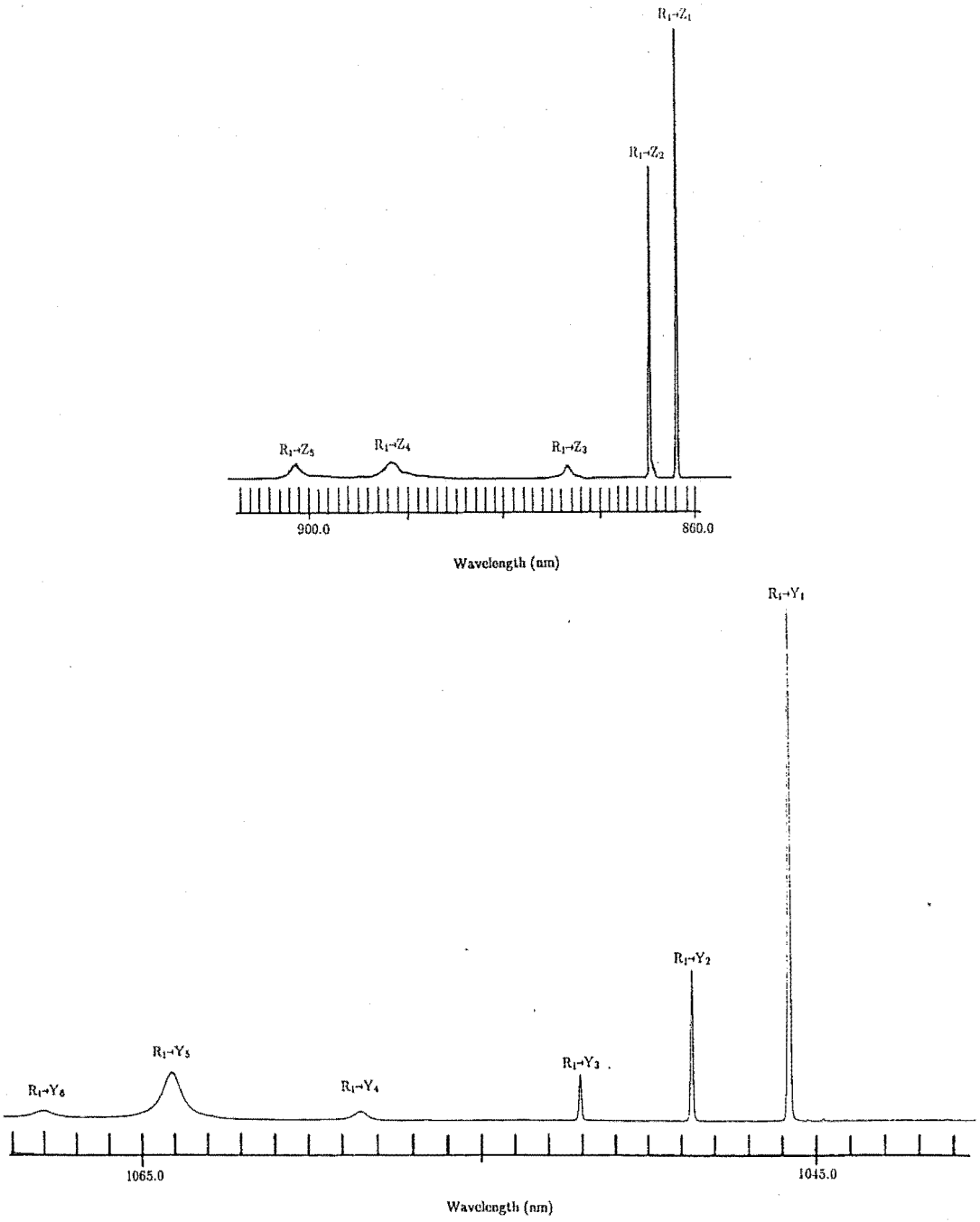

Figure 5.79: 10 K fluorescence spectrum for the $R_1 \rightarrow Z_{1,2,3,4,5}$ and $Y_{1,2,3,4,5,6}$ transitions of the $CaF_2 : Nd^{3+}$ M centre.

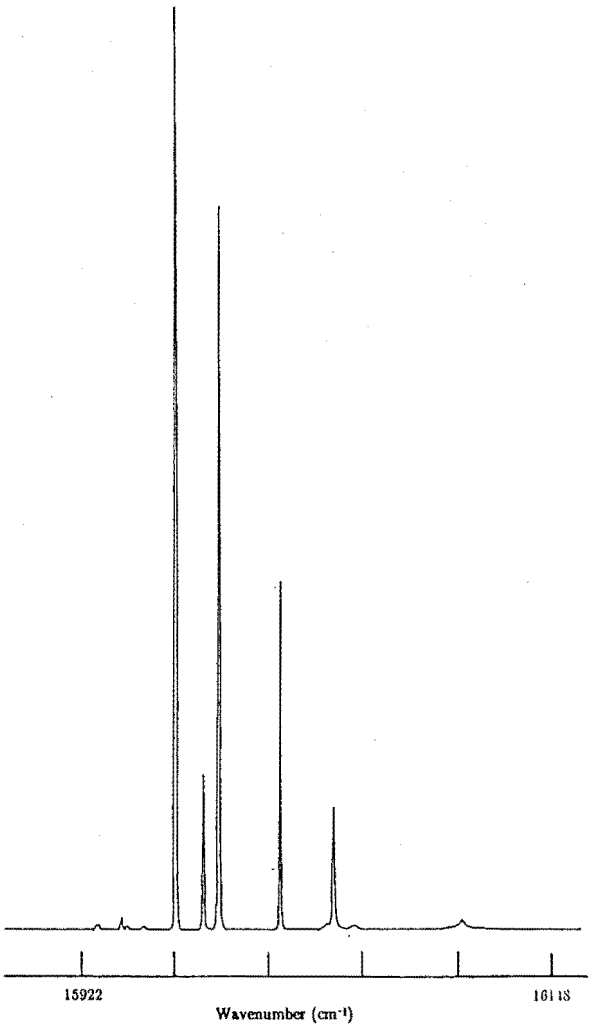

Figure 5.80: 10 K C multiplet excitation spectrum of the $CaF_2 : Nd^{3+}$ M centre.

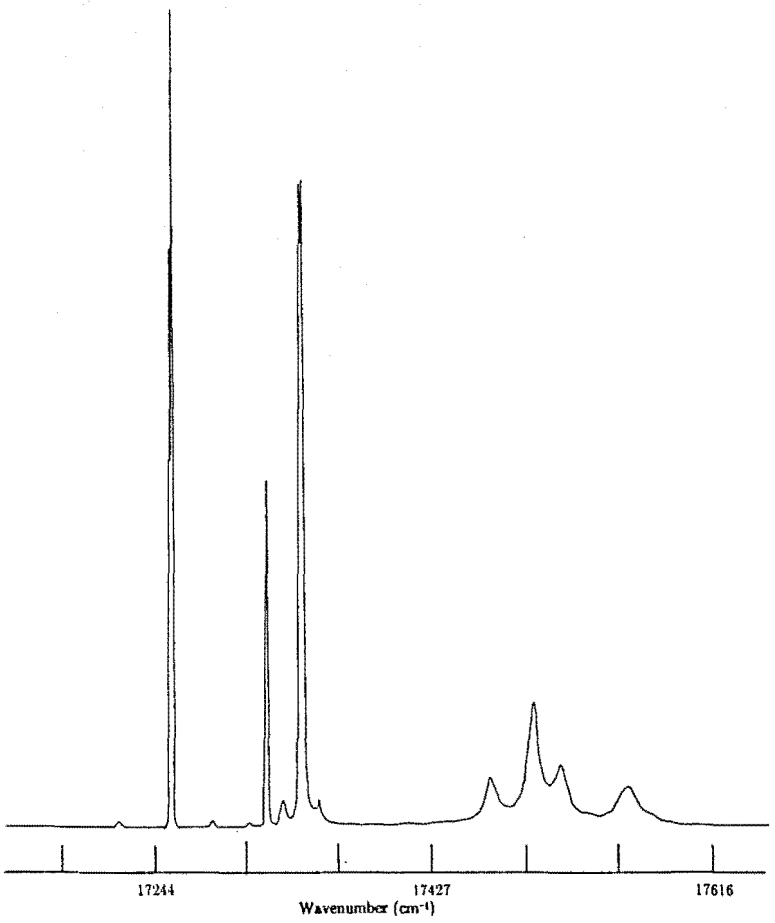

Figure 5.81: 10 K D multiplet excitation spectrum of the $CaF_2 : Nd^{3+}$ M centre.

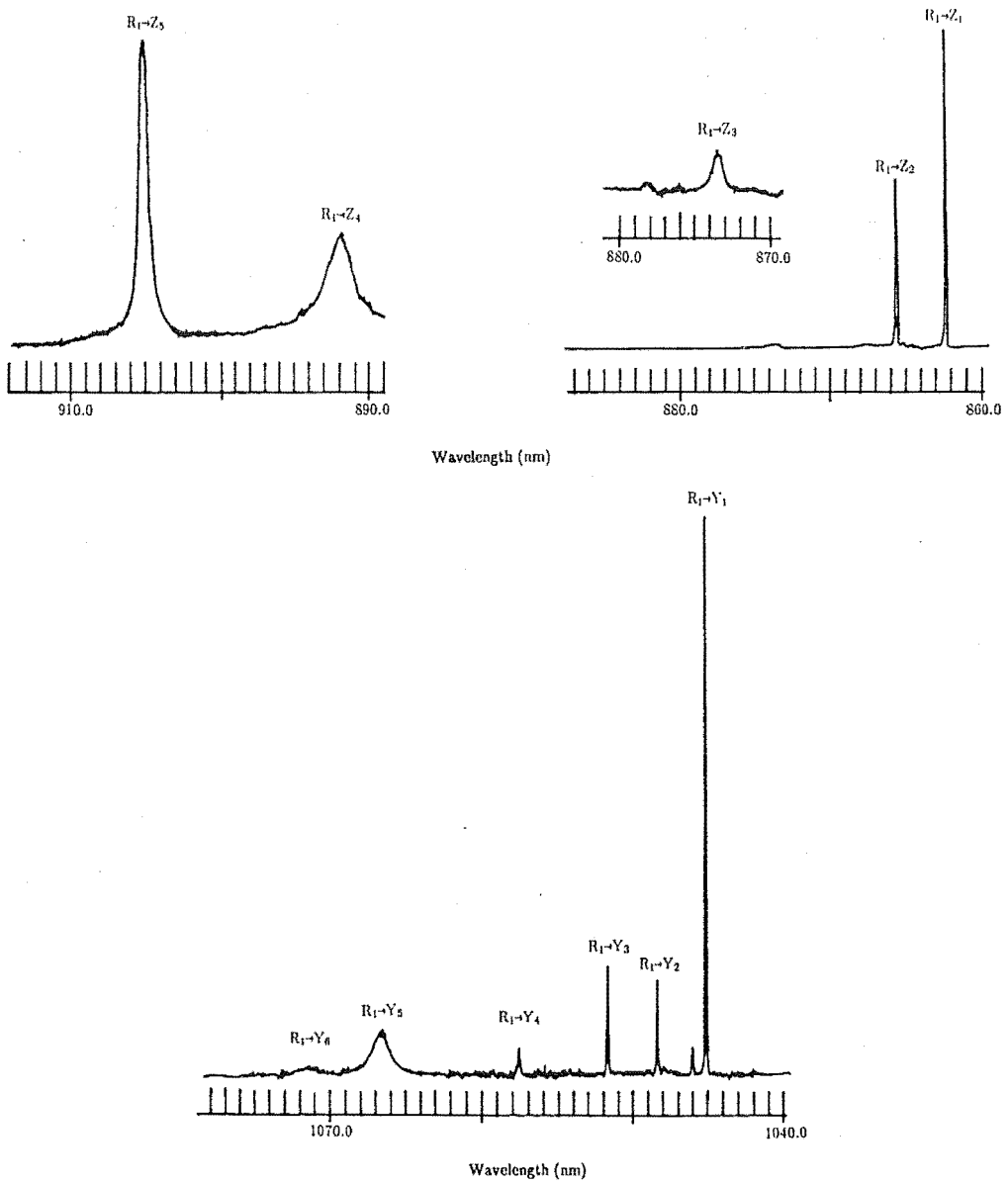

Figure 5.82: 10 K fluorescence spectrum for the $R_1 \rightarrow Z_{1,2,3,4,5}$ and $Y_{1,2,3,4,5,6}$ transitions of the $CaF_2 : Nd^{3+}$ N centre.

5.7.3 The N centre in $CaF_2 : Nd^{3+}$

The fluorescence spectra of this centre is presented in Fig. 5.84. The assignment of the energy levels of the ^4I multiplets was aided by the energy upconversion data and is listed in Table 5.12.

The fluorescence pattern of the N centre is very similar to that of the M centre suggesting a similar symmetry configuration for both of them. The comments made above for the M F^- centre are equally valid for the N centre, except that the energy difference between the Z_1 and Z_2 levels is 40.5 ($\pm$ 1.5) cm^{-1}.

The excitation spectra in Figs. 5.83 and 5.84 show the double line pattern for the D_1 and D_2 energy levels of the D multiplet, whereas the third energy level D_3, has a broad line profile. The energy difference between the two peaks of the double line pattern is 1 cm^{-1} for the D_1 and D_2 energy levels. A similar intensity pattern was observed in the excitation spectrum of the upconverted fluorescence as shown in Fig. 5.84. The different intensity distribution of these patterns in the excitation spectrum of the infrared fluorescence and the upconverted fluorescence could be attributed to the varying efficiency of the upconversion process for each energy level.

5.7.4 Other double rare earth ion centres in $CaF_2 : Nd^{3+}$

The fluorescence spectra of four new two-ion centres were observed in $CaF_2 : Nd^{3+}$. The similarity of their intensity patterns to the M centre and their continued presence after thermal treatment led to them being labelled and grouped within the M family as $M1$ to $M4$. However, their presence was not observed in any of the optical absorption spectra. Figs. 5.85 and 5.86 are a representative example of the fluorescence spectrum of these centres and their energy levels are listed in Table 5.14.

Energy upconversion was observed in the $M1$ and $M2$ centres but it was not possible to separate the two upconverted fluorescence spectra cleanly. This could be attributed to the coincidence of their crystal field components in the excited multiplet and the close similarity of these two centres which could also lead to cross relaxation in their upconversion processes. Energy upconversion is expected for the $M3$ and $M4$ centres even though observation of this is yet to be obtained.

5.7.5 Double rare earth ion centres in $SrF_2 : Nd^{3+}$

The fluorescence spectra of three new two-ion centres were observed in $SrF_2 : Nd^{3+}$. Their intensity patterns were very similar to that of the M centre found in $CaF_2 : Nd^{3+}$ which led to them being labelled and associated with

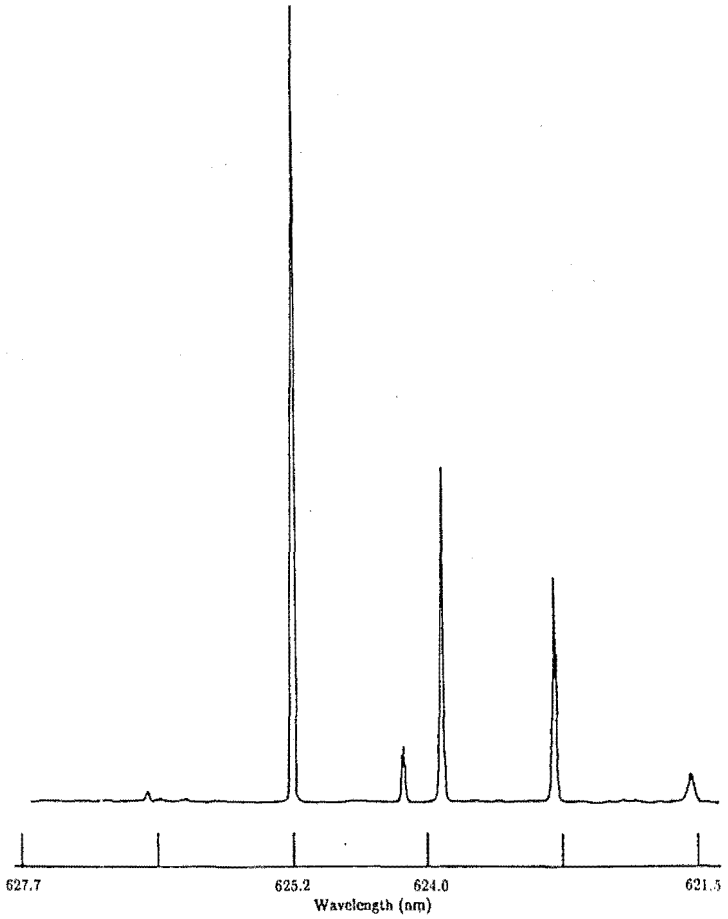

Figure 5.83: 10 K C multiplet excitation spectrum of the $CaF_2 : Nd^{3+}$ N centre.

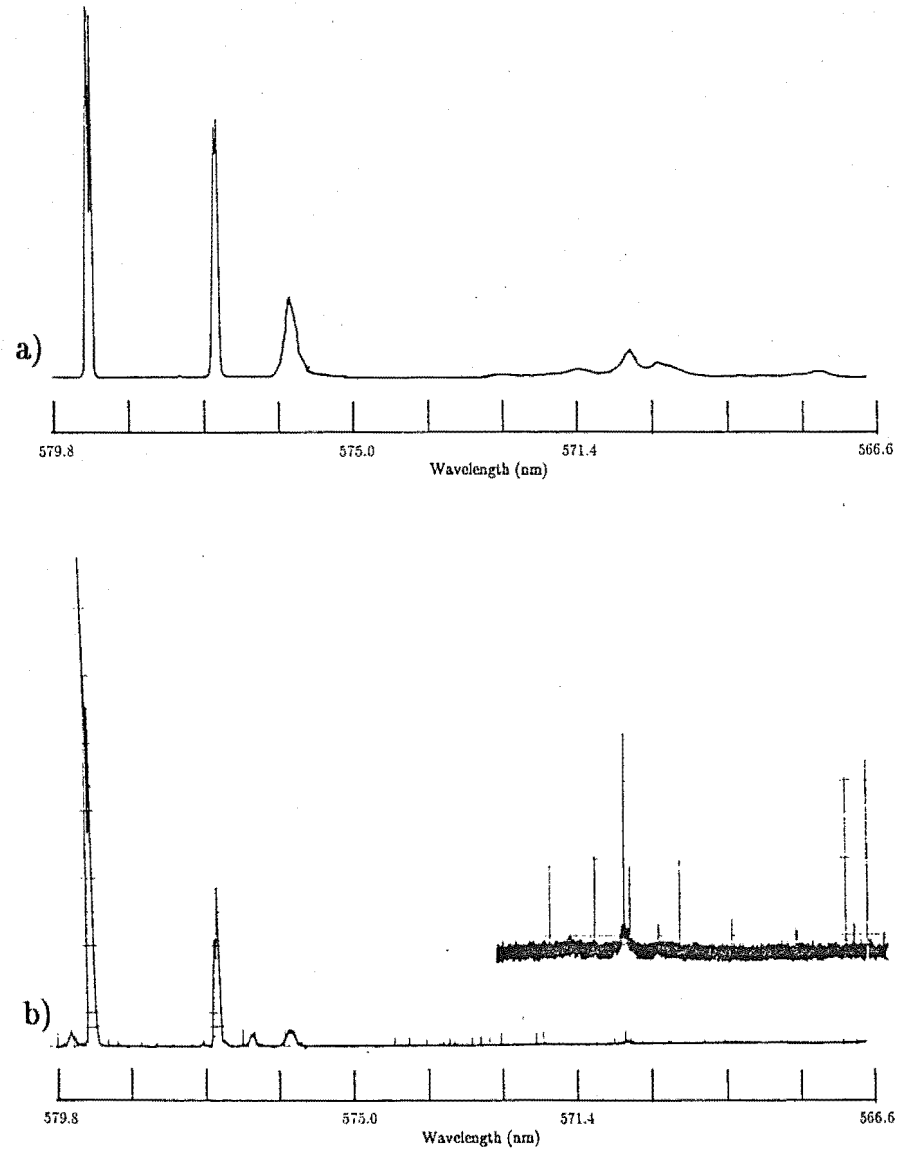

Figure 5.84: 10 K D multiplet excitation spectrum of the $CaF_2 : Nd^{3+}$ N centre.
a) monitoring the $R_1 \rightarrow Z_1$ transition;
b) monitoring the $L_1 \rightarrow Z_1$ transition.

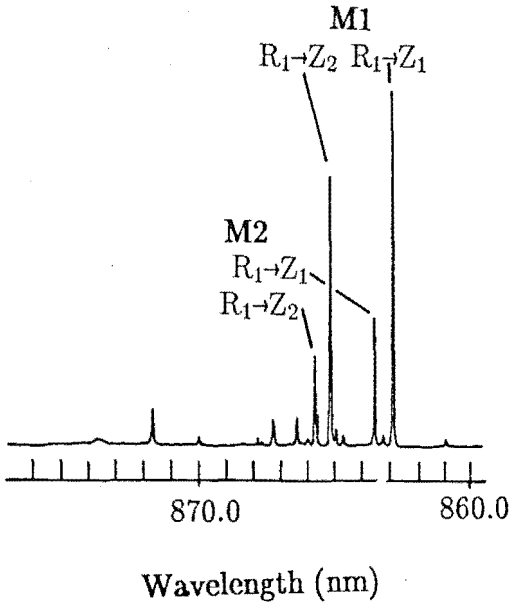

Figure 5.85: 10 K fluorescence spectrum of the $CaF_2 : Nd^{3+}$ $M1$ and $M2$ F^- centres.

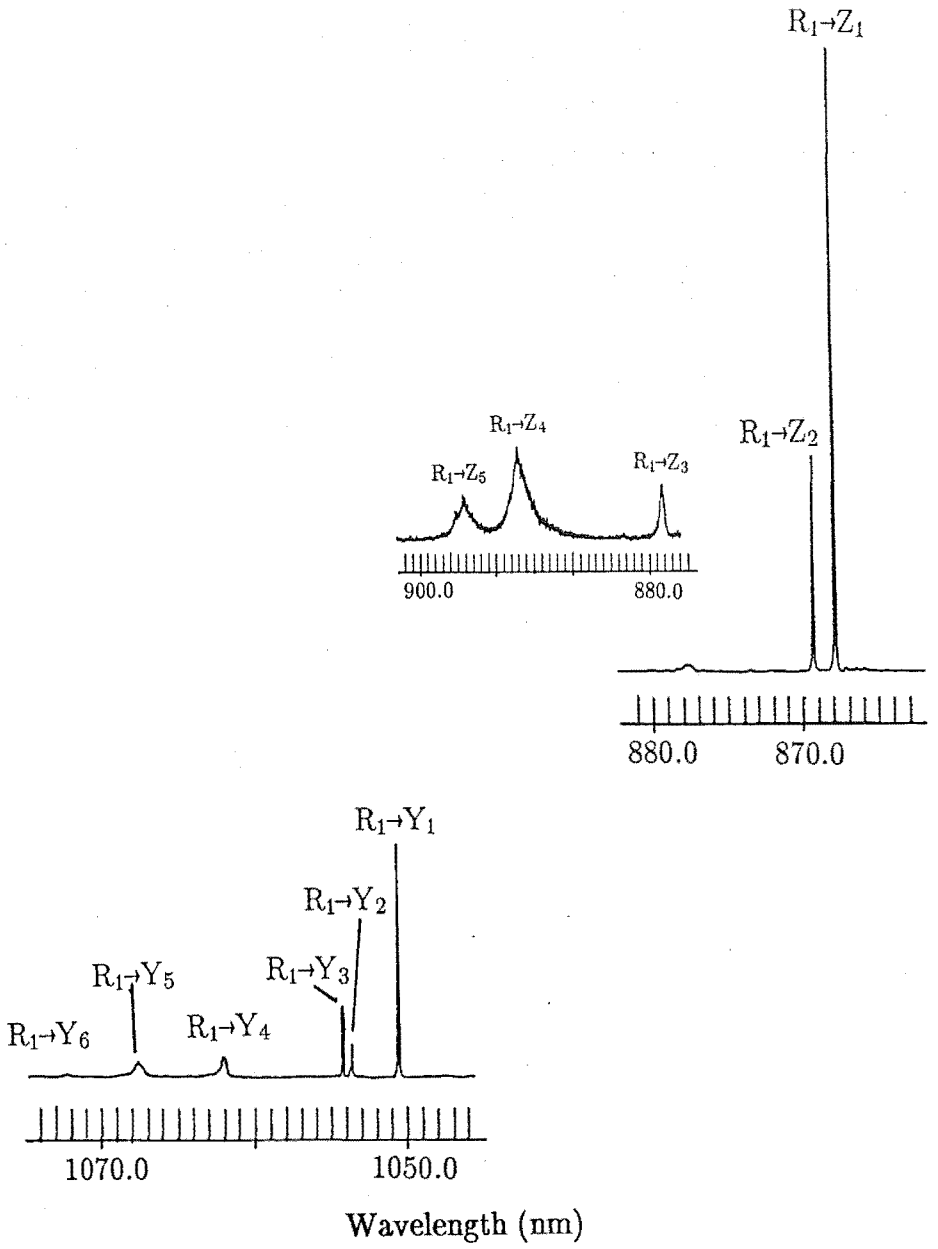

Figure 5.86: 10 K fluorescence spectrum for the $R_1 \rightarrow Z_{1,2,3,4,5}$ and $Y_{1,2,3,4,5,6}$ transitions of the $CaF_2 : Nd^{3+}$ $M4$ F^- centre.

the two-ion cluster centres found in $CaF_2 : Nd^{3+}$. This demonstrated the presence of low symmetry cluster centres in $SrF_2 : Nd^{3+}$ at concentrations of 0.05% Nd^{3+} ion and confirmed the EPR results of Kask and Kornienko (1968). The presence of these centres was not observed in any of the optical absorption spectra of $SrF_2 : Nd^{3+}$. Fig. 5.87 is a representative example of the fluorescence spectrum of these centres and their energy levels are listed in Table 5.13.

These two-ion centres in $SrF_2 : Nd^{3+}$ are expected to show similar energy upconversion processes to their counterparts in $CaF_2 : Nd^{3+}$ but no evidence of this was obtained. The absence of the upconverted fluorescence is attributed to the weakness of the fluorescence of these centres and the limited sensitivity of the equipment used.

5.7.6 Discussion

The similarity of the M, N and the Mi (i = 1,2,...) centres in $CaF_2 : Nd^{3+}$ and $SrF_2 : Nd^{3+}$ suggests a common underlying symmetry configuration is shared by these centres. The results are insufficient to verify the proposed model for these centres, or the origin of the double line pattern of the energy levels in the D multiplet of the M and N centres.

Fluorescence lifetime measurements of the $R_1 \rightarrow Z_1$ transition of the M and N centres gave 92 us (±10%) and 35 us (±10%) at 10 K respectively. The proposed model for the M centre (Osiko 1965, Osiko and Shcherbakov 1971) involves two Nd^{3+} ions whereby the charge compensation is achieved by two F^- ions in the interstitial positions as shown in Fig. 5.78. The reduced fluorescence decay constant of the $R_1 \rightarrow Z_1$ transition between the M and the C_{4V} centres could be attributed to the increased non-radiative contribution to the relaxation processes. This non-radiative contribution is an indication of the coupling between the two Nd^{3+} ions and of the interaction of the Nd^{3+} ions with the lattice phonons in the M centre. Barthem et al. (1987) have investigated the energy transfer rate within simple cluster centres in $LiYF_4 : Pr^{3+}$ and $LiYF_4 : Nd^{3+}$ and they attributed the short range interaction to superexchange and the long range interaction to electric dipole-dipole. A first approximation of the non-radiative relaxation rate can be deduced using the phenomenological approach as discussed in the analysis of the hydrogenic C_{4V} centres in Chapter 2. The use of the C_{4V} F^- centre in the phenomenological approach to estimate the non-radiative contribution in the relaxation processes of the M centre is justified because the energy difference between the fluorescing level and the next lowest energy levels of these two centres is very similar. The assumption that the decay constant of the $R_1 \rightarrow Z_1$ transition of the C_{4V} F^- centre is dominated by a radiative relaxation process simplifies the calculation as discussed in Chapter 5. Using the value of 1.3 ms (±10%) as the C_{4V} F^- centre fluorescence decay constant

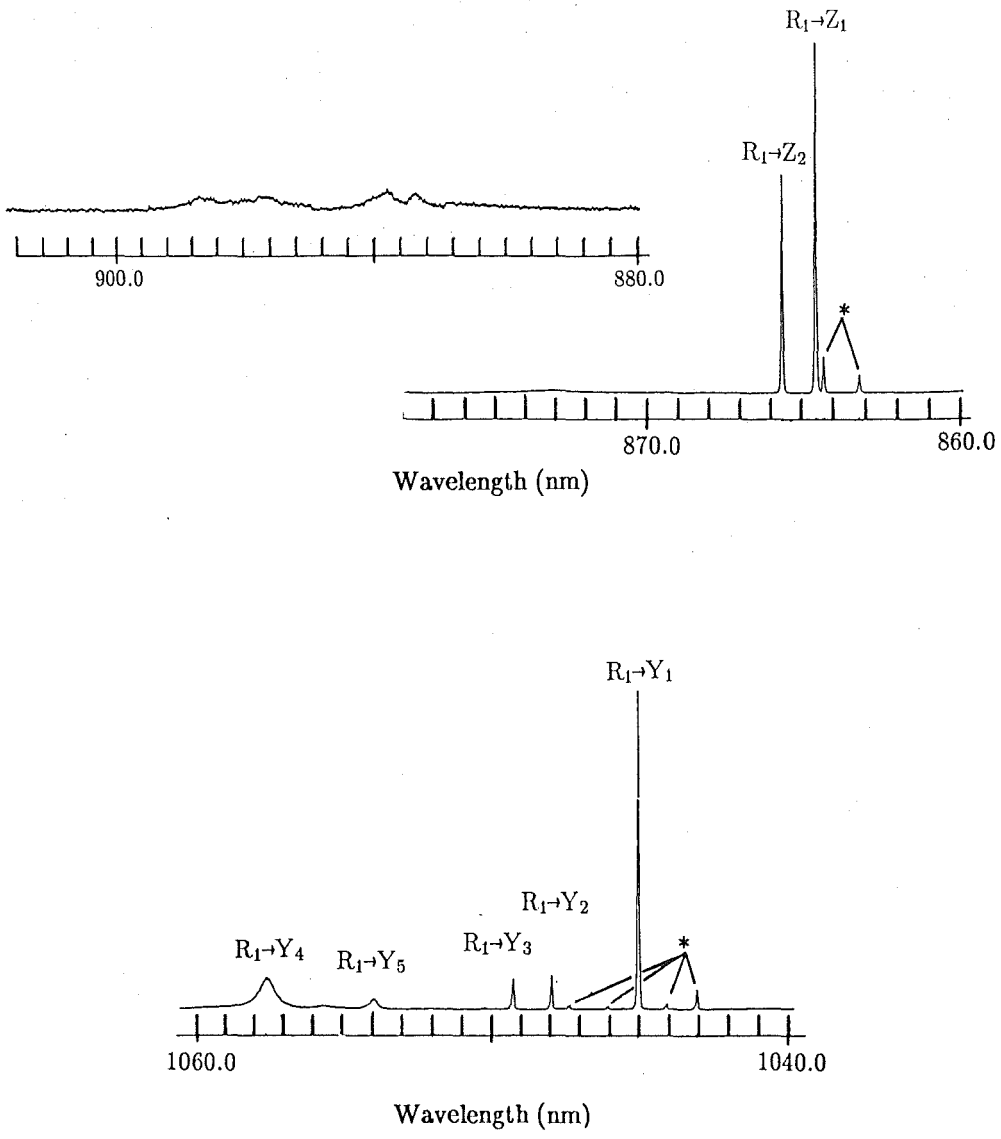

Figure 5.87: 10 K fluorescence spectrum for the $R_1 \rightarrow Z_{1,2,3,4,5}$ and $Y_{1,2,3,4,5,6}$ transitions of the $SrF_2 : Nd^{3+}$ $M1$ F^- centre. * unidentified line.

of the $R_1 \rightarrow Z_1$ transition, the non-radiative rate of the $R_1 \rightarrow Z_1$ transition of the M centre is given by equation 5.16 as :

$$\begin{aligned} \omega^{NR} &= \frac{1}{\tau_M} - \omega^R \\ &= \frac{1}{\tau_M} - \omega^R_{C_{4V}} \\ &= 10870 - 769 \\ &= 10100\ (\pm 12\%)\ s^{-1} \ . \end{aligned}$$

The results of a similar calculation for the N centre and the Mi ($i = 1,2,...$) centres are presented in Table 5.15. The results obtained for the double rare earth doped crystals, as discussed in Chapter 8, show that there is energy transfer between the two rare earth ions within the M centre and an increase in the coupling between the rare earth ions and the lattice phonons. The efficiency of the energy transfer depends on the matching of the energy levels of the two rare earth ions within the centre. In the present case where the ion pair is $Nd^{3+} - Nd^{3+}$, an effective non-radiative relaxation path could be achieved by an energy transfer from the R multiplet to the W multiplet, which is approximately half the energy of the $R_l \rightarrow Z_i$ transitions. The increase in the coupling of the rare earth ions to the lattice phonons could be related to the interaction between the two rare earth ions and to the addition of the second rare earth ion which results in the distortion of the local environment of the individual rare earth ions within the centre. Any such increase in electron phonon interaction is insensitive to the second rare earth ion introduced into the centre (see Chapter 8).

State		$SrF_2 : Nd^{3+}$		$CaF_2 : Nd^{3+}$		1	2
$^4I_{9/2}$	Z_1	0		0		0	0
	Z_2	354.9	(± 1.6)	323.8	(± 1.6)	324	85
	Z_3	455.4	(± 1.8)	443.6	(± 1.8)	442	440
	Z_4	474.8	(± 1.8)	477.7	(± 1.8)	478	475
	Z_5	862.5	(± 1.6)			943	925
$^4I_{11/2}$	Y_1	1917.8	(± 1.6)	2114.7	(± 1.6)	2110	
	Y_2	2302.8	(± 2.3)	2303.7	(± 1.8)	2303	
	Y_3	2316.2	(± 1.6)	2309.6	(± 1.8)	2309	
	Y_4	2346.4	(± 1.6)	2343.2	(± 1.6)	2340	
	Y_5			2619.6	(± 1.6)	2620	
	Y_6						
$^4F_{3/2}$	R_1	11477.1	(± 1.6)	11498.2	(± 1.6)	11496,9	11398,6
	R_2						11494,3
$^2H_{11/2}$	C_1	15972	(± 2)				
	C_2	16028	(± 2)				
	C_3	16099	(± 2)				
	C_4	16133	(± 2)				
	C_5	16200	(± 2)				
	C_6	16301	(± 2)				
		16336	(± 2)				
$^4G_{5/2}$,	D_1	17217	(± 2)	17172	(± 3)		
$^2G_{7/2}$	D_2	17226	(± 2)	17245	(± 2)		
	D_3	17377	(± 2)				
	D_4						
	D_5						
	D_6	17510	(± 5)				
	D_7	17554	(± 3)				

Table 5.10: 10 K energy levels (in air cm^{-1}) of the A' centre in $SrF_2 : Nd^{3+}$ and $CaF_2 : Nd^{3+}$. 1. data of Kariss et al. 1965. 2. data of Toledano 1972.

State		Experimental		State		Experimental	
$^4I_{9/2}$	Z_1	0		$^4F_{7/2}$,	A_1		
	Z_2	35.3	(± 1.6)	$^4S_{3/2}$	A_2	13583	(± 2)
	Z_3	150.1	(± 1.8)		A_3		
	Z_4	380.5	(± 1.8)		A_4		
	Z_5	502.1	(± 1.6)		A_5	13700	(± 1)
					A_6	13710	(± 1)
$^4I_{11/2}$	Y_1	2026.1	(± 1.6)				
	Y_2	2052.5	(± 1.8)	$^2H_{11/2}$	C_1	15992	(± 2)
	Y_3	2083.3	(± 1.8)		C_2	16004	(± 2)
	Y_4	2139.8	(± 1.8)		C_3	16013	(± 2)
	Y_5	2189.4	(± 2.3)		C_4	16042	(± 2)
	Y_6	2224.6	(± 1.8)		C_5	16068	(± 2)
					C_6	16131	(± 2)
$^4I_{13/2}$	X_1	3963	(± 1)				
	X_2	3986	(± 1)	$^4G_{5/2}$,	D_1	17258	(± 1)
	X_3	4027	(± 1)			17259	(± 1)
	X_4	4087	(± 1)	$^2G_{7/2}$	D_2	17319	(± 1)
	X_5	4133	(± 1)			17320	(± 1)
	X_6				D_3	17343	(± 1)
	X_7					17344	(± 1)
					D_4	17468	(± 3)
$^4I_{15/2}$	W_1	5800	(± 1)		D_5	17499	(± 5)
	W_1	5891	(± 1)		D_6	17517	(± 5)
	W_3				D_7	17561	(± 3)
	W_4						
	W_5			$^4G_{7/2}$	E_1	19116	(± 2)
	W_6	6284	(± 1)		E_2		
	W_7	6562	(± 1)		E_3		
	W_8	6640	(± 1)		E_4		
$^4F_{3/2}$	R_1	11580.0	(± 1.6)	$^2P_{1/2}$,	I_1	23416	(± 3)
	R_2	11622.2	(± 1.6)	$^2D_{5/2}$	I_2		
	R_1'	11574	(± 1)		I_3		
	R_2'	11616	(± 2)				
				$^4D_{3/2}$	L_1	28264	(± 3)
$^4F_{5/2}$,	S_1	12530	(± 1)		L_2	28282	(± 3)
$^2H_{9/2}$	S_2	12576	(± 1)				
	S_3	12581	(± 1)				
	S_4	12603	(± 1)				
	S_5	12628	(± 1)				
	S_6	12655	(± 1)				
	S_7	12762 ?	(± 1)				
	S_8	12850 ?	(± 1)				

Table 5.11: 10 K energy levels (in air cm^{-1}) of the M F^- centre in $CaF_2 : Nd^{3+}$. ? Tentative assignement.

State		Experimental		State		Experimental	
$^4I_{9/2}$	Z_1	0		$^4F_{9/2}$	B_1	14838	(± 1)
	Z_2	40.5	(± 1.5)		B_2		
	Z_3	145.1	(± 1.8)		B_3	14894	(± 1)
	Z_4	382.9	(± 1.8)		B_4	14910	(± 1)
	Z_5	544.1	(± 1.6)		B_5	14930	(± 1)
$^4I_{11/2}$	Y_1	2029.1	(± 1.6)	$^2H_{11/2}$	C_1	15991	(± 1)
	Y_2	2059.2	(± 1.8)		C_2	16019	(± 1)
	Y_3	2088.3	(± 1.8)		C_3	16029	(± 1)
	Y_4	2141.4	(± 1.6)		C_4	16056	(± 1)
	Y_5	2222.1	(± 2.3)		C_5	16088	(± 1)
	Y_6	2261.5	(± 1.6)		C_6	16161	(± 1)
$^4I_{13/2}$	X_1	3959	(± 3)	$^4G_{5/2}$,	D_1	17269	(± 1)
	X_2	3998	(± 2)			17270	(± 1)
	X_3	4032	(± 3)	$^2G_{7/2}$	D_2	17326	(± 1)
	X_4	4101	(± 2)			17327	(± 1)
	X_5	4144	(± 2)		D_3	17363	(± 1)
	X_6	4146	(± 1)		D_4	17499	(± 1)
	X_7	4358	(± 2)		D_5	17523	(± 1)
					D_6	17536	(± 1)
$^4F_{3/2}$	R_1	11601.2	(± 1.6)		D_7	17614	(± 1)
	R_2	11640.9	(± 1.6)				
	R_1'	11596	(± 1)	$^4G_{7/2}$	E_1	19128	(± 2)
	R_2'	11636	(± 2)		E_2		
					E_3		
$^4F_{5/2}$,	S_1	12295	(± 1)		E_4		
$^2H_{9/2}$	S_2	12337	(± 1)				
	S_3	12593	(± 1)	$^2P_{1/2}$,	I_1	23448	(± 3)
	S_4	12585	(± 1)	$^2D_{5/2}$	I_2		
	S_5	12621	(± 1)		I_3		
	S_6	12649	(± 1)				
	S_7	12678	(± 2)	$^4D_{3/2}$	L_1	28284	(± 3)
	S_8	12774	(± 2)		L_2	28312	(± 3)
$^4F_{7/2}$,	A_1	13477	(± 1)				
$^4S_{3/2}$	A_2	13481	(± 1)				
	A_3	13595	(± 1)				
	A_4	13690	(± 1)				
	A_5	13717	(± 1)				
	A_6	13723	(± 1)				

Table 5.12: 10 K energy levels (in air cm^{-1}) of the N F^- centre in $CaF_2 : Nd^{3+}$.

State		$M1$		$M2$		$M3$	
$^4I_{9/2}$	Z_1	0		0		0	
	Z_2	14.7	(± 1.6)	29.4	(± 1.6)	67	(± 1.6)
	Z_3	110.0	(± 1.6)	125.7	(± 1.6)	133.0	(± 1.6)
	Z_4	219.3	(± 1.8)	333.9	(± 1.8)	183.7	(± 1.6)
	Z_5	323.9	(± 1.8)	347.8	(± 1.8)	319.0	(± 1.6)
		385.5	(± 1.8)	392.9	(± 1.8)	329.0	(± 1.6)
		389.3	(± 1.6)	412.9	(± 1.8)	364.2	(± 1.8)
				425.3	(± 1.8)		
$^4I_{11/2}$	Y_1	1980.1	(± 1.6)	1999.8	(± 1.6)	1991.7	(± 1.6)
	Y_2	1997.5	(± 1.6)	2021.8	(± 1.8)	2022.6	(± 1.6)
	Y_3	2024.9	(± 1.6)	2057.2	(± 1.6)	2033.5	(± 1.8)
	Y_4	2035.8	(± 1.6)	2129.9	(± 1.6)	2099.1	(± 1.6)
	Y_5	2079.3	(± 1.6)	2164.3	(± 1.8)	2129.4	(± 1.6)
	Y_6	2111.6	(± 1.8)				
$^4F_{3/2}$	R_1	11568.7	(± 1.6)	11567.4	(± 1.6)	11547.3	(± 1.6)
	R_2						

Table 5.13: 10 K energy levels (in air cm^{-1}) of the $M1$, $M2$ and $M3$ F^- centres in $SrF_2 : Nd^{3+}$.

State		$M1$		$M2$		$M3$		$M4$	
$^4I_{9/2}$	Z_1	0		0		0		0	
	Z_2	30.8	(± 1.6)	28.1	(± 1.6)	21.4	(± 1.6)	18.6	(± 1.6)
	Z_3					145.4	(± 1.8)	149.6	(± 1.8)
	Z_4					375.7	(± 1.6)	38 0.6	(± 1.6)
	Z_5					466.5	(± 1.8)	467.0	(± 1.8)
						486.1	(± 1.8)	481.6	(± 1.8)
						504.6	(± 1.8)		
$^4I_{11/2}$	Y_1					2022.1	(± 1.6)	2010.3	(± 1.6)
	Y_2					20566	(± 1.8)	2037.4	(± 1.8)
	Y_3					2064.8	(± 1.8)	2042.8	(± 1.8)
	Y_4					2116.0	(± 1.6)	2112.5	(± 1.6)
	Y_5					2160.5	(± 1.6)	2160.2	(± 1.6)
						2166.7	(± 1.8)		
	Y_6					2201.1	(± 1.6)		
$^4F_{3/2}$	R_1	11587.5	(± 1.6)	11578.1	(± 1.6)	11571.4	(± 1.6)	11531.4	(± 1.6)
	R_2								

Table 5.14: 10 K energy levels (in air cm^{-1}) of the $M1$, $M2$, $M3$ and $M4$ F^- centres in $CaF_2 : Nd^{3+}$.

		$CaF_2 : Nd^{3+}$					
		M	N	$M1$	$M2$	$M3$	$M4$
τ	(ms $\pm$ 10%)	.092	.0348	.52	.45	.58	.49
W^{NR}	(s^{-1})	10101	27967	1154	1453	955	1272
	($\pm$ %)	11	11	23	21	26	22

		$SrF_2 : Nd^{3+}$	
		$M2$	$M3$
τ	(us $\pm$ 10%)	237	262
W^{NR}	(s^{-1})	3624	3222
	($\pm$ %)	28	30

τ = fluorescence lifetime
W^{NR} = non-radiative decay rate
W^R = radiative decay rate
= 769 ($\pm$ 10%) (s^{-1}) $CaF_2 : Nd^{3+}\ F^-\ C_{4V}$
= 595 ($\pm$ 10%) (s^{-1}) $SrF_2 : Nd^{3+}\ F^-\ C_{4V}$

Table 5.15: 10 K non-radiative decay rates for the $R_1 \rightarrow Z_1$ transition of the $Mi\ F^-$ centres in $SrF_2 : Nd^{3+}$ and $CaF_2 : Nd^{3+}$.

Chapter 6

Energy Upconversion

The complexity of the energy levels present in rare earth ions makes excited state interactions a very common process in excited rare earth doped materials. Ion-Ion interaction is a well established relaxation mechanism in rare earth salts. The efficiency of the energy transfer depends on the matching of the energy gap of the transitions and the nature of the coupling in the electronic system. Most of the earlier experimental work has been concerned with the variation of the lifetime of the fluorescence levels as a function of the concentration of rare earth ions and subsequently establishing energy transfer from one fluorescent ion to another of the same or different kind. The theories for resonant energy transfer were developed by Dexter (1953) and Forster (1959) for multi-polar coupling and by Inokuti and Hirayama (1965) for exchange coupling. The theory for non- resonant energy transfer was developed by Miyakawa and Dexter (1970), where the energy mismatch between the energy levels of the donor and the acceptor ions is compensated for by the creation or destruction of phonons.

There has been a large amount of experimental research into the energy transfer between rare earth ions and much interest has centred on the phenomenon of energy upconversion. The majority of these studies have been concerned with evaluating the importance of the energy transfer process in optimising particular applications, such as the infrared quantum counter (IRQC) and quenching or sensitising fluorescence in solid state laser operations. A comprehensive review of the energy transfer process in rare earth doped materials was given by Wright (1976) and Riseberg and Weber (1976). Many mechanisms have been proposed to explain the different types of upconversion fluorescence behaviour observed for rare earth ions in various host materials. The most efficient type of upconversion mechanism involves the sequential transfer of two or more excitations from the donor ion to another ion, as illustrated in Fig. 6.1. The two processes most commonly invoked for the energy upconversion of the RE^{3+} ions in various host materials (Lezama 1986, Vial et al. 1979, Reddy and Venkateswarlu 1983, Zalucha et al. 1973, 1974) are the sequential two photon excitation process

(STEP) and the energy transfer upconversion process (ETU). The first of these processes involves an ion being excited by absorbing a photon and relaxing to an intermediate level from which it is further excited to a higher energy level by absorbing another photon. The latter process requires the transfer of energy from one excited ion in an intermediate level to another leaving one in the ground state and the other in a higher excited level. Each of the two processes mentioned above requires two incident photons; the first process involves a single ion while the second requires two ions. No details of energy transfer processes are presented in this thesis; instead the references mentioned above may be consulted for a comprehensive analysis. Discussion here is restricted to the most probable mechanisms responsible for the upconverted fluorescence observed in $CaF_2 : Nd^{3+}$ and $SrF_2 : Nd^{3+}$.

The phenomenon of energy upconversion was observed for both the single rare earth ion C_{4V} F^- centres in $CaF_2 : Nd^{3+}$ and $SrF_2 : Nd^{3+}$, and for the M and N F^- cluster centres in $CaF_2 : Nd^{3+}$. No upconversion was observed in any of the hydrogenic centres of $SrF_2 : Nd^{3+}$ or $CaF_2 : Nd^{3+}$ due to insufficient sensitivity of the equipment to record fluorescence signals 10^4 times weaker than those of the F^- centres.

6.1 Tetragonal (C_{4V}) Centre

Upconverted fluorescence from the K ($^2P_{3/2}$) and L ($^4D_{3/2}$) multiplets was observed in $SrF_2 : Nd^{3+}$ and $CaF_2 : Nd^{3+}$ crystals with a 0.05% Nd^{3+} ion dopant concentration when the frequency of the dye laser was resonant with particular energy levels of the D multiplet. The upconverted fluorescence spectra are presented in Figs. 6.2 and 6.3 and the assigned energy levels are listed in Tables 5.1 and 5.2. No fluorescence from the C and D multiplets themselves was observed which is consistent with earlier observations for the C_{4V} F^- centre (see Chapter 5). Fig. 6.4 shows that the upconverted fluorescence is associated with a two photon process whereas the infrared fluorescence from the R_1 level is a single photon process. The upconverted fluorescence intensity for the L multiplet was 10^3 weaker than the direct fluorescence for the R multiplet. No upconverted fluorescence was observed when the C multiplet was excited.

The upconverted fluorescence spectrum of the L multiplet in $SrF_2 : Nd^{3+}$ showed the presence of the unidentified 165 cm^{-1} level close to the $L_1 \rightarrow Z_3$ transition and this further supports its association with the C_{4V} symmetry centre. A weak transition was observed to terminate at an energy level 268 cm^{-1} above the ground level which is close to the 257.7 cm^{-1} predicted by Freeth (1980) as the position for the Z_4 energy level. As this weak transition was not observed in the upconverted fluorescence spectrum of the K multiplet or in the near infrared fluorescence of the R_1 level its assignment is only

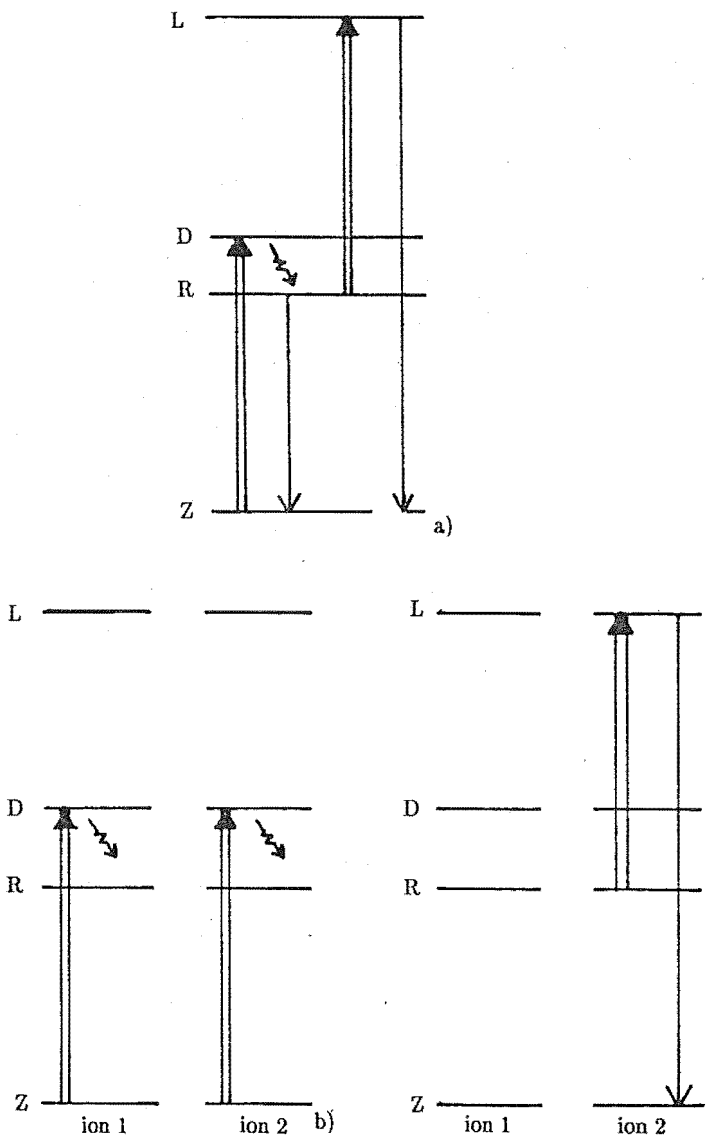

Figure 6.1: Schematic diagram showing two possible mechanisms for energy upconversion processes. a) Sequential two photon excitation process (STEP). b) Energy transfer upconversion process (ETU).

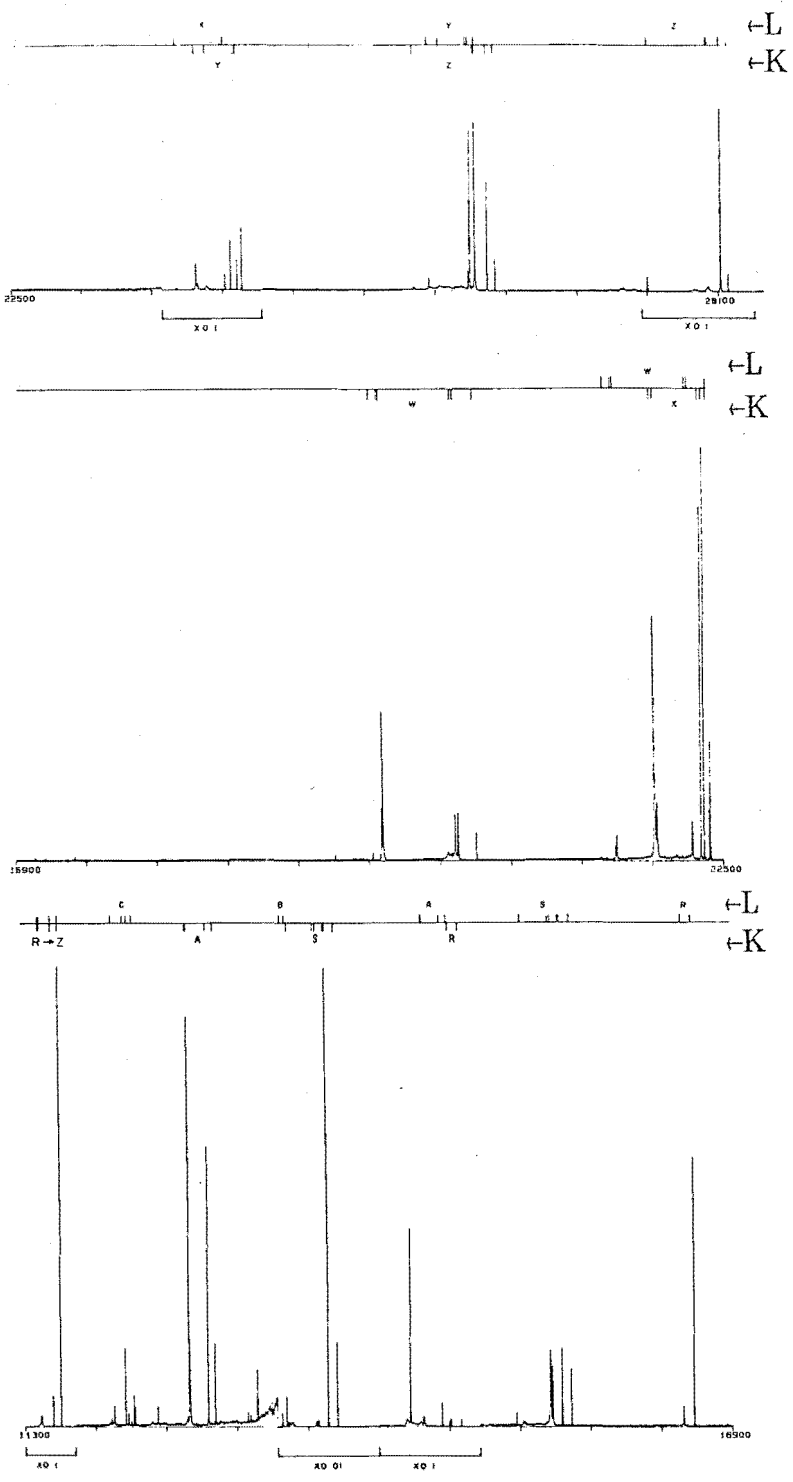

Figure 6.2: 10 K fluorescence spectrum of the $SrF_2 : Nd^{3+}$ C_{4V} F^- centre with laser excitation at 17346 (in air cm^{-1}) showing fluorescence transitions caused by upconversion processes.

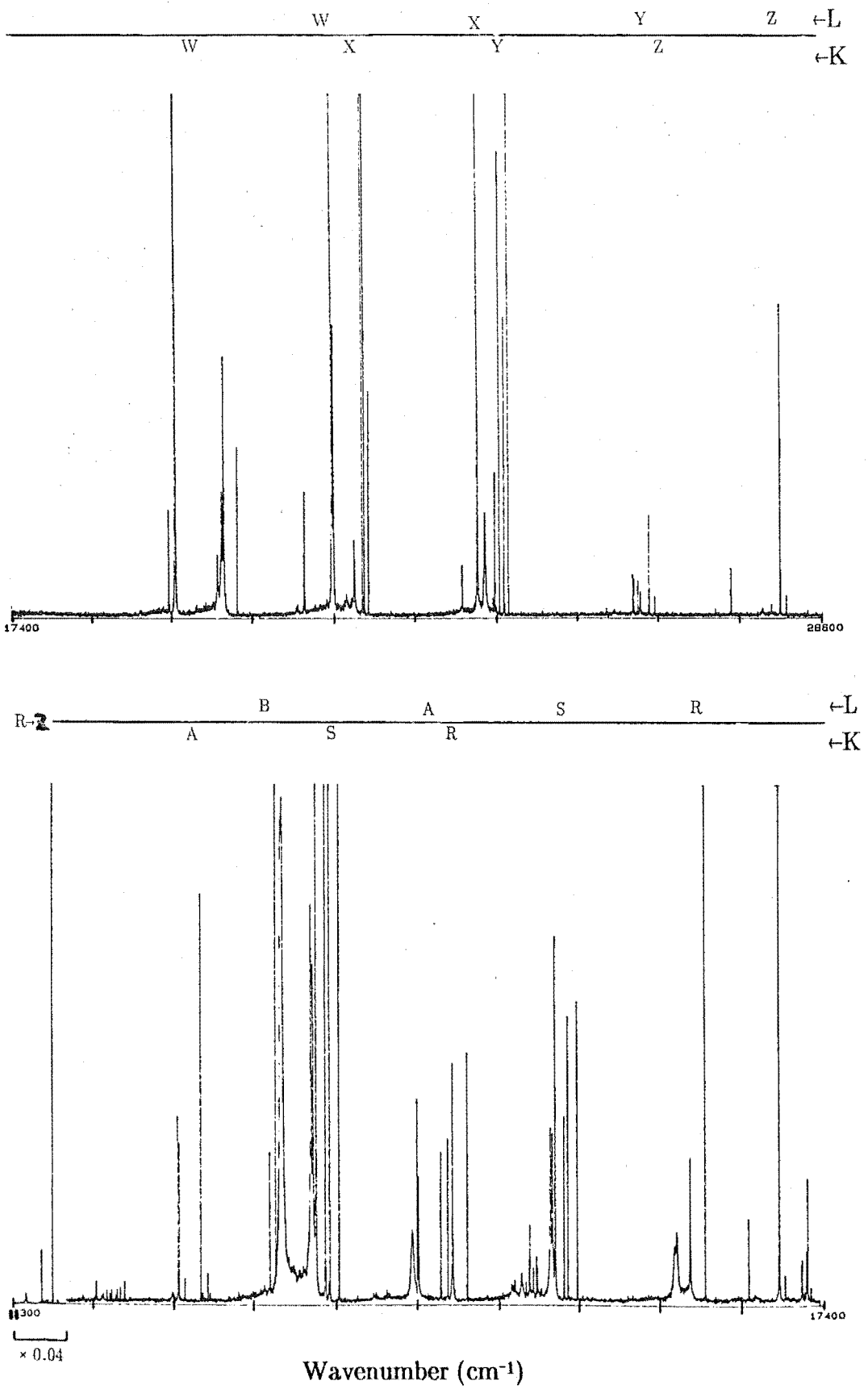

Figure 6.3: 10 K fluorescence spectrum of the $CaF_2 : Nd^{3+}$ C_{4V} F^- centre with laser excitation at 17385 (in air cm^{-1}) showing fluorescence transitions caused by upconversion processes.

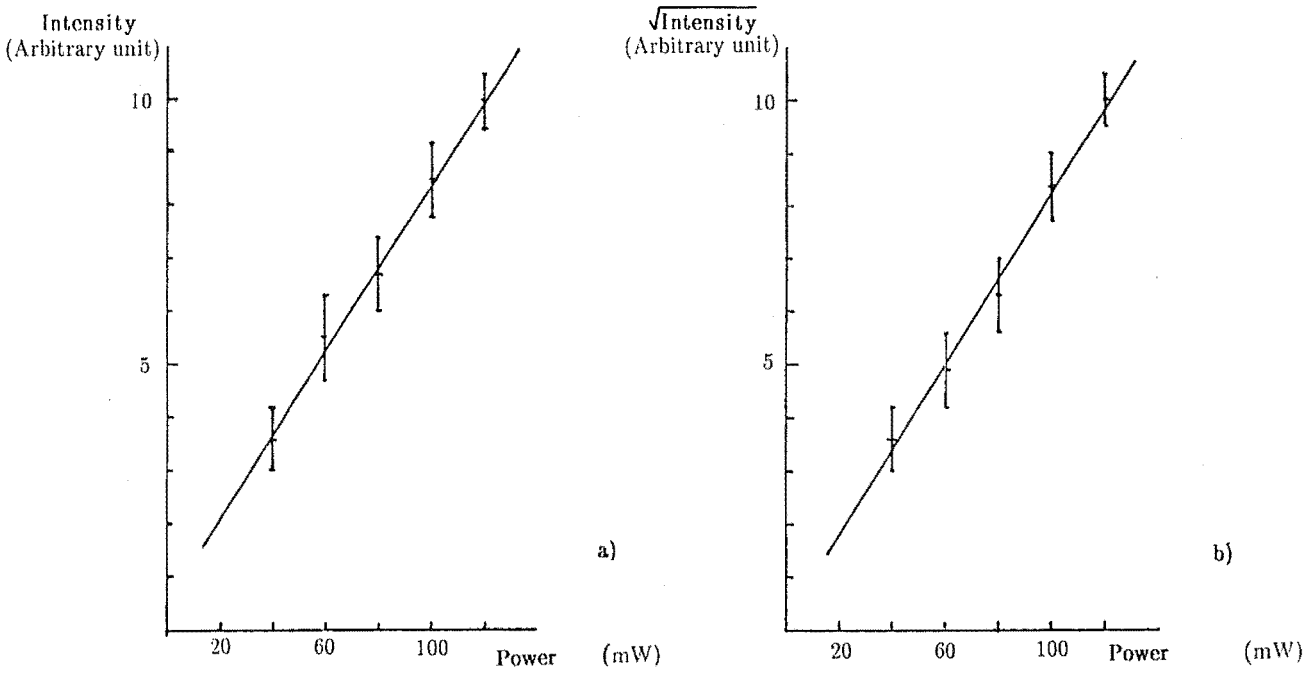

Figure 6.4: 10 K fluorescence of the $CaF_2 : Nd^{3+}$ C_{4V} F^- centre as a function of incident laser power for a) the $R_1 \rightarrow Z_1$ transition (862.3 nm); b) the $L_1 \rightarrow Z_2$ transition (28106.9 cm^{-1}).

tentative.

The excitation spectrum in Fig. 6.5 shows that identical excitation energies are needed to obtain the maximum intensities for both the upconverted and the infrared fluorescence. The excitation spectrum of the upconversion phenomenon also revealed an excitation at 16596 (± 3) cm^{-1}. This energy difference relative to the ground state would correspond to a level situated in the region between the C and D multiplets, but it exactly matches the energy difference between the L_1 and the R_1 energy levels. A detailed analysis showed that this upconversion excitation was accompanied by a weak infrared fluorescence from the R_1 level which was insensitive to the frequency tuning of the dye laser. Fig. 6.6 shows the broad phonon side band that caused the infrared fluorescence from the R_1 level and the upconverted fluorescence from the L multiplet when the laser was resonant with the energy difference between the L_1 and R_1 energy levels. This unambiguously identified the R_1 energy level as the intermediate level involved in the upconversion process which is further supported by the observed long fluorescence decay lifetime for this energy level (see Chapter 5). This observation, coupled with the C_{4V} symmetry centre being a single ion centre, strongly supports the STEP process as the dominant upconversion mechanism for Nd^{3+} ions.

The conclusion made above for the C_{4V} F^- centre in $SrF_2 : Nd^{3+}$ is equally valid for the corresponding centre in $CaF_2 : Nd^{3+}$ with the exception of the Z_4 energy level not being observed in the upconverted fluorescence spectrum. The energy difference between the L_1 and R_1 levels is 16515 (± 3) cm^{-1} (see Fig. 6.6).

An attempt to obtain the fluorescence decay lifetimes of the upconverted energy levels was unsuccessful. Although it would be preferable to investigate the possibility of upconversion with a higher power pulsed laser, the present indications favour the STEP process because of the following combined factors; the pulsed dye laser has a pulse width of 500 ps, a maximum repetition rate of 20 pulses per minute and the fluorescence decay time constant of the R_1 energy level is approximately 1 ms. This implies that there are no excited ions in the intermediate R_1 level when the next laser pulse arrives to complete the upconversion process. This supposition is consistent with the proposed STEP process. An attempt to populate the R multiplet by focusing light from an appropriate filtered white light source onto the crystal was not successful, probably because the light intensity was too low. The STEP upconversion process suggests a possible experiment using two lasers. A cw laser could be used to populate the R_1 level by exciting the non-upconverting C multiplet while a pulsed laser could scan the D multiplet to make upconverted fluorescence lifetime measurements. An improvement might be to use two pulsed dye lasers, so that the time difference between the pulses of the two lasers could give useful information about the efficiency of the upconversion process and the relaxation rate(s) between the excited

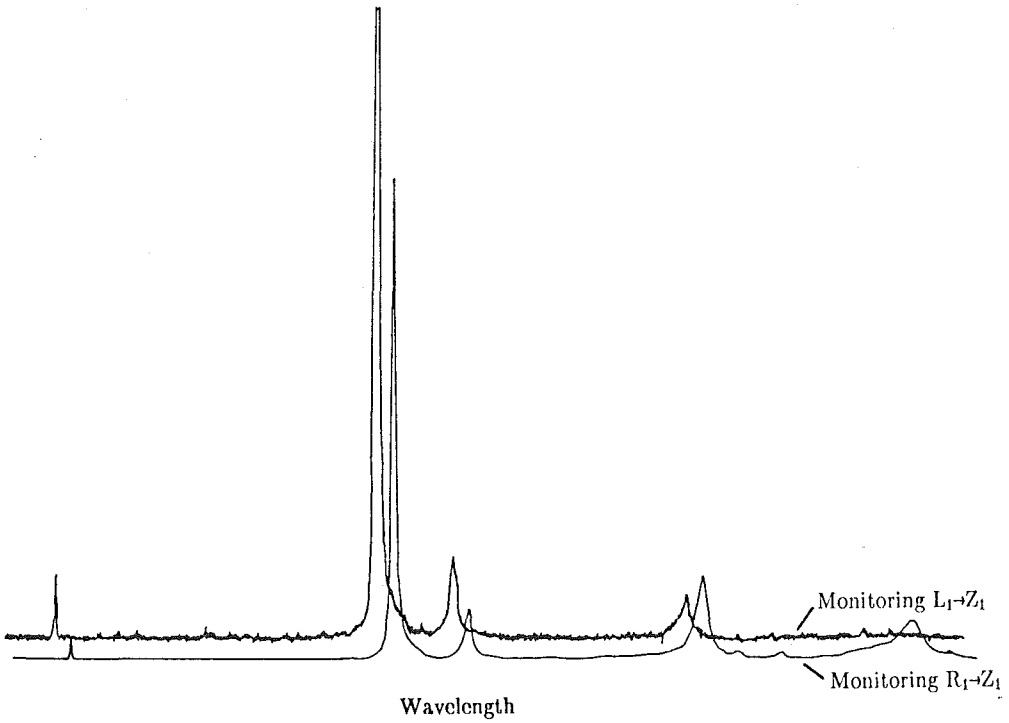

Figure 6.5: 10 K D multiplet excitation spectrum of the $SrF_2 : Nd^{3+}$ C_{4V} F^- centre. The slight displacement is due to the offset of the two chart recorder pens.

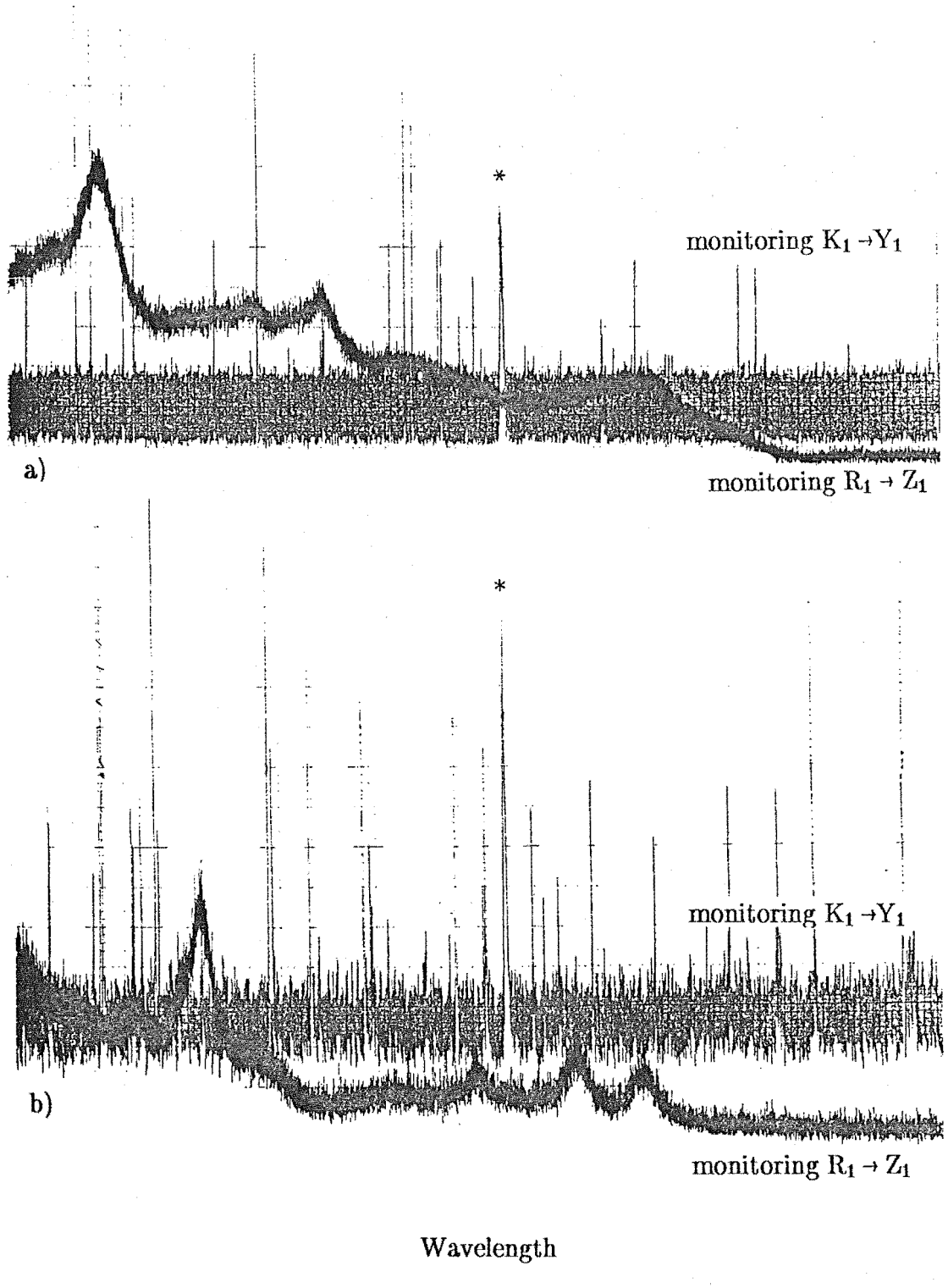

Figure 6.6: 10 K excitation spectrum of a) $CaF_2 : Nd^{3+}$; b) $SrF_2 : Nd^{3+}$ monitoring the upconverted and direct fluorescence of the C_{4V} F^- centre. * indicating the coincidence of the laser frequency with the energy separation of the L_1 and R_1 levels.

and the intermediate level(s).

6.2 Polarised Upconverted Fluorescence

Figs. 6.7 to 6.10 show representative examples of the polarised intensity pattern of the upconverted C_{4V} F^- centre fluorescence spectrum in $SrF_2 : Nd^{3+}$. The excitation of the energy level at 17346 cm^{-1} gives the strongest upconverted fluorescence as shown in Fig. 5.25, hence the polarisation of the upconverted fluorescence was studied by the excitation of this level. The polarisation results discussed earlier in Chapter 5 show that the excitation of this energy level is dominated by π polarisation. This simplified the task of unravelling the polarised upconversion intensity pattern since no σ polarisation was involved in populating the R_1 level. The second photon absorbed is restricted by equation 5.10 to give :

(yy)	(yx)
$I_{\pi\pi}$	$I_{\sigma\pi}$
	$I_{\sigma\sigma}$,

for $R_1 \rightarrow L \rightarrow Z$ transitions. For transitions between two energy levels of different symmetries, i.e. $\gamma_7 \rightarrow \gamma_6$, a 1:0 ratio is expected for the polarised upconverted (yx):(yy) fluorescence intensities. The symmetries of the energy levels Z_1 and Z_5 were identified to be γ_6 hence the energy level L_1 must have a γ_7 symmetry to produce the polarised intensity pattern of the $L_1 \rightarrow Z_1$ and Z_5 transitions shown in Fig. 6.7. This is further supported by the almost 1:0 ratio obtained for the (yx):(yy) polarisation ratios for the $L_1 \rightarrow R_1$ and $Y_{2,4,6}$ transitions, shown in Figs. 6.8 and 6.9. For transitions between two energy levels of the same symmetry, i.e. $\gamma_7 \rightarrow \gamma_7$, a more complex ratio is expected since both π and σ polarisations are allowed. The γ_6 symmetry of the K_1 energy level is deduced from the polarised intensity pattern of the $K_1 \rightarrow Z_2$ and R_2 transitions as shown in Figs. 6.9 and 6.10.

The above analysis should yield similar information for the C_{4V} F^- centre in $CaF_2 : Nd^{3+}$, but the polarised intensity patterns, as shown in Figs. 6.11 and 6.12 do not have clear polarisation ratios. This implies that the initial excitation must involve both π and σ polarisations which gives a complex polarised upconversion spectrum.

A summary of the polarised upconversion results is presented in Tables 5.1 and 5.2. Complementary and useful information could be acquired if a strong upconverted fluorescence could be obtained from excitation of an energy level of γ_7 symmetry.

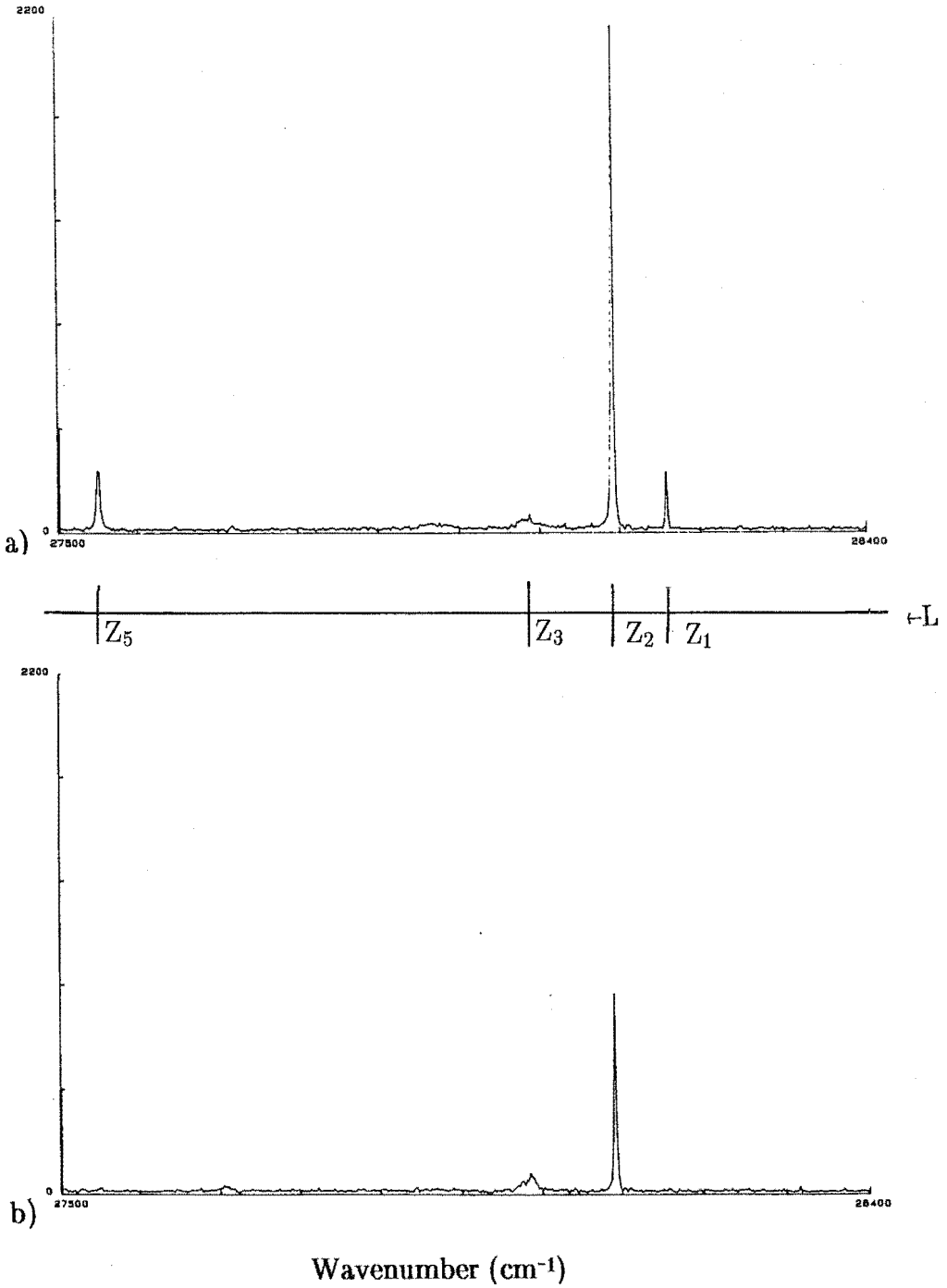

Figure 6.7: 10 K polarised fluorescence spectrum for the $L_1 \rightarrow Z_i$ transitions of the $SrF_2 : Nd^{3+}$ C_{4V} F^- centre for a) (yx) and b) (yy) polarisation.

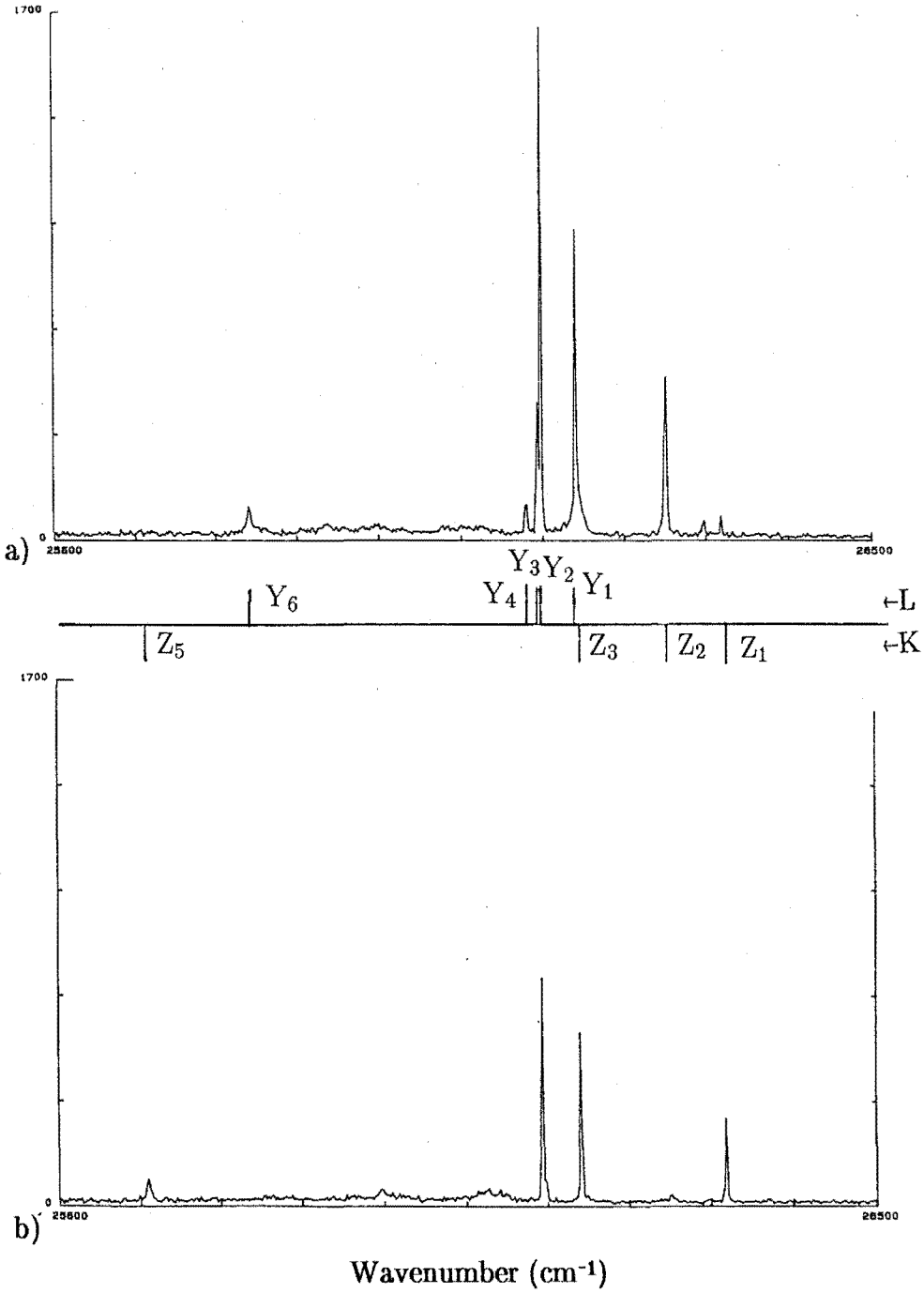

Figure 6.8: 10 K polarised fluorescence spectrum for the $L_1 \rightarrow Y_i$ and $K_1 \rightarrow Z_i$ transitions of the $SrF_2 : Nd^{3+}$ C_{4V} F^- centre for a) (yx) and b) (yy) polarisation.

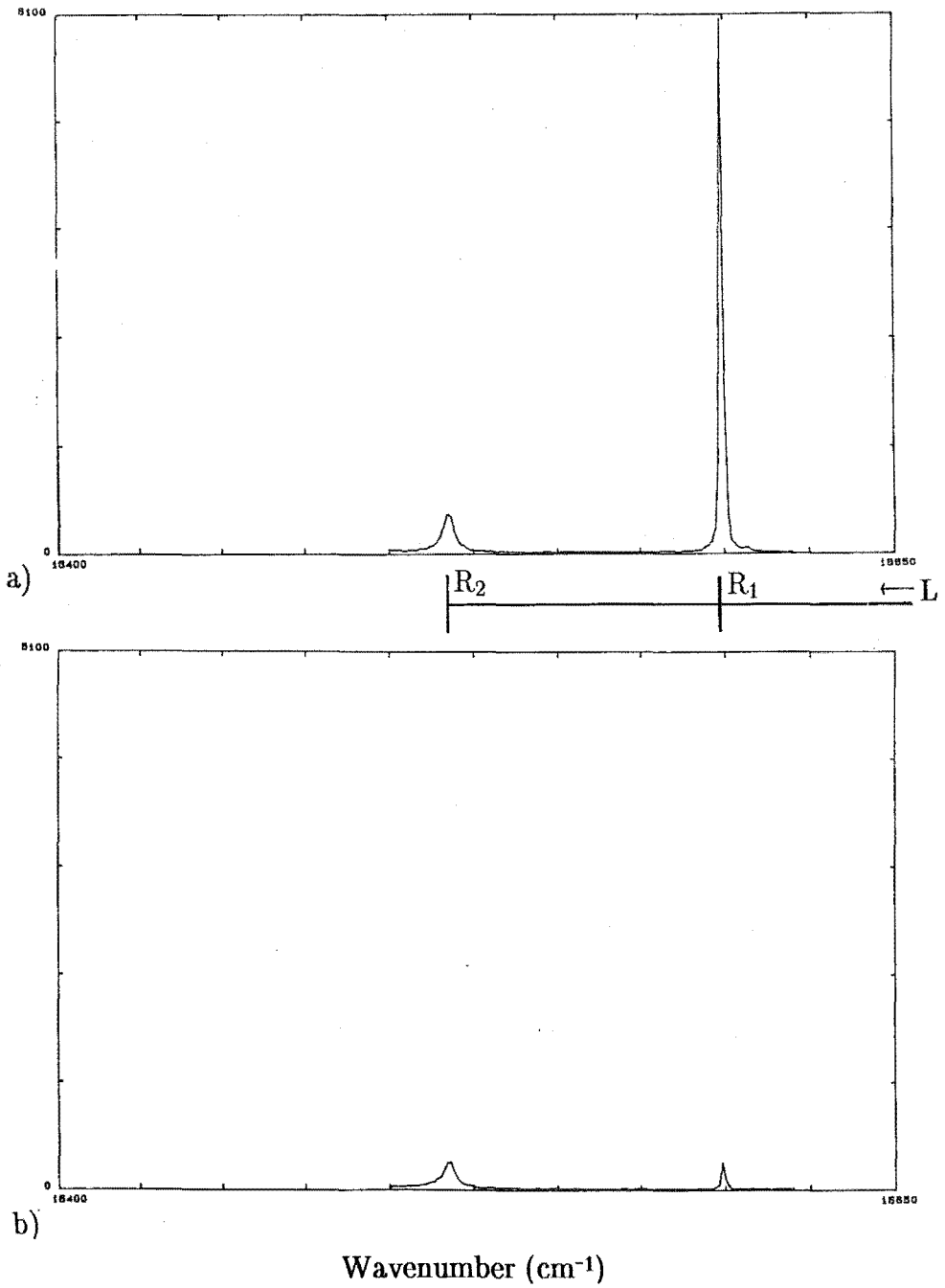

Figure 6.9: 10 K polarised fluorescence spectrum for the $L_1 \rightarrow R_i$ transitions of the $SrF_2 : Nd^{3+}$ C_{4V} F^- centre for a) (yx) and b) (yy) polarisation.

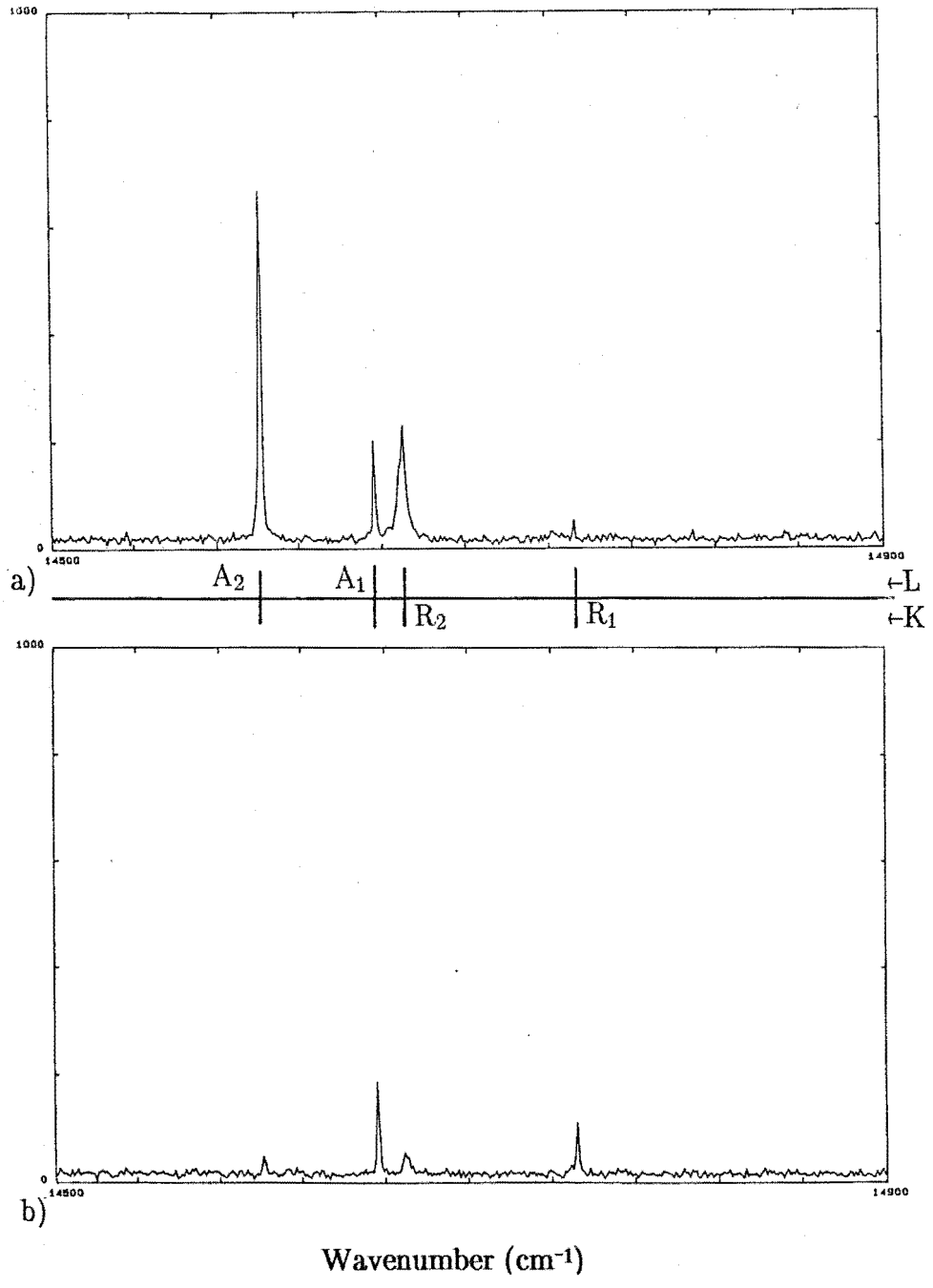

Figure 6.10: 10 K polarised fluorescence spectrum for the $L_1 \rightarrow A_i$ and $K_1 \rightarrow R_i$ transitions of the $SrF_2 : Nd^{3+}$ C_{4V} F^- centre for a) (yx) and b) (yy) polarisation.

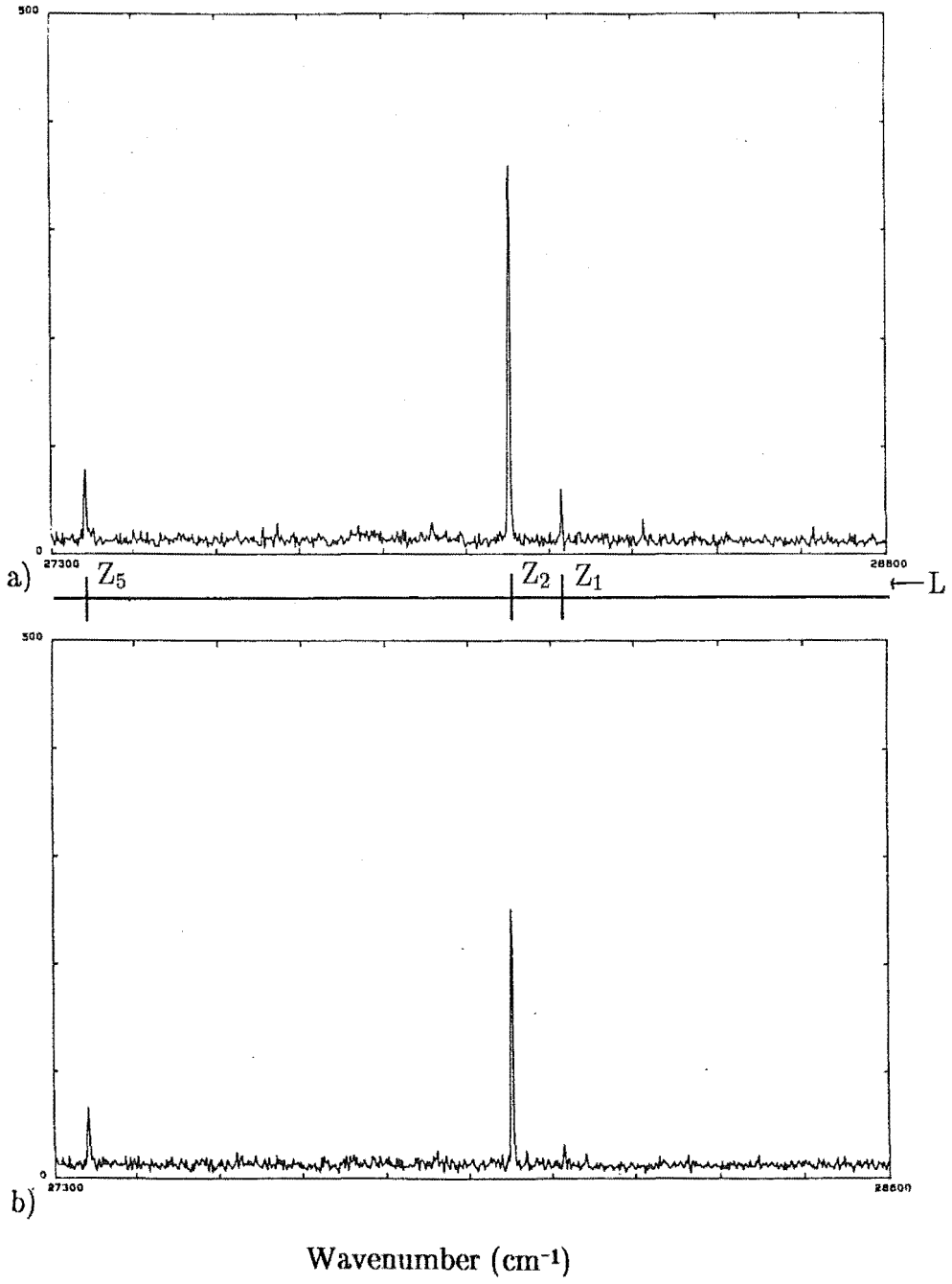

Figure 6.11: 10 K polarised fluorescence spectrum for the $L_1 \rightarrow Z_i$ transitions of the $CaF_2 : Nd^{3+}$ C_{4V} F^- centre for a) (yx) and b) (yy) polarisation.

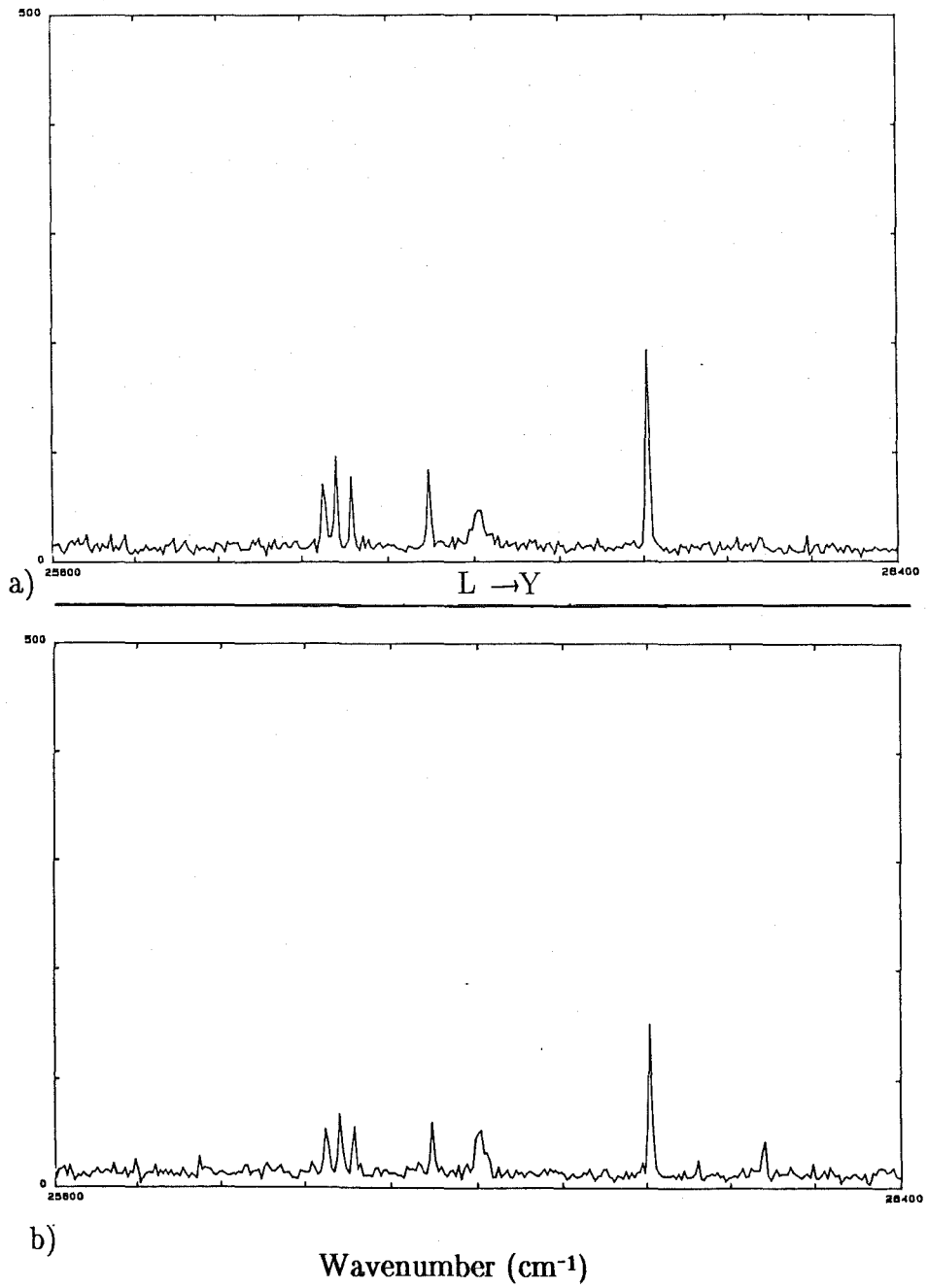

Figure 6.12: 10 K polarised fluorescence spectrum for the $L_1 \rightarrow Y_i$ transitions of the $CaF_2 : Nd^{3+}$ C_{4V} F^- centre for a) (yx) and b) (yy) polarisation.

6.3 M and N Centres

The upconverted fluorescence spectra of the M and N centres in $CaF_2 : Nd^{3+}$ are presented in Figs. 6.13 and 6.14, and the energy levels are listed in Tables 5.11 and 5.12. No upconverted fluorescence was observed when the C multiplet was excited, but weak fluorescence from the D multiplet and extremely weak fluorescence from the C multiplet were observed in the upconverted fluorescence spectrum when the D multiplet was excited (Figs. 6.15 and 6.16). The intensity of the upconverted L multiplet fluorescence of the M centre was found to vary quadratically with the input laser power (see Fig. 6.17) indicating a two photon process . The upconverted fluorescence from the L multiplet terminates at two new energy levels, R_1' and R_2', of the R multiplet. The energy differences between the R_i and the R_i' $(i = 1,2)$ energy levels are presented in Table 6.1. Extremely weak infrared fluorescence from the R_1' energy level was observed with an intensity of approximately 10^2 weaker than the fluorescence from the R_1 energy level. The $R_1' \rightarrow Z_2'$ transition was not observed because of extremely weak fluorescence intensity from R' levels. The presence of the R' levels was also observed in the upconverted fluorescence spectra of the M' centres in $CaF_2 : Nd^{3+} : RE^{3+}$ ($RE^{3+} : Ce^{3+}$ and Gd^{3+}), where extremely weak infrared fluorescence from the R' levels was also observed (see Chapter 8). The presence of the R' levels observed in these upconverted fluorescence spectra indicates a phonon assisted energy transfer process between the rare earth ions within these cluster centres.

Within the limitations of the present equipment, the excitation spectrum shows the infrared fluorescence from the R_1 level and the upconverted fluorescence to be excited by identical frequencies. This indicates a single centre effect rather than a multiple centre co-operative effect. The origin of the double line pattern on the energy levels of the $^4G_{5/2}$ multiplet has been discussed in Chapter 5. The absence of the excitation in the region between the C and D multiplets, as observed for the C_{4V} F^- centre, and the presence of the R' levels suggests the possibility of a combination of an ETU process within a single cluster centre.

No upconverted fluorescence of the M and N centres was observed when excited by the pulsed dye laser. It would be desirable to investigate the possibility of upconversion with a higher power pulsed laser to verify the upconversion process(es) attributed to these centres.

An energy upconversion process was also observed for the $M1$ and $M2$ centres in $CaF_2 : Nd^{3+}$. The upconverted fluorescence of these two centres was extremely weak and their spectra cannot be adequately separated from each other by selective excitation. This is due to the similarity of the $M1$ and $M2$ centres resulting in the overlapping of their energy levels within the excited D multiplet and because of possible energy transfer between these two centres.

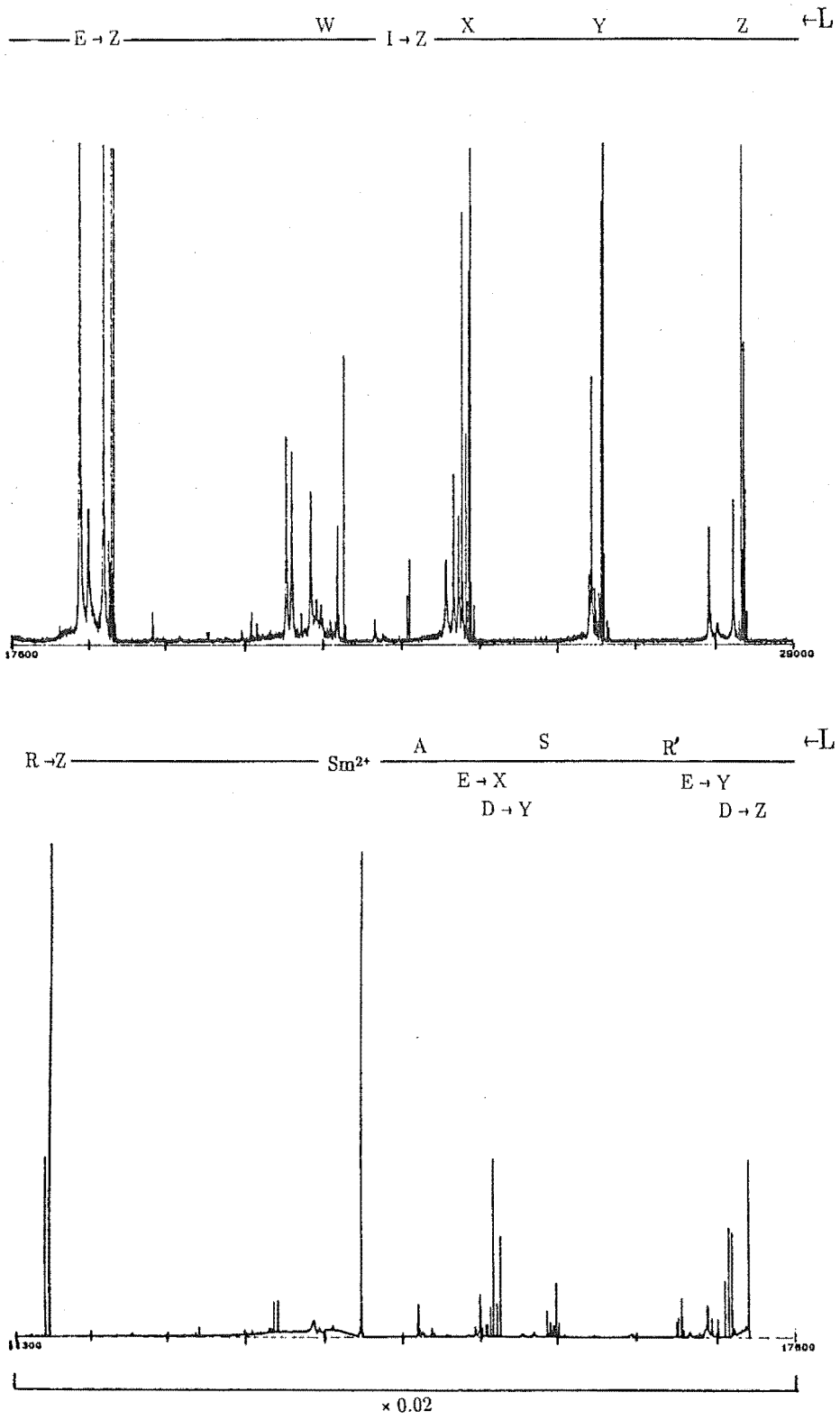

Figure 6.13: 10 K fluorescence spectrum of the $CaF_2 : Nd^{3+}$ M F^- centre for laser excitation at 17258 (in air cm^{-1}) showing the fluorescence transitions caused by upconversion processes.

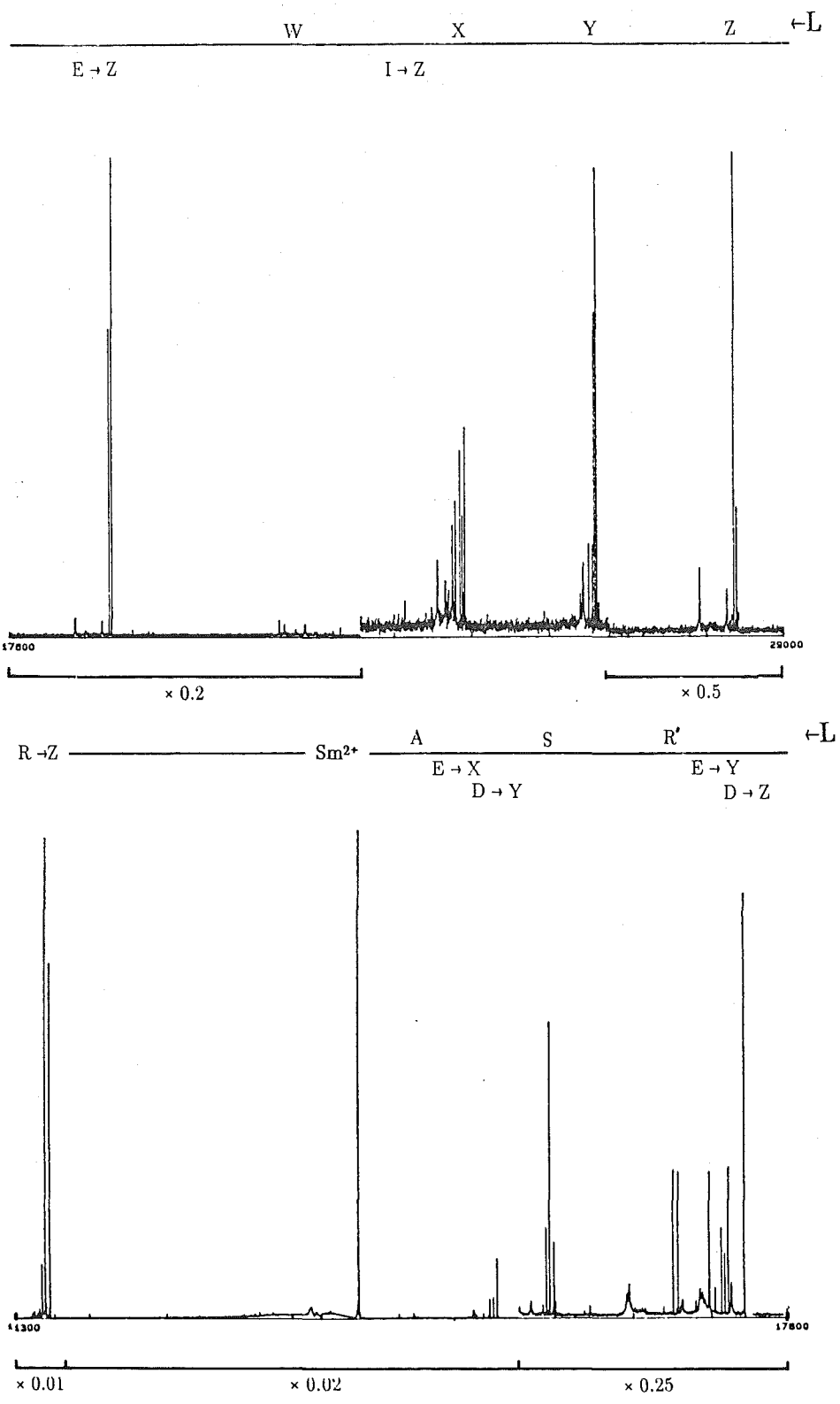

Figure 6.14: 10 K fluorescence spectrum of the $CaF_2 : Nd^{3+}$ N F^- centre for laser excitation at 17269 (in air cm^{-1}) showing the fluorescence transitions caused by upconversion processes.

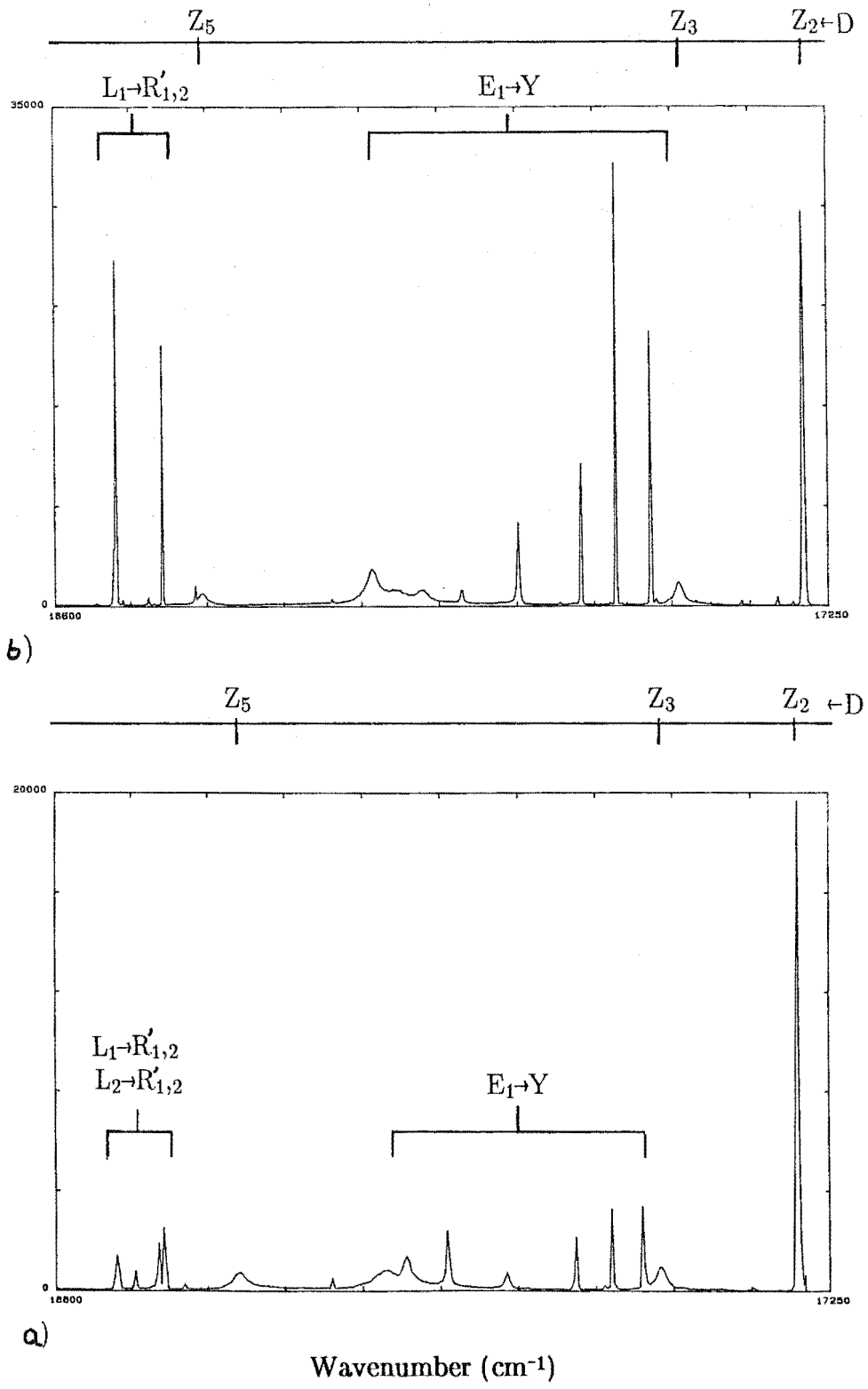

Figure 6.15: 10 K D multiplet fluorescence spectrum of the $CaF_2 : Nd^{3+}$ a) M F^- centre for laser excitation at 17258 cm^{-1}; b) N F^- centre for laser excitation at 17269 cm^{-1}. *undefined line

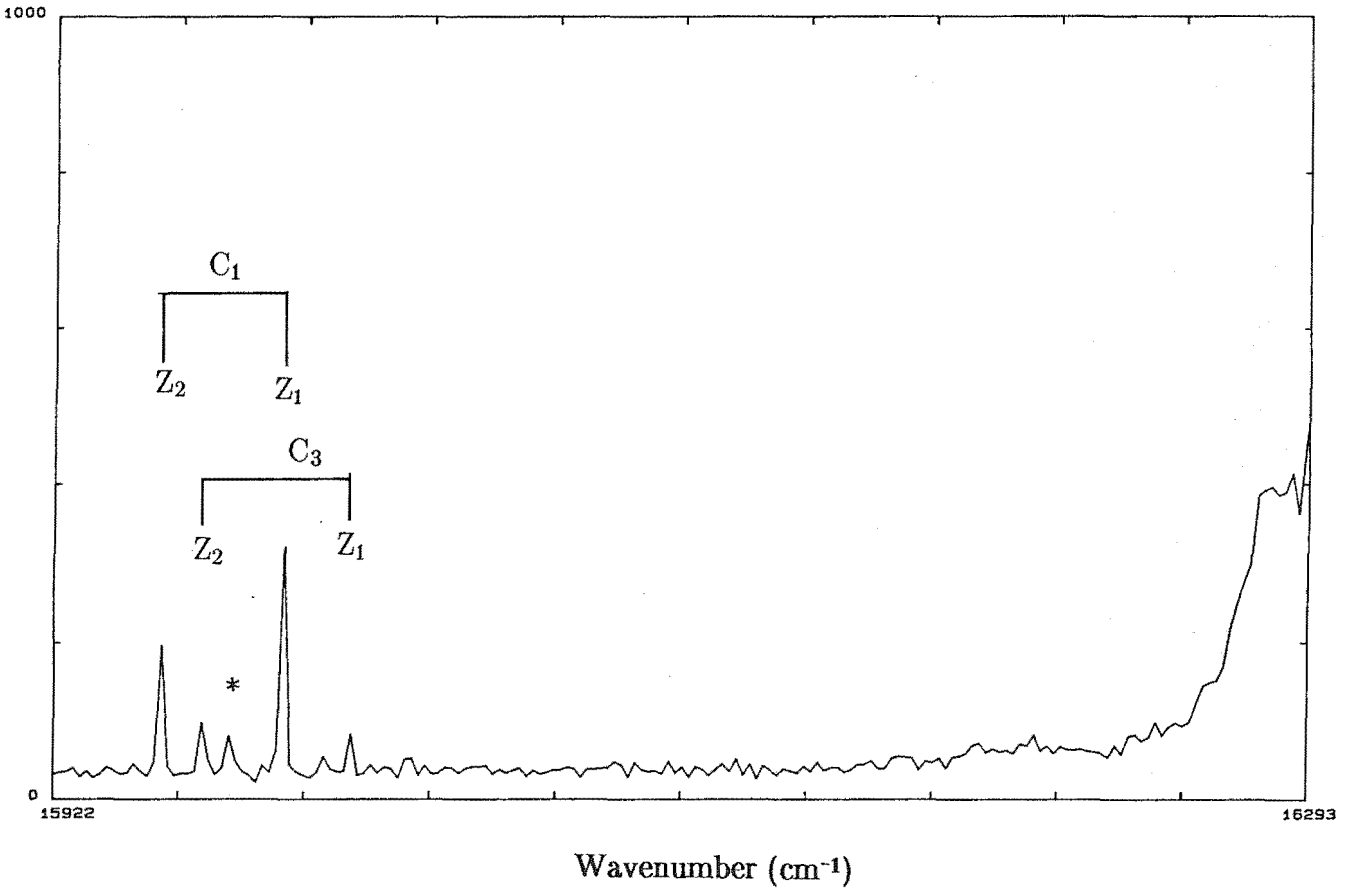

Figure 6.16: 10 K C multiplet fluorescence spectrum of $CaF_2 : Nd^{3+}$ M F^- centre for laser excitation at 17258 (in air cm^{-1}).

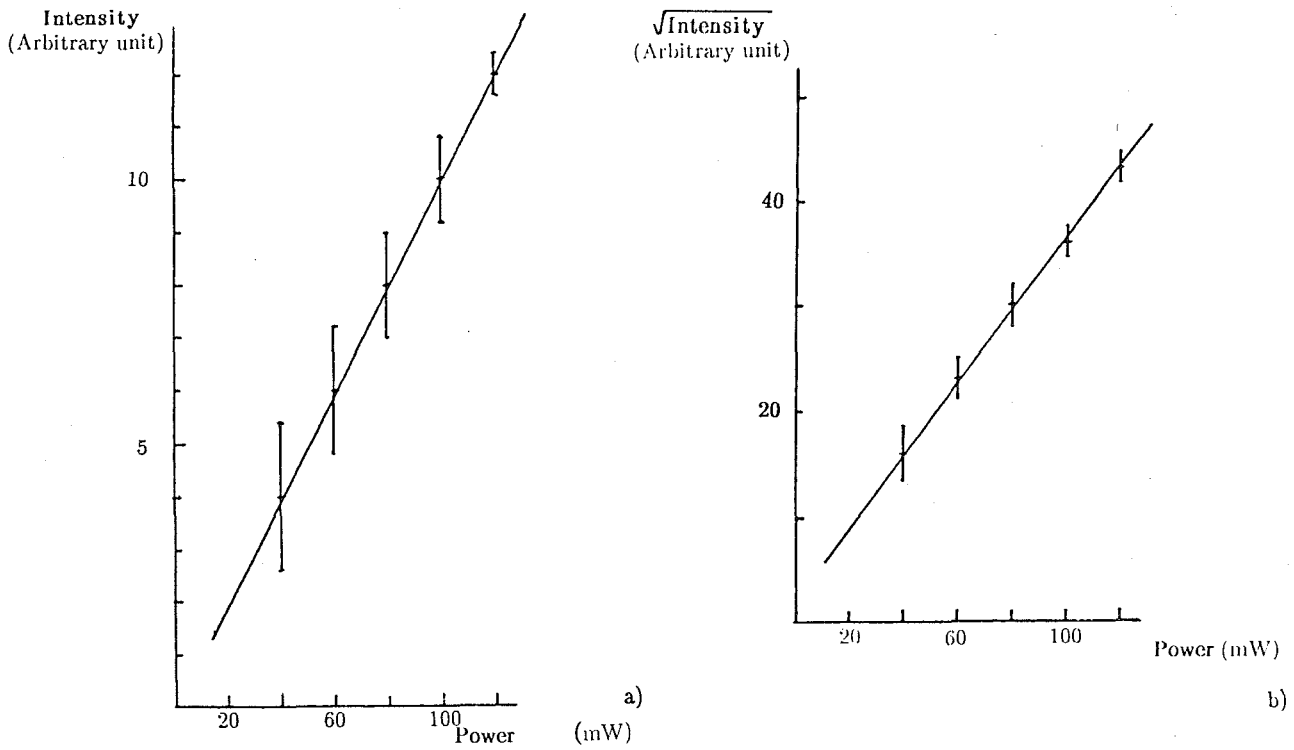

Figure 6.17: 10 K fluorescence of the $CaF_2 : Nd^{3+}$ M F^- centre as a function of incident laser power for a) the $R_1 \rightarrow Z_1$ transition (863.5 nm); b) the $L_1 \rightarrow Z_2$ transition (28223 cm^{-1}).

6.4 Discussion

A study of energy upconversion in the C_{4V} F^- centre in $SrF_2 : Nd^{3+}$ and $CaF_2 : Nd^{3+}$ and the M and N centres in $CaF_2 : Nd^{3+}$ has aided the assignment of the energy levels for these centres. It also provides an opportunity for investigation of the different energy transfer processes involved in energy upconversion.

The results show that the mechanism responsible for the upconversion phenomenon of the single ion C_{4V} F^- centre is likely to be a STEP process. The observation of the R_1' and R_2' energy levels in the multi-ion M and N centres suggests a phonon assisted ETU process within a single centre, although one cannot discount possible STEP contributions. A possible way to distinguish the two processes is by fluorescence lifetime measurements of the upconverted fluorescence and a careful analysis of the fluorescence spectra of the M and N centres in double rare earth ion doped samples.

It is necessary to enhance the concentration of the $M\acute{\imath}$ $(i = 1,2,..)$ centres in $SrF_2 : Nd^{3+}$ and $CaF_2 : Nd^{3+}$ before further investigation of the upconversion characteristics of these cluster centres can be usefully done. Nevertheless, upconversion has been successfully demonstrated for some Nd^{3+} centres, many transitions were observed and further work on optimally doped Nd^{3+} crystals would be worthwhile.

	M	N	M' $Nd^{3+} - Ce^{3+}$	$Nd^{3+} - Gd^{3+}$	$Nd^{3+} - Yb^{3+}$
$R_2 - R_1$	42 (±3.6)	40 (±3.6)	46 (±4)	35 (±3.6)	39.5 (±2.6)
$R_2' - R_1'$	42 (±3)	40 (±3)	46 (±4)	35 (±4)	
$R_i' - R_i$	-6 (±3.6)	-4 (±3.6)	-4 (±4)	-8 (±3.6)	
$Z_2 - Z_1$	35.3 (±1.6)	40.5 (±1.5)	37 (±1)	33.6 (±1.6)	30 (±1)

Table 6.1: The energy separation between chosen levels for the M and N F^- centres in $CaF : Nd^{3+}$ and the M' F^- centres in $CaF_2 : Nd^{3+} : RE^{3+}$. (in air cm^{-1}).

Chapter 7

Crystal Field and Superposition Model Calculations

7.1 Crystal Field Calculation

Parameterisation of the Nd^{3+} F^- tetragonal centre energy levels has been reported by Kiss (1963) and Freeth et al. (1982). The Kiss result is not satisfactory because of his choice of a cubic field to fit the centre. Freeth et al. (1982), using the intermediate coupling wavefunctions of $LaF_3 : Nd^{3+}$ (Carnall et al. 1979), have achieved a good overall fit to the Z and Y energy levels, with a standard deviation of 2.2 cm^{-1} for $SrF_2 : Nd^{3+}$ and 0.7 cm^{-1} for $CaF_2 : Nd^{3+}$. Their results predicted the experimentally unobserved Z_4 level to be at 257.7 cm^{-1} for $SrF_2 : Nd^{3+}$ and 312 cm^{-1} for $CaF_2 : Nd^{3+}$. Also, they observed that the inclusion of intermediate coupling has the effect of interchanging the C_{4V} irreps (γ_6 and γ_7) designation of the two close levels Y_2 and Y_3 in $CaF_2 : Nd^{3+}$ as compared to $SrF_2 : Nd^{3+}$, which is in agreement with their experimental Zeeman data.

A re-analysis of the C_{4V} centres in $SrF_2 : Nd^{3+}$ and $CaF_2 : Nd^{3+}$ is appropriate here because results from the upconverted fluorescence spectra positively identified most of the ^4I energy levels as well as those of other multiplets, providing sufficient data to calculate the intermediate coupling wavefunctions for the C_{4V} F^- centres, rather than use those for $LaF_3 : Nd^{3+}$.

The energy levels of the tetragonal centres were analysed using the crystal field Hamiltonian derived from the point group basis, as shown in equation 2.8. Computer programmes were written to calculate the appropriate crystal field matrix elements and the intermediate coupling reduction factors. The latter were calculated using the intermediate coupling wavefunctions obtained by a computer programme, provided by Dr. C.A. Freeth, which diagonalised the combined electrostatic and spin-orbit matrices. This computer programme uses an iterative least squares fitting procedure to calculate the Racah parameters E^1, E^2 and E^3 and the spin-orbit parameter, ξ, to give an optimum fit to the known multiplet barycentres. The calculated and ex-

perimental barycentres and the least squares fitted parameters are presented in Table 7.1 while the intermediate coupling reduction factors and wavefunctions are presented in Tables. 7.2, 7.3 and 7.4. These intermediate coupling wavefunctions for the C_{4V} F^- centres in $SrF_2 : Nd^{3+}$ and $CaF_2 : Nd^{3+}$ were used in the crystal field calculations.

Freeth (1980) has shown that it is essential to include intermediate coupling in the crystal field analyses of the Nd^{3+} C_{4V} centres, even though the intermediate coupling wavefunctions showed the four ^4I_J multiplets (Z, Y, X and W) to be almost pure $L = 6$, $S = 3/2$ states (see Tables 7.3 and 7.4). The crystal field analyses which follow were assigned with a spin-orbit parameter, ξ_i, for each multiplet, where $i = Z$, Y, X and W. The differing values show the departure of the multiplet spacing from the Lande interval rule indicating the slight breakdown of the Russell-Saunders coupling scheme.

Crystal field J mixing is significant (Freeth 1980) and must be included in the crystal field analyses. This is achieved by including all the matrix elements ($\langle LSJ|V_{CF}|LSJ'\rangle$) of the crystal field not diagonal in J in the calculation.

To calculate the magnetic splitting factors, $s_{\|}$ and $s_{\perp}$, the Zeeman and crystal field matrices were diagonalised simultaneously. The orbital angular momentum reduction factor, k, was included in the Zeeman interaction Hamiltonian as described in Chapter 2. Calculations (Freeth 1980) have shown that the splitting factors are sensitive to the composition of the eigenfunction, hence the measured splitting factors for the ground state have been included wherever possible in the crystal field calculations.

The R multiplet was not included in the final crystal field calculations because of its interactions with other close lying multiplets. The inclusion of all these interactions would require a crystal field calculation using all the 364 levels of the $4f^3$ configuration.

7.2 C_{4V} Centres in $SrF_2 : Nd^{3+}$

A crystal field analysis of the C_{4V} F^- centre in $SrF_2 : Nd^{3+}$ and its hydrogenic analogues were carried out in the manner described above.

In the C_{4V} F^- centre all the known energy levels in the ^4I multiplets and the g-values of the Z_1 level (McMahon) were included in the crystal field analysis. An attempt to fit the 164 cm^{-1} unidentified level was unsuccessful and, when the level located at 268 cm^{-1} (by upconversion) was included as Z_4, it deviated from the calculated value by approximately 10 cm^{-1}. A calculation using the intermediate coupling wavefunctions of the $LaF_3 : Nd^{3+}$ gave similar results which raises doubts as to the assignment of this level to Z_4. When both the levels at 164 cm^{-1} and 268 cm^{-1} were excluded from the crystal field analysis, a better overall fit between the experimental and

the calculated energy levels was obtained, as expected. The least squares fitted crystal field parameters, spin-orbit parameters and the orbital reduction parameter that gave the optimum fit to experimental data are presented in Table 7.5. The calculated and the observed energy levels are compared in Table 7.6.

The $s\langle 111\rangle$ splitting factors for the Y levels were calculated using the parameters in Table 7.7 and are compared with the experimental and calculated values of Freeth et al. (1982) using the relationship :

$$s\langle 111\rangle = \frac{1}{\sqrt{3}} \left(s_{\parallel}^2 + 2s_{\perp}^2\right)^{1/2} \quad .$$

The calculated splitting factors for the Y_1 and Y_4 levels compare well with those calculated by Freeth (1980) (see Table 7.7) and are slightly larger than the experimental values (Freeth 1980).

A crystal field analysis of the T^-, D^- and H^- analogues of the C_{4V} F^- centre were carried out using the intermediate coupling wavefunctions for the $SrF_2 : Nd^{3+}$ C_{4V} F^- centre as there is no data on the W and X multiplets for the hydrogenic C_{4V} centres. The results predict the experimentally unobserved Z_4 level to be at 302.8 cm^{-1} for T^-, 295.8 cm^{-1} for D^- and 295.7 cm^{-1} for H^-. An attempt to fit the additional line observed in the region of the $R_1 \rightarrow Z_5$ transition for the D^- and H^- analogues (see Fig. 5.1) was unsuccessful. The least squares fitted parameters that gave the optimum fit to experimental data are presented in Table 7.5 while the calculated and the observed energy levels are compared in Tables 7.8 to 7.10. The C_{4V} irreps designation (γ_6 and γ_7) of the Y_2 and Y_3 levels interchanged for the T^-, D^- and H^- analogues compared to those of the F^-, is consistent with the polarisation data as disscused in Chapter 5.

7.3 C_{4V} Centres in $CaF_2 : Nd^{3+}$

A crystal field analysis of the C_{4V} F^- and D^- centres $CaF_2 : Nd^{3+}$ was carried out in a similar manner to that described for the corresponding $SrF_2 : Nd^{3+}$ C_{4V} centres. The energy levels of the ^4I multiplets and the g-values for the Z_1 level (Bleaney et al. 1956) were included in the crystal field analyses and the least squares fitted parameters which gave the optimum fit to the experimental data are presented in Table 7.5, while the calculated and observed energy levels are compared in Tables 7.11 and 7.12. The results predict the experimentally unobserved Z_4 level to be at 312.1 cm^{-1} for F^- and 306.8 cm^{-1} for D^-. The results show the γ_7 and γ_6 designation of the close lying Y_2 and Y_3 levels for both the F^- and D^- centres are interchanged compared to the F^- centres in $SrF_2 : Nd^{3+}$. The inclusion of the R levels has the same effect as intermediate coupling in causing the interchanging of the γ_6 and γ_7 designation of the Y_2 and Y_3 levels.

For the F^- centre, the splitting factors for the ^4I multiplets were calculated for magnetic field strength varying from 1 to 5 tesla and are presented in Fig. 7.1. The splitting factors of the Z and Y multiplets exhibit similar patterns to those calculated by Freeth (1980) and the values are compared in Table 7.7. In the $s_{\|}$ case, where the applied magnetic field is parallel to the four-fold axis of the C_{4V} centre, the two Zeeman levels (γ_5' and γ_6') belonging to the doubly degenerate Y_3 (γ_6) level cross over in energy at a magnetic field strength of 3 tesla. Recalculations of the splitting factors using Freeth's crystal field parameters show that the re-adjusted set of crystal field parameters, which was used to obtained a better match of the Y_2 and Y_3 levels, has the effect of shifting the cross over of the two Zeeman levels of Y_3 to a higher magnetic field. The energy of the Zeeman transitions between the Y levels and the Z_1 ground level were calculated following the transitions rules computed by Freeth (1980) and are presented in Fig. 7.2. The results show no improvement on those calculated by Freeth (1980) which indicate that inclusion of all the energy levels of the ^4I multiplets cannot exactly fit the Zeeman transitions.

7.4 Superposition Model Calculation for the C_{4V} Centres

Direct information about the distortion of the C_{4V} centres in $CaF_2 : Nd^{3+}$ appears to be limited to the ENDOR data of Kiro et al. (1971) for the F^- and the H^- centres. The ENDOR results show the Nd^{3+} ion is displaced by $0.08a_o$, where a_o (0.137 nm for CaF_2 and 0.145 nm for SrF_2) is one quarter of the cubic lattice parameter, from the centre of the cube towards the intersitial charge compensation ion, hence causing only a small distortion of the C_{4V} F^- centre in $CaF_2 : Nd^{3+}$. An even smaller distortion is expected for the larger SrF_2 lattice with greater separation of the Nd^{3+} from the charge compensating F^- ion. Reid and Butler (1982) have calculated the values for the co-ordination angles, θ_a and θ_b, for the $CaF_2 : Nd^{3+}$ F^- C_{4V} centre to be 63^o ($\pm 2^o$) and 123^o ($\pm 2^o$) respectively (see Fig. 2.1).

A computer programme based on that of Reid (1988) was used to calculate the distortion of the C_{4V} centres in $CaF_2 : Nd^{3+}$ and $SrF_2 : Nd^{3+}$. Superposition model calculations require knowledge of the distances between the rare earth ion and its surrounding ligands. The ENDOR (Kiro et al. 1971) results show the displacement of the Nd^{3+} ion in the C_{4V} centres in $CaF_2 : Nd^{3+}$. However, no information was presented concerning the likely displacement of the F^- ions surrounding the Nd^{3+} ion. Hence, the following assumptions (following those of Reid 1981) are necessary : for both $SrF_2 : Nd^{3+}$ and $CaF_2 : Nd^{3+}$ the Nd^{3+} ion is displaced from the centre of the cube by $0.08a_o$ towards the interstitial charge compensating ion. The distances between the

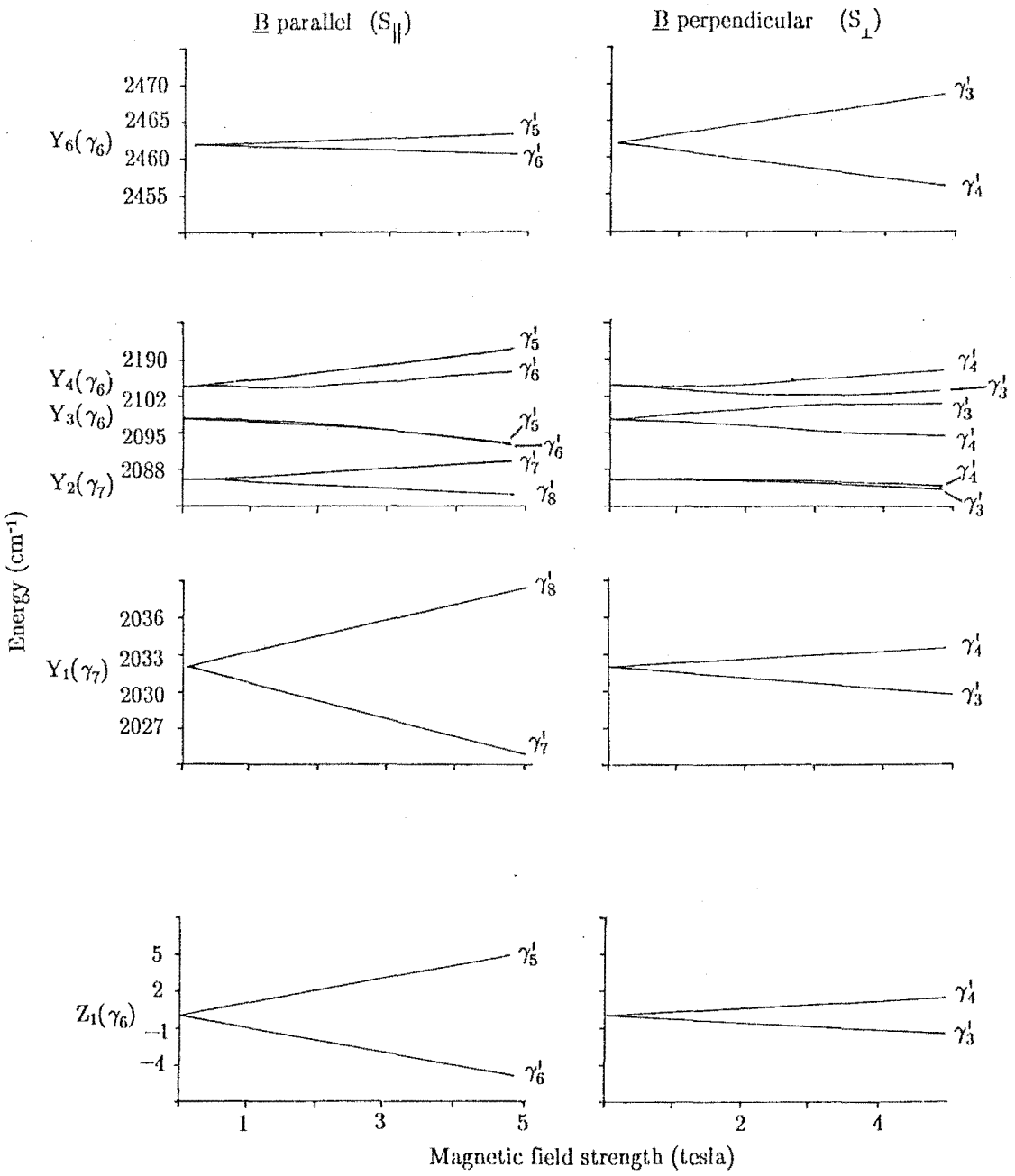

Figure 7.1: Calculated $^4I_{9/2}$ (Z_1) and $^4I_{11/2}$ (Y) C_{4V} Zeeman energy levels for $CaF_2 : Nd^{3+}$ as a function of parallel and perpendicular $\underline{B}$.

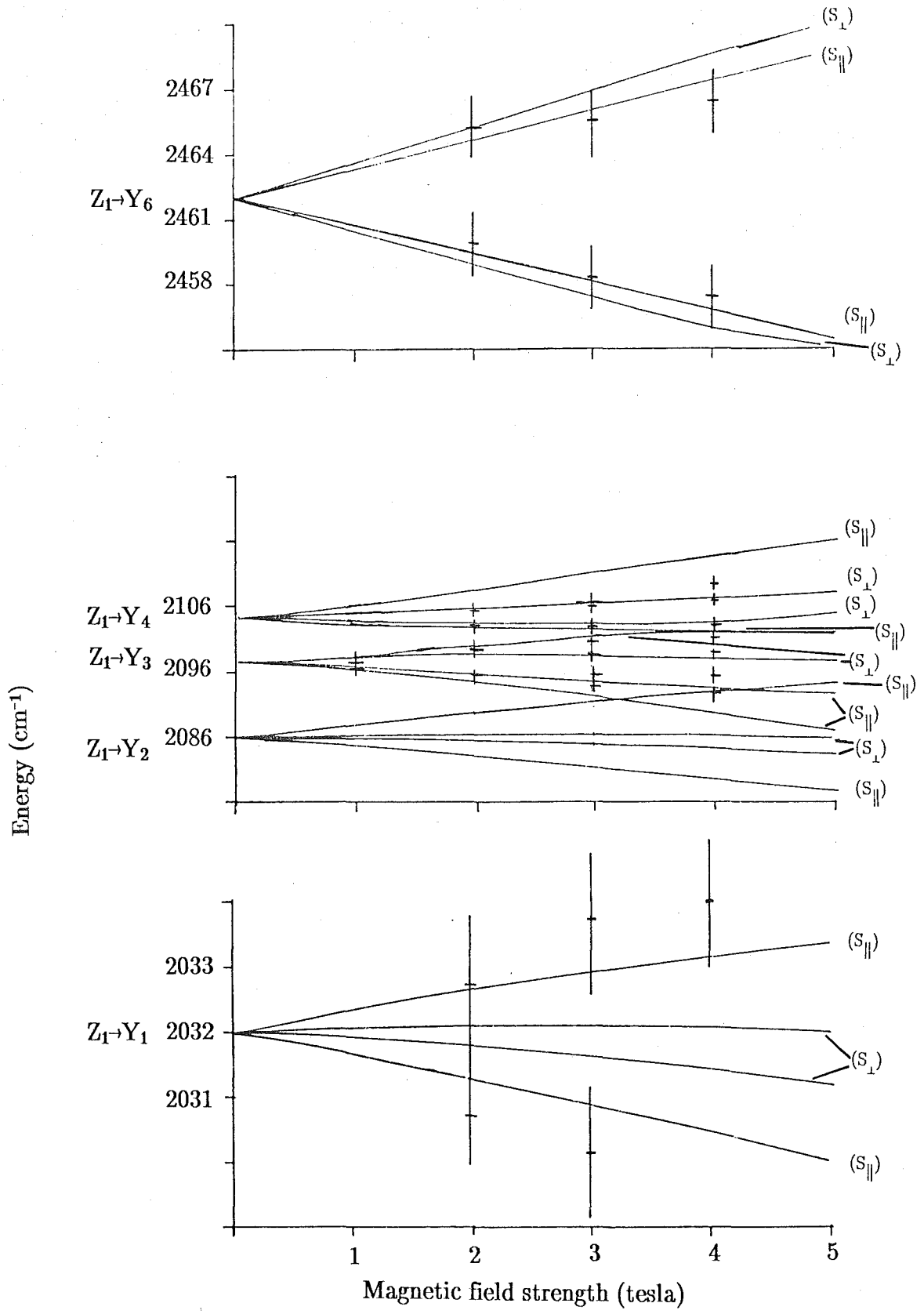

Figure 7.2: Calculated C_{4V} $^4I_{9/2}$ (Z_1) $\rightarrow$ $^4I_{11/2}$ (Y) Zeeman transitions in $CaF_2 : Nd^{3+}$ for $\underline{B} \parallel \underline{k}$. + experimental data of Freeth (1980)

$\underline{B}$ ⟨100⟩ crystal direction

eight surrounding F^- ions are assumed constant. For the F^- ions (see Fig. 2.1) at positions 1 to 4 the distance is $((2+(1-0.08)^2)^{1/2})a_o$ and for the F^- ions at positions 5 to 8 the distance is $((2+(1+0.08)^2)^{1/2})a_o$. The charge compensating F^- ion in the interstitial position is at a distance $(2-0.08)a_o$ from the Nd^{3+} ion; the intrinsic parameters $\overline{A}_4$ and $\overline{A}_6$ follow a power law $(R_0/R)^{t_k}$, where $t_4 = 6.3$ (± 1.4) and $t_6 = 10.1$ (± 10.1) are the values obtained for a cubic symmetry centre (Newman 1978).

The ratios B^4_{tet}/B^4_{oct} and B^6_{tet}/B^6_{oct} for various values of the co-ordination angles θ_b and θ_a have been calculated. Fig. 7.3 shows the calculated results for the C_{4V} centre where the ratios B^4_{tet}/B^4_{oct} and B^6_{tet}/B^6_{oct} are plotted against the angle θ_b for various values of θ_a. The co-ordination angles for the various C_{4V} centres in $CaF_2 : Nd^{3+}$ and $SrF_2 : Nd^{3+}$ are calculated from their appropriate crystal field parameters and the results are presented in Table 7.13. The results are comparable with those of Reid and Butler (1982), but the results for $SrF_2 : Nd^{3+}$, $CaF_2 : Nd^{3+}$ and those of Reid and Butler gave values for θ_b smaller than the cubic value of 125.3°. This cannot be the case as it would mean the ligand ions at positions 5 to 8 move closer towards the direction of the charge compensating ion (i.e. attraction). Reid and Butler (1982) have noted that some of their assumptions could be modified to increase this angle; namely decreasing the power dependence or increasing the distance between the Nd^{3+} ion and the F^- ions in positions 5 to 8 (see Fig. 2.1). Additional results from ENDOR on the exact position of the surrounding ligand ions are needed to improve the present calculations.

7.5 Discussion

The superposition model predicted that the ratio B^4_{oct}/B^6_{oct} is smaller for the tetragonal centre than the cubic centre, hence the O_h part of the crystal field is not the same as that for the Nd^{3+} ion in a cubic centre.

Kiro et al. (1969) concluded that $(g_\parallel - g_\perp)_{H^-}$ is greater than $(g_\parallel - g_\perp)_{F^-}$ for $CaF_2 : Nd^{3+}$ which is indicative of a larger tetragonal distortion in the case of the H^- centre. The g-values for the F^-, D^- and H^- centres in $CaF_2 : Nd^{3+}$ and the F^- centre in $SrF_2 : Nd^{3+}$ (Bleaney et al. 1956, Kiro et al. 1969) show that the D^- and H^- centres in $CaF_2 : Nd^{3+}$ have a larger tetragonal distortion than the F^- centre in $CaF_2 : Nd^{3+}$. These results are in agreement with the ratios of the crystal field parameters B^4_{tet}/B^4_{oct}, B^6_{tet}/B^6_{oct} and B^4_{oct}/B^6_{oct} obtained for the various C_{4V} centres. The co-ordination angles derived from the superposition model do not give such a clear indication of the distortion for the various C_{4V} centres. The crystal field parameters obtained from the energy level calculations gave a good overall fit to the energy levels of high energy multiplets (Reid 1988). This gives one confidence in using the obtained crystal field wavefunctions for other calculations, such

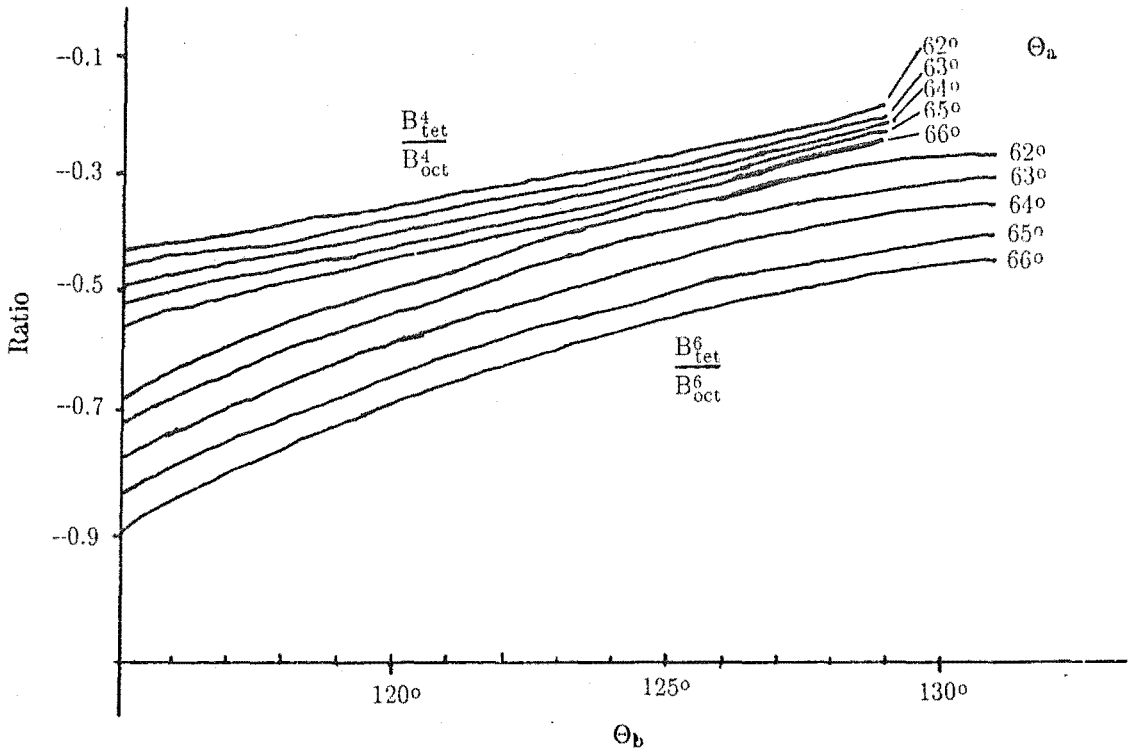

Figure 7.3: Superposition model parameter ratios for $CaF_2 : Nd^{3+}$ and $SrF_2 : Nd^{3+}$ for the case $t_4 = 6.3$, $t_6 = 10.1$ and for the Nd^{3+} ion displaced by $0.08a_o$ towards the interstitial charge compensating ion.

as intensity calculations outlined by Wybourne (1965).

An attempt was made to carry out a crystal field analysis of the M centre observed in $CaF_2 : Nd^{3+}$. Following the suggestions of Butler (1987) and assuming that the configuration for the M centre as shown in Fig. 5.78 is correct, a first approximation would be to consider only one of the two Nd^{3+} ions and the two charge compensating F^- ions. This reduces the symmetry of the M centre to C_{2V} as shown in Fig. 7.4. Such a first approximation would also have application for the similar M' centres in $CaF_2 : Nd^{3+} : RE^{3+}$ (which will be presented in Chapter 8). These M' centres have the same configuration as that of the M centre (Voron'ko et al. 1968) but with one of the two Nd^{3+} ions being substituted by a RE^{3+} ion.

This first approximation calculation was tried for the M centre, but was found to be unsatisfactory, as will be shown below. However, details are presented to indicate the relevant steps required in this calculation. The basic assumption of the superposition model is that the crystal field effects of individual ions are additive and independent of each other. Therefore, the interactions of the Nd^{3+} ion with each of the two charge compensating F^- ions can be calculated separately before combining to give the overall effect of the centre. Each of the charge compensating F^- ions and the Nd^{3+} ion form C_{4V} symmetry species with their principal four-fold axis perpendicular to each other. Hence :

$$H_{F'} = H_{C_{4V}}$$

and

$$H_{F''} = R_y\left(\frac{\pi}{2}\right) H_{F'} \quad ,$$

where $R_y(\pi/2)$ is a rotation about the y axis by $\pi/2$. Therefore, the combined Hamiltonian for the configuration is :

$$\begin{aligned}
H_{tot} &= H_{F'} + H_{F''} \\
&= H_{C_{4V}} + R_y\left(\frac{\pi}{2}\right) H_{F'} \\
&= H_{C_{4V}} + R_y\left(\frac{\pi}{2}\right) H_{C_{4V}} \\
&= 2X^{4+0+0+0}U^{4+0+0+0} + 2X^{6+0+0+0}U^{6+0+0+0} \\
&\quad + \frac{1}{2}X^{2+2+0+0}\left(U^{2+2+0+0} + \sqrt{3}U^{2+2+2+0}\right) \\
&\quad + \frac{1}{2}X^{4+2+0+0}\left(U^{4+2+0+0} + \sqrt{3}U^{4+2+2+0}\right) \\
&\quad + \frac{1}{2}X^{6+2+0+0}\left(U^{6+2+0+0} + \sqrt{3}U^{6+2+2+0}\right) \\
&= 2B^4_{oct}\left[\sqrt{\frac{7}{12}}C^{(4)}_0 + \sqrt{\frac{5}{24}}\left(C^{(4)}_4 + C^{(4)}_{-4}\right)\right]
\end{aligned}$$

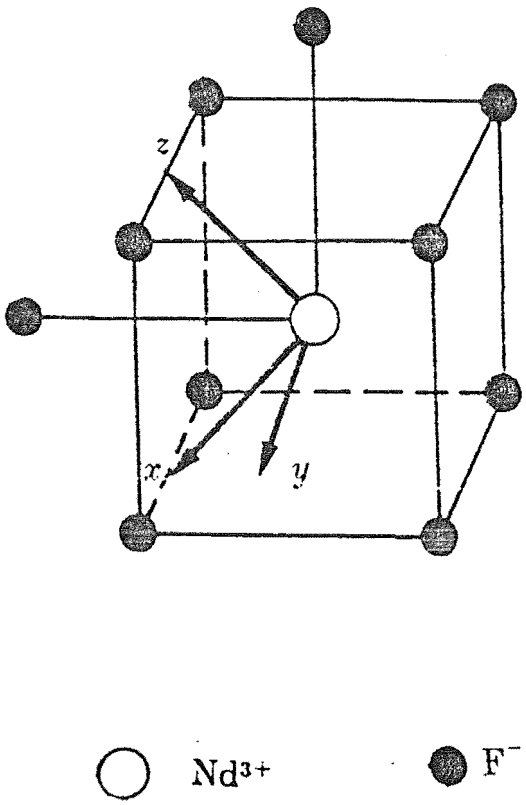

Figure 7.4: Model of a C_{2V} symmetry centre derived from the M centre by the removal of one of the two Nd^{3+} ions of the M F^- centre.

$$
\begin{aligned}
&+2B^6_{oct}\left[\sqrt{\frac{7}{16}}\left(C^{(6)}_4+C^{(6)}_{-4}\right)-\sqrt{\frac{1}{8}}\,C^{(6)}_0\right]\\
&+\frac{1}{2}B^2_{tet}\left[-C^{(2)}_0-\sqrt{\frac{3}{2}}\left(C^{(2)}_2+C^{(2)}_{-2}\right)\right]\\
&+\frac{1}{2}B^4_{tet}\left[\sqrt{\frac{5}{12}}\,C^{(4)}_0-\sqrt{\frac{7}{24}}\left(C^{(4)}_4+C^{(4)}_{-4}\right)-\sqrt{\frac{3}{2}}\left(C^{(4)}_2+C^{(4)}_{-2}\right)\right]\\
&+\frac{1}{2}B^6_{tet}\left[\sqrt{\frac{7}{8}}\,C^{(6)}_0+\frac{1}{4}\left(C^{(6)}_4+C^{(6)}_{-4}\right)\right.\\
&\quad\left.+\sqrt{\frac{15}{32}}\left(C^{(6)}_2+C^{(6)}_{-2}\right)+\sqrt{\frac{33}{32}}\left(C^{(6)}_6+C^{(6)}_{-6}\right)\right]\ .
\end{aligned}
$$

This method has the advantage of all the parameters being able to relate to those of the known C_{4V} centre and no free parameters are generated.

The preliminary results gave a least squares energy level fit to fourteen levels of the ^4I_J multiplets to 11.8 cm^{-1}, but the crystal field parameter B^2_{tet} is of opposite sign to that for the C_{4V} centres, which is not consistent with the parameterisation scheme adopted. It is concluded that the effects of the second Nd^{3+} ion cannot be neglected and any comprehensive future calculation would need to include interactions between the two Nd^{3+} ions within the M centre.

State	$SrF_2 : Nd^{3+}$ Experimental	Theory (cm^{-1})	Deviation	$CaF_2 : Nd^{3+}$ Experimental	Theory (cm^{-1})	Deviation
$^4F_{3/2}$	11366	11299	67	11394	11289	105
$^4S_{3/2}$	13469	13408	61	13461	13397	64
$^2H_{11/2}$	15825	15872	-47	15847	15899	-52
$^4GF_{5/2}$	17047	16950	97	17026	16936	90
$^2P_{1/2}$	23232	23141	91	23235	23136	99
$^4D_{3/2}$	27991	28151	-160	27946	28122	-176

	$SrF_2 : Nd^{3+}$ (cm^{-1})	$CaF_2 : Nd^{3+}$ (cm^{-1})
Standard Deviation	94.7	105.4
E^1	4948.35	4949.86
E^2	27.22	27.03
E^3	477.39	477.03
ξ	991.97	991.12

Table 7.1: Calculated and experimental free ion energies for the Nd^{3+} ion.

	$SrF_2 : Nd^{3+}$		
States	k=2	k=4	k=6
$^4I_{9/2}$-$^4I_{9/2}$	0.9401	0.9468	0.9435
$^4I_{11/2}$-$^4I_{9/2}$	-0.9979	-0.9968	-0.9835
$^4I_{11/2}$-$^4I_{11/2}$	0.9802	0.9714	0.9696
$^4I_{13/2}$-$^4I_{9/2}$	0.1637	0.9458	1.0017
$^4I_{13/2}$-$^4I_{11/2}$	-1.0009	-1.0154	-0.9895
$^4I_{13/2}$-$^4I_{13/2}$	1.0140	1.0004	0.9884
$^4I_{15/2}$-$^4I_{9/2}$	1.0000	0.1157	1.0717
$^4I_{15/2}$-$^4I_{11/2}$	-0.1283	-0.8960	-1.0134
$^4I_{15/2}$-$^4I_{13/2}$	0.9872	1.0093	0.9887
$^4I_{15/2}$-$^4I_{15/2}$	1.0369	1.0055	0.9808

	$CaF_2 : Nd^{3+}$		
States	k=2	k=4	k=6
$^4I_{9/2}$-$^4I_{9/2}$	0.9405	0.9470	0.9439
$^4I_{11/2}$-$^4I_{9/2}$	-0.9980	-0.9968	-0.9836
$^4I_{11/2}$-$^4I_{11/2}$	0.9803	0.9714	0.9697
$^4I_{13/2}$-$^4I_{9/2}$	0.1664	0.9460	1.0017
$^4I_{13/2}$-$^4I_{11/2}$	-1.0009	-1.0154	-0.9896
$^4I_{13/2}$-$^4I_{13/2}$	1.0139	1.0004	0.9885
$^4I_{15/2}$-$^4I_{9/2}$	1.0000	0.1211	1.0712
$^4I_{15/2}$-$^4I_{11/2}$	-0.1304	-0.8963	-1.01331
$^4I_{15/2}$-$^4I_{13/2}$	0.9872	1.0093	0.9888
$^4I_{15/2}$-$^4I_{15/2}$	1.0367	1.0055	0.9809

Table 7.2: Intermediate coupling factors for the Nd^{3+} ion computed from the parameters in Table 7.1.

Eigenvalues	Eigenvectors						
$J = \frac{1}{2}$	^4D	^2P					
23136.1	0.2920709	0.9563967					
28746.2	0.9563967	-0.2920709					
$J = \frac{3}{2}$	^4S	^4D	^4F	^2P	$^2D1$	$^2D2$	
11289.2	0.0640467	0.0131023	-0.9636822	0.0718437	-0.2440541	0.0481556	
13396.6	0.9637349	0.0181013	0.0944109	0.2444500	-0.0470927	-0.0007161	
21144.8	-0.2211273	0.1239941	0.2107780	0.6496454	-0.6835504	0.0449511	
26597.2	0.1228222	-0.3313241	0.1229808	-0.6366830	-0.6712272	-0.0640595	
28121.8	0.0554107	0.8424216	0.0445130	-0.3220327	-0.1307767	0.4055446	
33731.4	-0.0077605	-0.4058032	0.0294968	0.0630342	0.0577083	0.9094448	
$J = \frac{5}{2}$	^4D	^4F	^4G	$^2D1$	$^2D2$	$^2F1$	$^2F2$
12486.9	-0.0013381	0.9844865	-0.0264017	0.1666214	-0.0055011	-0.0318487	-0.0357794
16935.9	0.0103738	-0.0332217	-0.9918940	0.0051890	0.0186965	-0.0850824	-0.0855539
23263.0	0.0549002	-0.1634493	0.0203493	0.9631667	0.2002373	-0.0360611	-0.0277602
28359.3	-0.9087343	-0.0202842	-0.0308567	0.1324514	-0.3723191	0.0902725	0.0923280
35444.7	-0.4075606	0.0109390	0.0623874	-0.1586291	0.7808992	-0.2621407	-0.3552436
40063.6	0.0677261	-0.0493536	0.1001033	0.0408327	-0.4593866	-0.5511766	-0.6829771
69264.2	-0.0196498	-0.0001665	0.0130433	-0.0120981	0.0080052	-0.7808865	0.6240590
$J = \frac{7}{2}$	^4D	^4F	^4G	$^2F1$	$^2F2$	$^2G1$	$^2G2$
13516.7	0.0038805	0.9380941	0.0548999	-0.0325842	-0.0425678	-0.2586099	0.2172499
16813.2	-0.0021601	-0.3100892	0.5487411	0.0146678	0.0161777	-0.5758894	0.5201901
18931.4	-0.0090330	0.1471072	0.8306690	0.0520110	0.0568569	0.4103457	-0.3375581
30549.5	0.9934527	-0.0077861	0.0163223	-0.0948470	-0.0598586	0.0120653	0.0001590
41489.9	0.1041275	0.0446444	-0.0696140	0.5452725	0.8233986	-0.0789459	-0.0279013
48794.4	-0.0046479	0.0108743	-0.0239139	-0.0408858	0.1128177	0.6505032	0.7494894
68007.1	-0.0456747	-0.0034081	0.0131829	-0.8294747	0.5480853	-0.0596350	-0.0758046
$J = \frac{9}{2}$	^4F	^4G	^4I	$^2G1$	$^2G2$	$^2H1$	$^2H2$
0	0.0044401	0.0098363	0.9797915	-0.0220590	0.0199918	0.0683630	-0.1852899
12149.4	-0.3295128	-0.1511262	0.1750134	0.3583959	-0.3113989	-0.3056381	0.7205005
14956.3	-0.8620016	0.0284088	-0.0828284	0.1597402	-0.1162282	0.1655872	-0.4275986
19538.0	-0.2262307	0.8333481	0.0405094	-0.2827261	0.2859272	-0.1478451	0.2629885
21166.6	0.3111262	0.5251599	-0.0287585	0.5767954	-0.4889211	0.0115314	-0.2339035
33061.0	0.0031241	0.0738273	0.0070695	-0.0287021	-0.1092263	0.9184007	0.3718546
47840.6	-0.0191111	0.0233357	-0.0005536	-0.6573417	-0.7459179	-0.0950885	-0.0394531
$J = \frac{11}{2}$	^4G	^4I	$^2H1$	$^2H2$	^2I		
2145.86	-0.0088533	-0.9931870	-0.0435640	0.1063902	0.0168698		
15899.3	-0.2395617	0.1125648	-0.3962627	0.8774116	-0.0553555		
21811.8	0.9592536	0.0186146	-0.2351788	0.1544424	0.0180119		
28433.5	-0.0798713	0.0188355	-0.3268076	-0.1128470	0.9347343		
34684.0	-0.1264313	-0.0144071	-0.8239938	-0.4268995	-0.3501408		
$J = \frac{13}{2}$	^4I	^2I	^2K				
4393.28	0.9967204	-0.0270745	0.0762595				
18636.8	-0.0787683	-0.1085763	0.9909625				
29917.0	-0.0185499	-0.9937194	-0.1103528				
$J = \frac{15}{2}$	^4I	^2K	^2L				
6691.8	0.9903430	0.1381041	-0.0121634				
20889.3	0.1371698	-0.9633335	0.2305928				
29621.9	-0.0201284	0.2300345	0.9729743				

Table 7.3: Energies and eigenvectors for the intermediate coupled states of $CaF_2 : Nd^{3+}$ using the parameters of Table 7.1.

Eigenvalues	Eigenvectors						
$J = \frac{1}{2}$	^4D	^2P					
23141.2	0.2913567	0.9566145					
28768.6	0.9566145	-0.2913567					
$J = \frac{3}{2}$	^4S	^4D	^4F	^2P	$^2D1$	$^2D2$	
11298.7	-0.0642426	-0.0130323	0.9635662	-0.0720845	0.2445379	-0.0474149	
13407.7	0.9635902	0.0181101	0.0947622	0.2448465	-0.0472816	-0.0008793	
21143.0	-0.2214922	0.1224365	0.2111827	0.6488324	-0.6846175	0.0408390	
26591.5	-0.1230236	0.3347944	-0.1223719	0.6362417	0.6692017	0.0718928	
28151.3	0.0558288	0.8413501	0.0454701	-0.3245690	-0.1371043	0.4034885	
33761.6	-0.0075110	-0.4056528	0.0303264	0.0610088	0.0513419	0.9100064	
$J = \frac{5}{2}$	^4D	^4F	^4G	$^2D1$	$^2D2$	$^2F1$	$^2F2$
12497.3	-0.0012556	0.9843801	-0.0264502	0.1672344	-0.0049504	-0.0319268	-0.0358241
16950.2	0.0103894	-0.0333379	-0.9918774	0.0053963	0.0187447	-0.0851938	-0.0855647
23225.1	0.0562928	-0.1639879	0.0207478	0.9620665	0.2045112	-0.0363527	-0.0281108
28389.5	-0.9092967	-0.0205319	-0.0307757	0.1351325	-0.3700699	0.0901580	0.0920313
35494.1	-0.4060058	0.0110225	0.0627126	-0.1618392	0.7795386	-0.2640764	-0.3570661
40094.2	0.0683673	-0.0494895	0.1000004	0.0428054	-0.4616290	-0.5511389	-0.6813141
69296.4	-0.0196543	-0.0001446	0.0129989	-0.0121029	0.0081074	-0.7802450	0.6248602
$J = \frac{7}{2}$	^4D	^4F	^4G	$^2F1$	$^2F2$	$^2G1$	$^2G2$
13522.2	0.0038865	0.9363119	0.0559023	-0.0326440	-0.0425714	-0.2619497	0.2206453
16791.3	-0.0020960	-0.3162245	0.5390805	0.0142682	0.0158053	-0.5786774	0.5235159
18931.8	-0.0090488	0.1453837	0.8369017	0.0521673	0.0569075	0.4029624	-0.3317207
30574.4	0.9934308	-0.0078008	0.0163506	-0.0950311	-0.0599224	0.0120617	0.0001603
41520.7	0.1043346	0.0446576	-0.0696555	0.5461602	0.8227783	-0.0789630	-0.0278897
48839.7	-0.0046428	0.0109143	-0.0238808	-0.0408503	0.1129777	0.6512911	0.7487832
68033.1	-0.0456800	-0.0033865	0.0131559	-0.8288659	0.5489814	-0.0597953	-0.0758549
$J = \frac{9}{2}$	^4F	^4G	^4I	$^2G1$	$^2G2$	$^2H1$	$^2H2$
0	0.0044690	0.0098651	0.9796610	-0.0221981	0.0201344	0.0687765	-0.1857919
12120.5	0.3259580	0.1504784	-0.1758451	-0.3585485	0.3121325	0.3071091	-0.7210315
14959.1	-0.8620129	0.0269330	-0.0825892	0.1626162	-0.1191273	0.1656590	-0.4258041
19539.9	-0.2323550	0.8264795	0.0407961	-0.2893777	0.2923026	-0.1483626	0.2647390
21151.1	0.3103207	0.5361689	-0.0283774	0.5715595	-0.4852287	0.0107264	-0.2306001
33101.5	0.0030071	0.0737976	0.0072041	-0.0294388	-0.1088182	0.9177813	0.3734467
47885.7	0.0191913	-0.0232790	0.0005544	0.6581944	0.7451493	0.0951941	0.0395000
$J = \frac{11}{2}$	^4G	^4I	$^2H1$	$^2H2$	^2I		
2148.80	-0.0088709	-0.9931448	-0.0438187	0.1066753	0.0168826		
15872.1	-0.2374817	0.1129625	-0.3981336	0.8770990	-0.0550352		
21826.4	0.9597642	0.0184341	-0.2345593	0.1521726	0.0183932		
28440.1	-0.0798005	0.0188313	-0.3248789	-0.1128068	0.9354173		
34726.8	-0.1265239	-0.0144385	-0.8240177	-0.4282941	-0.3483421		
$J = \frac{13}{2}$	^4I	^2I	^2K				
4398.51	0.9967031	-0.0271096	0.0764725				
18615.2	-0.0789809	-0.1084109	0.9909637				
29920.9	-0.0185742	-0.9937365	-0.1101946				
$J = \frac{15}{2}$	^4I	^2K	^2L				
6698.50	0.9902906	0.1384766	-0.0121965				
20872.0	0.1375594	-0.9635048	0.2296429				
29645.8	-0.0200488	0.2290909	0.9731985				

Table 7.4: Energies and eigenvectors for the intermediate coupled states of $SrF_2 : Nd^{3+}$ using the parameters of Table 7.1.

	$SrF_2 : Nd^{3+}$			
Parameter	F^-	T^-	D^-	H^-
B^2_{tet}	-636.5664	-825.9755	-828.5967	-924.2687
B^4_{tet}	740.7437	964.1430	979.2485	835.9038
B^6_{tet}	546.4211	743.9291	759.4352	720.1694
B^4_{oct}	-1934.0097	-1724.2582	-1762.7335	-1682.8069
B^6_{oct}	-2043.1795	-2042.1504	-1996.2067	-2012.1938
k	0.9817	0.0000	0.0000	0.0000
ξ_Y	1023.6424	1020.2525	1023.3460	1022.6380
ξ_X	964.4836	964.4716 †	964.4716 †	964.4716 †
ξ_W	908.1466	908.1406 †	908.1406 †	908.1406 †

	$CaF_2 : Nd^{3+}$	
Parameter	F^-	D^-
B^2_{tet}	-851.2381	-1252.1435
B^4_{tet}	860.3390	963.1140
B^6_{tet}	662.9399	882.2264
B^4_{oct}	-2057.4449	-1846.5618
B^6_{oct}	-2399.3914	-2343.5641
k	0.9826	0.9810
ξ_Y	1020.5949	1021.5759
ξ_X	962.2063	962.2063 †
ξ_W	905.9414	905.9414 †

Table 7.5: The final least squares fitted parameters for the F^- C_{4V} centres in $CaF_2 : Nd^{3+}$ and $SrF_2 : Nd^{3+}$. † see text.

State			Experimental		Calculated	Deviation
$^4I_{9/2}$	Z_1	γ_6	0			
	Z_2	γ_7	60.0	(± 1.6)	57.2	2.8
	Z_3	γ_7	157.0	(± 1.8)	161.5	-4.5
			164.0	(± 1.8)		
	Z_4	γ_6			254.2	
	Z_5	γ_6	637.0	(± 1.6)	633.2	3.8
$^4I_{11/2}$	Y_1	γ_7	2006.0	(± 1.6)	2006.3	-0.3
	Y_2	γ_6	2044.0	(± 1.8)	2044.4	-0.4
	Y_3	γ_7	2050.0	(± 1.8)	2051.2	-1.2
	Y_4	γ_6	2061.0	(± 1.6)	2060.7	0.3
	Y_5	γ_7	2280.0	(± 2.6)	2280.0	0.0
	Y_6	γ_6	2366.0	(± 1.6)	2364.0	2.0
$^4I_{13/2}$	X_1	γ_7	3942	(± 2)	3941.6	0.4
	X_2	γ_6	3984	(± 2)	3982.2	1.8
	X_3	γ_6	4009	(± 2)	4008.7	0.3
	X_4	γ_7			4015.2	
	X_5	γ_7			4207.7	
	X_6	γ_7	4348	(± 1)	4344.8	3.2
	X_7	γ_6	4365.0	(± 1.5)	4370.7	-5.7
$^4I_{15/2}$	W_1	γ_6	5784	(± 2)	5776.1	8.9
	W_1	γ_7	5923	(± 2)	5924.2	-1.2
	W_3	γ_6	5946	(± 2)	5952.9	-6.9
	W_4	γ_7			6002.3	
	W_5	γ_6			6271.9	
	W_6	γ_6	6516	(± 1)	6518.7	-2.7
	W_7	γ_7	6527	(± 2)	6526.0	1.0
	W_8	γ_7	6593	(± 2)	6592.1	0.9
g-value						
$^4I_{9/2}$	Z_1	γ_6	$g_\parallel$	4.2750 †	4.2743	0.0007
			$g_\perp$	1.5070 †	1.5077	-0.0007

Table 7.6: Energy levels (in air cm^{-1}) and g-values for the C_{4V} F^- centre in $SrF_2 : Nd^{3+}$. The standard deviation obtained is 3.3 cm^{-1}. † McMahon.

$SrF_2 : Nd^{3+}$

	Observed		Calculated			
	Energy Level	$s\langle 111\rangle$	Energy Level	$s_\perp$	$s_\parallel$	$s\langle 111\rangle$
Y_4	2062.0 ($\pm$1.3)	3.3 ($\pm$0.4)	2061.0 ($\pm$1.6)	3.65	3.46	3.58
Y_1	20060 ($\pm$1.2)	2.9 ($\pm$0.4)	2006.0 ($\pm$1.6)	2.57	4.57	3.37

$CaF_2 : Nd^{3+}$

	Observed			Calculated		
	Energy Level	$s_\parallel$	$s_\perp$	Energy Level	$s_\parallel$	$s_\perp$
Y_6	2461.5 ($\pm$1.5)	1.6 ($\pm$1.1)	4.8 ($\pm$1.1)	2462 ($\pm$2)	1.3	5.5
Y_5	2357 ($\pm$5)			2354 ($\pm$3)	5.3	1.6
Y_4	2104 ($\pm$1.2)		3.5 ($\pm$0.4)	2105 ($\pm$1)	2.3	3.9
Y_3	2095.0 ($\pm$1.3)	0.9 ($\pm$0.6)	2.4 ($\pm$0.6)	2096 ($\pm$1)	0.1	3.7
Y_2	2085.0 ($\pm$1.3)			2086 ($\pm$1)	3.1	0.3
Y_1	2031.2 ($\pm$1.3)	6.9 ($\pm$0.6)		2032 ($\pm$1)	5.9	1.7

Table 7.7: 3 tesla Zeeman splitting of the Y multiplet energy levels of the C_{4V} F^- centre in $SrF_2 : Nd^{3+}$ and $CaF_2 : Nd^{3+}$ crystals. (in air cm^{-1}).

State			Experimental		Calculated	Deviation
$^4I_{9/2}$	Z_1	γ_6	0		0	
	Z_2	γ_7	81.2	($\pm$1.8)	81.5	0.3
	Z_3	γ_7	172.4	($\pm$1.6)	175.1	-2.7
	Z_4	γ_6			302.8	
	Z_5	γ_6	651.5	($\pm$1.5)	650.0	1.5
$^4I_{11/2}$	Y_1	γ_7	2002.8	($\pm$1.2)	2001.5	1.3
	Y_2	γ_7	2669.7	($\pm$1.3)	2067.8	1.9
	Y_3	γ_6	2074.2	($\pm$1.6)	2072.5	1.7
	Y_4	γ_6	2090.3	($\pm$1.7)	2094.4	-4.1
	Y_5	γ_7	2276.8	($\pm$2.2)	2283.9	-7.9
	Y_6	γ_6	2388.7	($\pm$1.3)	2387.0	1.7

Table 7.8: Energy levels (in air cm^{-1}) for the C_{4V} T^- centre in $SrF_2 : Nd^{3+}$. The standard deviation obtained is 2.9 cm^{-1}.

State			Experimental		Calculated	Deviation
$^4I_{9/2}$	Z_1	γ_6	0		0	
	Z_2	γ_7	80.3	($\pm$1.5)	78.4	1.9
	Z_3	γ_7	165.1	($\pm$1.5)	168.0	-2.9
	Z_4	γ_6			295.8	
	Z_5	γ_6	643.8	($\pm$1.2)	642.5	1.3
$^4I_{11/2}$	Y_1	γ_7	2004.6	($\pm$1.4)	2002.0	2.6
	Y_2	γ_7	2068.8	($\pm$1.4)	2068.1	0.7
	Y_3	γ_6	2074.2	($\pm$1.2)	2069.6	4.6
	Y_4	γ_6	2089.4	($\pm$1.4)	2094.1	-4.7
	Y_5	γ_7	2276.0	($\pm$3.0)	2282.9	-6.9
	Y_6	γ_6	2389.6	($\pm$1.4)	2386.5	3.1

Table 7.9: Energy levels (in air cm^{-1}) for the C_{4V} D^- centre in $SrF_2 : Nd^{3+}$. The standard deviation obtained is 3.8 cm^{-1}.

State			Experimental		Calculated	Deviation
$^4I_{9/2}$	Z_1	γ_6	0		0	
	Z_2	γ_7	79.4	($\pm$1.5)	79.6	-0.6
	Z_3	γ_7	186.1	($\pm$1.5)	183.9	2.2
	Z_4	γ_6			295.7	
	Z_5	γ_6	642.8	($\pm$1.2)	643.8	-1.0
$^4I_{11/2}$	Y_1	γ_7	2005.7	($\pm$1.4)	2003.3	2.4
	Y_2	γ_7	2071.2	($\pm$1.4)	2073.9	-2.7
	Y_3	γ_6	2076.0	($\pm$1.2)	2076.6	-0.6
	Y_4	γ_6	2092.3	($\pm$1.4)	2091.5	0.8
	Y_5	γ_7	2279.9	($\pm$3.0)	2285.1	-5.1
	Y_6	γ_6	2391.6	($\pm$1.4)	2386.5	5.1

Table 7.10: Energy levels (in air cm^{-1}) for the C_{4V} H^- centre in $SrF_2 : Nd^{3+}$. The standard deviation obtained is 2.8 cm^{-1}.

State			Experimental		Calculated	Deviation
$^4I_{9/2}$	Z_1	γ_6	0		0	
	Z_2	γ_7	82	($\pm$ 1)	80.2	1.8
	Z_3	γ_7	198	($\pm$ 2)	204.1	-5.1
	Z_4	γ_6			315.3	
	Z_5	γ_6	746	($\pm$ 3)	741.1	4.9
$^4I_{11/2}$	Y_1	γ_7	2032	($\pm$ 1)	2029.7	2.3
	Y_2	γ_7	2086	($\pm$ 1)	2085.8	0.2
	Y_3	γ_6	2096	($\pm$ 1)	2097.4	-1.4
	Y_4	γ_6	2105	($\pm$ 1)	2103.9	0.1
	Y_5	γ_7	2354	($\pm$ 3)	2355.5	-1.5
	Y_6	γ_6	2462	($\pm$ 2)	2461.4	0.6
$^4I_{13/2}$	X_1	γ_7	3960	($\pm$ 1)	3956.1	3.9
	X_2	γ_6	4022	($\pm$ 1)	4018.1	3.9
	X_3	γ_6	4045	($\pm$ 3)	4048.6	-3.6
	X_4	γ_7			4055.2	
	X_5	γ_7			4264.8	
	X_6	γ_7	4442 ?	($\pm$ 3)	4438.7	3.3
	X_7	γ_6	4465	($\pm$ 1)	4468.4	-4.4
$^4I_{15/2}$	W_1	γ_6	5764	($\pm$ 1)	5755.3	8.7
	W_1	γ_7	5952	($\pm$ 1)	5942.6	9.4
	W_3	γ_6	5974 ?	($\pm$ 3)	5979.3	-5.3
	W_4	γ_7	6036 ?	($\pm$ 3)	6039.4	-3.4
	W_5	γ_6			6325.8	
	W_6	γ_6	6632	($\pm$ 1)	6632.1	-0.1
	W_7	γ_7	6639	($\pm$ 1)	6639.9	0.9
	W_8	γ_7			6719.5	
g-value						
$^4I_{9/2}$	Z_1	γ_6	$g_\parallel$	4.4120 †	4.4114	0.0006
			$g_\perp$	1.3010 †	1.3014	-0.0004

Table 7.11: Energy levels (in air cm^{-1}) and g-values for the C_{4V} F^- centre in $CaF_2 : Nd^{3+}$. The standard deviation obtained is 2.7 cm^{-1}. † Bleaney et al. (1956). ? Tentative assignment.

State			Experimental		Calculated	Deviation
$^4I_{9/2}$	Z_1	γ_6	0		0	
	Z_2	γ_7	110.0	(± 1.5)	111.2	-1.2
	Z_3	γ_7	234.0	(± 1.5)	231.4	2.6
	Z_4	γ_6			360.0	
	Z_5	γ_6	762.7	(± 1.2)	762.6	0.1
$^4I_{11/2}$	Y_1	γ_7	2023.5	(± 2.5)	2023.2	0.3
	Y_2	γ_7	2119.8	(± 1.2)	2122.3	-2.5
	Y_3	γ_6	2129.1	(± 1.1)	2137.0	-7.9
	Y_4	γ_6	2148.9	(± 2.3)	2143.8	5.1
	Y_5	γ_7	2371.9	(± 2.3)	2373.7	-1.8
	Y_6	γ_6	2500.1	(± 1.2)	2501.0	-0.9
g-value						
$^4I_{9/2}$	Z_1	γ_6	$g_\parallel$	4.8000 †	4.8001	-0.0001
			$g_\perp$	0.9670 †	0.9673	-0.0003

Table 7.12: Energy levels (in air cm^{-1}) and g-values for the C_{4V} D^- centre in $CaF_2 : Nd^{3+}$. The standard deviation obtained is 3.1 cm^{-1}. † Bleaney et al. (1956).

	$SrF_2 : Nd^{3+}$			
Ratio	F^-	T^-	D^-	H^-
B^4_{tet}/B^4_{oct}	-0.383	-0.559	-0.555	-0.5
B^6_{tet}/B^6_{oct}	-0.267	-0.364	-0.380	0.36
B^4_{oct}/B^6_{oct}	0.947	0.844	0.883	0.84
θ_a	63 ($\pm$1)	66 ($\pm$1)	65 ($\pm$1)	63 ($\pm$1)
θ_b	125.0 ($\pm$1.5)	124.0 ($\pm$1.5)	123.0 ($\pm$1.5)	121.0 ($\pm$1.5)

	$CaF_2 : Nd^{3+}$	
Ratio	F^-	D^-
B^4_{tet}/B^4_{oct}	-0.418	-0.522
B^6_{tet}/B^6_{oct}	-0.276	-0.376
B^4_{oct}/B^6_{oct}	0.857	0.788
θ_a	64 ($\pm$1)	63 ($\pm$2)
θ_b	126 ($\pm$1)	120.5 ($\pm$1.5)

Table 7.13: The co-ordination angles (θ_a, θ_b) calculated from the ratios of the final least squares fitted parameters for the C_{4V} centres in $CaF_2 : Nd^{3+}$ and $SrF_2 : Nd^{3+}$.

Chapter 8

Double rare earth ion doped CaF_2

8.1 Introduction

The M and N centres in $CaF_2 : Nd^{3+}$ were shown in Chapter 5 to be multi-ion cluster centres and it would be of interest to investigate the energy transfer processes between the rare earth ions within these centres. Voron'ko et al. (1968) have shown that the Nd^{3+} ions in $CaF_2 : Nd^{3+}$ crystal can form cluster centres with other rare earth ions. They also showed the presence of two new lines at 864.1 nm and 865.8 nm whose position remained identical on varying the second rare earth ion in $CaF_2 : Nd^{3+} : RE^{3+}$, starting with Gd^{3+} and proceeding towards the heavier ions of the lanthanide series. Bagdasarov et al. (1965) have established that these two lines belong to the same Y_1 centre which also appears in $CaF_2 : Nd^{3+}$ crystals after exposure to gamma irradiation treatment. The formation of the Y_1 centre was attributed to the migration of the interstitial fluorine ions. Voron'ko et al. (1971) have investigated $CaF_2 : Yb^{3+}$ crystals co-doped with a small concentration of Nd^{3+} ions and they observed a change in the concentration of the Yb^{3+} impurity defects with the removal of the Yb^{3+} C_{4V} centres and formation of the Nd^{3+} Y centres. The Y centre was attributed to a tetragonal C_{4V} centre capturing another F^- ion. Voron'ko et al. (1968) have attributed the formation of the complex centres in the $CaF_2 : Nd^{3+} : RE^{3+}$ crystals to the Nd^{3+} ions being partially replaced by another RE^{3+} ion in the M and N centres and have denoted these centres M' and N' respectively. They have also established that the magnitude of the shift in frequency between the M and M' centres in the R multiplet increases linearly with the increasing difference between the ionic radii. However, this dependence is not shown by the last two ions, Yb^{3+} and Lu^{3+}, in the lanthanide series. They concluded that the frequency shift is not solely dependent on the charge and radius of the ion. Kask and Kornienko (1968) found from their EPR results that the symmetry of the $Nd^{3+} - RE^{3+}$ centres and the M centre is different because of the difference in the direction of the principal g- tensor axes. The change in symmetry of the crystalline field at the site of the Nd^{3+} ion originates,

possibly, from a shift of one of the two F^- ions found in the immediate surroundings of the Nd^{3+} and RE^{3+} ions. However, they argued that the method of formation of these centres is identical to the M centre because of the similar behaviour in the temperature dependence of their fluorescence decay times.

The energy upconversion results of the M and N centres suggests the possibility of phonon assisted ETU processes within a single centre, hence investigation of these types of centres in double doped rare earth ions should yield information about the energy transfer processes between the rare earth ions within these centres. The second rare earth ions chosen to be co-doped with the $CaF_2 : Nd^{3+}$ were Ce^{3+}, Gd^{3+} and Yb^{3+} for the following reasons : 1) Voron'ko et al. (1968) have observed the M' centres in the $CaF_2 : Nd^{3+} : RE^{3+}$ crystals double doped with these rare earth ions; 2) none of these three ions have energy levels overlapping the Nd^{3+} energy levels in the region of interest and 3) the Yb^{3+} ion has only one excited multiplet, $^2F_{5/2}$, at approximately 10000 cm^{-1} which is slightly lower in energy than the fluorescing R multiplet of the Nd^{3+} ion.

The $CaF_2 : Nd^{3+} : RE^{3+}$ crystals were grown under the same conditions and by the same method as the $CaF_2 : Nd^{3+}$ and $SrF_2 : Nd^{3+}$ crystals. The concentration of the second rare earth ion was set to 0.1% molar concentration while the concentration of the Nd^{3+} ion was either 0.02% or 0.05%. A concentration of 0.1% was chosen for the second rare earth ion to give a greater probability of obtaining mixed $Nd^{3+} - RE^{3+}$ cluster centres. The $CaF_2 : Nd^{3+} : RE^{3+}$ with 0.02% Nd^{3+} was chosen for minimum formation of more complex cluster centres while the 0.05% samples served as a standard for comparing with the single rare earth ion doped $CaF_2 : Nd^{3+}$ crystals.

The shorthand notation of $Nd^{3+} - RE^{3+}$ will be used henceforth to denote $CaF_2 : Nd^{3+} : RE^{3+}$ crystals.

8.2 Optical absorption

The optical absorption spectra of the Nd^{3+} R multiplet in the $Nd^{3+} - Ce^{3+}$, $Nd^{3+} - Gd^{3+}$ and $Nd^{3+} - Yb^{3+}$ crystals are presented in Fig. 8.1. These spectra show the frequency shifts of the M' centre from the M centre in the R multiplet and the presence of the 864.1 nm line in the $Nd^{3+} - Yb^{3+}$ spectrum, which was assigned to the Y_1 centre (Bagdasarov et al. 1965). The presence of the 869.5 nm line and the A' centre in the $Nd^{3+} - Ce^{3+}$ (not shown in Fig. 8.1) and $Nd^{3+} - Yb^{3+}$ absorption spectra suggests the presence of oxygen impurity in these crystals, most probably a result of impurities in the YbF_3 and CeF_3 used. This was confirmed by the growth of subsequent crystals, with a small amount ($\approx 1\%$) of PbF_2 in the crystal melt, which were free of these centres. The optical absorption results show

that the energy difference between the R_1 and R_2 levels of the M' centres in $Nd^{3+} - Ce^{3+}$, $Nd^{3+} - Gd^{3+}$ and $Nd^{3+} - Yb^{3+}$ is 46 (± 4), 34.6 (± 3.2) and 29.5 (± 2.6) cm^{-1} respectively, as compared to the corresponding energy difference of 42.2 (± 3.2) cm^{-1} for the M centre in $Nd^{3+} - Nd^{3+}$.

The absorption spectrum for the $^2F_{5/2}$ multiplet of the Yb^{3+} ion in the $Nd^{3+}-Yb^{3+}$ crystals, Fig. 8.2, shows the presence of tetragonal, cubic, trigonal and a number of rhombic centres (Kirton and Mclaughlan 1967). As the trigonal centre lines observed were removed by the addition of the PbF_2 to the crystal melt, they are attributed, like the A' centre, to the oxygen compensating centres. In $CaF_2 : Nd^{3+} : Yb^{3+}$, a redistribution of intensity of the absorption lines for the $^2F_{5/2}$ multiplet of the Yb^{3+} ion was observed. Because of the Nd^{3+} concentration chosen, the Nd^{3+} R multiplet spectra (Fig. 8.1) showed distinct lines of the M' centre, which is formed from $Nd^{3+} - Yb^{3+}$ pairs, whereas the Yb^{3+} $^2F_{5/2}$ multiplet spectra (Fig. 8.2) showed no additional lines that could be attributed to the M' centre.

8.3 Laser selective excitation

The fluorescence spectra of the M' centres in the $Nd^{3+} - Ce^{3+}$, $Nd^{3+} - Gd^{3+}$ and $Nd^{3+} - Yb^{3+}$ centres are presented in Figs. 8.3 to 8.6. The fluorescence intensity pattern of these centres resembles the M centre and the energy difference between the Z_1 and Z_2 levels is 37 (± 1), 33.6 (± 1.6) and 30 (± 1) cm^{-1} for the M' centres of $Nd^{3+} - Ce^{3+}$, $Nd^{3+} - Gd^{3+}$ and $Nd^{3+} - Yb^{3+}$ crystals respectively. In the $Nd^{3+} - Yb^{3+}$ crystals, the fluorescence of the M' centre from the Nd^{3+} R multiplet was accompanied by the fluorescence of a rhombic centre from the Yb^{3+} $^2F_{5/2}$ multiplet, as shown in Fig. 8.6. This clearly demonstrates the co-existence of two different rare earth ions in the M' centre. The fluorescence spectrum of the M' centre of $Nd^{3+} - Yb^{3+}$ reveals the presence of two extra lines 863.8 and 865.8 nm, belonging to another centre, which was impossible to separate from the M' centre by selective excitation, as it had an overlapping absorption line.

Energy upconversion was observed for the M' centres in the double rare earth doped crystals. The upconverted fluorescence spectrum of the M' centre is presented in Figs. 8.8 to 8.10 and the energy levels are listed in Tables. 8.1 to 8.3. The visual appearance of the upconverted fluorescence of the M' centre in both $Nd^{3+} - Ce^{3+}$ and $Nd^{3+} - Gd^{3+}$ was violet blue, similar to the M centre, whereas the M' centre in $Nd^{3+} - Yb^{3+}$ gave a bright green colour which is attributable to a redistribution of the upconverted fluorescence intensity to give emission from a lower level than in the other three cases. The presence of the R' levels was observed in the upconverted fluorescence spectra of the M' centres in $Nd^{3+} - Ce^{3+}$ and $Nd^{3+} - Gd^{3+}$ crystals. This was discussed in Chapter 6 along with the results of the M and

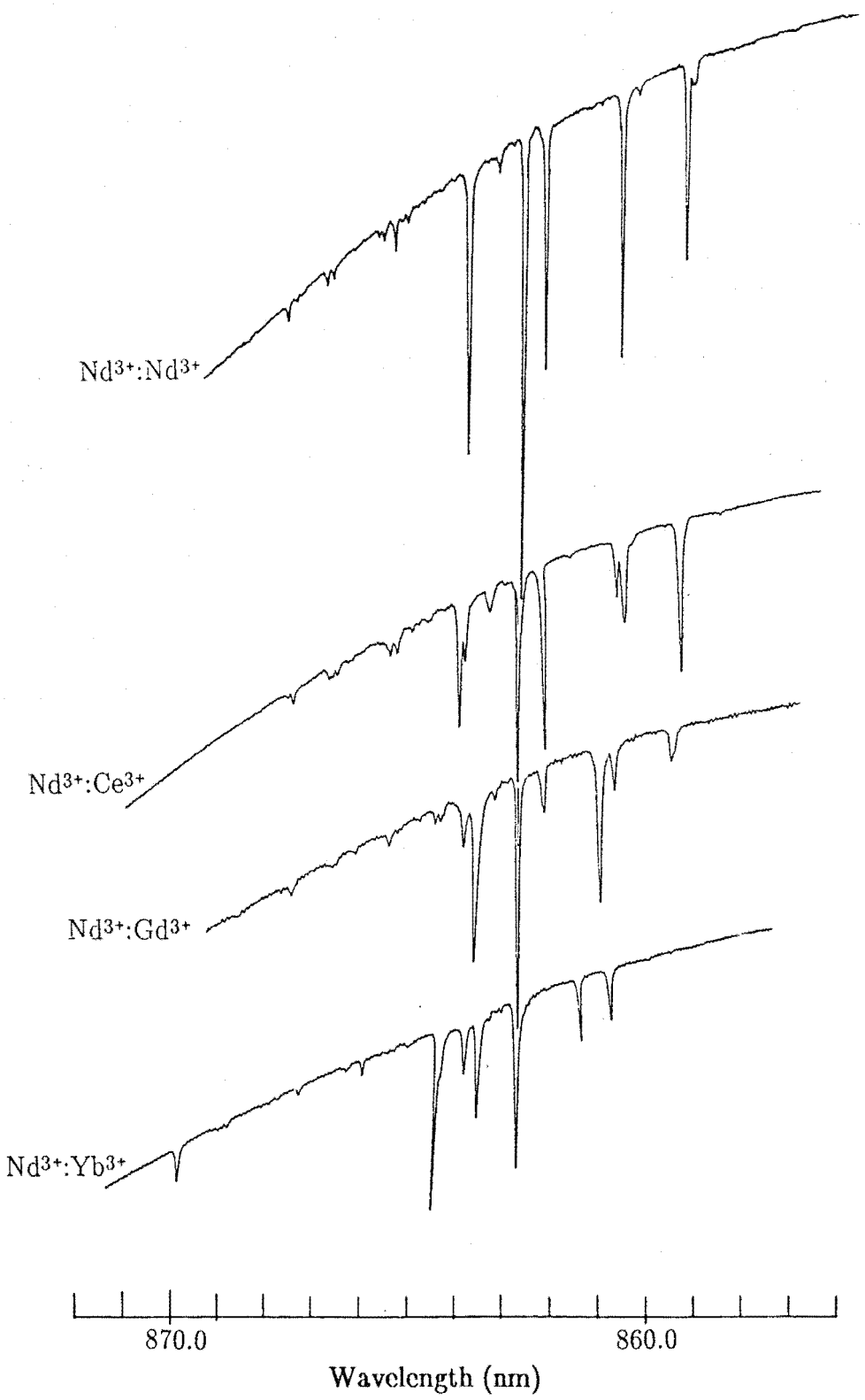

Figure 8.1: 10 K R multiplet absorption spectrum of $CaF_2 : Nd^{3+} : RE^{3+}$ crystals where $RE^{3+} : Ce^{3+}$, Gd^{3+} and Yb^{3+}.

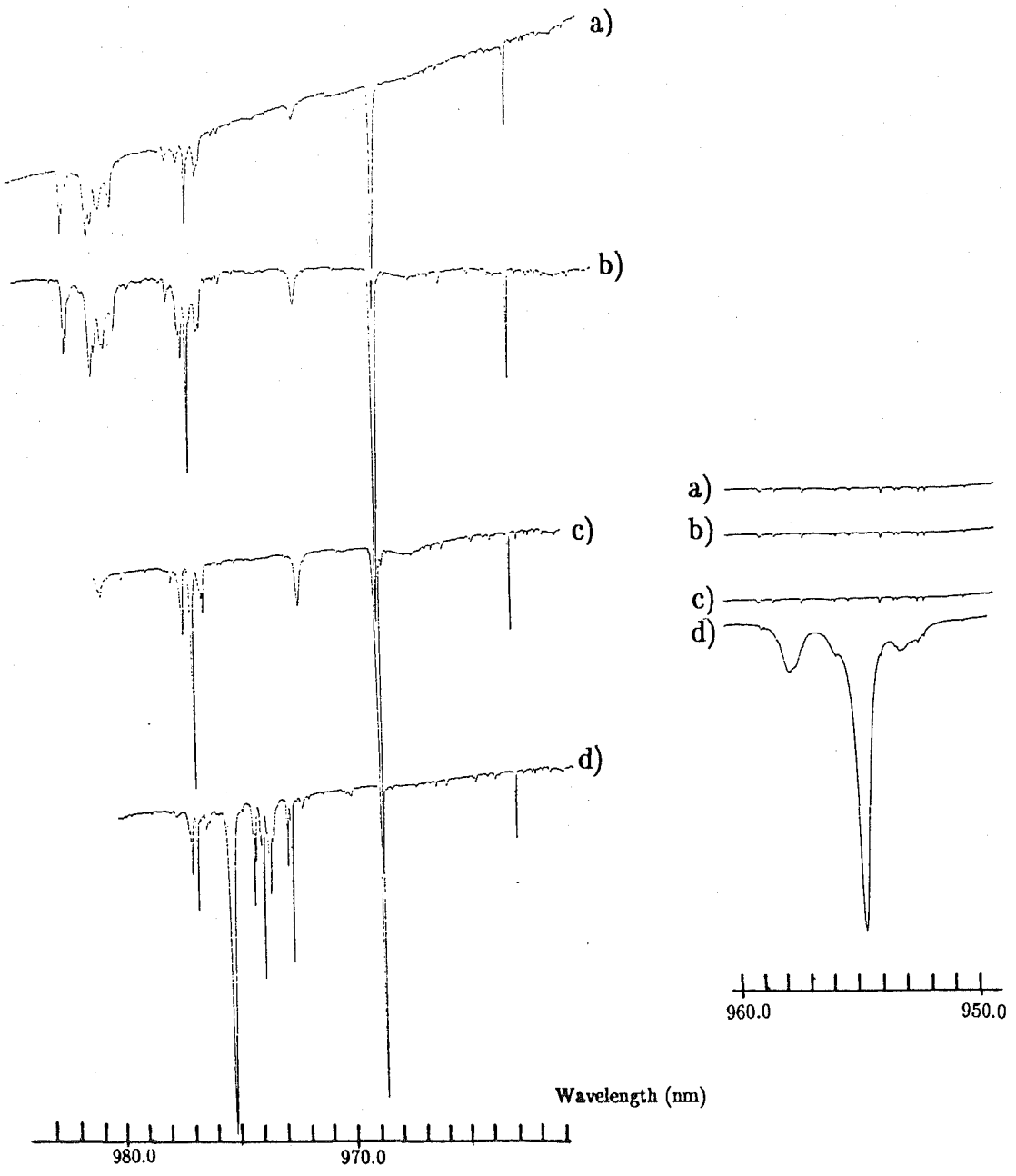

Figure 8.2: 10 K absorption spectrum of the $^2F_{5/2}$ multiplet transition of the Yb^{3+} ion measured for the following crystals :
a) $CaF_2 : 0.01\% Yb^{3+}$ $(+PbF_3 \approx 1\%)$
b) $CaF_2 : 0.02\% Nd^{3+} : 0.01\% Yb^{3+}$ $(+PbF_3 \approx 1\%)$
c) $CaF_2 : 0.01\% Yb^{3+}$
d) $CaF_2 : 0.02\% Nd^{3+} : 0.01\% Yb^{3+}$

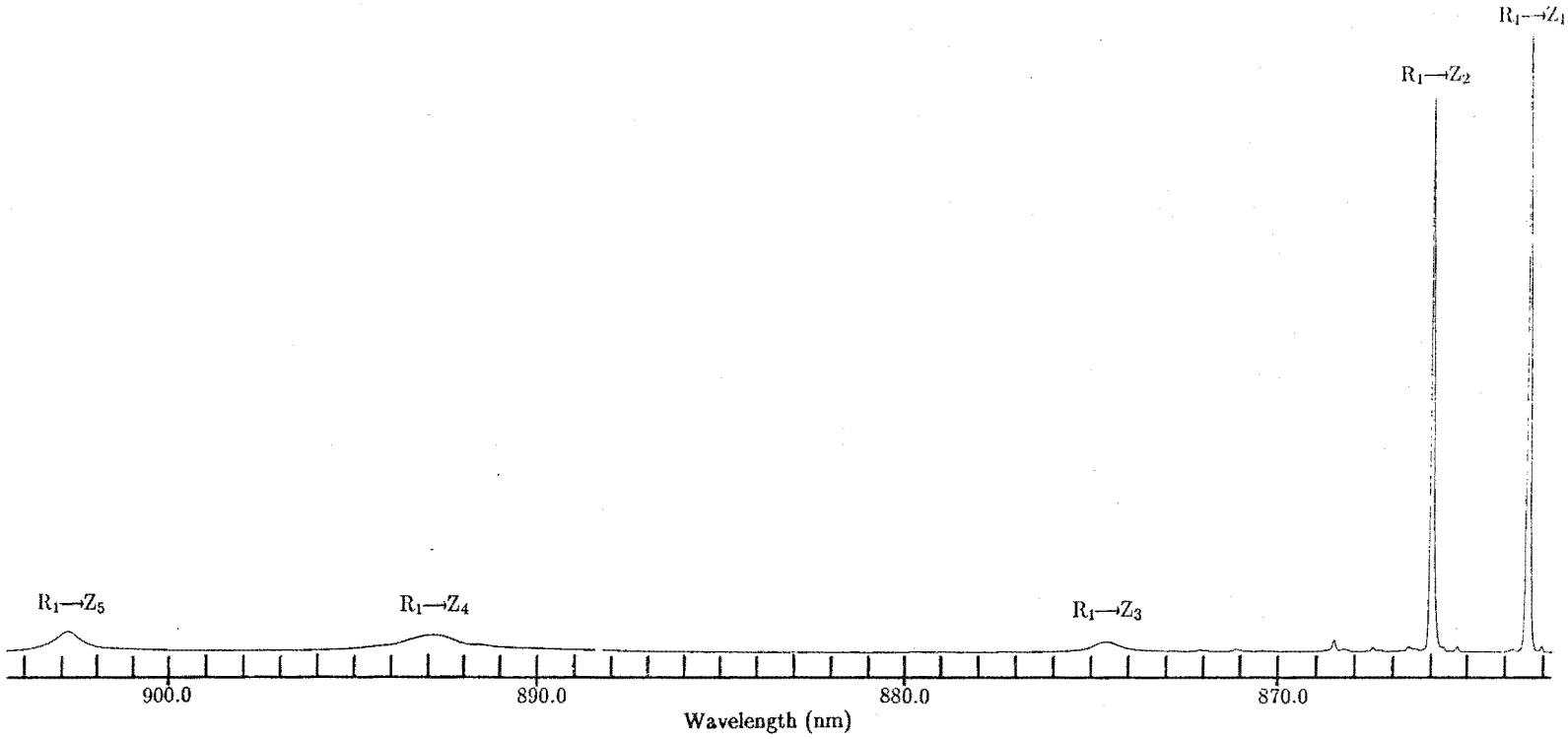

Figure 8.3: 10 K fluorescence spectrum for the $R_1 \rightarrow Z_i$ transitions of the $CaF_2 : Nd^{3+} : Ce^{3+}\ M'\ F^-$ centre.

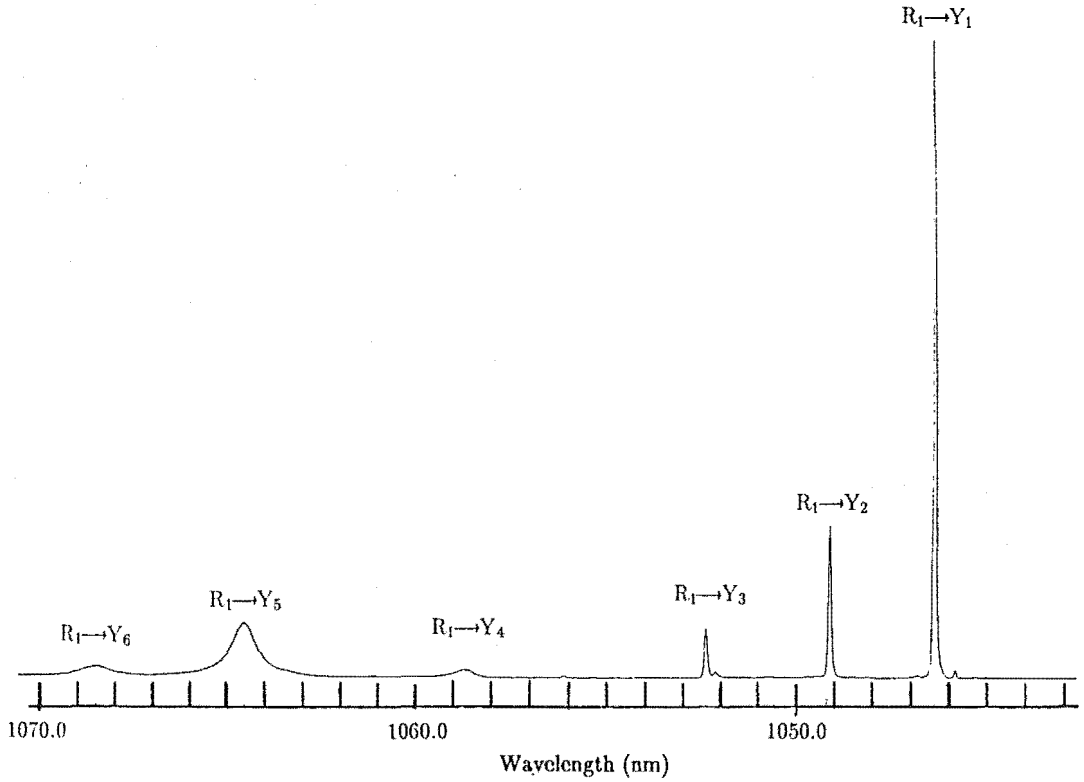

Figure 8.4: 10 K fluorescence spectrum for the $R_1 \rightarrow Y_i$ transitions of the $CaF_2 : Nd^{3+} : Ce^{3+}\ M'\ F^-$ centre.

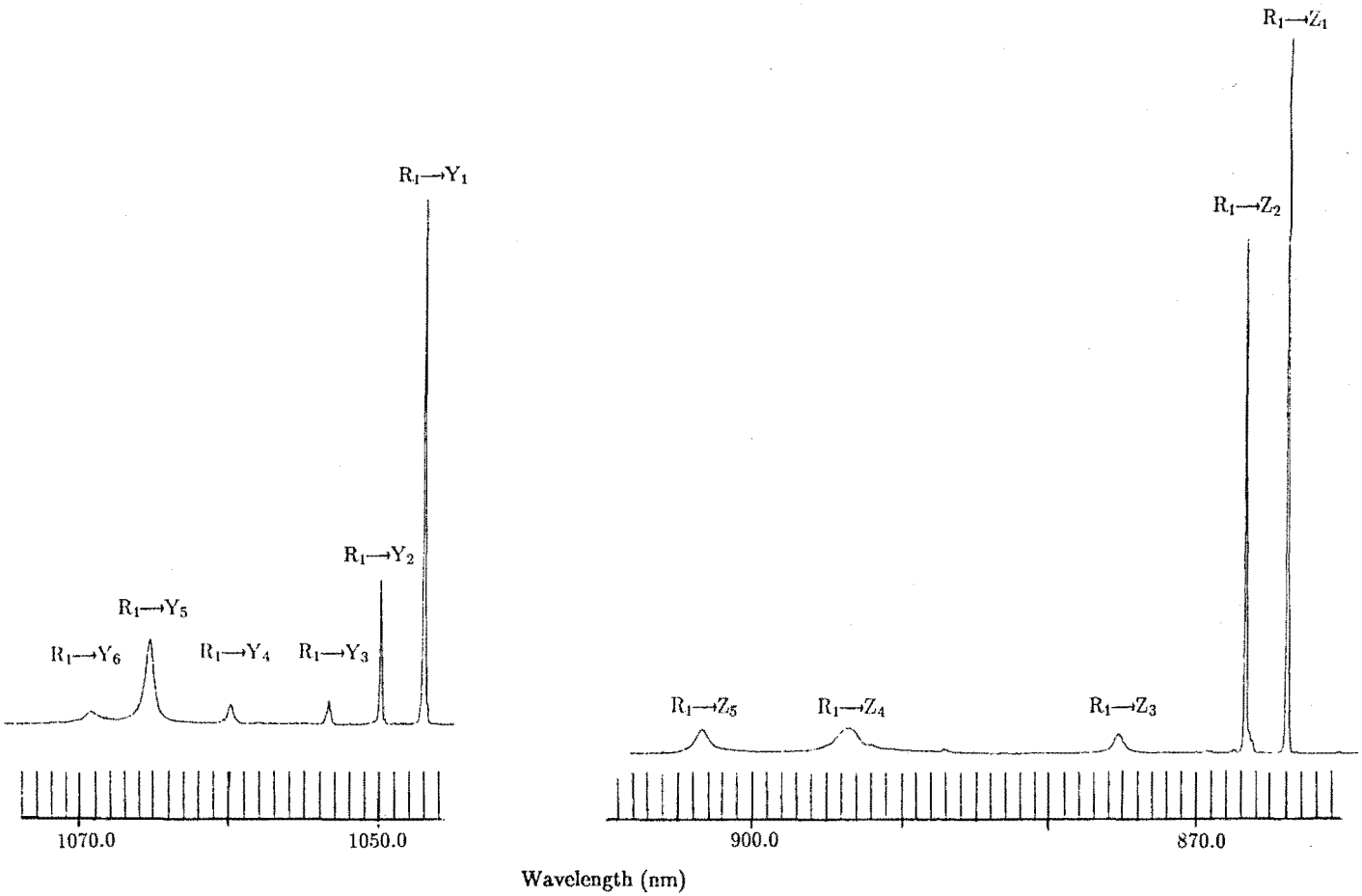

Figure 8.5: 10 K fluorescence spectrum for $R_1 \rightarrow Z_i$ and $R_1 \rightarrow Y_i$ transitions of the $CaF_2 : Nd^{3+} : Gd^{3+}\ M'\ F^-$ centre.

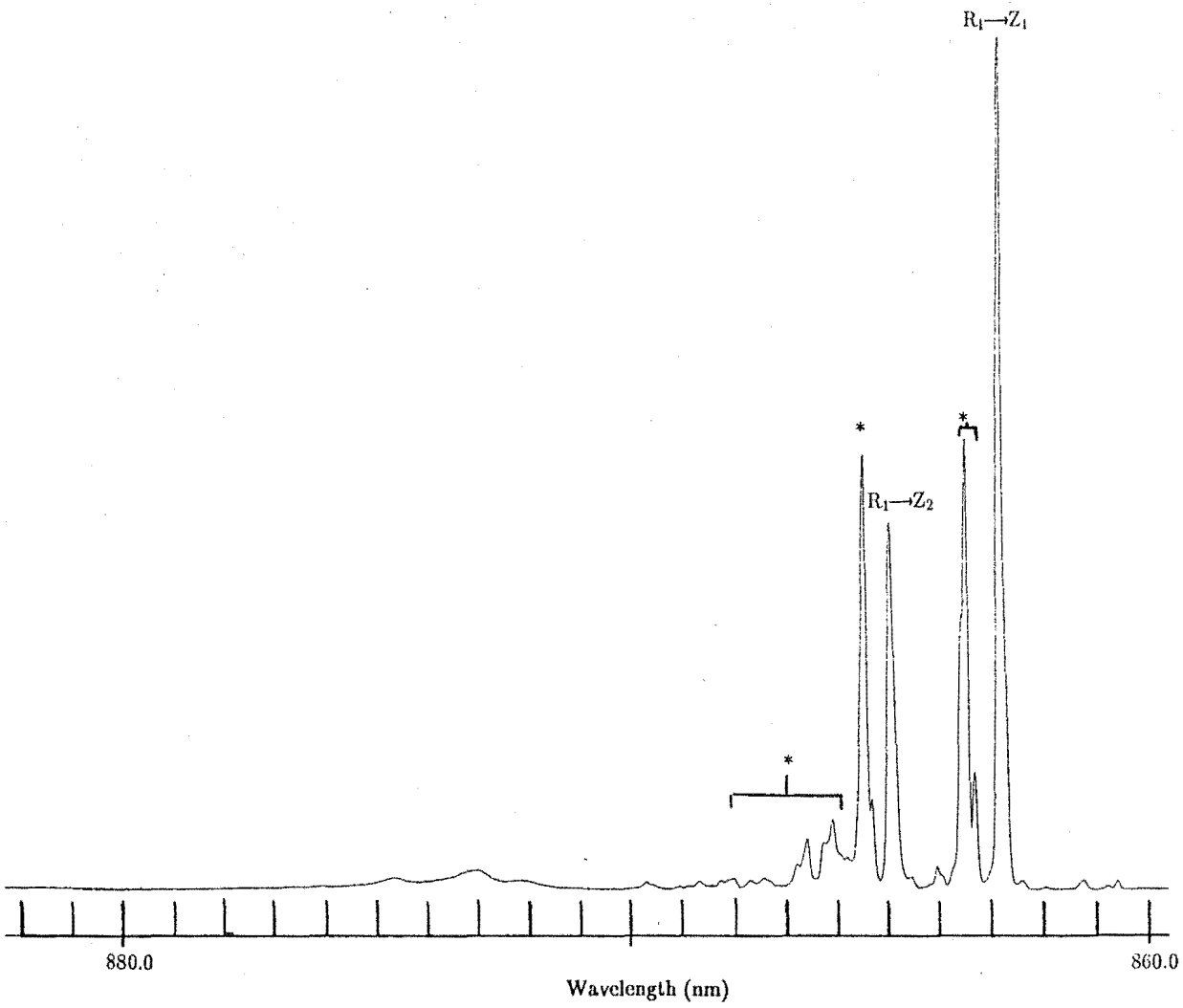

Figure 8.6: 10 K fluorescence spectrum for the $R_1 \rightarrow Z_i$ transitions of the $CaF_2 : Nd^{3+} : Yb^{3+}\ M'\ F^-$ centre. * unidentified line.

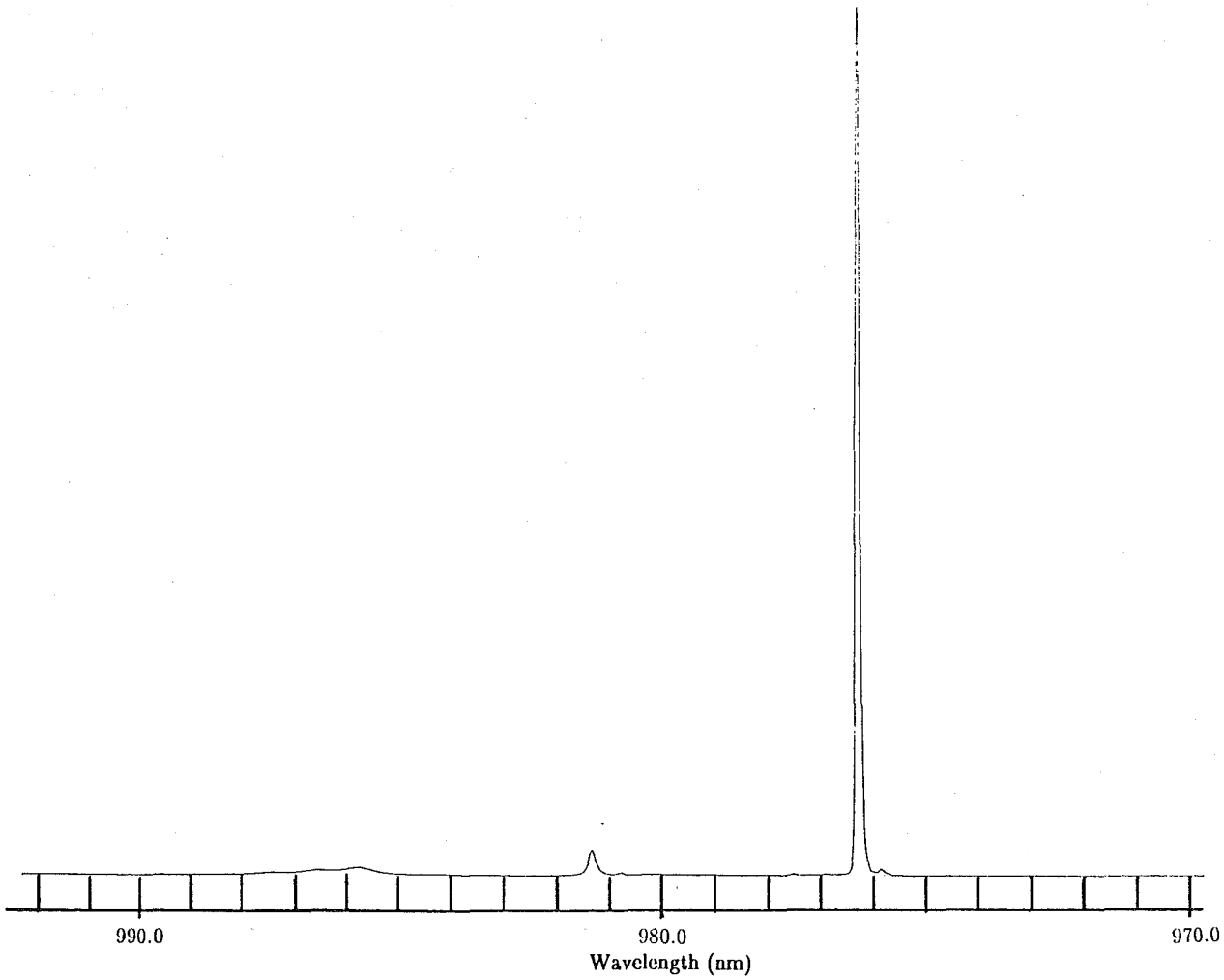

Figure 8.7: 10 K fluorescence spectrum of the ${}^2F_{5/2}$ multiplet transitions of the Yb^{3+} ion for the $CaF_2 : Nd^{3+} : Yb^{3+}$ M' F^- centre.

N centres and the relevant results are compared in Table. 6.1. No conclusion can be drawn from these results other than indicating a phonon assisted energy transfer process between the rare earth ions within these centres. This energy transfer process appears to be insensitive to the nature of the second ion. No upconverted fluorescence was observed when the crystals were excited by the pulsed dye laser.

The excitation spectrum of the M' centres, in Figs. 8.11 to 8.16, does not show the double line pattern for the $^4G_{5/2}$ energy levels within the D multiplet as observed in the M and N centres. This supports the earlier proposal (Chapter 5) that the double line patterns observed in the M and N centres are the result of ion pair splitting of identical excited energy levels of the two rare earth ions within the same centre.

The fluorescence decay times of the $R_1 \rightarrow Z_1$ transition was measured as 0.61 ms ($\pm 10\%$), 0.59 ms ($\pm 10\%$) and 83.1 us ($\pm 10\%$) for the M' centre in $Nd^{3+} - Ce^{3+}$, $Nd^{3+} - Gd^{3+}$ and $Nd^{3+} - Yb^{3+}$ respectively. The similar decay times for the M' centre in $Nd^{3+} - Ce^{3+}$ and $Nd^{3+} - Gd^{3+}$ suggests the coupling between the Nd^{3+} ion and the RE^{3+} ion is similar for these centres. The unusually short decay lifetime of the M' centre in $Nd^{3+} - Yb^{3+}$ is attributed to efficient energy transfer between the Nd^{3+} ion and the Yb^{3+} ion within this centre due to the close match of two of their energy levels. The $^2F_{5/2}$ multiplet of the Yb^{3+} ion lies close to, and is lower in energy than the emitting R multiplet of the Nd^{3+} ion providing an efficient non-radiative relaxation channel to de-excite the R multiplet of the Nd^{3+} ion. The non- radiative contribution to the relaxation process of the M' centre can be estimated by following the procedures discussed in Chapter 5 for the M and N centres. The calculated results are listed in Table 8.4 and they show that the dominant interaction in the non-radiative contribution is between the rare earth ions which in turn depends upon on the matching of the energy levels of the two ions within this centre. These results show that the electron-phonon interaction between the rare earth ions and the lattice phonons is only changed slightly by alteration of the second rare earth ion in the centre.

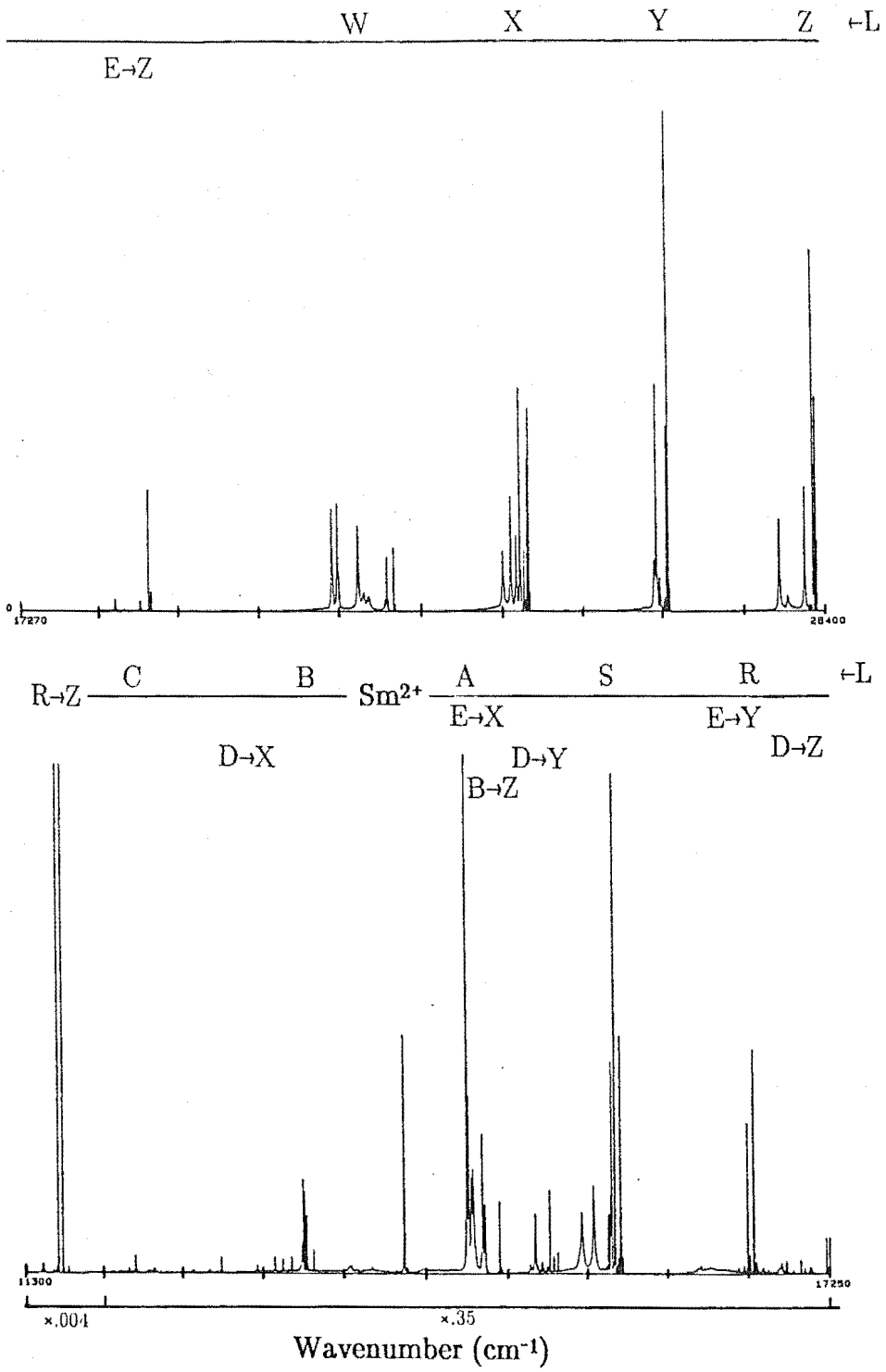

Figure 8.8: 10 K fluorescence spectrum of the $CaF_2 : Nd^{3+} : Ce^{3+}$ M' F^- centre showing the fluorescence transitions caused by upconversion processes.

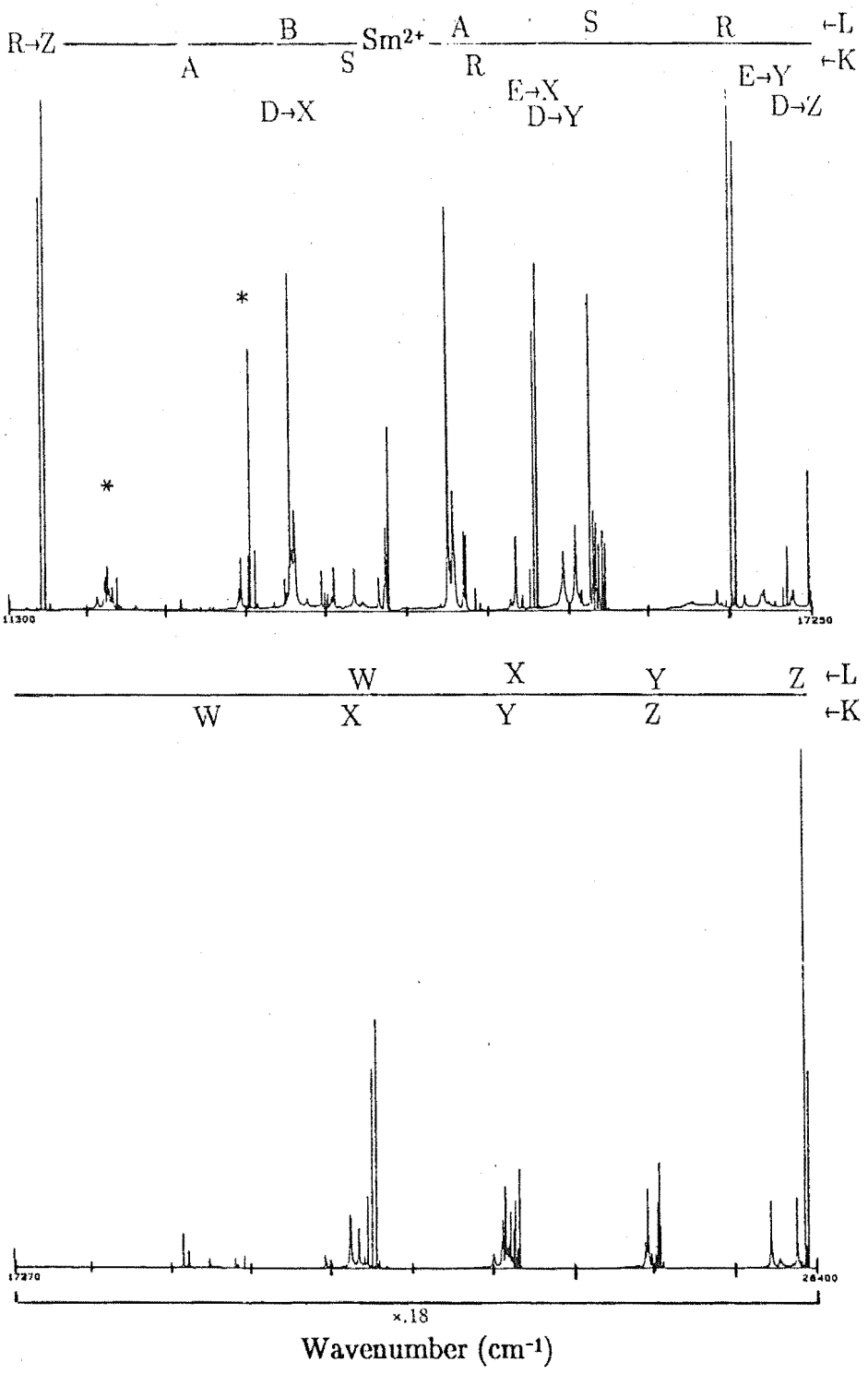

Figure 8.9: 10 K fluorescence spectrum of the $CaF_2 : Nd^{3+} : Gd^{3+}$ M' F^- centre showing the fluorescence transitions caused by upconversion processes.

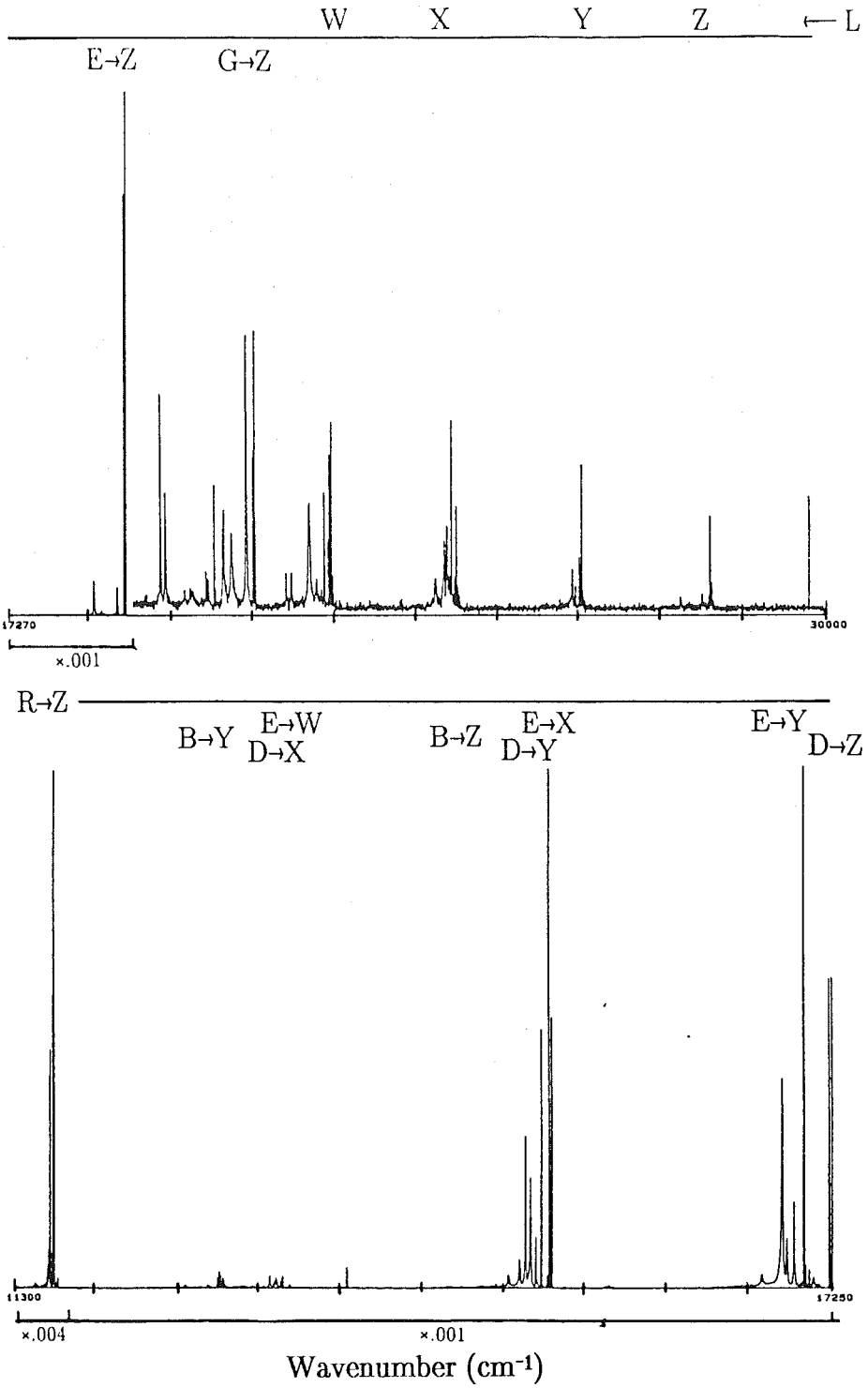

Figure 8.10: 10 K fluorescence spectrum of the $CaF_2 : Nd^{3+} : Yb^{3+}$ M' F^- centre showing the fluorescence transitions caused by upconversion processes.

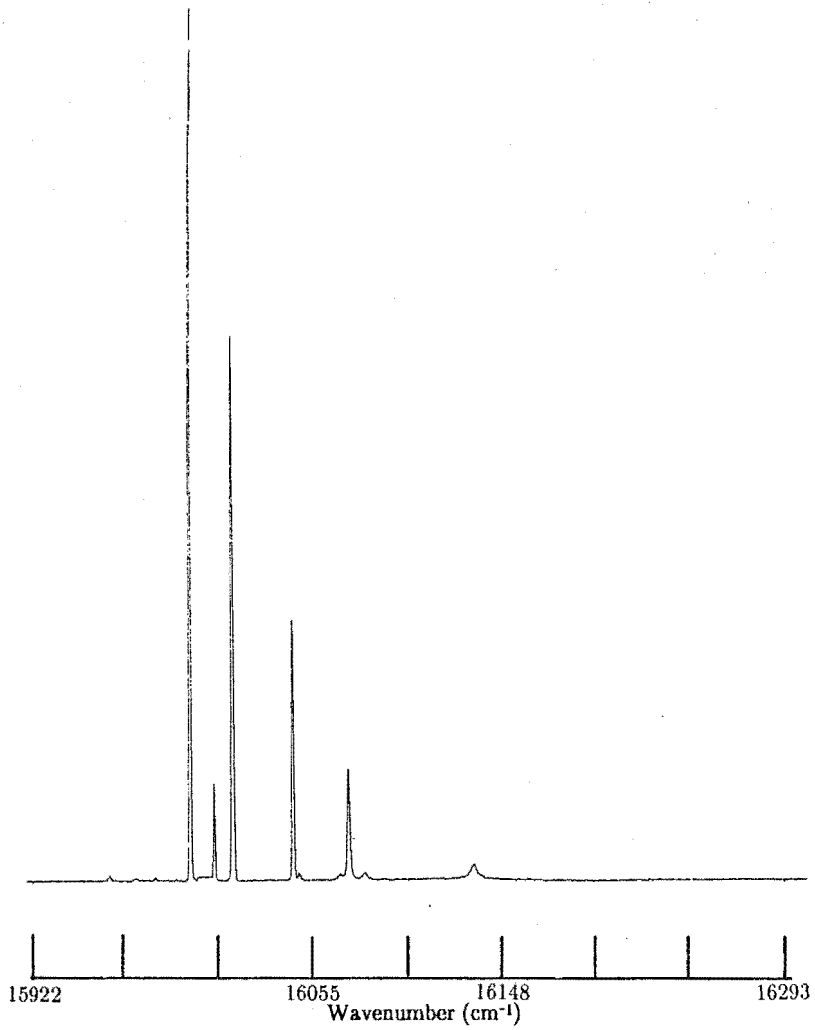

Figure 8.11: 10 K C multiplet excitation spectrum of the $CaF_2 : Nd^{3+} : Ce^{3+}$ M' F^- centre.

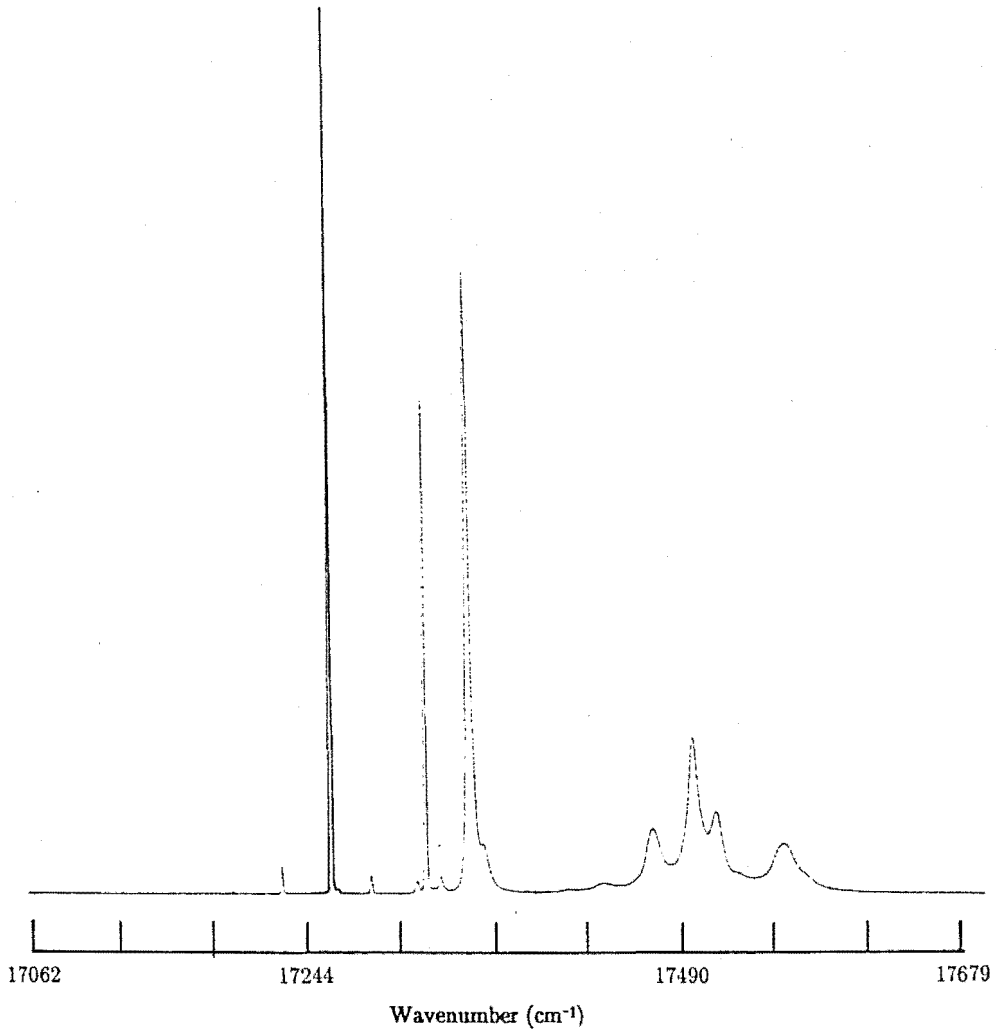

Figure 8.12: 10 K D multiplet excitation spectrum of the $CaF_2 : Nd^{3+} : Ce^{3+}$ M' F^- centre.

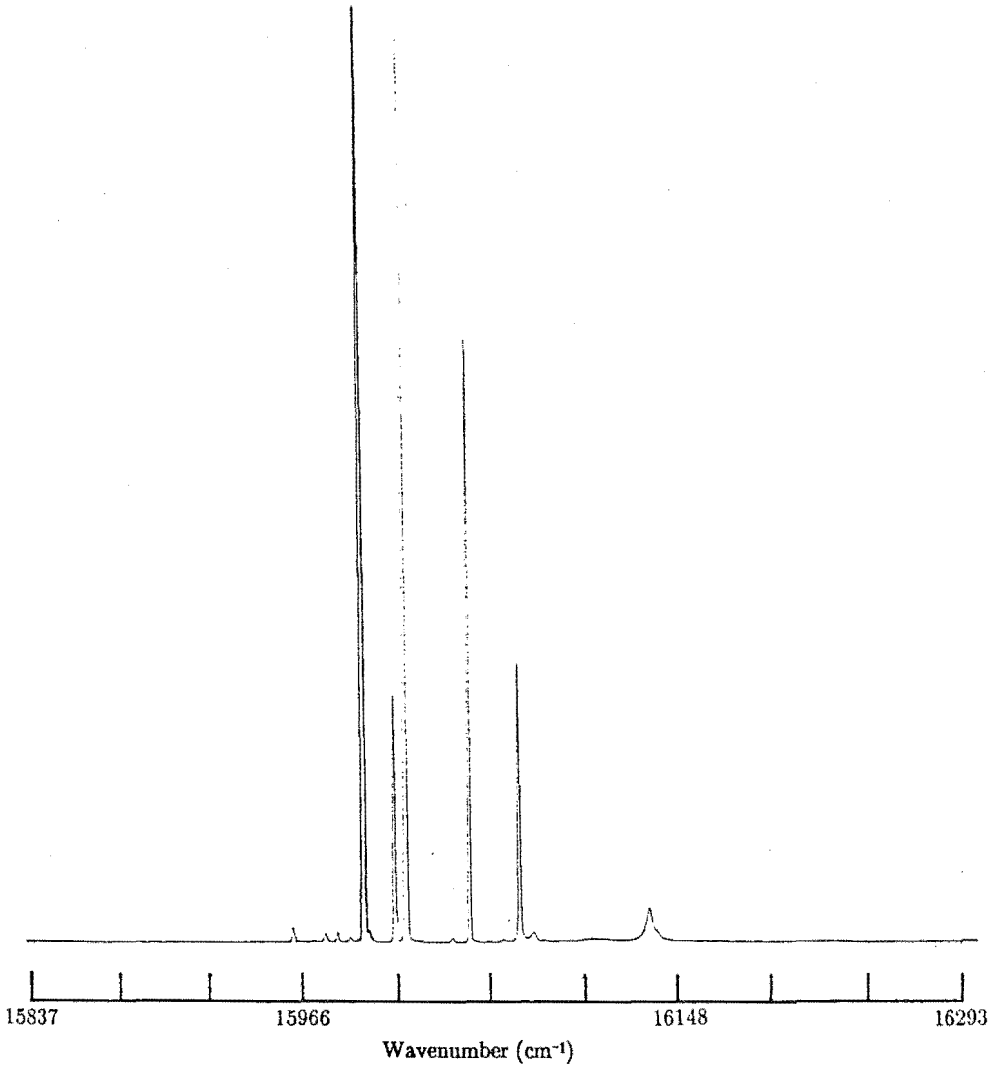

Figure 8.13: 10 K C multiplet excitation spectrum of the $CaF_2 : Nd^{3+} : Gd^{3+}$ M' F^- centre.

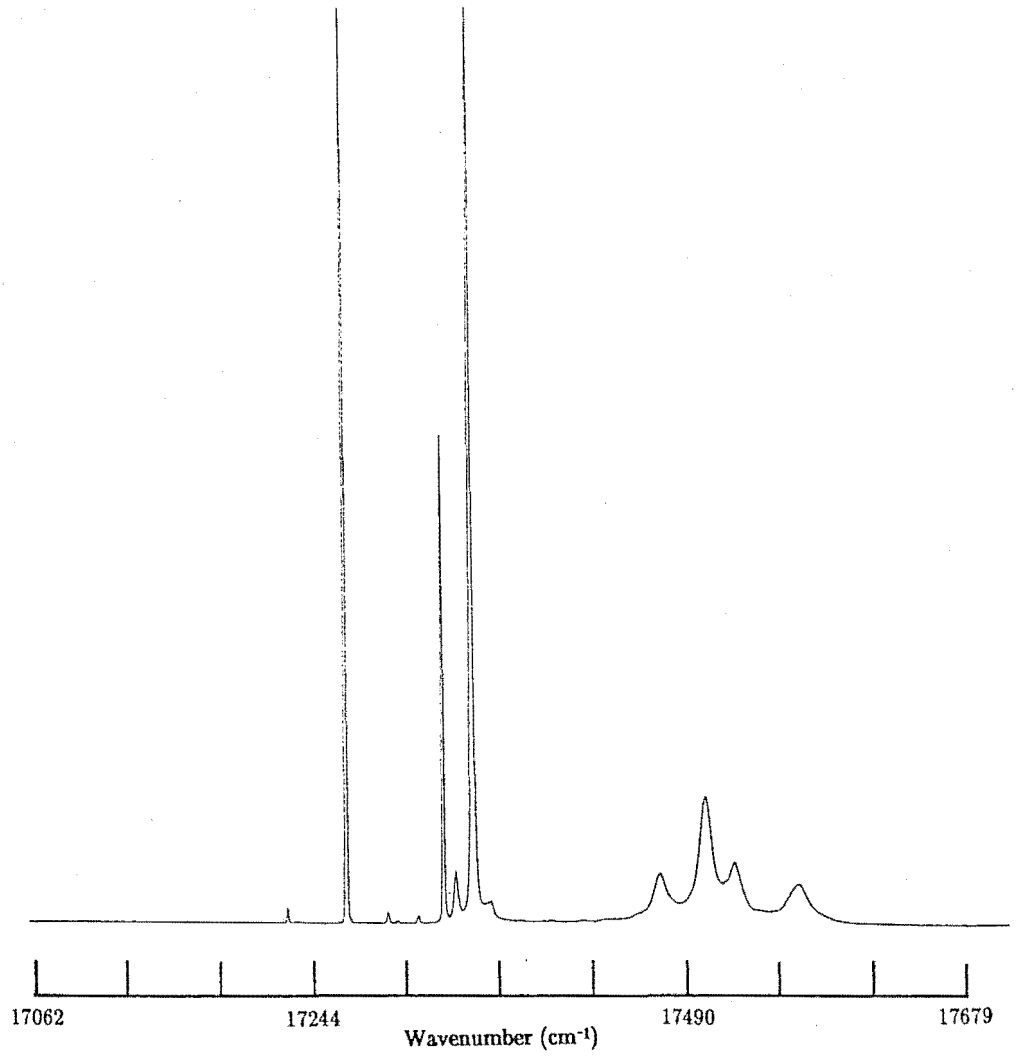

Figure 8.14: 10 K D multiplet excitation spectrum of the $CaF_2 : Nd^{3+} : Gd^{3+}$ $M^{'}$ F^{-} centre.

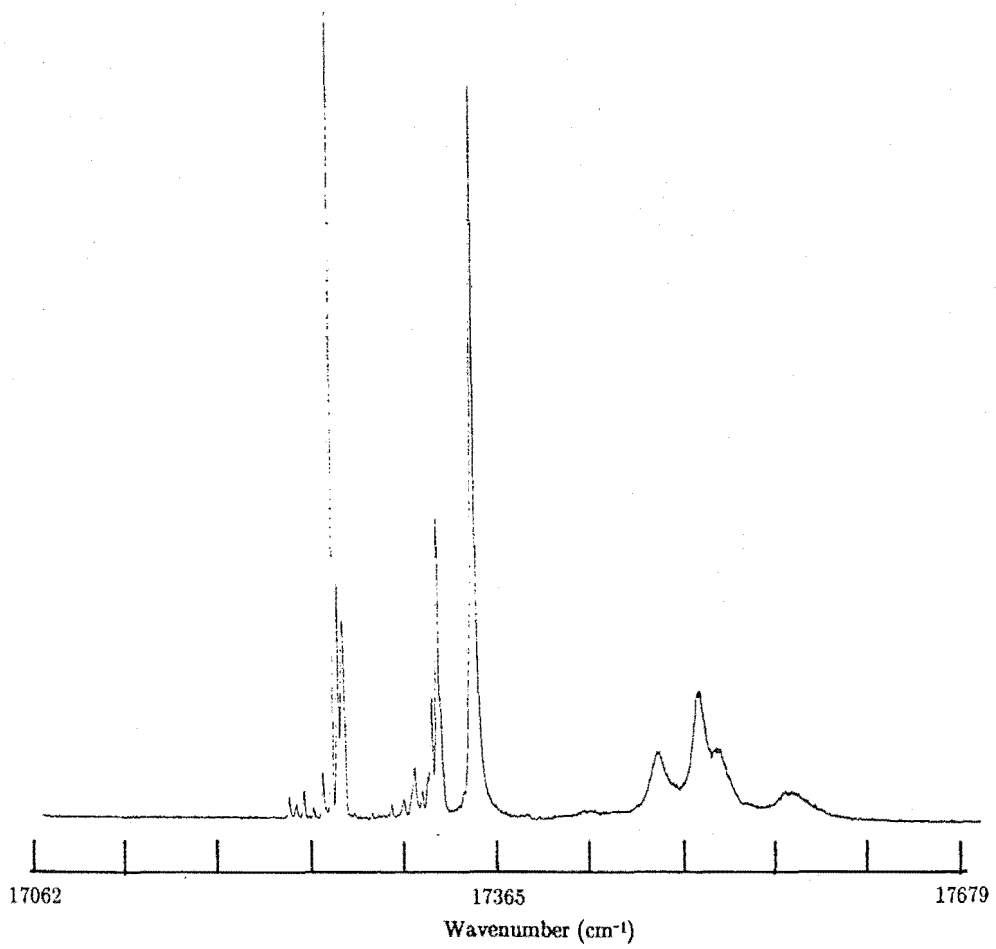

Figure 8.15: 10 K D multiplet excitation spectrum of the $CaF_2 : Nd^{3+} : Yb^{3+}$ M' F^- centre monitoring the 8631.8 nm line of the Nd^{3+} R multiplet.

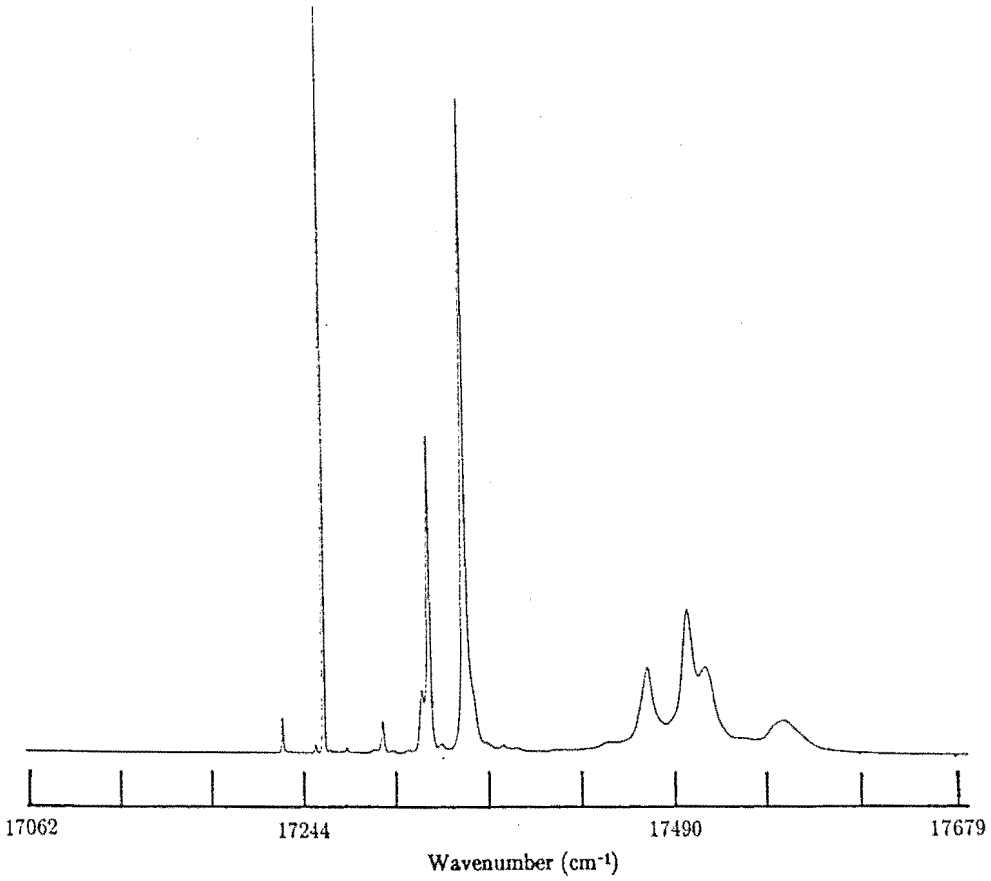

Figure 8.16: 10 K D multiplet excitation spectrum of the $CaF_2 : Nd^{3+} : Yb^{3+}$ M' F^- centre monitoring the 9765 nm line of the Yb^{3+} $^2F_{5/2}$ multiplet.

8.4 Conclusion

The results show that the configuration of the M' centre observed in $CaF_2 : Nd^{3+} : RE^{3+}$ is similar to the M centre observed in $CaF_2 : Nd^{3+} : RE^{3+}$ and $CaF_2 : Nd^{3+}$ crystals and that there are interactions between the two rare earth ions within these centres ($RE^{3+} : Ce^{3+}$, Gd^{3+} and Yb^{3+}).

Energy upconversion was observed in the M' centre of the investigated $CaF_2 : Nd^{3+} : RE^{3+}$ crystals and the results indicate a phonon assisted energy transfer process between the rare earth ions within these centres.

State		Experimental		State		Experimental	
$^4I_{9/2}$	Z_1	0		$^4F_{7/2}$,	A_1	13462	(± 1)
	Z_2	37	(± 1)	$^4S_{3/2}$	A_2	13584	(± 1)
	Z_3	150	(± 1)		A_3		
	Z_4	380	(± 1)		A_4		
	Z_5	503	(± 1)		A_5	13698	(± 1)
					A_6	13703	(± 1)
$^4I_{11/2}$	Y_1	2025	(± 1)				
	Y_2	2052	(± 1)	$^4F_{9/2}$	B_1	14825	(± 2)
	Y_3	2082	(± 2)		B_2		
	Y_4	2141	(± 1)		B_3	14885	(± 1)
	Y_5	2189	(± 2)		B_4	14895	(± 1)
	Y_6	2224	(± 1)		B_5	14910	(± 1)
$^4I_{13/2}$	X_1	3964	(± 1)	$^2H_{11/2}$	C_1	15989	(± 2)
	X_2	3987	(± 1)		C_2	16001	(± 2)
	X_3	4029	(± 1)		C_3	16005	(± 2)
	X_4	4089	(± 1)		C_4	16040	(± 3)
	X_5	4137	(± 3)		C_5	16065	(± 3)
	X_6	4211	(± 1)		C_6	16130	(± 2)
	X_7	4323	(± 2)				
				$^4G_{5/2}$,	D_1	17260	(± 1)
$^4I_{15/2}$	W_1	5804	(± 1)	$^2G_{7/2}$	D_2	17320	(± 2)
	W_1	5836	(± 1)		D_3	17346	(± 2)
	W_3	5876	(± 1)		D_4	17471	(± 2)
	W_4	5932 ?	(± 1)		D_5	17496	(± 2)
	W_5				D_6	17512	(± 2)
	W_6	6286 ?	(± 2)		D_7	17563	(± 2)
	W_7	6564	(± 1)				
	W_8	6642	(± 1)	$^4G_{7/2}$	E_1	19118	(± 2)
					E_2		
$^4F_{3/2}$	R_1	11578	(± 2)		E_3		
	R_2	11624	(± 2)		E_4		
	R_1'	11574	(± 2)				
	R_2'	11620	(± 2)	$^2P_{1/2}$	I_1	23418	(± 2)
$^4F_{5/2}$,	S_1	12561	(± 1)	$^4D_{3/2}$	L_1	28266	(± 2)
$^2H_{9/2}$	S_2	12583	(± 1)		L_2	28283	(± 2)
	S_3	12605	(± 1)				
	S_4	12630	(± 1)				
	S_5	12637	(± 1)				
	S_6	12659	(± 1)				
	S_7	12765	(± 2)				
	S_8	12853	(± 2)				

Table 8.1: 10 K energy levels (in air cm^{-1}) of the M' F^- centre in $CaF_2 : Nd^{3+} : Ce^{3+}$. ? Tentative assignment.

State		Experimental		State		Experimental	
$^4I_{9/2}$	Z_1	0		$^4F_{7/2}$,	A_1	13459	(± 1)
	Z_2	33.6	(± 1.6)	$^4S_{3/2}$	A_2	13583	(± 1)
	Z_3	147.2	(± 1.3)		A_3		
	Z_4	381.6	(± 2.3)		A_4		
	Z_5	505.7	(± 1.6)		A_5	13694	(± 1)
					A_6	13699	(± 1)
$^4I_{11/2}$	Y_1	2026.1	(± 1.6)				
	Y_2	2051.6 ?	(± 3.4)	$^4F_{9/2}$	B_1	14827	(± 1)
	Y_3	2080.6	(± 1.8)		B_2	14855	(± 1)
	Y_4	2137.2	(± 1.8)		B_3	14882	(± 1)
	Y_5	2188.6	(± 1.6)		B_4	14894	(± 1)
	Y_6	2223.8	(± 1.8)		B_5	14902	(± 1)
$^4I_{13/2}$	X_1	3962	(± 1)	$^2H_{11/2}$	C_1	15998	(± 2)
	X_2	3986	(± 1)		C_2		
	X_3	4022	(± 1)		C_3	16018	(± 2)
	X_4	4086	(± 1)		C_4	16048	(± 2)
	X_5	4130	(± 1)		C_5	16074	(± 2)
	X_6	4209	(± 1)		C_6	16138	(± 2)
	X_7	4321	(± 1)				
				$^4G_{5/2}$,	D_1	17269	(± 2)
$^4I_{15/2}$	W_1	5799	(± 1)	$^2G_{7/2}$	D_2	17313	(± 2)
	W_1	5890	(± 1)		D_3	17342	(± 2)
	W_3	5902	(± 1)		D_4	17477	(± 2)
	W_4	5927 ?	(± 1)		D_5	17507	(± 5)
	W_5				D_6	17527	(± 5)
	W_6	6282 ?	(± 1)		D_7	17573	(± 2)
	W_7	6564	(± 1)				
	W_8	6641	(± 1)	$^4G_{7/2}$	E_1	19117	(± 3)
					E_2		
$^4F_{3/2}$	R_1	11583.6	(± 1.6)		E_3		
	R_2	11618.2	(± 1.6)		E_4		
	R_1'	11576	(± 2)				
	R_2'	11611	(± 2)	$^2P_{1/2}$,	I_1	23407 ?	(± 3)
				$^2D_{5/2}$	I_2	23416 ?	(± 3)
$^4F_{5/2}$,	S_1	12258	(± 1)		I_3		
$^2H_{9/2}$	S_2	12579	(± 1)				
	S_3	12604	(± 1)	$^2P_{3/2}$	K_1	26297	(± 3)
	S_4	12628	(± 1)				
	S_5	12651	(± 1)	$^4D_{3/2}$	L_1	28266	(± 3)
	S_6	12732	(± 1)		L_2	28284	(± 3)
	S_7	12760	(± 1)				
	S_8	12849	(± 1)				

Table 8.2: 10 K energy levels (in air cm^{-1}) of the M' F^- centre in $CaF_2 : Nd^{3+} : Gd^{3+}$. ? Tentative assignment.

State		Experimental		State		Experimental	
$^4I_{9/2}$	Z_1	0		$^4F_{9/2}$	B_1	14844	(± 2)
	Z_2	30	(± 1)		B_2	14852	(± 2)
	Z_3	136	(± 1)		B_3		
	Z_4	388	(± 2)		B_4		
	Z_5	500	(± 2)		B_5		
$^4I_{11/2}$	Y_1	2027	(± 1)	$^2H_{11/2}$	C_1	15987	(± 2)
	Y_2	2048	(± 1)		C_2	16003	(± 2)
	Y_3	2065	(± 1)		C_3		
	Y_4	2135	(± 1)		C_4		
	Y_5	2185	(± 1)		C_5		
	Y_6	2222	(± 2)		C_6		
$^4I_{13/2}$	X_1	3965	(± 1)	$^4G_{5/2}$,	D_1	17254	(± 2)
	X_1	3988	(± 1)	$^2G_{7/2}$	D_2		
	X_3	4012	(± 6)		D_3		
	X_4	4086	(± 2)		D_4		
	X_5	4128	(± 1)		D_5		
	X_6	4209	(± 1)		D_6		
	X_7	4327	(± 2)		D_7		
$^4I_{15/2}$	W_1	5915	(± 2)	$^4G_{7/2}$	E_1	19115	(± 2)
	W_2	5931 ?	(± 3)		E_2		
	W_3	5965 ?	(± 2)		E_3		
	W_4	5991 ?	(± 2)		E_4		
	W_5	6040 ?	(± 2)				
	W_6	6284	(± 2)	$^4D_{9/2}$,	G_1	21123	(± 2)
	W_7	6553	(± 1)	$^2D_{3/2}$	G_2	21137	(± 2)
					G_3		
$^4F_{3/2}$	R_1	11584	(± 1)		G_4		
	R_2	11613.5	(± 1.6)				
				$^2P_{3/2}$	K_1	23417	(± 2)
					K_2	23422	(± 2)
				$^4D_{3/2}$	L_1	28252	(± 2)
					L_2	28276	(± 2)

Yb^{3+} multiplet

State	Experimental	
$^2F_{5/2}$	0	
	52.2	(± 1.6)
	98.1	(± 1.6)

Table 8.3: 10 K energy levels (in air cm^{-1}) of the M' F^- centre in $CaF_2 : Nd^{3+} : Yb^{3+}$. ? Tentative assignment.

		M	N	M' $Nd^{3+}-Ce^{3+}$	$Nd^{3+}-Gd^{3+}$	$Nd^{3+}-Yb^{3+}$
τ	(ms)	.092	.0348	.61	.59	.0831
	($\pm$%)	10	10	10	10	10
W^{NR}	(s^{-1})	10101	27967	870	926	11265
	($\pm$%)	11	11	28	18	11

τ = fluorescence lifetime
W^{NR} = non-radiative decay rate
W^{R} = radiative decay rate
= 769 ($\pm$10%) (s^{-1}) $CaF_2 : Nd^{3+}\ F^-\ C_{4V}$

Table 8.4: 10 K non-radiative decay rates for the $R_1 \rightarrow Z_1$ transition of the $M'\ F^-$ centres in $CaF_2 : Nd^{3+} : RE^{3+}$.

Chapter 9

Conclusion

Laser selective excitation techniques have successfully identified energy levels of several Nd^{3+} centres in SrF_2 (18) and CaF_2 (11), and energy levels of a mixed $Nd^{3+} - RE^{3+}$ centre in double rare earth doped CaF_2 (where RE^{3+} : Ce^{3+}, Gd^{3+} and Yb^{3+}).

The energy levels of the ^4I and other multiplets for the tetragonal F^- centre in $CaF_2 : Nd^{3+}$ and $SrF_2 : Nd^{3+}$ and the M and N F^- centres in $CaF_2 : Nd^{3+}$ were unambiguously identified. For the F^- centres energy upconversion processes involving the R multiplet as the intermediate level were observed. The upconversion mechanism for the tetragonal centre is dominated by a sequential two photon excitation process (STEP), whereas in the case of the M and N centres the mechanism is dominated by a phonon-assisted energy transfer upconversion process (ETU).

The hydrogenic charge compensating centres in $CaF_2 : Nd^{3+}$ and $SrF_2 : Nd^{3+}$ were also studied. The hydrogenic nature of these charge compensating centres was confirmed by the observation of isotope shifts and by observation of vibronic transitions which involved the local mode vibrational frequencies of the hydrogenic ions. Some of the multiple charge compensating hydrogenic centres exhibit bleaching behaviour which can be either recoverable or non-recoverable. These effects are attributed to the migration of hydrogenic ions adjacent to the rare earth ion. Two new H^- charge compensating centres, $H1$ and $H2$, exhibit bleaching behaviour whereby the bleaching of one centre can subsequently cause the recovery of the other centre. The difference in recovery and decay rates of the two centres suggests that there is more than one mechanism involved in the interconversion process between the two hydrogen centres. A line of a single new photoproduct centre was also observed for the C_{S4} D^- centre in $SrF_2 : Nd^{3+}$.

For the tetragonal F^- centre and its hydrogenic analogues in both $CaF_2 : Nd^{3+}$ and $SrF_2 : Nd^{3+}$, the C_{4V} irreducible representation of some of the energy levels were identified by polarisation studies of the laser selective excitation spectra.

A single oxygen charge compensating centre was observed in hydrogenated

$CaF_2 : Nd^{3+}$ and $SrF_2 : Nd^{3+}$. Polarisation results show that the symmetry of this centre is neither tetragonal nor trigonal but is of lower symmetry.

It was established that the M' centres observed in $CaF_2 : Nd^{3+} : RE^{3+}$ (where RE^{3+} : Ce^{3+}, Gd^{3+} and Yb^{3+}) have a configuration similar to the M centre observed in $CaF_2 : Nd^{3+}$. The M' centres also display energy upconversion processes similar to those of the M centre. It was determined that the non-radiative relaxation processes for these two rare earth ion centres are, principally, energy transfer processes between the rare earth ions within the centre.

Crystal field analyses have been carried out for the tetragonal centres observed in both $CaF_2 : Nd^{3+}$ and $SrF_2 : Nd^{3+}$ and confirmed the C_{4V} irreps designation of some of the energy levels assigned by the polarisation results.

A simplified superposition model was used to analyse the ion positions in the C_{4V} centres. The superposition model calculations gave the correct signs for the crystal field parameters and predicted that the ratio B^4_{oct}/B^6_{oct} is smaller for the tetragonal centre than for the cubic centre. The co-ordination angles, θ_a and θ_b, derived from the superposition model did not give a clear indication of the distortion for the various C_{4V} centres; the values calculated for θ_b in particular are not physically reasonable.

In summary, laser selective excitation studies have been successfully applied to the Nd^{3+} ion in CaF_2 and SrF_2 for the first time and yielded the energy levels of 8 F^- and 2 hydrogenic centres in $CaF_2 : Nd^{3+}$ and 4 new F^- and 6 hydrogenic centres for $SrF_2 : Nd^{3+}$. These results form the basis for further investigations paralleling those done for the Er^{3+} case (Cockroft 1987).

Appendix A

Computerising the Data Acquisition system

Past experience has shown that a personal computer can be incorporated into many experiments to automate the data acquisition procedures and to produce a close to 'real time' display of the experimental data either graphically or numerically.

The choice of computer depends on a number of constraints, namely the computing power required to provide 'real time' analysis of the experimental data and the ease of interfacing it with other devices. The cost of the computer and its associated hardware can also be a decisive factor. In the context of Raman Spectroscopy and Laser Selective Excitation no complicated 'real time' data processing is required and the anticipated speed in data acquisition is not less than one second per data point, this being the usual photon counting integration time constant. An Apple IIe desk top computer with twin disc drive was chosen as a dedicated machine for the data acquisition system. It meets the requirements mentioned above and interfacing the Apple computer to other devices was made particularly easy by the provision of seven auxiliary expansion slots and by the availability of much inexpensive hardware produced by numerous manufacturers.

The underlying concept of the present approach is to make the Apple computer the central 'general manager' of the data acquisition system. Communications between various devices are made through the computer so that it has control of the whole system, as illustrated in Fig. A.1.

The type of communication link between the Apple computer and various devices depends on the interfacing ability of the existing equipment and the speed required. Fig. A.2 shows the relative cost and sophistication of different types of computer interfaces commonly used. In the present case a bidirectional communication link between the Apple computer and the Spex. Compudrive (CD2A) is established through a Super Serial Card (SSC) at 4800 baud. It was decided to make full use of the CD2A's intelligence to control the spectrometer while the computer would only programme the

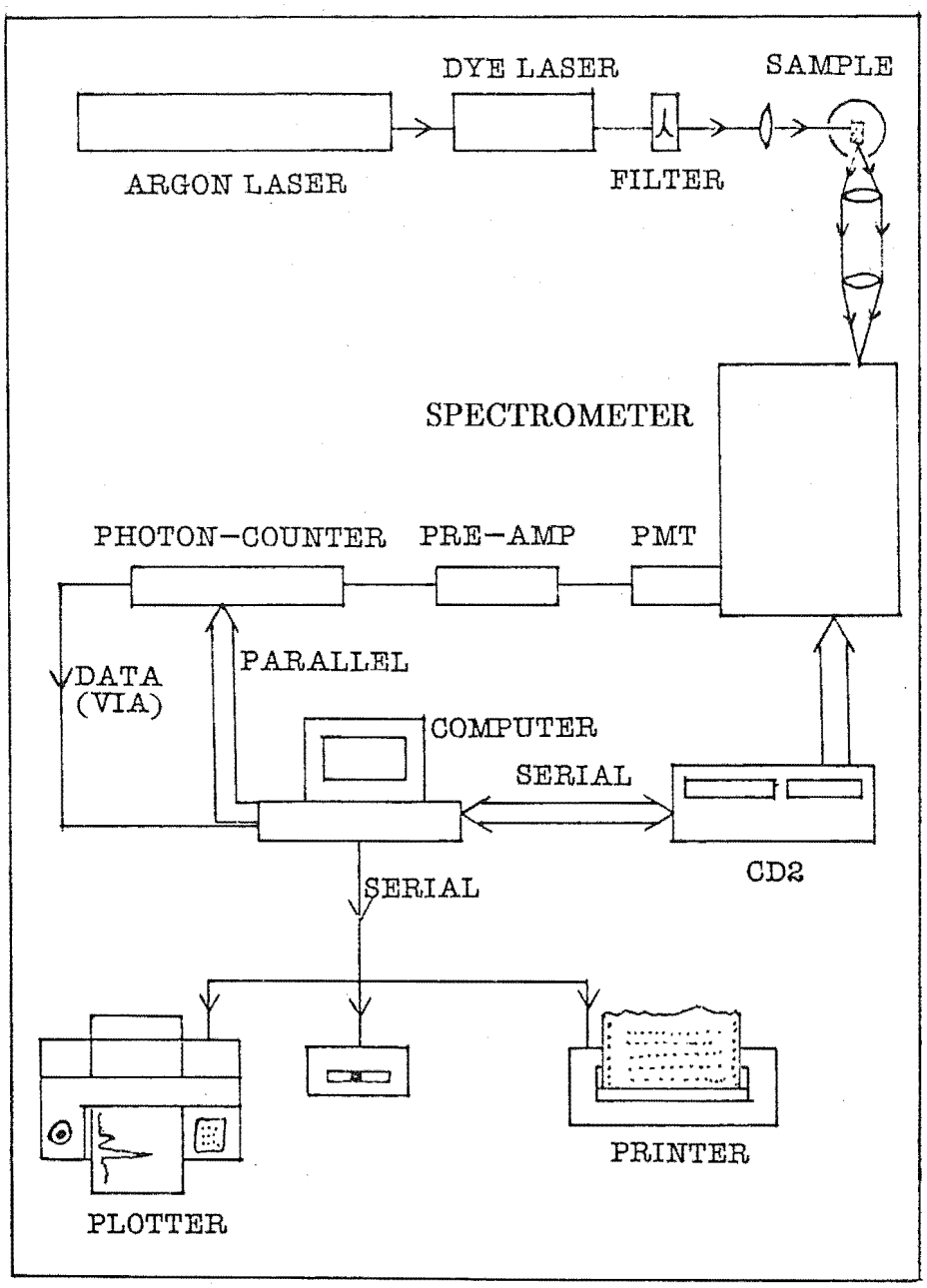

Figure A.1: Schematic diagram showing the general layout of the apparatus and the communication links between various devices of the data acquisition system.

CD2A and receive the status of the spectrometer from it. Both the plotter and the printer are also linked to the Apple computer via a SSC at 9600 baud. Data transfer between the photon counter (PAR model 1112) and the Apple computer can be via either a Peripheral Interface Adapter (PIA) or a Versatile Interface Adapter (VIA). The VIA was chosen for its ability to enable remote programming of the photon counter. See Table A.1 for a brief list of the relevant specifications of each device.

Data are updated in groups of ten and are permanently stored on 5.25 inch floppy discs. The plotter and the printer are updated every 10 data points to give a close to 'real time' display of the spectrum and the data values. The printer output became a back-up when a plotting and peak finding programme was made available. Data for each spectrum and its relevant experimental parameters are permanently stored on 5.25 inch floppy discs in sequential access text files. They are stored in a compact form to maximise storage space on the floppy disc, with a trade off of a slight reduction in the speed of retrieving data from the disc and plotting.

Under Applesoft, a sequential text file (TXT) consists of one or more records separated from each other by carriage return characters (hexadecimal $\$0D$, high order hexadecimal $\$8D$ or decimal 13). The end of a text file is signalled by the End of File (EOF) position stored in the directory entry for the file. Usually, only valid ASCII (American Standard Code for Information Interchange) characters are allowed in a TXT file in order for them to be accessible to Basic programmes. Each character (text) or digit (numerics) occupies a byte in the file and is stored as an ASCII character equivalent in hexadecimal notation. For example, Applesoft takes five bytes of disc space to store the number 25342 and the ASCII characters equivalent in high order hexadecimal notation are $B2$, $B5$, $B3$, $B4$ and $B2$. This is not very efficient use of disc space. In the present case, the output of the photoncounter is in BCD (Binary Coded Decimal) format with three significant figures plus a number giving the power of ten (exponent, E), e.g. 2.53E5. If the number 2.53E5 is to be stored on disc, it will take six bytes of disc space in the format of 253000. The last three digits have no significant value except for locating the decimal point, which can be specified by a byte giving that position (the exponent, E). Since each digit is in BCD format which only occupies a nibble (four bits or half a byte), each byte can store two BCD digits. Therefore, the four digits (three significant figures and the exponent) can be stored in just two bytes, which is a great saving of disc space especially for large value numbers. Fig. A.3 gives a clearer illustration of how the present approach compacts and stores data. In Applesoft's TXT file the carriage return character is used to separate records, so care is required to handle the coincidence of data having 13 amongst their digits. In Basic, a GET A$ command is used to retrieve data from the disc in order to overcome this minor problem.

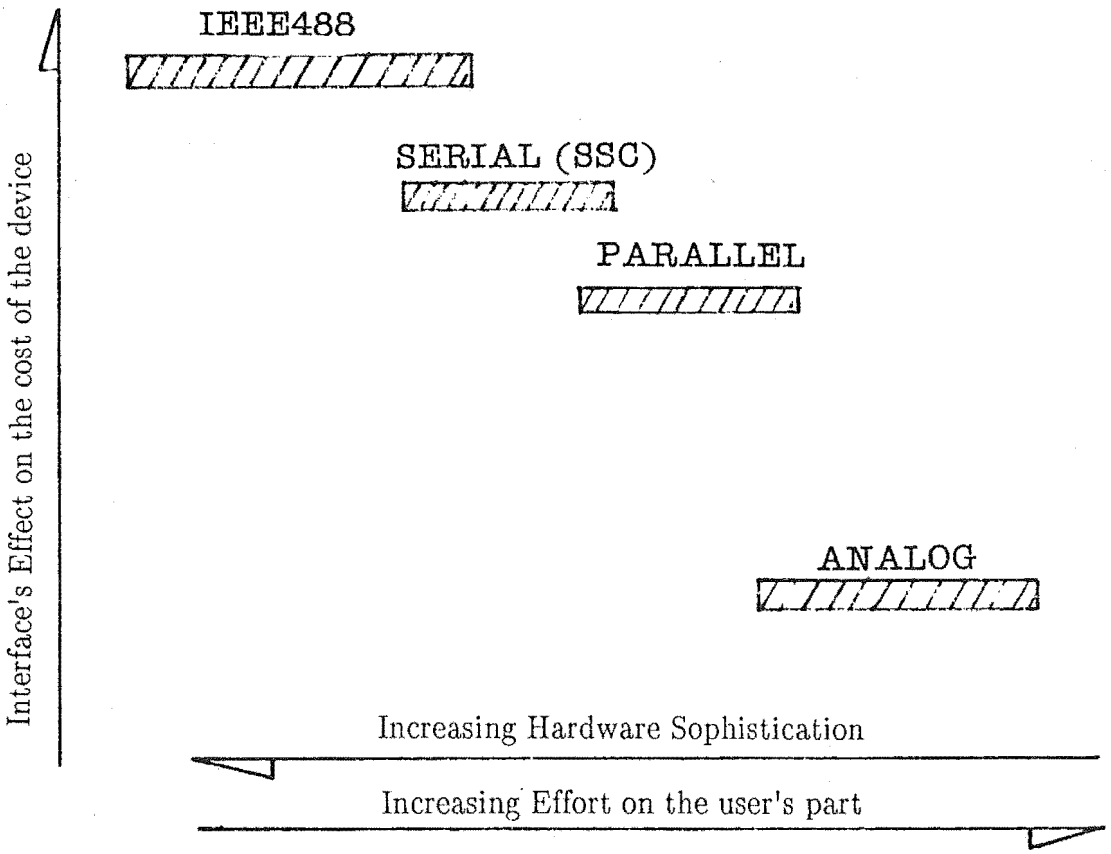

Figure A.2: Diagram showing the relative cost and sophistication of various common computer interface links.

Computer	:	**Apple IIe**
		- 64 K byte RAM.
		- 80 column card.
		- twin disc drive.
	future options	- extra memory;
		- double high resolution graphic;
		- Basic compiler.
Plotter	:	**HP7475A**
		- accept A3 and A4 paper.
		- 6 pens.
		- 0.025 m.m. resolution.
		- 0.1 m.m. repeatability.
		- versatile graphic language.
		- 1 K buffer.
		- programmable pen speed.
Printer	:	**C.Itoh 8510B**
		- printing rate 120 cps .
		- 2 K buffer.

Table A.1: Specifications of the Apple computer, Plotter and Printer.

Past experience has shown that the executional speed of the Basic language is adequate when used in a dedicated control system where extremely high speed is not essential. The Basic language has the advantages of ease of programme development and maintenance as well as being easy to learn and understand. The original concept was to have packages of machine language sub- routines to handle various interface I/O protocols and the Basic programme to handle the communication with the operator. At present the entire programme is written in Basic and seems to handle all the functions with reasonable speed and ease. The programme is written in the Apple's ProDos operating system and a brief summary of its disc structure is given in Table A.2. The programme is designed to give appropriate interactive control between the operator and all the connected devices. It checks all inputs for valid entry and has error handling facilities for most circumstances.

Programming is an evolving process where continuing improvements and modifications to meet needs are a necessity. Specific possible future developments include interfacing assembly language sub-routines to the Basic programme for more efficient I/O; a filter routine to extract weak signals from an exceptionally noisy background; incorporation of interrupt capabilities to maximise the computer flexibility; and a faster data decoding and plotting routine. Any future developments must conform to the data format and the compact storage structure for compatibility.

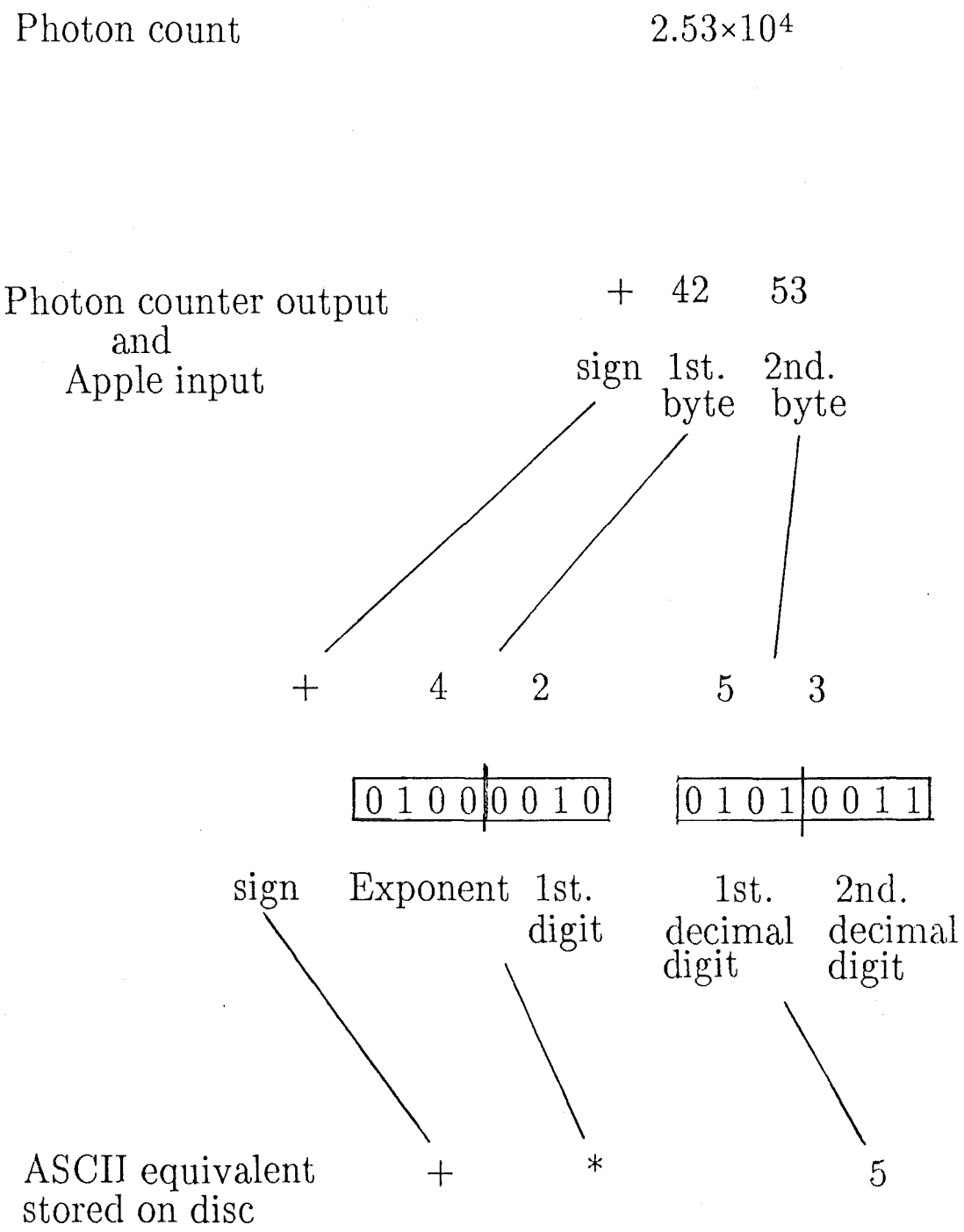

Figure A.3: An example illustrating the method used to compact the data for storing on floppy discs.

Apple ProDos

Disc structure is a hybrid of Dos 3.3 and Apple Pascal.

From Pascal	-	basic layout of the disc using the same physical logical sector order.
	-	2 sector block of 512 bytes.
	-	2 block load section.
	-	4 block directory and files stored in block order.
From Dos 3.3	-	the concept of sector use bit maps.
	-	track/sector list.

From the standpoint of combined speed of disc access and efficient use of space, ProDos surpasses its predecessors.

Table A.2: Extract from CALL-A.P.P.L.E. (Feb.1985) by S.C.K.Hunter.

Appendix B

Analysis of the Signal strength in the Fluorescence Lifetime measurements

This appendix gives a brief analysis of the signal strength in the pulsed laser pumped fluorescence experiments and the methods used in determining the fluorescence decay time constant. This summary was written in close consultation with Mr. C.H. Rowe who designed the circuit to implement the integral method.

It is common practice to use fast pulse amplifiers on the output of a photomultiplier to monitor and quantify the fluorescence decay pulse appearing on the anode of the detector.

With high peak fluorescence intensities there are few difficulties with this approach. Superimposed noise on the decay function may be integrated out by coherently adding the signal plus noise on successive decay pulses. This is the function of the box car averager. For N successive pulses, this procedure will improve the signal to noise, s/n, ratio by $\sqrt{N}$. That is, 100 successive pulses will improve s/n by a factor of 10.

In the case of low level signals, where the signal is better described as a succession of clearly resolved photon pulses, the fluorescence decay function becomes a frequency modulated pulse train with the highest pulse density at the start of the measuring interval. In this case, the s/n ratio varies in proportion to $\sqrt{N_p}$, where N_p is the total number of photon counts in the measured interval. As each photon event is nominally independent of the others the distribution obeys stochastic (random) or Poissonian statistics. There is thus a finite probability that two photon events will coincide within a specified time interval, and the photon pulses will 'stack', that is added in amplitude.

While the above method is well understood and applied readily, it does have the disadvantages of requiring good impedence matching and an inability to discriminate against induced noise especially at low signal levels unless a well designed discriminator is incorporated into the design.

The signal input of the box car averager system presently used was found

to be charge sensitive, i.e. responded to the total area underneath each photon pulse. An ordinary fast pulse amplifier increases the amplitude of each photon pulse but the total area underneath each pulse is relatively unchanged. This, together with the low fluorescence intensity measured could be the reason for the extremely weak signal which was observed. A slight improvement was achieved when the fast pulse amplifier was replaced by a photon counting amplifier built by the electronics workshop of this department. This amplifier had a discriminator to offset the dark current and could amplify and shape each photon pulse to an uniform width and height, as illustrated in Fig. B.1. This increases the total area underneath each photon pulse, but has the potential disadvantage of pulse 'stacking' especially for strong fluorescence signals. The low fluorescence intensity (small number of photons) together with the inability of the present design, to discriminate large induced noise from the solenoid of the temperature controller of the liquid nitrogen cooled photomultiplier makes this method unsuitable for the present situation. A well designed 'window' discriminator would greatly improve the performance of this method.

In the present context of measuring the fluorescence decay lifetime of an excited energy level, the decay is assumed to be an exponential function. It is well known that both the mathematical integral and the differential of a common first order exponential function are themselves exponential, the time constant remaining unaffected by such manipulation.

In the context of a photomultiplier detector, it is a device in which a charge is dumped onto a well-insulated electrode (the anode) which has a small but finite capacitance. The geometry of the dynode-anode structure is such that a considerable change in potential of the anode, will not affect the charge collecting function, i.e. the system has a very high effective source impedence. Thus, if a capacitor is placed in the anode circuit, it will act as a precision charge integrator. This precision charge integrator may be reset after a specified time interval prior to the next laser pulse, hence the resetable integrator.

Amongst a number of practical advantages of this technique is the rejection of induced noise as it should integrate to zero, and the lack of requirement for impedence matching as the reflected signal due to impedence mismatch should also integrate to zero. The disadvantage of this method is that the long term steady value, or the 'base line', is not reliably determined since it is dependent on the fluorescence intensity, which is in turn dependent on the intensity of each laser pulse.

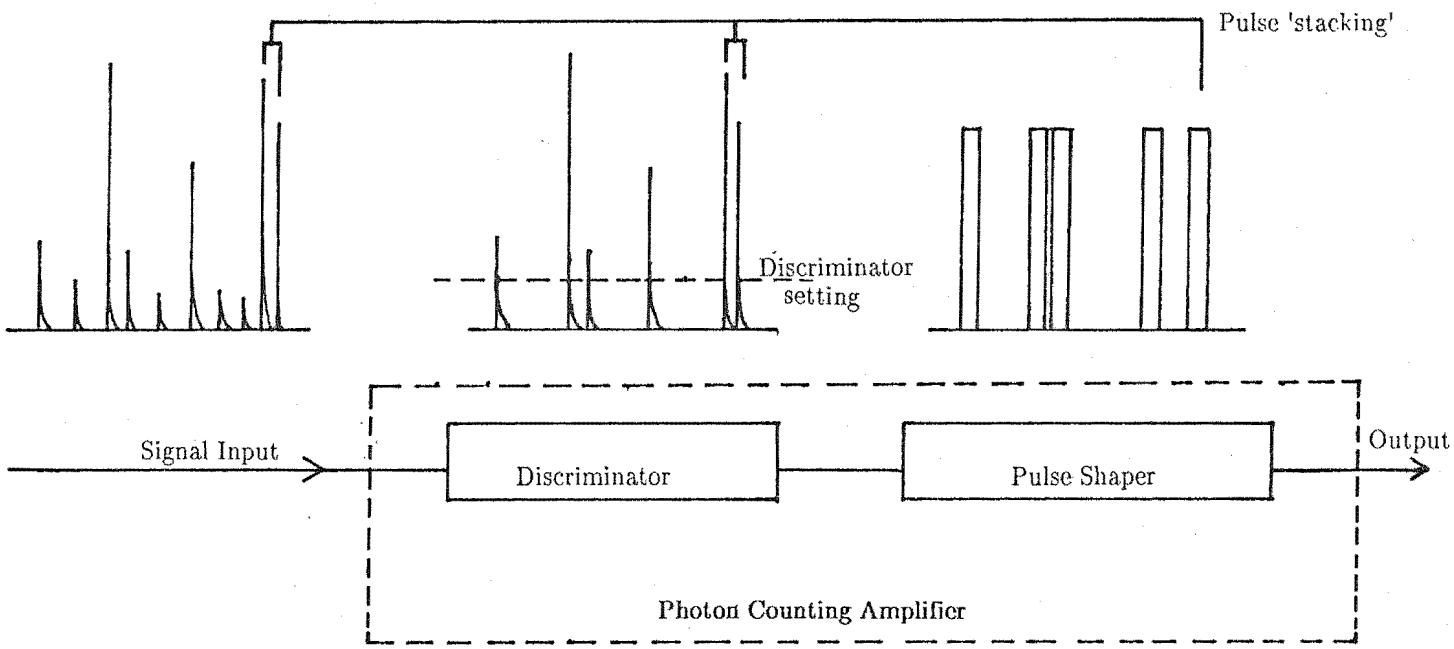

Figure B.1: Schematic diagram of the photon counting amplifier evaluated for the fluorescence lifetime measurements.

B.1 Data Reduction Methods

There are a variety of analytical procedures available to allow the determination of the time constant of the exponential decay function. The algorithm usually requires the assumption of the type of exponential function being fitted, i.e. single or multiple exponential decay function(s). In the present analysis, a single time constant is assumed for the exponential decay function of the form :

$$y = Ae^{(-k.t)} \tag{B.1}$$

where

$$k = (\tau)^{-1} \quad ,$$

and τ is the fluorescence decay time. It is important to ensure that the long term value or the base line is reliably determined or that the algorithm is such that the 'base line' value is eliminated in the reduction procedures. This is essential when the integral method is used. It was observed that the data reduction routine provided by the software package SR265 is relatively sensitive to the long term value of the exponential function being fitted, as illustrated by Fig. B.2, where a 33% change in the derived time constant resulted from just a 1.25% change in the base line value. Clearly this algorithm is unacceptable as it stands.

Theoretically, a simple exponential decay function can be uniquely determined by just three points. For example, let t_1, t_2 and t_3 be times a fixed interval x apart, where :

$$\begin{aligned} t_2 &= t_1 + x \\ t_3 &= t_2 + x \quad , \end{aligned}$$

then equation B.1 can be solved as 3 simultaneous equations to give :

$$k = -\frac{1}{x} ln \left(\frac{y_3 - y_2}{y_2 - y_1} \right) \quad . \tag{B.2}$$

This algorithm is very susceptible to noise and does not use most of the available data but facilitates a means of determining the time constant of a very long lifetime decay (Harris et al. 1983). Another way to eliminate the problem of the base line is to construct an exponential function independent of the base line. This can be achieved by dividing the original exponential function into two halves and subtracting one half from the other, as illustrated in Fig. B.3. Although this method can eliminate the 'base line' problem, it introduces noise onto the data and effectively reduces the number of data points by half. Additionally, it will work only for a simple exponential function.

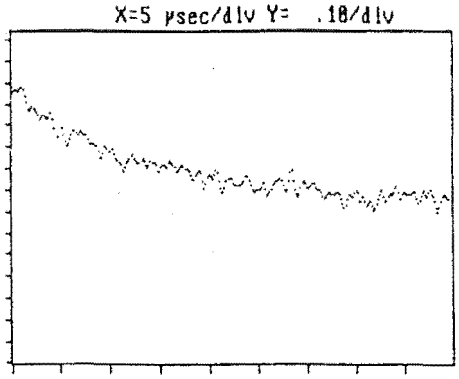

Original fluorescence decay

'base line' shifted by –4.0

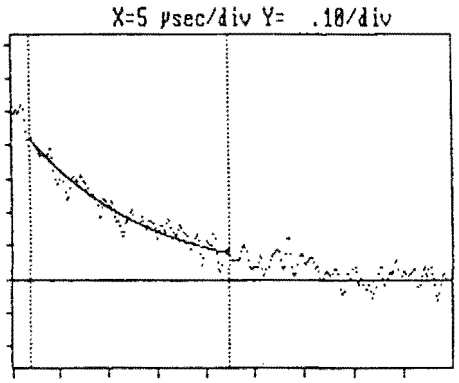

Y = A *exp(-B*(X- 1.95))
A= .418 B= .8296E-01 /μsec

$\tau = \frac{1}{B} = 12$ us.

'base line' shifted by –3.95

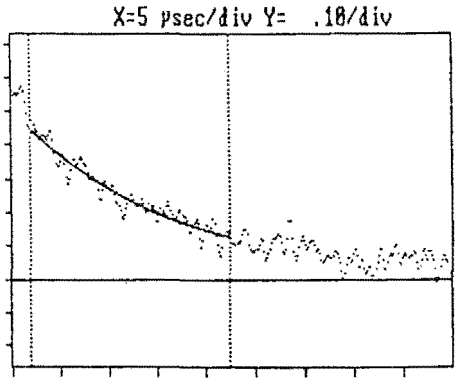

Y = A *exp(-B*(X- 1.95))
A= .446 B= .6265E-01 /μsec

$\tau = \frac{1}{B} = 16$ us.

Figure B.2: Diagram illustrating the sensitivity of the exponential data reduction routine of the SR265 software package to the asymptote value set for an exponential function.

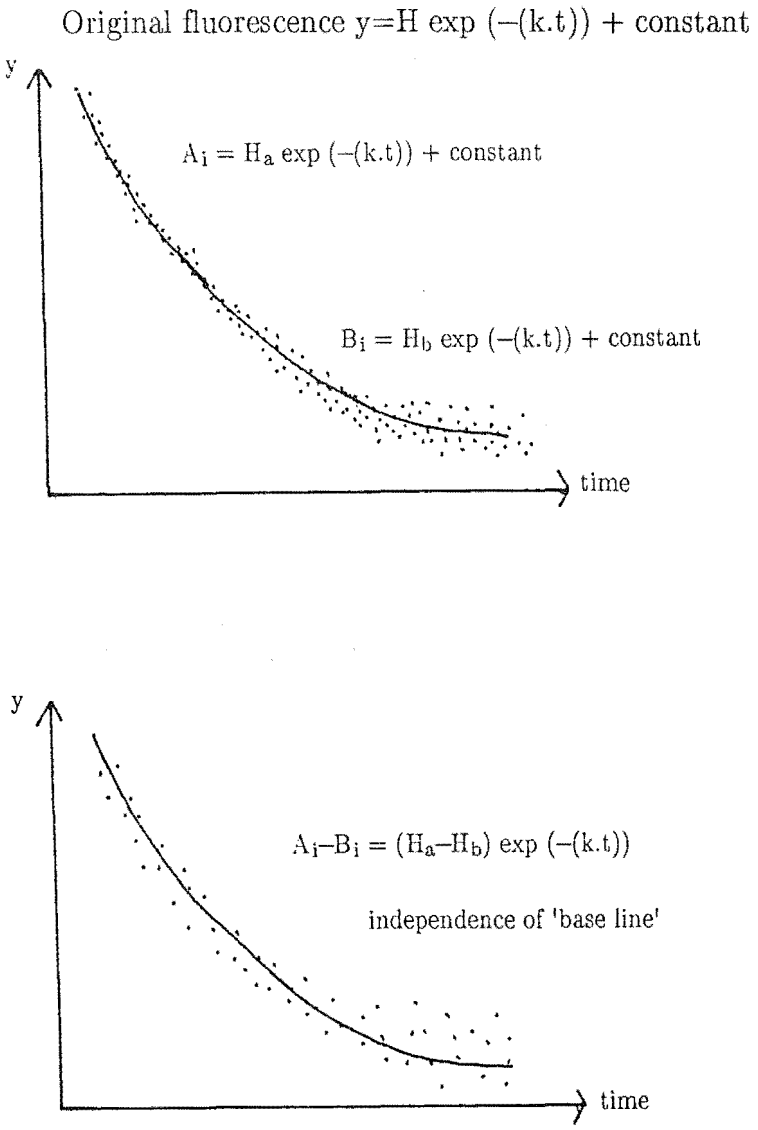

Figure B.3: Schematic diagram illustrating one of the methods that can eliminate the problem caused by the uncertain asymptote value of an exponential function.

Ideally, a least squares fit of the exponential function to the data should give a more satisfactory result. However, this was not attempted in the time available because of difficulties in gaining access to the experimental data files produced by the SR265 programme. A compromise was achieved by averaging the results obtained using the first two methods mentioned above and comparing them with the estimated decay time constant observed directly on a single pulse oscilloscope trace. The $\pm 10\%$ uncertainty quoted for the decay time constants is typical of the type of scatter achieved by these methods.

References

Asawa C.K., Robinson M. , *Phys. Rev. 141, 251 (1966)*

Ashburner I.J., Newman R.C., Mclaughlan S.D. , *Phys. Lett. 27A, 212 (1968)*

Bagdasarov Kh. S., Voron'ko Yu.K., Kaminskii A.A, Krotova L.V., Osiko V.V. , *Phys. Stat. Sol. 12, 905 (1965)*

Baker J.M. , *Crystals with the Fluorite Structure , Ed. Hayes W. (Clarendon Press, Oxford, 1974)*

Baker J.M., Wood R.L. , *J. Phys. C. : Solid State Phys. 13, 4751 (1980)*

Barthem R.B., Buisson R., Vial J.C. , *J Lumines. 38, 190 (1987)*

Bleaney B., Lyewwllyn P.M., Jones D.A. , *Proc. Phys. Soc. B 69, 858 (1956)*

Born M., Huang K. , *Dynamical Theory of Crystal Lattice. (Clarendon Press, Oxford, 1954)*

Butler P.H. , *Point Group Symmetry Applications Methods and Tables (Plenum, N.Y., 1981)*

Butler P.H. , *Private communication, 1987*

Butler P.H., Wybourne B.W. , *Int. J. Quantum Chem. 10, 599 (1976)*

Carnall W.T., Crosswhite H., Crosswhite H.M. , *Argonne National Laboratory Report*

Cockroft N. , *Ph.D. Thesis, University of Canterbury (1987)*

Cockroft N.J., Han T.P.J., Reeves R.J., Jones G.D., Syme R.W.G. , *Optics Lett. 12, 36 (1987)*

Cockroft N.J., Thompson D., Jones G.D., Syme R.W.G. , *J. Chem. Phys. 86, 521 (1987)*

Condon E.U., Shortley G.H. , *The Theory of Atomic Spectra , (Cambridge University Press, 1951)*

Dexter D.L. , *J. Chem. Phys. 21, 836 (1953)*

Dieke G.H. , *Spectra and Energy Levels of Rare Earth ion in Crystals , Ed. Crosswhite H.M., Crosswhite H. (Interscience, N.Y., 1968)*

Edgar A. , *Ph.D. Thesis, University of Canterbury, 1974*

Edgar A., Freeth C.A., Jones G.D. , *Phys. Rev. B. 15, 5023 (1977)*

Elliot R.J., Hayes W., Jones G.D., MacDonald H.F., Sennett C.T. , *Proc. Roy. Soc. (London) A 289, 1 (1965)*

Fong F.K., Naberhuis S.L., Miller M.M. , *J. Chem. Phys. 56, 4020 (1972)*

Forster Th. , *Faraday Soc. 27, 7 (1959)*

Freeth C.A. , *Ph.D. Thesis, University of Canterbury, 1980*

Freeth C.A. , *Private communication, 1988*

Freeth C.A., Jones G.D. , *J. Phys. C. : Solid State Phys. 15, 6833 (1982)*

Gustafson F.J., Wright J.C. , *Analytical Chemistry 51, 1762 (1979)*

Hall J.H., Schumacher R.T. , *Phys. Rev. 127, 1892 (1962)*

Harris R.C. , *Clin. Chem. 29, 2079 (1983)*

Hayes W., *Crystals with the Fluorite Struture , (Clarendon Press, Oxford, 1974)*

Hayes W., Macdonald H.F., Elliott R.J. , *Phys. Rev. Lett. 15, 961 (1965)*

Inokuti M., Hirayama F. , *J. Chem. Phys. 43, 1978 (1965)*

Jacobs I.T. , *Ph.D. Thesis, University of Canterbury, 1971*

Jones G.D., Peled S., Rosenwaks S., Yatsiv S. , *Phys. Rev. 183, 353 (1969)*

Judd B.R. , *Operator Techniques in Atomic Spectroscopy , (McGraw Hill, N.Y., 1963)*

Kaminskii A.A., Kornienko L.S., Prokhorov A.M. , *Sov. Phys. JETP. 21, 844 (1965)*

Kaminskii A.A., Sobolev B.P., Bagdasarov Kh.S., Kevorkov A.M., Fedorov P.P., Sarkisov S.E., *Phys. Stat. Sol. A. 26, K63 (1974)*

Kariss Ya.E., Tolstoi M.N., Feofilov P.P. , *Opt. Spectrosc. 18, 247 (1965)*

Kask N.E., Kornienko L.S. , *Sov. Phys. Solid State 9, 1795 (1968)*

Kask N.E., Kornienko L.S. , *Sov. Phys. JTEP. 26, 331 (1968)*

Kask N.E., Kornienko L.S., Fakir M. , *Sov. Phys. Solid State 6, 430 (1964)*

Kask N.E., Kornienko L.S., Rybaltovskii A.O. , *Sov. Phys. Solid State 7, 2614 (1966)*

Kiel A. , *Multi-phonon Spontaneous Emmission in Paramagnetic Crystals in : Quantum Electronics. , Ed. Grivet P., Bloembergen N.(Columbia University Press, N.Y., 1964)*

Kiro D., Low W. , *Magnetic Resonance , Ed. Coogan C.K., Ham N.S., Stuart S.H., Pilbrow J.R., Wilson G.V.H. (N.Y., London, Plenum)*

Kiro D., Low W., Schipper D.J. , *Phys. Lett. 29A, 586 (1969)*

Kirton J., Mclaughlan S.D. , *Phys. Rev. 155, 279 (1967)*

Kiss Z.J. , *J. Chem. Phys. 38, 1476 (1963)*

Koster G.F., Dimmock J.O., Wheeler R.G., Statz H. , *Properties of the thirty-two point groups , (M.I.T. Press, Cambridge, Massachusetts, 1963)*

MacFarlane R.M. , *Phys. Rev. B. 1, 989 (1970)*

Maradudin A.A., Peretti J. , *Phys. Rev. 161, 852 (1967)*

McMahon T. , *Private communication with C.A. Freeth.*

Miyakawa T., Dexter D.L. , *Phys. Rev. B. 1, 2961 (1970)*

Moore D.S. , *Ph.D. Thesis, University of Wisconsin, Madison (1980)*

Newman D.J. , *Adv. Phys. 20, 197 (1971)*

Newman D.J. , *Aust. J. Phys. 31, 79 (1978)*

Newman R.C. , *Infrared Studies of Crystal Defects. , Ed. Coles B.R. and Mott N. (Monographs on Phys., 1973)*

Osiko V.V. , *Sov. Phys. Solid State 7, 1047 (1965)*

Osiko V.V., Shcherbakov I.A. , *Sov. Phys. Solid State 13, 820 (1971)*

Partlow W.D., Moos H.W. , *Phys. Rev. 157, 252 (1967)*

Popov V.V., Suyatin B.D. , *Sov. Phys. Solid State 16, 620 (1974)*

Prokhorrov A.M., Sychugov V.A., Schipulo G.P. , *Sov. Phys. JETP. 29, 970 (1969)*

Reddy B.R., Venkateswarlu P. , *J. Chem. Phys. 79, 5845 (1983)*

Reeves R.J. , *Ph.D Thesis, University of Canterbury, 1987*

Reeves R.J., Jones G.D., Cockroft N.J., Han T.P.J., Syme R.W.G. , *J. Lumin. 38, 198 (1987)*

Reid M.F. , *Ph.D. Thesis, University of Canterbury, 1981*

Reid M.F. , *Private communication, 1988*

Riseberg L.A., Gandrud W.B., Moos H.W. , *Phys. Rev. 159, 262 (1967)*

Riseberg L.A., Moos H.W. , *Phys. Rev. 174, 429 (1968)*

Riseberg L.A., Weber M.J. , *Relaxation Phenomena in Rare-Earth Luminescence (Progress in Optics XIV) , Ed. Wolf E. (North Holland, 1976)*

Schaefer G. , *J. Phys. Chem. Solids 12, 233 (1960)*

Secemski E., Kiro D., Low W., Schipper D.J. , *Phys. Lett. 31A, 45 (1970)*

Smalley J. , *Private communication with G.D. Jones.*

Stacy J.J., Edelstein N., Mclaughlin R.D., Conway J.G. , *J. Chem. Phys. 58, 807 (1973)*

Tallant D.R., Miller M.P., Wright J.C. , *J. Chem. Phys. 65, 510 (1976)*

Toledano J.C. , *J. Chem. Phys. 57, 1046 (1972)*

Vial J.C., Buisson R., Madeore F., Poirier M. , *Le Journal De Physique 40, 913 (1979)*

Vignaneswara U., Ramachandra Rao D., Venkateswarlu P. , *J. Chem. Phys. 67, 3448 (1977)*

Villermain-Lecolier G., Morlot G., Strimer P., Aubry J.P., Hadni A. , *Phys. Rev. B. 15, 130 (1977)*

Voron'ko Yu.K., Dmitruk M.V., Osiko V.V., Shcherbakov I.A. , *Sov. Phys. Solid State 13, 1348 (1971)*

Voron'ko Yu.K., Kaminskii A.A., Osiko V.V. , *Sov. Phys. JETP. 22, 295 (1966)*

Voron'ko Yu.K., Kaminskii A.A., Osiko V.V., Prokhorov A.M. , *Sov. Phys. JETP. Lett. 1, 120 (1965)*

Voron'ko Yu.K., Mikaelyan R.G., Osiko V.V. , *Sov. Phys. JETP. 26, 318 (1968)*

Voron'ko Yu.K., Osiko V.V., Shcherbakov I.A. , *Sov. Phys. JETP. 28, 838 (1969)*

Weber M.J. , *Phys. Rev. 171, 283 (1968)*

Wright J.C. , *Radiationless Processes in molecules and Condensed Phases Topics in Applied Physics, vol. 15. Ed. Fong F.K.*

Wybourne B.G. , *Spectroscopic Properties of Rare Earths , (Interscience Publishers, N.Y., 1965)*

Zalucha D.J., Sell J.A., Fong F.K. , *J. Chem. Phys. 60, 1660 (1974)*

Zalucha D.J., Wright J.C., Fong F.K. , *J. Chem. Phys. 59, 997 (1973)*